HARVARD UNIVERSITY
Graduate School of Arts and Sciences

DISSERTATION ACCEPTANCE CERTIFICATE

The undersigned, appointed by the

Division of Medical Sciences

Program in Neuroscience

have examined a dissertation entitled

Neurochemically distinct median raphe subsystems: unique hodology and presynaptic specializations

presented by Rebecca Alexis Senft

candidate for the degree of Doctor of Philosophy and hereby certify that it is worthy of acceptance.

Signature: David Ginty

Typed Name: Dr. David Ginty

Signature:

Typed Name: Dr. Bernat Kocsis

Signature: Todd Anthony

Typed Name: Dr. Todd Anthony

Signature: Corey Harwell (Jul 19, 2021 17:33 EDT)

Typed Name: Dr. Corey Harwell

Date: July 16, 2021

NEUROCHEMICALLY DISTINCT MEDIAN RAPHE SUBSYSTEMS: UNIQUE HODOLOGY AND PRESYNAPTIC SPECIALIZATIONS

A dissertation presented
by
Rebecca Alexis Senft
to
The Division of Medical Science
in partial fulfillment of the requirements
for the degree of
Doctor of Philosophy
in the subject of
Neurobiology

Harvard University

Cambridge, Massachusetts

July 2021

Dissertation Advisor: Susan M. Dymecki Rebecca Alexis Senft

Neurochemically distinct median raphe subsystems: unique hodology and presynaptic specializations

ABSTRACT

From their somata residing in the brainstem, neurons expressing the master serotonergic regulator gene *Pet1* (aka *Fev*) extend axonal projections to forebrain regions underlying such diverse functions as sleep, memory, olfaction, and emotional processing. Recent research has shown that *Pet1* neurons previously considered a serotonergic monolith are in fact highly diverse molecularly and hodologically, and further, that this diversity underlies subpopulation differences in function. Molecularly distinct subpopulations of *Pet1* neurons are not randomly distributed within the raphe nuclei but arise in part through developmental patterning (and associated gene expression). The second rhombomere (r2) of the developing hindbrain gives rise to two groups of *Pet1* cells: one classically serotonergic and one primarily glutamatergic (expressing high levels of vesicular glutamate transporter 3, VGLUT3, but with low expression of other serotonin neuron identity genes despite expression of *Pet1*). We mapped the projections arising from these two groups, finding r2-*Pet1* boutons of distinct (serotonergic vs. glutamatergic) phenotypes largely segregated to separate target regions, excepting the septum, which exhibited a mixed phenotype. Serotonin+ r2-*Pet1* boutons predominated in olfactory bulb, thalamus, and suprachiasmatic nucleus and VGLUT3+ boutons in the hippocampus, septum, and cortex. These results, combined with additional retrograde viral tracing and bouton phenotyping experiments, support a model of separable neuronal subsystems within the r2-*Pet1* lineage. Furthermore, some r2-*Pet1* neurons were observed to form pericellular baskets, an

intricate presynaptic specialization involving axons decorating the soma and proximal dendrites of their postsynaptic partner. We found that r2-*Pet1* pericellular baskets exhibit regional target specificity for certain subtypes of GABAergic neurons, often interneurons. We also revealed that pericellular baskets in the septum are commonly "composites" formed from axons of multiple *Pet1* neurons, indeed from multiple *Pet1* lineages, converging to form baskets on the same postsynaptic target cell. Further, these septal baskets were enriched for serotonin^{+}/VGLUT3^{+} co-positive boutons, indicating they are potentially specialized sites for co-transmission of glutamate and serotonin. We discuss at length the potential function of these pericellular baskets, as well as their roles as centers for neurotransmitter convergence deployed by *Pet1* neurons as well as across different classes of neurons expressing diverse neurotransmitter phenotypes. Through this research, we aim to inform brain organization and new circuit nodes for potential therapeutic considerations.

"I have no idea where this will lead us,
but I have a definite feeling it will be a place both wonderful and strange."

-- Special Agent Dale Cooper (Twin Peaks)

Acknowledgments

I am immensely grateful to all the mentors, teachers, peers, and friends I have had the pleasure of interacting with throughout my PhD training. The successes I've had as a researcher and scientist is owed to the people who trained me, discussed ideas with me, and supported me. It's impossible to thank everyone who's had a hand in my research, but here are some of the people who've greatly impacted my training and progress.

First, thank you to my PhD adviser, Dr. Susan Dymecki for your support and mentorship throughout these past six years. I feel immensely lucky to have found your lab. I distinctly remember one morning around 2 weeks into my rotation where I thought "Wow, the people in this lab are so supportive and kind and my PI makes the effort to meet with me, even as a rotation student. I really hope they want me to join…" And luckily for me, it worked out! I have always felt very at home in the Dymecki lab and much of that is due to Susan's ability to create a scientific community from a group of people.

Thank you to all Dymecki lab members who have made the lab what it is today. In no particular order, thank you to my fellow graduate students, Dr. Krissy Lyon and Nikita Sturrock who shared a bay with me and collaborated with me on a variety of projects, some successful, others less so, but they were always more fun to do with friends. Thank you to past graduate students Dr. Tedi Asher, who helped me get started in the lab during my rotation and taught me a ton about science, mouse work, and the serotonin neuron system, and Dr. Morgan Freret, who shared her science with me and was instrumental in the work that forms chapter two of this dissertation.

Thank you to the postdocs and research associates of the lab who have taught me all the technical skills I have, read drafts of my work, and vetted my ideas; my work is much stronger because of all your advice and input. Specifically, thank you to Dr. YoonJeung Chang for all our conversations about science and life and everything in between; to Dr. Ben Okaty for sharing his vast amount of expertise on the serotonin neuron system and neuroscience in general with me. I've also greatly enjoyed having someone else to talk to about movies. Thank you to Drs. Giacomo Maddaloni and Olga Alekseyenko for always being willing to share your expertise with me and for really fun collaborations to end my PhD with; to Dr. Yasmin Escobedo Lozoya for her enthusiasm and for our long scientific discussions and brainstorming sessions. Thank you to past research associate Dr. Ben Rood for helping me get started in the lab. Thank you also to Ms. Jia Jia Mai, our lab manager throughout the first five years of my PhD, who was always willing to train me on mouse work, genotyping, and was always willing to help troubleshoot and lend a helping hand. Thank you also to Ms. Mallory Rice, who has been instrumental in keeping our lab organized and whose scientific illustrations make our lab's work more understandable and approachable.

I would also like to thank mentors and peers from outside my lab that have played a formative role in shaping my training as a grad student and scientist. First, thank you to Dr. Paula Montero Llopis of the MicRoN core, whose support and belief in me has sustained me throughout my PhD. She also taught me so much about microscopy and our conversations have strengthened my research and her advice has guided me throughout my PhD. Thank you also do Ryan Stephansky and Dr. Tim J. Elliot-Ross, also of the MicRoN core, who helped me with training, consultations, and troubleshooting. Also, on the subject of microscopy and image

analysis, I am also grateful to Dr. Jennifer Waters and all the microscopists of the Nikon Imaging Center for their educational courses and workshops on microscopy. I also greatly benefitted from training at the Mouse Behavior Core of the Neurodiscovery Center, specifically from Dr. Barbara Caldarone who runs the core and trained me in several mouse behavioral assays and Paul Lorello, who trained me in mouse EEG surgery. I'd also like to thank Cimarron Schuyler, of the Harvard Center for Comparative Medicine, who very patiently helped train me on a variety of mouse handling and dose administration techniques. I would also like to acknowledge the help of Pavel Gorelik and Dr. Ofer Mazor of the Harvard Instrumentation Core who trained me in laser cutting and fabrication. They also designed and helped construct several apparatuses used in the lab for mouse behavior. Dr. Kruika Joshi of Dr. Veronique Vanderhorst's lab taught me how to analyze EEG traces using Spike2. I'd also like to thank Dr. Jin Hyung Cho, Dr. Xiao Han, Dr. Jiho Choi, Dr. Miguel Turrero Garcia, Dr. Steven Swendeman, and Dr. Jaime Ross for their support and for conversations about my research and future directions as a scientist.

I am also grateful to the Program in Neuroscience, which has been a tremendous community to me throughout my PhD. I'd like to thank my classmates for their support, especially during the early years and specifically Dr. Elizabeth Lamkin who was an inspiration and mentor figure for me. I'd like to thank PiN administration that keeps the program running, specifically Karen Harmin and Susan Jackson for their administrative support and Drs. David Ginty, Rosaline Segal, John Assad and Tari Tan for leading the program and coordinating the curriculum. I'd also like to thank Dr. Rick Born for giving me the opportunity to TA his classes. I would like to thank my exam committee of Drs. Bernat Kocsis, Todd Anthony, and Corey Harwell for reading this dissertation and giving me feedback. Finally, I'd like to thank Drs. David Ginty,

Amar Sahay and Gord Fishell for serving on my dissertation advisory committee and always doing whatever they could to connect me to experts and people who could train me and advising me on scientific directions to pursue. Their support was also critical throughout the highs and lows of my PhD.

Before ending, I'd like to thank some of the non-neuroscience people in my life that have supported me throughout my PhD. First, I'd like to thank my partner, Erika for always being supportive and helping me stay balanced throughout my PhD. I can't imagine being where I am now without you. I'd also like to thank Dr. Alexander Noyes, a dear friend I met in college, for celebrating and supporting me. I'd also like to thank Jessie Hummel for her friendship, my sister Jessica, my parents, and Erika's parents for always supporting me and thinking the world of me.

Finally, I would like to thank my funding sources: my PhD research was funded by the National Institute of Health (NIH) training grant NIH T32 EY007110, the Genetics Department at Harvard Medical School, and NIH fellowship F31 NS 108406.

TABLE OF CONTENTS

List of Figures

Chapter I.

Introduction

Authors and Contributions

I wrote this chapter with input from my adviser, Dr. Susan M. Dymecki.

Overview

Neurons expressing the master serotonergic regulator gene *Pet1* (also known as *Fev*) modulate a range of functions, from vital homeostatic processes involving thermal balance and respiratory dynamics to stress coping responses and aspects of learning and memory. This diverse functional repertoire is enabled via a complex network of highly collateralized efferent projections from these *Pet1* neurons that collectively reach throughout the brain and spinal cord (Jacobs and Azmitia 1992). A major pursuit in the field has revolved around deconstructing this system, deciphering which specific serotonergic (*Pet1*$^{+}$) neurons innervate which brain targets and underlie specific behaviors and physiological and cognitive processes. This pursuit is made more complex – but perhaps also facilitated – by recently revealed heterogeneity of *Pet1* neurons.

Recent investigations into the mouse *Pet1* neuronal system have described subtypes of *Pet1* neurons whose functions are circumscribed, specialized, and separable, reflected in differences at multiple levels – molecularly, developmentally, hodologically, neurochemically, and functionally (reviewed in Deneris and Gaspar 2018; Okaty et al. 2019). For example, the Dymecki lab and others have developed intersectional (Cre- and Flp-dependent) genetic tools to label and manipulate subtypes of *Pet1* neurons, thereby allowing system study at finer resolution (Awatramani et al. 2003; Jensen et al. 2008). Our general approach has involved combining a pan-serotonergic *Pet1-Flpe* transgenic driver iteratively with overlapping Cre

drivers to recombine or "activate" expression of dual, Cre-/Flp-dependent reporter and/or effector transgenes only in cells with a history of both Cre and Flpe expression. (Awatramani et al. 2003; Jensen et al. 2008; Kim et al. 2009; Brust et al. 2014; Okaty et al. 2015; Plummer et al. 2015; Teissier et al. 2015; Sciolino et al. 2016). By leveraging these tools, we can split the *Pet1* neuron system into smaller, molecularly and therefore likely mechanistically, distinct subgroups for experimental study. Such discovery and detailed mapping of functionally distinct subsystems within the serotonergic system informs not only basic brain architecture but also more specific nodes for possible therapeutic interventions.

Molecularly distinct subpopulations of *Pet1* neurons arise in part through networks of gene expression turned on during embryonic development (Jensen et al. 2008; Alonso et al. 2013; Okaty et al. 2015). *Pet1* neurons arise from a ventral progenitor zone within the embryonic hindbrain, which is organized rostrocaudally into segmented progenitor cell compartments called rhombomeres (Keynes and Lumsden 1990; Lumsden 1990). *Pet1* neurons of a shared rhombomeric origin (loosely referred to as a *Pet1* rhombomeric 'lineage') have broadly similar patterns of gene expression in the adult mouse as assessed by single cell RNA sequencing (scRNAseq; Okaty et al. 2015). Further, these *Pet1* rhombomeric lineages exhibit specificity in their patterns of innervation and functional repertoires. However, even within a *Pet1* neuron rhombomeric lineage, molecularly distinct subtypes can emerge.

The second rhombomere (r2) of the developing hindbrain gives rise to two neurochemically distinct groups of *Pet1* neurons: one, expectedly, that is serotonergic, and another, surprisingly, that is primarily glutamatergic and lacks serotonin despite persistent expression of *Pet1* and a subset of genes associated with serotonin neuron identity (Okaty et al.

2015). Current tools for axonal projection mapping have allowed for en masse study of r2-*Pet1* neurons, which revealed efferents targeting many forebrain regions critical for memory, circadian rhythms, and emotional behaviors such as the hippocampus, suprachiasmatic nucleus of the hypothalamus, and septum (Bang et al. 2012). In line with predictions based on these innervation targets, manipulating the activity of r2-*Pet1* neurons en masse alters sensorimotor gating (Okaty et al. 2015) and the durability of cocaine-conditioned memories and place preference behaviors (Baskin et al. 2020). However, unknown is the contribution made by each of the two constituent r2-*Pet1* subpopulations and how they may relate to separable circuits and subserved functions. The focus of this dissertation is characterizing the efferent locations and neurochemical phenotypes of r2-*Pet1* axonal boutons and their remarkable presynaptic specializations. Through this work, we reveal what appear to be two separable *Pet1* neuronal subsystems. This introductory chapter provides necessary background information on the development and molecular heterogeneity of *Pet1* neurons in general and the specific subset of *Pet1* neurons studied in this dissertation (r2-*Pet1* cells), including known functional roles and projection-mapping results.

PET1 NEURONS, THEIR ANATOMICAL ORGANIZATION AND DEVELOPMENT

The gene *Pet1* encodes a transcription factor of the E26 transformation-specific (ETS) family that binds to and orchestrates the expression of a suite of genes necessary for post-mitotic precursor neurons to acquire a serotonin (5-hydroxytryptamine; 5-HT) neuron identity (Fyodorov et al. 1998; Hendricks et al. 2003). Several of these serotonergic pathway genes are directly regulated by PET1 binding *in vivo*. These include: *Tph2*, encoding tryptophan

hydroxylase 2 (TPH2), which is the rate-limiting enzyme in the serotonin synthesis pathway; *Sert* (aka *Slc6a4*), encoding the serotonin reuptake transporter; and *Htr1a*, encoding the 5-HT autoreceptor 5-HT1a (Liu et al. 2010; Jacobsen et al. 2011). PET1 activity is also necessary for inducing the expression of: *Ddc*, encoding DOPA decarboxylase (DDC), the enzyme catalyzing the final step in serotonin synthesis; *Vmat2*, encoding the vesicular monoamine transporter 2 (VMAT2) that packages monoamines like serotonin into vesicles; and MAOB, encoding Monoamine Oxidase B (MAO-B), an enzyme that degrades serotonin (reviewed in Deneris and Wyler 2012; Okaty et al. 2019).

In the brain, *Pet1* expression is generally thought to be limited to serotonin-producing neurons (Pfaar et al. 2002; Hendricks et al. 2003) and *Pet1* drivers of recombinase expression such as *ePet1-cre* and *Pet1-Flpe* have been used as tools to access and manipulate 5-HT neurons (Scott et al. 2005; Jensen et al. 2008; Liu et al. 2010). However, recent work has shown some *Pet1*-expressing neurons in the mouse brainstem are, at least at the time of tissue harvest, immunonegative for 5-HT and TPH2 and express low levels of *Tph2* mRNA (Alonso et al. 2013; Pelosi et al. 2014; Okaty et al. 2015, 2020; Sos et al. 2017). Some of these neurons also express a limited subset of 5-HT neuron identity genes, including *Ddc*, *Htr1a*, and *Vmat2* (Okaty et al. 2015). This 'partial' serotonergic identity may suggest that these cells retain an ability to become 5-HT^{+} under certain environmental conditions or internal states (Okaty et al. 2019). Thus, in the brain, *Pet1* expression marks serotonergic neurons and also a smaller group of related but serotonin^{-} neurons. Understanding the *Pet1* neuronal system necessitates mapping the efferents and downstream circuitry regulated by both of these types of *Pet1* cells. Further, both types of

Pet1 neurons are likely sensitive to 5-HT-mediated feedback through 5-HT1a autoreceptor expression, suggesting possible interactions mediated by intra-raphe serotonin release.

Pet1-expressing neurons distribute throughout the brainstem raphe nuclei, similarly in humans and rodents. Altogether, serotonin neurons comprise a group representing less than 0.05% of all neurons in the brain and numbering 20,000-26,000 neurons in mice (Ishimura et al., 1988) and 300,000-450,000 in humans (Halliday et al. 1988; Baker et al. 1990, 1991; Hornung 2003). In adult rodents, *Pet1* neurons are found in clusters described as nuclei B1 through B9 proceeding from most caudal brainstem to most rostral (Dahlstroem and Fuxe 1964; Figure 1.1). The median raphe, the focus of this dissertation, is a midline rostral grouping of neurons that includes nuclei B8 and B5, which are also referred to respectively as the caudal linear nucleus along with the prepontine raphe nucleus, and the pontine raphe nucleus (Jacobs and Azmitia 1992; Alonso et al. 2013). The median raphe houses a fraction of all serotonin neurons, in mice ~1,700 with ~2,400 neurons marked by *Pet1* drivers, the latter, larger number also encompassing those *Pet1* neurons lacking immunodetectable 5-HT (Pelosi et al. 2014; Sos et al. 2017; Okaty et al. 2020). Additionally of interest is B9, a lateralized group of cells also referred to as the supralemniscal raphe nucleus that is present in rostral sections containing the median raphe (Alonso et al. 2013). This general anatomical organization is shared across mammalian species (Jacobs and Azmitia 1992).

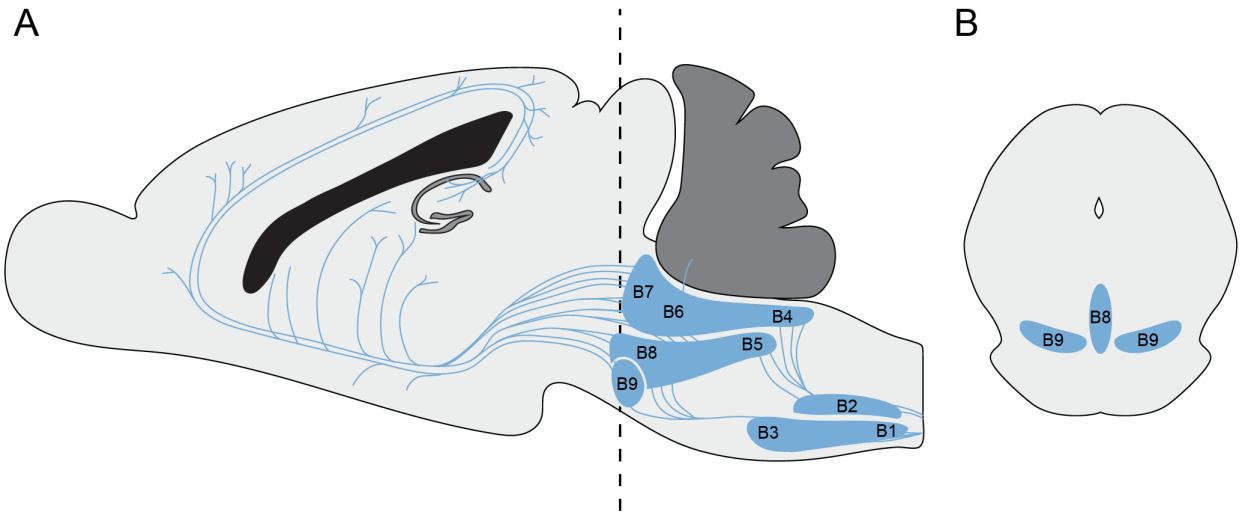

Figure 1.1. Anatomy of brainstem raphe nuclei in mouse

Sagittal schematic of the mouse brain depicting serotonergic raphe nuclei (B1-B9) and axonal projections to the forebrain in blue (A). A coronal schematic corresponding to the dotted line in A is shown with B8 and B9 labeled (B).

The mature organization of *Pet1*-expressing neurons arises through developmental patterning, which forms the basis for one means of delineating *Pet1* neurons into physiologically relevant subgroups. *Pet1* neurons are born between E10 and E12 in rodents and originate from a ventral progenitor zone that spans the rostrocaudal extent of the hindbrain (Olson and Seiger 1972; Lidov and Molliver 1982; Wallace and Lauder 1983). At this time, the embryonic hindbrain is organized into transverse segments called rhombomeres, distinguished by unique combinatorial expression of transcription factors that act to turn on different programs of gene expression (Schneider-Maunoury et al. 1993; McKay et al. 1994; Lumsden and Krumlauf 1996; Deschamps et al. 1999; Chambers et al. 2009). Thus, *Pet1* neuron precursors too are segmented by these patterns of gene expression. In some neuron types, rhombomere-restricted gene expression can give rise to specific functional groups, though others span several rhombomeres

(Pattyn et al. 2003; Pasqualetti et al. 2007). Rhombomere-specific gene expression has lasting impacts on aspects of *Pet1* neuron identity. *Pet1* neurons from the same rhombomeric lineage maintain similarities in their patterns of gene expression in the adult (Okaty et al. 2015, 2020) and compose functional units (Kim et al. 2009; Brust et al. 2014; Okaty et al. 2015; Teissier et al. 2015), making rhombomeric origin is a critical lens through which to explore *Pet1* neurons (Jensen et al. 2008).

This dissertation focuses on a rhombomeric lineage of median raphe *Pet1* neurons derived from rhombomere 2 (r2), the r2-*Pet1* subgroup. This group is accessed by partnering a rhombomere 2-specific transgene driving Cre expression (*r2Hoxa2-cre;* Awatramani et al. 2003) with the pan-serotonergic *Pet1-Flpe* transgene and a dual recombinase response Cre- and Flp-dependent reporter or effector *R26* allele (Jensen et al. 2008; Figure 1.2). r2-*Pet1* neurons are distributed throughout the median raphe (B8, B5) and B9 nucleus in the mouse (Figure 1.3), where they are intermingled with *Pet1* neurons from r1 and r3 (Jensen et al. 2008; Okaty et al. 2015). However, unlike many other lineages of *Pet1* neuron, r2-*Pet1* neurons exhibit a striking molecular subdivision based on genes related to neurotransmitter release, prompting our neurochemical profiling of r2-*Pet1* efferents (Chapter 2).

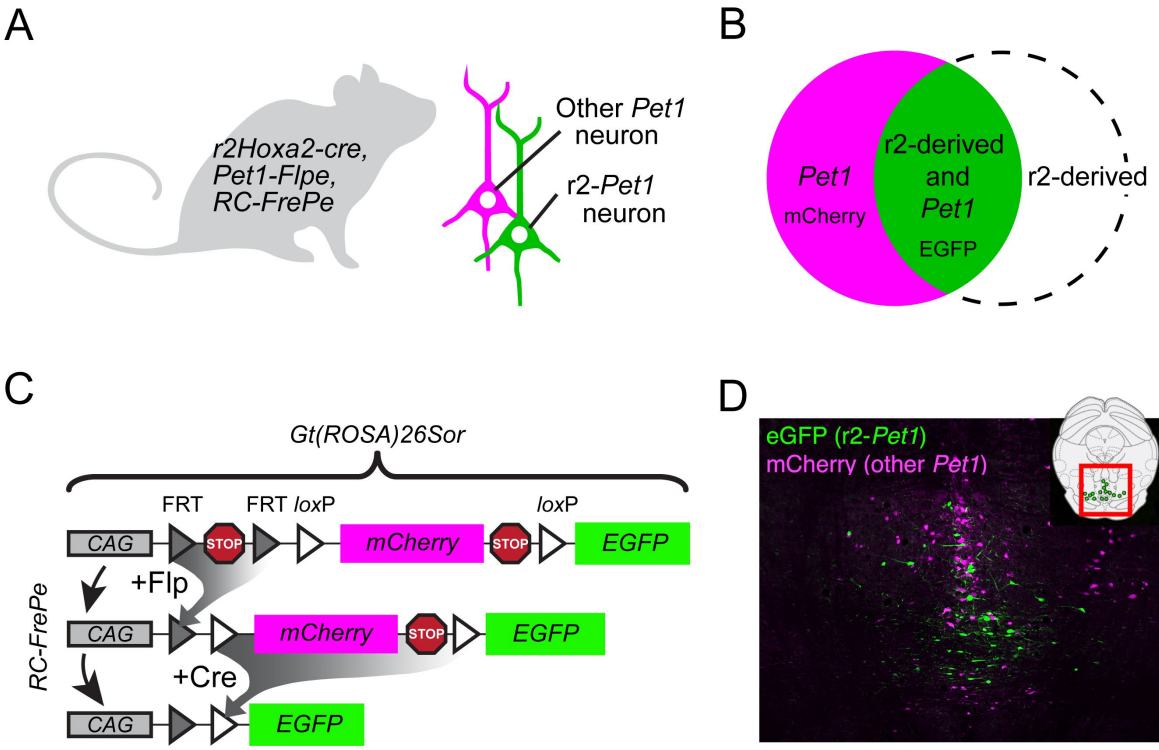

Figure 1.2 Example of an intersectional transgene for labeling *Pet1* neuron subpopulations

A cartoon of a triple transgenic *r2Hoxa2-cre, Pet1-Flpe, RC-FrePe* mouse with differentially fluorescently labeled r2-*Pet1* neurons and other *Pet1* neurons (A) and corresponding Venn diagram illustration depicting 'intersectional' r2-*Pet1* neurons and 'subtractive' (i.e., non-r2) *Pet1* populations (B). An example schematic showing recombination of the *Gt(ROSA)26Sor* knock-in allele *RC-FrePe* (Brust et al. 2014) (C). In r2-*Pet1* neurons (green), the expression of Flpe and Cre causes recombination at the FRT and *lox*P sites (respectively), resulting in EGFP expression, fluorescently labeling r2-*Pet1* neurons. In the subtractive (non-r2) *Pet1* neuron population (red), Flpe-mediated removal of the stop cassette flanked by FRT sites results in red fluorescent labeling by mCherry expression. Example image in (D). Panels A and C adapted from (Senft et al. 2021).

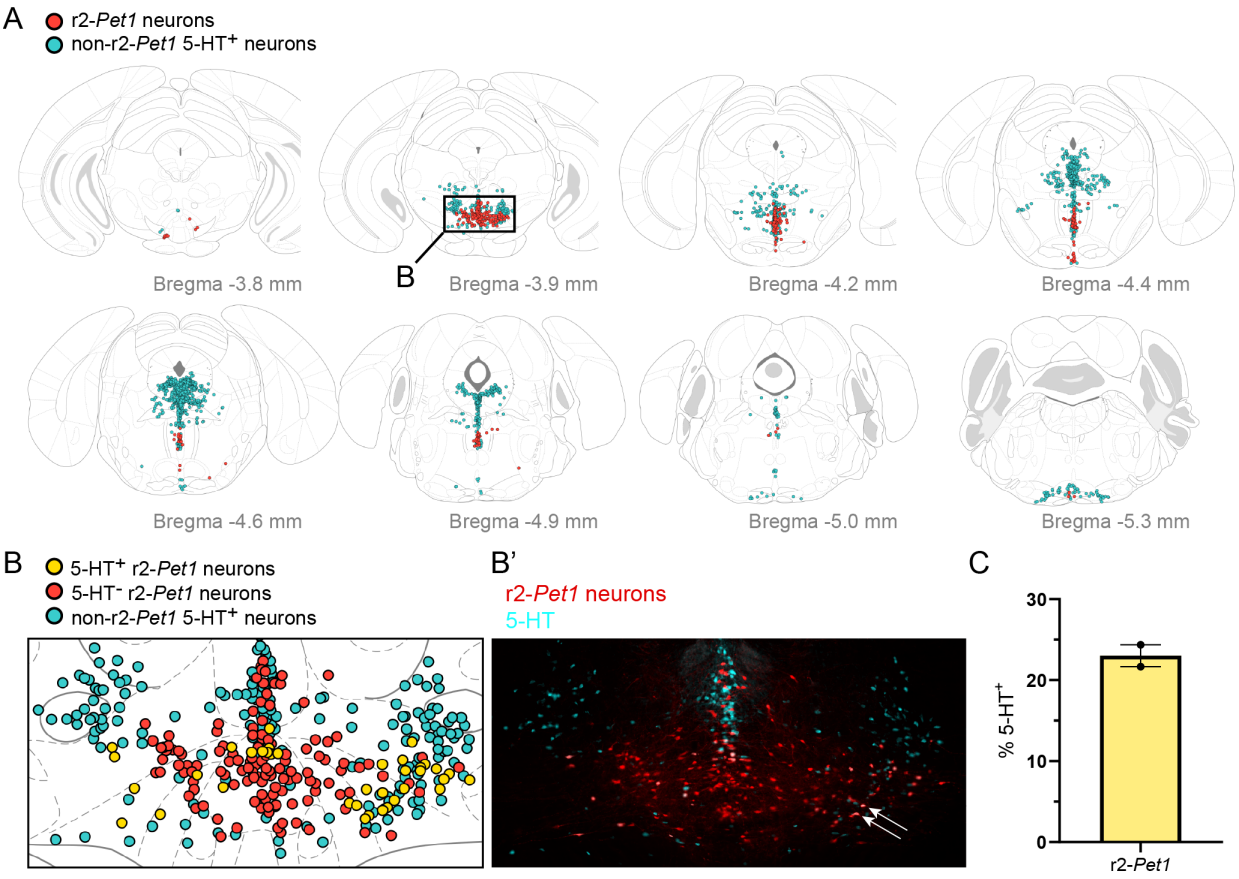

Figure 1.3. Distribution and serotonin immunoreactivity of r2-*Pet1* neurons

Cell somata of r2-*Pet1* neurons as labeled with the *RC-Ai65* reporter allele (red) relative to the distribution of non-r2-*Pet1* 5-HT$^+$ somata (teal) throughout the rostro-caudal axis (A). An inset shows the location most abundant for r2-*Pet1* somata, intermingled with other 5-HT$^+$ neurons (B) and corresponding fluorescence image (B'). A minority of r2-*Pet1* neurons were 5-HT$^+$ (yellow dots in B and arrows indicate a few of many examples in B'), quantified in C. Atlas schematics in A are adapted from Franklin and Paxinos, 2008.

R2-*PET1* NEURONS: MOLECULAR PROPERTIES AND EN MASSE EFFERENT PROJECTIONS

r2-*Pet1* neurons in the adult brainstem exhibit one of two gross soma phenotypes based on expression of genes related to neurochemical identity. scRNAseq of r2-*Pet1* neurons revealed that roughly one third of r2-*Pet1* neurons exhibit a typical serotonergic phenotype, with high expression of serotonin neuron identity genes, including *Tph2* and *Sert* (Okaty et al., 2015).

Approximately two-thirds of the r2-*Pet1* neuron population, though, lack immunodetectable levels of 5-HT at the soma and express low levels of *Tph2* and *Sert* mRNA, even in the face of *Pet1* expression; these cells do express other monoamine synthesis and packaging-related genes such as *Ddc* and *Vmat2*. This nonclassical *Tph2*^{low} subset of r2-*Pet1* neurons expresses high levels of *Vglut3* (also known as *Slc17a8)*, encoding the glutamate transporter 3 (VGLUT3) that packages glutamate into synaptic vesicles and indicates glutamate neurotransmission (Trudeau 2004; Amilhon et al. 2010; El Mestikawy et al. 2011). Notably, many serotonergic neurons (e.g. in the dorsal raphe nucleus) express high levels of both *Tph2* and *Vglut3* (Okaty et al. 2015) and have been shown to co-transmit 5-HT and glutamate (Liu et al. 2014; Sengupta et al. 2017; Ren et al. 2018). However, for r2-*Pet1* neurons of the MR, this is not the case – most cells are either serotonergic or glutamatergic but not both (Okaty et al. 2015). We refer to these serotonergic and putative glutamatergic r2-*Pet1* neuron subpopulations as r2-*Pet1*$^{Tph2\text{-high}}$ and r2-*Pet1*$^{Vglut3\text{-high}}$ respectively.

Though the projections of r2-*Pet1* neurons have been mapped grossly (Bang et al. 2012), the contribution of the r2-*Pet1*$^{Tph2\text{-high}}$ and r2-*Pet1*$^{Vglut3\text{-high}}$ subtypes to these efferents is unknown. Using an intersectional allele, *RC-FrePe* (Brust et al. 2014), in which eGFP is expressed intersectionally in neuron somata and projections, Bang et al. (2012) mapped the innervation targets of r1- r2- and collectively r3/5 *Pet1* neurons. r2-*Pet1* neurons densely innervate the hippocampus, septum, suprachiasmatic nucleus of the hypothalamus, basolateral amygdala, and parietal and prelimbic cortex. This pattern differed from r1-*Pet1* neurons, which had widespread axons also innervating the ventral tegmental area and striatum and from r3/5-*Pet1* neurons, which heavily innervated the brainstem, including the dorsal tegmental nucleus of Gudden,

parabrachial nucleus and locus coeruleus. A caveat in this study is the *RC-FrePe* allele intersectionally expresses cytoplasmic eGFP, which would label not only axonal boutons but also fibers of passage that make no functional sites of neurotransmitter release. The authors also did not explore the neurochemical phenotype of axonal boutons in innervated regions. This motivated our exploration of r2-*Pet1* axonal boutons using the *R26 RC-FPSit* allele, wherein an intersectionally expressed synaptophysin-GFP fusion protein labels sites where neurotransmitter vesicles are released. By combining this genetic strategy with multiplexed immunohistochemistry, we queried the neurochemical phenotypes of r2-*Pet1* axonal boutons at key regions revealed by Bang et al., 2012. Our findings (Chapter 2) suggest two distinct and separable subsystems, r2-*Pet1*$^{Vglut3\text{-high}}$ innervating the hippocampus, septum, and cortex and r2-*Pet1*$^{Tph2\text{-high}}$ innervating the olfactory bulb, suprachiasmatic nucleus, and the paraventricular nucleus of the thalamus.

R2-*PET1* NEURONS FORM PRESYNAPTIC STRUCTURES CALLED PERICELLULAR BASKETS

In the process of mapping and neurochemically profiling efferents of r2-*Pet1* axons, we observed that in select target regions, some of their axons form pericellular baskets: specialized presynaptic structures wherein many axonal boutons decorate the soma and proximal dendrites of a downstream neuron (Curtis et al. 1970; Köhler et al. 1982). The numerous boutons in pericellular baskets and their positioning proximal to the postsynaptic soma and axonal hillock confer upon the presynaptic neuron privileged control over its target neuron, such as the ability to potentially override inputs received at distal dendritic locations (Miles et al. 1996; Acsády et al. 2000; Veres et al. 2017). Pericellular baskets have been observed for 5-HT^{+} fibers (Köhler et al.

1982; Gall and Moore 1984; DeFelipe et al. 1991; Dinopoulos et al. 1993; Font et al. 1997; Aznar et al. 2004; Riedel et al. 2008) as well as for other fiber types, including glutamatergic, GABAergic, noradrenergic, dopaminergic, substance P and enkephalinergic fibers (Ljungdahl et al. 1978; Gall and Moore 1984; Verney et al. 1987; Font et al. 1997; Paspalas and Papadopoulos 1999; Acsády et al. 2000; Hioki et al. 2004; Somogyi et al. 2004; Riedel et al. 2008; Amilhon et al. 2010; Armstrong and Soltesz 2012; Bartos and Elgueta 2012; Fasano et al. 2017; Szőnyi et al. 2019a). These different types of pericellular basket often overlap in their regional distributions, such as in the septum (Köhler et al. 1982; Gall and Moore 1984; Riedel et al. 2008), though few accounts have explored the degree to which neurochemically distinct pericellular baskets target the same downstream soma (Aznar et al. 2004; Riedel et al. 2008) or the identity of cells targeted by pericellular baskets, except in the case of cortical basket cell interneurons whose targets and physiology are well-characterized (Armstrong and Soltesz 2012; Fasano et al. 2017). We sought to characterize those pericellular baskets made by *Pet1* neurons. We profiled bouton neurochemical phenotypes and examined whether axons from different *Pet1* lineages form baskets around the same downstream neurons. We further investigated the cell types targeted by *Pet1* pericellular baskets (Chapter 2). Finally, we queried the literature to explore the potential functions and interactions between different neurotransmitter systems that form pericellular baskets (Chapter 3).

r2-*Pet1* neurons regulate sensorimotor gating and drug reward memory

Research manipulating r2-*Pet1* neurons en masse has identified functions subserved in the mouse. This section will focus on observed effects of modulating r2-*Pet1* neuron activity on

sensorimotor gating and cocaine memory durability, though a variety of behavioral assays have been tested (Okaty et al. 2015; Teissier et al. 2015). Previous work has chronically silenced r2-*Pet1* neurons by intersectionally expressing the tetanus toxin light chain, which cleaves VAMP2 and thus prevents synaptic vesicle exocytosis (Kim et al. 2009; Okaty et al. 2015). Mice were then assayed in a battery of behavioral tests, which revealed altered behavior in the prepulse inhibition (PPI) assay, in which mice are placed on a transducer platform that measures the magnitude of their reflexive startle in response to acoustic stimuli. Prepulse inhibition refers to the phenomenon in which the magnitude of startle to a loud stimulus is reduced if it is preceded by a softer stimulus (a prepulse) (Geyer et al. 2002). PPI is reduced in psychiatric disorders like schizophrenia (Mena et al. 2016) and post-traumatic stress disorder (Grillon et al. 1996; Pineles et al. 2016; Shoji and Miyakawa 2018). Acute serotonin depletion disrupts PPI (Fletcher et al. 2001; Mann et al. 2008) and serotonin receptor agonists have been shown to modify PPI in rodents (Sipes and Geyer 1994; Dulawa et al. 2000; Vigli et al. 2019). Mice with chronically silenced r2-*Pet1* neurons exhibited increased PPI relative to littermate controls, suggesting enhanced sensorimotor gating (Okaty et al. 2015). This effect was of comparable magnitude to that observed on silencing all Pet1 neurons and was not recapitulated by silencing r1- and isthmus derived *Pet1* neurons. These findings suggest that the task of modulating sensorimotor gating is selectively performed by r2-*Pet1* neurons as opposed to other *Pet1* neurons. Circuitry that regulates PPI is still being mapped in rodents, but in addition to brainstem regions, the hippocampus, medial septum, and medial prefrontal cortex are all implicated as modulators of PPI (Swerdlow et al. 2001) and are innervated by r2-*Pet1* fibers. We queried the neurochemical

phenotype of r2-*Pet1* boutons in several PPI circuit nodes to query the subtype(s) of r2-*Pet1* neuron that may specifically modulate PPI (Chapter 2 and 4).

A second study from our group has found that r2-*Pet1* neurons regulate the durability of cocaine-conditioned memory (Baskin et al. 2020). Authors acutely chemogenetically inhibited r2-*Pet1* neurons using an intersectional allele expressing the designer receptor exclusively activated by designer drug (DREADD) modified human muscarinic M4 receptor (hM4Di) (Armbruster et al. 2007) in a Cre- and Flp- dependent manner (Ray et al. 2011). In the presence of the DREADD-specific ligand, clozapine-N-oxide (CNO), $G_{i/o}$ coupled to hM4Di induces a hyperpolarizing G protein inward-rectifying potassium channel (GIRK) current, inhibiting neuronal firing (Armbruster et al. 2007). Mice expressing hM4Di in r2-*Pet1* neurons were used to assess how acutely inhibiting these neurons affects the expression and development of cocaine-conditioned place preference (CPP), in which mice are repeatedly dosed with cocaine and exposed to a particular environmental context to condition the animals to associate the drug stimulus with the context (McKendrick and Graziane 2020). A separate vehicle injection and visually distinct (and often also distinct in odor or tactile sensation) environmental context is used for a control. After conditioning, the preference for the drug-associated environment vs. vehicle-associated is assessed in the absence of cocaine. Typical behavior is for the memory of the rewarding cocaine stimulus to drive a conditioned response to spend more time in the cocaine-associated chamber during the test phase. Upon repeated presentation to the cocaine-conditioned environment without further cocaine injection, the cocaine memory becomes extinguished and behavioral place preference disappears. The authors first inhibited r2-*Pet1* neurons during the testing phase only, finding no effect of r2-*Pet1* neuron inhibition on the

expression of an already formed association between an environmental context and cocaine (Baskin et al. 2020). However, inhibiting r2-*Pet1* neurons throughout the conditioning phase resulted in a failure to extinguish the preference for the cocaine-associated context, even in the cocaine-free state. This suggests that r2-*Pet1* neurons are normally important in limiting the durability of the cocaine-conditioned memory. Cocaine-conditioned place preference is a complex behavior involving many neural substrates that process memory of previous drug experience, evaluate the drug for positive or negative valence over the course of conditioning, and initiate the locomotor activity and exploration of the possible chambers (McKendrick and Graziane 2020). There are then several possible candidate regions receiving r2-*Pet1* innervation that could be responsible for these effects. These include the hippocampus, important in retrieval and extinction of place preference (Hitchcock and Lattal 2018) and the prelimbic cortex and lateral hypothalamus, which both exhibit increased *c-fos* expression upon reinstating CPP after extinction, indicating these regions are active during cocaine memory reinstatement (Brown et al. 2010). The relative contribution of each subpopulation of r2-*Pet1* neuron to CPP extinction is unknown, though each subpopulation is poised to release different neurotransmitters and could influence CPP and PPI through neurochemically distinct mechanisms. Knowledge of how the r2-*Pet1*$^{Tph2\text{-high}}$ versus r2-*Pet1*$^{Vglut3\text{-high}}$ subtypes innervate the regions involved in CPP and PPI will allow us to form hypotheses for how these behavioral effects are manifested and could further generate hypotheses for other behaviors that may be differentially regulated by the r2-*Pet1*$^{Tph2\text{-high}}$ versus r2-*Pet1*$^{Vglut3\text{-high}}$ subgroups.

SUMMARY AND GOALS FOR THIS DISSERTATION

In this first chapter, I have introduced *Pet1* neurons, a molecularly diverse group of cells that encompasses brain serotonergic neurons plus cell variants that harbor little somatic 5-HT nor *Tph2* and *Sert* mRNA but do express other serotonergic pathway genes such as *Ddc* and *Vmat2*, and express *Vglut3* suggesting glutamate neurotransmission. Both the classical serotonergic as well as non-classical glutamatergic *Pet1* neuron subtypes arise from rhombomere 2 (r2) *Pet1* cells. Studying how these two r2-*Pet1* subgroups segregate or intermingle their projections will greatly enhance our overall understanding of how the median raphe is organized. Additionally, through this mapping, we can generate hypotheses regarding specific neural substrates and circuits underlying r2-*Pet1* regulation of sensorimotor gating and cocaine memory durability.

In this dissertation research, I have leveraged the intersectional genetic tools developed by the Dymecki lab to neurochemically profile the axonal boutons of r2-*Pet1* cells. From these results, I developed a model of how the neurotransmitter phenotype of r2-*Pet1* neuron subgroups maps onto their hodology. I also describe r2-*Pet1* pericellular baskets, unique presynaptic specializations formed by multiple neurotransmitter systems that provide privileged input to downstream targeted neurons. From these results, I launch an exploration into the potential role of these baskets as sites of neurotransmitter convergence and speculate on possible functions. Finally, the appendices provide additional data querying potential functions of r2-*Pet1* neurons and the *Pet1* neuron system more broadly in regulating behavior and describe some of the microscopy and image analysis tools developed as part of my dissertation work.

CHAPTER II.

NEUROCHEMICALLY AND HODOLOGICALLY DISTINCT ASCENDING VGLUT3 VERSUS SEROTONIN SUBSYSTEMS COMPRISE THE R2-*PET1* MEDIAN RAPHE

Authors and Contributions

This chapter was published as Senft, R.A., Freret, M.E., Sturrock, N., and Dymecki, S.M., Neurochemically and Hodologically Distinct Ascending VGLUT3 versus Serotonin Subsystems Comprise the r2-Pet1 Median Raphe. Journal of Neuroscience 24 March 2021, 41 (12) 2581-2600;

***Author contributions**: M.E.F. and I each designed, performed, and analyzed data from* in situ *hybridization experiments on r2-*Pet1 *cells. M.E.F. and I designed the bouton neurochemical phenotyping experiment, I designed the imaging and quantification for the data. I designed, performed, and analyzed data from the retrograde tracing, basket bouton phenotyping and basket target quantification experiments. N.S. designed and performed the experiments characterizing* Piezo2-Pet1 *neurons and she analyzed the soma data, while I analyzed the bouton phenotyping data. Every author contributed to writing the manuscript, with myself writing the majority. Figures were generally made by the author analyzing the data for that experiment with input from myself and S.M.D.*

Abstract

Brainstem median raphe (MR) neurons expressing the serotonergic regulator gene *Pet1* send collateralized projections to forebrain regions to modulate affective, memory-related, and circadian behaviors. Some *Pet1* neurons express a surprisingly incomplete battery of serotonin pathway genes, with somata lacking transcripts for *tryptophan hydroxylase 2 (Tph2*) encoding the rate-limiting enzyme for serotonin (5-hydroxytryptamine, 5-HT) synthesis, but abundant for *vesicular glutamate transporter 3* (*Vglut3*) encoding a synaptic-vesicle associated glutamate transporter. Genetic fate maps show these non-classical, putatively glutamatergic *Pet1* neurons

in the MR arise embryonically from the same progenitor cell compartment – hindbrain rhombomere 2 (r2) – as serotonergic TPH2^{+} MR *Pet1* neurons. Well established is the distribution of efferents *en masse* from *r2*-derived, *Pet1*-neurons; unknown is the relationship between these efferent targets and the specific constituent source-neuron subgroups identified as r2-*Pet1*$^{Tph2\text{-high}}$ versus r2-*Pet1*$^{Vglut3\text{-high}}$. Using male and female mice, we found r2-*Pet1* axonal boutons segregated anatomically largely by serotonin^{+} versus VGLUT3^{+} identity. The former present in the suprachiasmatic nucleus, paraventricular nucleus of the thalamus, and olfactory bulb; the latter are found in the hippocampus, cortex, and septum. Thus r2-*Pet1*$^{Tph2\text{-high}}$ and r2-*Pet1*$^{Vglut3\text{-high}}$ neurons likely regulate distinct brain regions and behaviors. Some r2-*Pet1* boutons encased interneuron somata, forming specialized presynaptic "baskets" of VGLUT3^{+} or VGLUT3^{+}/5-HT^{+} identity; this suggests that some r2-*Pet1*$^{Vglut3\text{-high}}$ neurons may regulate local networks, perhaps with differential kinetics via glutamate versus serotonin signaling. Fibers from other *Pet1* neurons (non-r2-derived) were observed in many of these same baskets, suggesting multifaceted regulation. Collectively, these findings inform brain organization and new circuit nodes for therapeutic considerations.

INTRODUCTION

Neurons of the brainstem median raphe (MR) that express the serotonergic regulator gene *Pet1* (aka *Fev*) project to numerous forebrain sites (Kosofsky and Molliver 1987; Kiyasova and Gaspar 2011; Bang et al. 2012; Gaspar and Lillesaar 2012) to modulate diverse processes including emotional behavior (Abela et al., 2020, Teissier et al., 2015), sensorimotor gating (Okaty et al. 2015), memory (Ohmura et al. 2010; Baskin et al. 2020), and sleep and circadian

rhythms (Meyer-Bernstein and Morin 1996; Glass et al. 2003; Iwasaki et al. 2018). Recent work shows that some of these MR *Pet1* neurons, even with their expression of *Pet1*, lack detectable transcript levels for various serotonin pathway genes (Pelosi et al. 2014; Okaty et al. 2015; Sos et al. 2017; Okaty et al. 2019; Ren et al. 2019), but demonstrate high levels of *Slc17a8* (alias *Vglut3*) mRNA, which encodes the type-3 transporter (VGLUT3) for loading glutamate into synaptic vesicles. Genetic fate maps coupled with single-cell transcriptomic analyses show that these *Vglut3*$^{+}$, *Tph2*$^{-}$, putative glutamatergic MR *Pet1* neurons arise embryonically from the same progenitor cell compartment – hindbrain rhombomere 2 (r2) – as do more classically serotonergic *Tph2*$^{+}$, serotonin (5-HT)$^{+}$ MR *Pet1* neurons (Okaty et al. 2015). Though the brain regions innervated by the collective r2-derived *Pet1* neuron population have been mapped (Bang et al. 2012), the degree to which the non-classical, r2-*Pet1*$^{Vglut3\text{-high}}$ neuron subgroup and the classical, r2-*Pet1*$^{Tph2\text{-high}}$ neuron subgroup differentially contribute to these projections is unknown. Here we present progress towards resolving this circuitry.

One possibility is that the r2-*Pet1*$^{Tph2\text{-high}}$ and r2-*Pet1*$^{Vglut3\text{-high}}$ neuron subgroups exhibit converging circuitry, innervating the same target regions and potentially exerting regulatory effects of different directions and/or timescales. An alternative extreme is that they exhibit divergent circuitry, each innervating different brain regions to control different functions. Also possible is a combination of both as a function of target site. Because neurochemical identity (serotonin and TPH2 versus VGLUT3 as a proxy for glutamate) largely distinguishes the r2-*Pet1*$^{Tph2\text{-high}}$ from r2-*Pet1*$^{Vglut3\text{-high}}$ neuron somata, we reasoned it might also distinguish their boutons and thus target brain regions, which in turn could help discern from among these circuitry possibilities.

In this study, we used dual recombinase-based genetic labeling strategies (Awatramani et al. 2003; Bang et al. 2012), retrograde viral tracing, immunohistology, and single-cell *in situ* mRNA detection combined with confocal microscopy to describe the neurochemical identity and distribution of axonal boutons arising from the r2-*Pet1* neuron population. We found anatomical segregation of r2-*Pet1* axonal boutons by serotonin$^+$ versus VGLUT3$^+$ identity, suggesting that the r2-*Pet1*$^{Tph2\text{-high}}$ and r2-*Pet1*$^{Vglut3\text{-high}}$ neuron subgroups innervate distinct brain regions. Further, we found that some VGLUT3$^+$ r2-*Pet1* boutons comprised a specialized presynaptic structure that has been called a pericellular basket (Köhler et al. 1982; Hornung and Celio 1992; Dinopoulos et al. 1993; Riedel et al. 2008), here found encasing the soma and dendrites of individual hippocampal, cortical, and septal GABAergic neurons of specific subclasses. This finding suggests that some r2-*Pet1*$^{Vglut3\text{-high}}$ neurons may have a privileged capacity to control local network excitability. In the septum, we observed co-positive VGLUT3$^+$/5-HT$^+$ r2-*Pet1* boutons and they were enriched in these pericellular baskets, suggesting this may be a specialized site of 5-HT/glutamate co-transmission. Further, we observed that the septal cells targeted by r2-*Pet1* baskets commonly also received serotonin$^+$ fibers from other (non-r2) *Pet1* neurons, suggesting even additional regulatory complexity. This work provides a foundational framework for pursuit of downstream circuits and cells relevant to specific behavioral modulation by r2-*Pet1* neurons, and further extends our knowledge of the functional organization of the median raphe nucleus.

MATERIALS AND METHODS

Animals

All experimental procedures were approved by Harvard's Institutional Animal Care and Use Committee (IACUC). Mice were housed in a colony maintained on a 12 hr light-dark cycle. All transgenic strains described below have been previously backcrossed to the C57BL/6J inbred strain (The Jackson Laboratory, stock no. 000664) for at least nine generations. In all experiments, adult mice were used (at least P60), as previous research has shown the postnatal maturation of serotonin neuron fiber morphology is finalized before this age (Maddaloni et al. 2017).

For projection mapping studies, r2-*Pet1* neuron boutons were visualized by cell-autonomous expression of a synaptophysin-GFP (synGFP) fusion protein using intersectional genetics. These studies used triple-transgenic mice harboring the rhombomere 2 (r2)-specific Cre driver *Hoxa2-cre* (alias *r2Hoxa2-cre*); Awatramani et al., 2003) and the Flp driver *Pet1-Flpe* (Jensen et al. 2008) in combination with the dual Cre/Flp-responsive allele *Gt(ROSA)26Sor*$^{tm10(CAG-Syp/EGFP+,-tdTomato)Dym}$ (termed *RC-FPSit*, The Jackson Laboratory stock no. 030206 (Niederkofler et al. 2016)). Triple-transgenic *r2Hoxa2-cre, Pet1-Flpe, RC-FPSit*$^{+/-}$ mice were generated by crossing double-transgenic *Pet1-Flpe, RC-FPSit*$^{-/-}$ males to *r2Hoxa2-cre* females. To fluorescently label the somata and fibers of r2-*Pet1* neurons with EGFP (called the intersectional cell population) and all other *Pet1* neurons with mCherry (called the subtractive cell population), we generated triple-transgenic mice bearing the drivers *r2Hoxa2-cre* and *Pet1-Flpe,* together with the dual Cre/Flp-responsive *ROSA26* allele *Gt(ROSA)26Sor*$^{tm8(CAG-mCherry,-EGFP)Dym}$ (termed *RC-FrePe*; The Jackson Laboratory stock no. 029486 (Brust et al., 2014; Dymecki et al., 2010; Figure 2.1). Triple-transgenic *r2Hoxa2-cre, Pet1-Flpe, RC-FrePe*$^{+/-}$ mice were generated by crossing double-transgenic *Pet1-Flpe* hemizygous*, RC-FrePe*$^{-/-}$ homozygous males to hemizygous *r2Hoxa2-cre*

females. We also utilized a similar intersectional line *Gt(ROSA)26Sor*$^{tm1.3(CAG-tdTomato,-EGFP)Pjen}$ (termed *RC-FLTG;* Plummer et al., 2015) and comparable breeding strategy to visualize r2-*Pet1* and other *Pet1* subtractive fibers (The Jackson Laboratory stock no. 026932). To fluorescently mark *Piezo2-Pet1* neurons, we generated triple-transgenic mice bearing the drivers *Piezo2-GFP-IRES-cre* (Woo et al. 2014) and *Pet1-Flpe,* combined with the conditional allele *Gt(ROSA)26Sor*$^{tm65.1(CAG-tdTomato)Hze}$ (termed *RC-Ai65;* The Jackson Laboratory stock no. 021875; Madisen et al., 2012, 2015). Triple-transgenic *r2Hoxa2-cre, Pet1-Flpe, RC-Ai65*$^{+/-}$ mice were generated by crossing double-transgenic *Pet1-Flpe* hemizygous*, RC-Ai65*$^{-/-}$ homozygous mice with heterozygous *Piezo2-GFP-IRES-cre* mice.

Tissue Preparation for IHC and FISH

All experiments used brain sections from mice perfused transcardially with 0.1 M phosphate-buffered saline (PBS), followed by 4% paraformaldehyde (PFA) as previously published (Brust et al. 2014). Brains were fixed overnight in 4% PFA/PBS for 24 hours at 4ºC. For bouton neurochemical phenotyping or RNAscope experiments, tissue was then cryoprotected in 30% sucrose/PBS for 48-72 hr at 4°C and then embedded in tissue freezing medium (TFM; Triangle Biomedical Services) for storage at –80°C. Tissue was sectioned into free floating (20-μm for single-molecule FISH and 40-μm for IHC) coronal sections in series of 6 or 8. For retrograde tracing, sections at 50-μm thickness were cut on a vibratome (Leica VT1000S) and stored in 28% sucrose 30% ethylene glycol cryoprotectant at -30ºC.

Figure 2.1. The developmentally specified r2-*Pet1* neuron lineage comprises two transcriptomically polarized subtypes, one appearing more serotonergic (*Tph2*-high, *Vglut3*-low) and the other more glutamatergic (*Tph2*-low, *Vglut3*-high).

r2-*Pet1* cells are derived from progenitor cells in the rhombomere (r) 2 domain of the embryonic hindbrain that postmitotically express *Pet1* and are intermingled with other lineages in the adult brainstem median raphe (B8 and B5) and B9 nuclei (A). We genetically access r2-*Pet1* cells using *ROSA26 (R26)* knock-in dual Cre- and Flp-responsive intersectional alleles partnered with the r2- and serotonin lineage-specific drivers *r2Hoxa2-cre* and *Pet1-Flpe,* respectively (B, C). By fluorescent *in situ* hybridization performed on brain sections (D), all EGFP-labeled r2-*Pet1* cells expressed detectable levels of *Pet1* transcripts (E), and *Pet1* mRNA levels in r2-*Pet1* cells weakly correlated with *Tph2* transcript abundance, r=0.3413; n=38 cells, p=0.036, Spearman correlation (E'). r2-*Pet1* cells comprise transcriptomically distinct subtypes, one appearing more serotonergic and expressing high levels of *Tph2* and low levels of *Vglut3* (r2-*Pet1*$^{Tph2\text{-high}}$), and one appearing more glutamatergic with the inverse pattern of gene expression (r2-*Pet1*$^{Vglut3\text{-high}}$) as seen in RNA FISH-IHC fluorescent photomicrographs of tissue sections in which EGFP-labeling marks r2-*Pet1* neurons (F) and quantification of puncta counts per r2-*Pet1* cell (G,H). Coronal brain schematics for all figures adapted from Franklin and Paxinos, 2008 with permission, copyright Academic Press-Elsevier.

(Figure 2.1 continued)

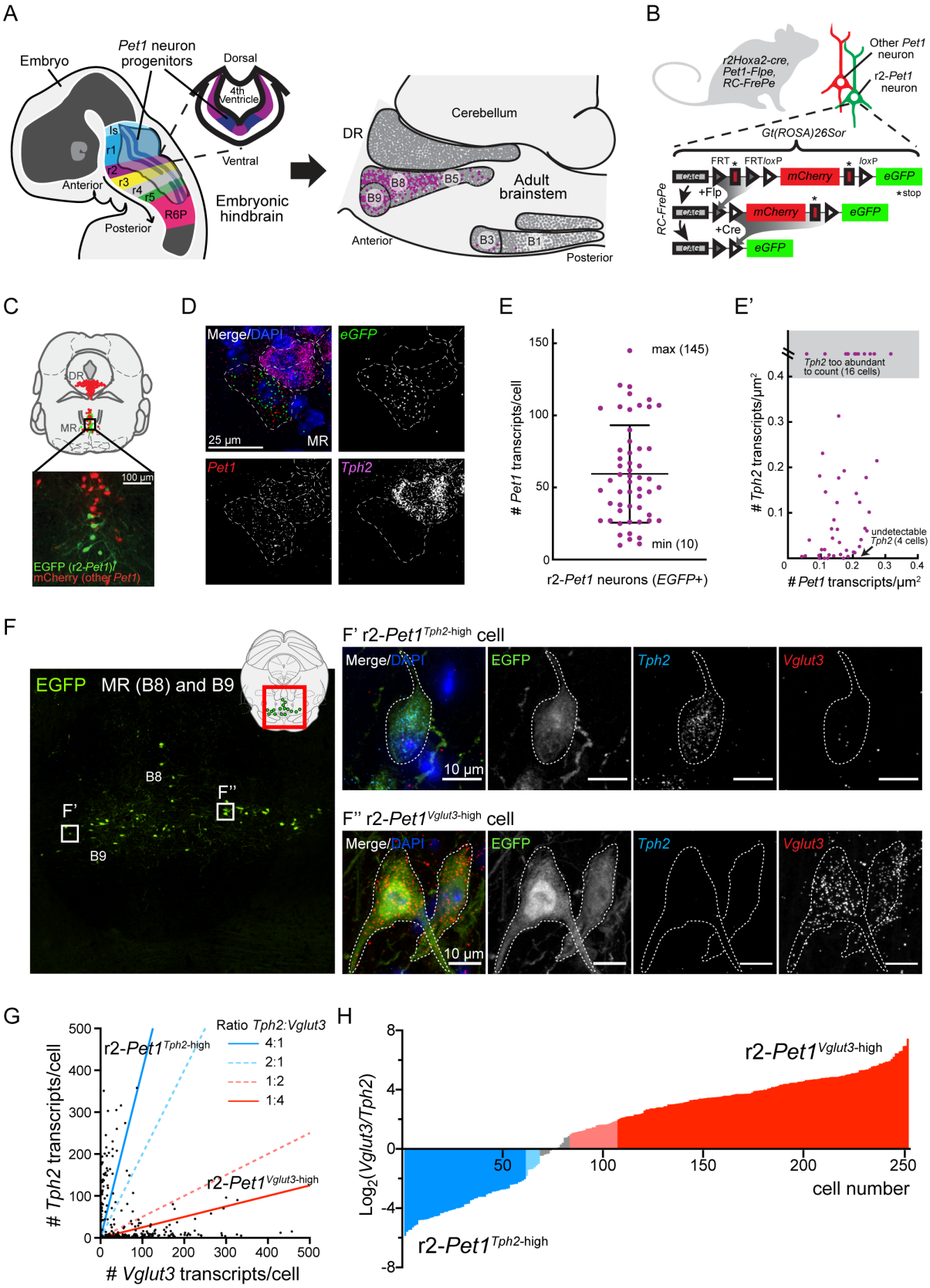

Immunohistochemistry

We performed immunohistochemistry (IHC) using the following antibodies and dilutions: anti-calbindin (Sigma-Aldrich, catalog no. C9848, mouse monoclonal, 1:2000), anti-calbindin D-28k (Swant, catalog no. 300, mouse monoclonal, 1:3000), anti-DsRed (Takara, catalog no. 632496, rabbit polyclonal, 1:1000), anti-γ-aminobutyric acid (GABA) (Millipore, catalog no. ABN131, rabbit polyclonal, 1:250), anti-GFP (Aves Labs, catalog no. GFP-1020, chicken polyclonal, 1:1500), anti-Mouse IgG biotinylated (Invitrogen, catalog no. A16021, donkey polyclonal, 1:500), anti-neurokinin B (Novus Biologicals, catalog no. NB300-201SS, rabbit polyclonal, 1:500), anti-red fluorescent protein (Chromotek, catalog no. 5f8, rat monoclonal, 1:1000), anti-Rabbit IgG biotinylated (Jackson ImmunoResearch, catalog no. 711-065-152, donkey polyclonal, 1:200), anti-Reelin (Novus Biologicals catalog no. AF3820, goat polyclonal, 1:500), anti-5-HT (Abcam, catalog no. ab66047, goat polyclonal, 1:500), anti-5-HT2C (Santa Cruz Biotech., catalog no. sc-15081, goat polyclonal, 1:100), anti-5-HT3A (Alomone labs, catalog no. ASR-031, rabbit polyglonal, 1:500), anti-somatostatin (Sigma catalog no. HPA019472, rabbit polyclonal, 1:500), anti-TPH2 (Novus Biologicals, catalog no. NB100-74555, rabbit polyclonal, 1:1000), anti-VGLUT3 (Synaptic Systems, catalog no. 135-203, rabbit polyclonal, 1:500), anti-VGLUT3 (Synaptic Systems, catalog no. 135-204, guinea pig polyclonal, 1:500), and anti-VIP (Immunostar catalog no. 20077, rabbit polyclonal, 1:500).

Floating sections were incubated for 1 hr at room temperature in a blocking solution of tris-buffered saline (TBS) containing 3% normal donkey serum (NDS; Jackson ImmunoResearch) and 0.3% triton-X-100 (Sigma-Aldrich). Sections were then transferred to a solution containing primary antibodies diluted in TBS with 1% NDS and 0.3% triton-X-100 and incubated for 24 hr at

4°C on a nutator mixer (BD Clay Adams). After three TBS washes, sections were transferred to a solution containing secondary antibodies diluted in TBS with 1% NDS and 0.3% triton-X-100and incubated in a light-protected chamber for 2 hr at room temperature. Detection of 5-HT3A receptor followed previously established protocols (Chang et al. 2016), with ethanol dehydration prior to blocking. For detection of subtractive *Pet1* fibers (non-r2-*Pet1* fibers) in composite basket phenotyping experiments and for detection of calbindin-expressing interneurons in the basket target quantification experiments, we used a modified protocol. Briefly, amplification of signal was achieved by modifying the second day protocol using a biotinylated secondary antibody to primary antibody host IgG (see above) for two hours at room temperature. Following manufacturer recommendations, the calbindin D-28k antibody was dissolved in TBS with 10% NDS. For DsRed, we dissolved the biotinylated antibody in TBS with 2% NDS and 0.1% triton-x-100. To reduce nonspecific signal, we also used an avidin-biotin blocking kit (Vector Laboratories, catalog no. SP-2001) on IHC day 1 following manufacturer instructions. In general, for detection of primary antibodies, species-matched Alexa 488, Alexa 568, Cy5, and Alexa 647-conjugated secondary antibodies (Jackson ImmunoResearch) were used. For visualizing biotinylated antibodies, we incubated sections with Alexa 555-conjugated streptavidin (ThermoFisher, catalog no. S32355, 1:500) during the same step as secondary antibodies. Sections were then washed three times in fresh TBS at room temperature as before, with 1 μg/ml DAPI (Life Technologies) added to the last wash step lasting 15 min. Sections were mounted onto No. 1.5 coverslips (Electron Microscopy Sciences) and then attached to SuperFrost Plus histological slides (Fisher Scientific) using Aqua-Poly/Mount medium (Polysciences, Inc.) or ProLong Glass anti-fade mountant (ThermoFisher)

Multiplexed Fluorescent In Situ *Hybridization (FISH)*

Single-molecule mRNA FISH (smFISH) was performed on fresh frozen or fixed tissue sections according to the manufacturer's instructions (RNAscope, Advanced Cell Diagnostics; Wang et al., 2012). Sections were mounted onto SuperFrost Plus slides (Fisher Scientific) and dried on a slide warmer at 45°C for 30 minutes to promote section adhesion before proceeding with the RNAscope protocol recommended by suppliers (Advanced Cell Diagnostics). The RNAscope Manual Assay 2.5 was performed using the Multiplex Fluorescence Detection Kit (ACD, catalog no. 320851) and probes for *eGFP* (ACD, catalog no. 400281), *Fev (Pet1;* ACD, catalog no. 413241-C3), *Tph2* (ACD, catalog no. Mm-318691-C2), and *Vglut3* (ACD, catalog no. Mm-431261-C1). For combined smFISH and IHC, following FISH, sections were then immunostained for EGFP as above and counterstained with DAPI. Slides were mounted using ProLong Gold Antifade Mounting media (Life Technologies) and #1.5 thickness glass coverslips.

Retrograde Tracing Experiments

To label r2-*Pet1* cells that project to the hippocampus, we injected 3 adult (2 male, 1 female) *r2Hoxa2-cre, Pet1-Flpe, RC-FrePe*$^{-/+}$ mice with AAV2-retro-*CAG*-tdTomato-WPRE virus (Addgene 59462-AAVrg) bilaterally into the dorsal hippocampus (coordinates ML: ±1.4 mm, AP -2.06 mm, Z: -1.75 mm). The retrograde serotype of this virus allows infection of projection neurons that innervate the region targeted by viral injections and results in virus-induced marking of infected neurons by tdTomato. Three weeks post-surgery, mice were perfused and tissue processed as above. Sections were stained for EGFP and VGLUT3 or 5-HT using a modified

immunohistochemistry protocol. Briefly, sections were rinsed 3x in PBS, then 1x in PBS with 0.1% Triton-X-100 (PBST, Sigma) before blocking in PBST with 5% NDS for two hours at room temperature. After incubating with primary antibodies for 48 hours at 4°C, sections are rinsed 3x in PBST and then incubated with secondary antibodies in PBST with 2% NDS for two hours at room temperature. After 3x in PBST (last rinse for 10 minutes with 1.5 ug/mL DAPI), sections were mounted on #1.5 thickness coverslips and then adhered to slides with Prolong Glass mounting media.

Confocal and widefield microscopy

Confocal imaging was performed using a Nikon Ti inverted spinning disk microscope equipped with a Yokogawa CSU-W1 Spinning disk scanhead with 50 µm pinhole disk, a PI Z piezo stage insert, a TOPTICA iChrome MLE laser launch and a Plan Apo λ 60X 1.4 N.A. oil objective for bouton neurochemical phenotyping and RNAscope experiments. For retrograde tracing experiments, a 20X Plan Apo λ 20x/0.75 N.A. Air DIC objective was used to generate tiled images. We also used this objective to quantify cell types targeted by r2-*Pet1* baskets and to quantify the proportion of baskets that formed composites with other *Pet1* fibers. Images were captured using an Andor Zyla 4.2 Plus sCMOS monochrome camera and Nikon Elements Acquisition Software AR 5.02. In all colocalization experiments, single-label controls were used to determine imaging settings to eliminate channel bleedthrough. Signal from the different channels was acquired sequentially using a Semrock Di01-T405/488/568/647 multi-band pass dichroic mirror and band pass emission filters for green (Chroma ET525/36m), red (Chroma ET

605/52m) and far read (Chroma ET 705/72m) channels. Z stack acquisition was optimized to minimize axial shift between channels.

Several pericellular basket example images were taken using a laser scanning confocal Zeiss Axio Observer Z1 equipped with LSM780 Scan Head, motorized stage, and with either a Plan Apo 63x/1.4 Oil DIC III or Plan Apo 40x/1.3 Oil DIC III objective. These images were acquired using 405, 488, 561, and 633 nm laser lines and signal from each channel was acquired sequentially using Quasar PMT and GAaSP 32 Channel Spectral detectors. The range of wavelengths collected for each channel was determined using the Zeiss Zen Black (2011) software's Smart Setup settings and compared to negative control slides. Voxel size was set to 0.21 x 0.21 x 1.13 microns.

Widefield fluorescent micrographs were collected using a Zeiss Axioplan2 upright microscope with manual stage and Axiocam 506 monochrome camera. Samples were illuminated with a Lumencor SOLA LED light engine. Signal from the different channels was acquired sequentially with FITC, DsRed, and Cy5 filter sets and used either a 10x/0.45 N.A. Air Plan Apochromat or 20x/0.8 Air Plan Apochromat objective. For all images, when brightness/contrast settings were adjusted using ImageJ, identical settings were used for each channel applied uniformly across images within a given experiment. Images are presented as maximum intensity z-stack projections generated using Fiji (NIH; Schneider et al., 2012).

Bouton neurochemical immunophenotyping analysis and quantification

Histological studies for bouton neurochemical phenotyping were performed using tissue

collected from postnatal day (P) 50–100 male (n=5) and female (n=6) triple-transgenic *r2Hoxa2-cre, Pet1-Flpe, RC-FPSit* mice from multiple litters. To determine whether r2-*Pet1* neuron boutons contained VGLUT3, 5-HT, or both, tissue was stained for EGFP, VGLUT3, and 5-HT (see above for antibodies). We collected four images of each region of interest per animal when possible (mean number of images per region per animal = 3.82) using a Nikon Ti spinning disk microscope with 1.4 N.A. 60X objective (see above). Colocalization of synGFP boutons with VGLUT3 and/or 5-HT was performed in a semi-automated manner in Imaris (Bitplane v. 9.1.2 (Jan 29, 2018) Build 45902). Briefly, each channel (synGFP, 5-HT, and VGLUT3) was converted into a spots object based on user-defined thresholds. If present, visual artifacts (such as highly autofluorescent cells of the olfactory bulb) were manually removed. The Matlab (v. 2017b) plugin "Colocalize Spots" was used to test for colocalization based on distance between synGFP centroids and 5-HT or VGLUT3 centroids. A distance threshold of 1 μm was chosen empirically based on positive control (staining for synGFP with two secondary antibodies conjugated to different fluorophores) and negative control (randomly shuffling the synGFP channels of test images of a particular region to mismatch synGFP and VGLUT3 or synGFP and 5-HT signals) experiments. In these positive and negative control experiments, these analysis parameters resulted in a 1.03% false negative rate and 2.16% false positive rate (Figure 2.2A-C). The same approach was used to neurochemically phenotype r2-*Pet1* and other *Pet1* boutons contributing to baskets in the lateral septum using images from adult *r2Hoxa2-cre, Pet1-Flpe, RC-FrePe* mice (n=3).

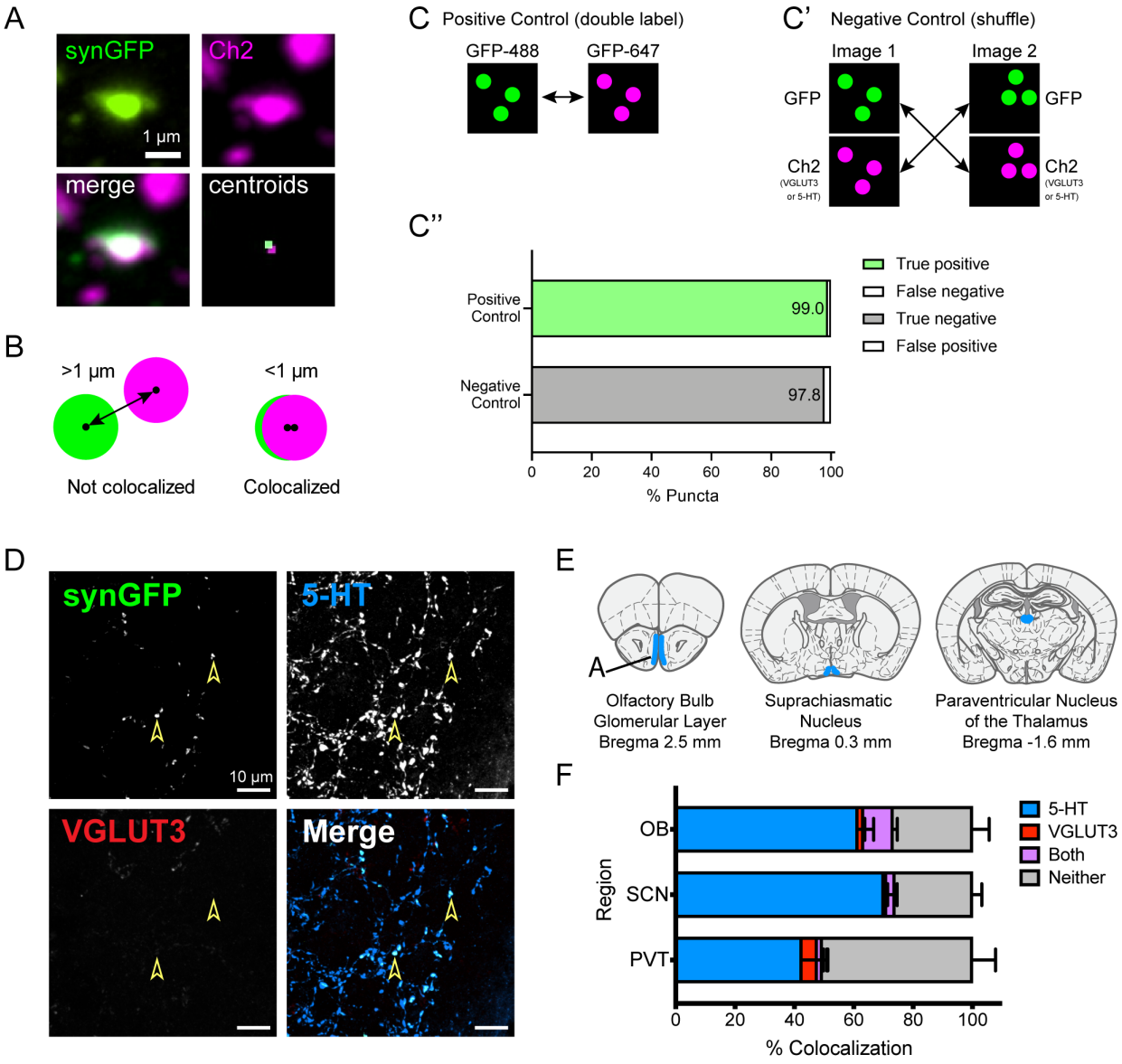

Figure 2.2. The olfactory bulb (OB), suprachiasmatic nucleus of the hypothalamus (SCN), and paraventricular nucleus of the thalamus (PVT) are innervated by 5-HT$^+$ r2-*Pet1* boutons.

Example photomicrograph of a colocalized bouton (A) and criteria for object-based colocalization (B). Positive control labeling of EGFP with multiple fluorophores (C) and a negative shuffled channel control (C′) were used to assess false negative and false positive rates, quantified in C′′. Fluorescent photomicrograph from the olfactory bulb glomerular layer showing r2-*Pet1* boutons labeled by 5-HT (arrowheads demarcate two of many) but not VGLUT3 (D). Coronal schematics with regions demonstrating this innervation pattern in blue (E) and quantification of colocalization (F).

Single-molecule mRNA FISH transcript quantification

For semi-automated analysis of mRNA transcript number in r2-*Pet1* neurons, three-color smFISH was performed to detect *eGFP, Pet1,* and *Tph2* in triple-transgenic *r2Hoxa2-cre, Pet1-Flpe, RC-FrePe* mice from multiple litters. ImageJ was used to perform a 50 pixel rolling-ball background subtraction, to adjust window/level settings, and to generate threshold-transformed masks of each fluorescence channel. For each *eGFP*-marked r2-*Pet1* cell, *Tph2* and *Pet1* transcripts were automatically quantified using the "Analyze Particles" function in Fiji (Schindelin et al. 2012) with a particle size of 1-10 pixels. Alternatively, a custom ImageJ analysis script (Okaty et al. 2020) was used to count *Vglut3* and *Tph2* mRNA puncta within $EGFP^+$ cell somata using the Default or MaxEntropy thresholds to segment cell somata and the 'Find Maxima' function with a noise tolerance of 1000 to identify mRNA puncta. Analysis was performed on maximum intensity projections of z-stacks as this method reduced computational load and time and produced results that were highly similar to a full 3D counting approach in Imaris (data not shown).

Quantification of cell somata in retrograde tracing experiments

For retrograde tracing experiments, images from virus-injected brains were analyzed by manual counting of $EGFP^+$ and $tdTomato^+$ cells using the Cell Counter plugin for Fiji (NIH). First, we selected display settings using single label controls. We quantified the percent of cells expressing VGLUT3 or 5-HT for $tdTomato^+/EGFP^+$ cells as well as for all $tdTomato^+$ cells and all $EGFP^+$ cells.

Quantification of Pet1 composite baskets in septum

To quantify the proportion of septal cells targeted by r2-*Pet1* baskets that also received boutons from non-r2 *Pet1* cells we analyzed triple transgenic using n=4 (2 male, 2 female) *r2Hoxa2-cre, Pet1-Flpe, RC-FrePe* mice and 1 *r2Hoxa2-cre, Pet1-Flpe, RC-FLTG* (male) mouse. First, we manually identified EGFP$^+$ r2-*Pet1* baskets using only the green channel; then, each encased cell was manually reviewed for whether it was also targeted by mCherry$^+$ non-r2 *Pet1* fibers. We quantified the proportion of r2-*Pet1*-targeted somata receiving 1) a non-r2 *Pet1* basket (thus receiving a composite basket) 2) non-r2 *Pet1* boutons that didn't meet basket criteria or 3) receiving no boutons from other *Pet1* cells.

*Quantification of cell somata targeted by r2-*Pet1 *baskets*

To quantify the proportion of VGLUT3$^+$ and calbindin$^+$ somata encased by r2-*Pet1* baskets in the cortex, hippocampus, and septum we executed the following. For VGLUT3$^+$ somata and for calbindin$^+$ somata in hippocampus and septum a user manually segmented cells in Fiji using the magic wand tool on a median-filtered image (radius=5 for calbindin and 10 for VGLUT3). For calbindin$^+$ cells in the cortex, cell somata were amenable to automated segmentation using a custom Fiji macro. Briefly, the macro first corrected for uneven illumination by subtracting from the calbindin channel a gaussian blurred image (radius=100) of that channel. This was followed by a minor gaussian blur (radius=2) and autothresholding using the "Triangle" method. Resulting cell objects were filtered using the "Analyze Particles" function to limit cells to sizes between 40-300 μm^2 area and 0.4-1.00 circularity; clumped cells were split using the "Adjustable Watershed" plugin with a tolerance of 1. Finally, these images were manually reviewed and any autofluorescent vasculature incorrectly counted by the macro as cells were removed. To examine cells in specific subregions of each image, another custom

script sorted cells into user-defined ROIs. After segmentation, another custom script was used to quantify the area of r2-*Pet1* boutons overlapping the quadrants of each cell body. Each cell was divided into quadrants with a gap at the center to prevent a bouton located at the center to be counted in all quadrants. The script then segmented r2-*Pet1* fibers following the same automated method above (but without filtering for cell-sized objects) and counting the bouton area in each quadrant. Cells were counted as receiving a basket if they had innervation in 3 or more quadrants of at least 1 μm^2 each and an overall innervation of more than 12 μm^2. These parameters produced data that corresponded well to manually counting basket. All code is publicly available on Github in the repository "auto-basket-detector-2D" by user rsenft1.

Statistical analyses

Statistical tests were performed in Prism 8 (Graphpad). To explore the relationship between *Tph2* and *Pet1* expression, we performed a Spearman correlation on cells with countable *Tph2* levels. To compare the neurochemical phenotypes of boutons in baskets against those outside baskets, we performed a within-animal two-tailed paired t-test. To compare the percent of hippocampal-projecting r2-*Pet1* cells stained for 5-HT versus the percent stained for VGLUT3, we performed a paired t-test. We also used paired t-tests to compare the neurochemical phenotypes of r2-*Pet1* versus other *Pet1* boutons contributing to composite baskets and to compare r2-*Pet1* basket targets across regions. Results are reported as mean ± standard error of the mean (SEM) unless otherwise stated.

RESULTS

r2-Pet1 somata stratify by Tph2 versus Vglut3 mRNA levels even with abundant Pet1 transcripts

Previous molecular analyses of the r2-*Pet1* neuron population suggested two categories of constituent cells based on neurotransmitter-related transcript levels: one cell subgroup abundant in *Tph2* mRNA, and the other abundant in *Vglut3* mRNA but demonstrating low or no detectable *Tph2* transcripts (Okaty et al. 2015). This inverse relationship between *Tph2* and *Vglut3* mRNA abundance characterizing these two *Pet1*-expressing cell subgroups, referred to as r2-*Pet1*$^{Tph2\text{-high}}$ and r2-*Pet1*$^{Vglut3\text{-high}}$, contrasts most other regions of the *Pet1*$^{+}$ brainstem raphe. More typical among raphe *Pet1*$^{+}$ cells are abundant levels of both *Tph2* and *Vglut3*, or solely *Tph2*, with these serotonergic (TPH2^{+}) cells intermingled among various non-*Pet1* raphe neurons, many of which are themselves glutamatergic. The distinctive, largely "one-or-the-other" neurochemical stratification distinguishing r2-*Pet1* cell bodies suggests that the cognate axonal boutons might also show exclusivity for neurochemical phenotype (5-HT versus VGLUT3 indicative of glutamate release (Amilhon et al. 2010)) and thus provide a means to resolve the efferent circuitry for each subgroup from within the broad innervation profile mapped for the r2-*Pet1* population *en masse* (Bang et al. 2012). Before embarking on bouton phenotyping, however, we first set out to re-examine *Tph2*, *Vglut3*, and *Pet1* transcript levels in r2-*Pet1* neuron somata using the sensitive and specific approach of multiplexed fluorescent *in situ* hybridization (FISH) for mRNA detection.

We first performed single-molecule transcript analyses in tissue sections from triple-transgenic (*r2Hoxa2-cre, Pet1-Flpe, RC-FrePe*) mice in which EGFP protein and mRNA expression selectively marked the r2-*Pet1* neuron population (Figure 2.1A-D), on top of which *Pet1* and *Tph2* mRNA could be visualized (Figure 2.1D). As expected given use of the *Pet1-Flpe* driver, all *eGFP* transcript-marked cells showed *Pet1* transcripts (fluorescent puncta), with a mean absolute

count of 59.4 ± 4.6 *Pet1* mRNA puncta per cell, corresponding to an absolute range of 10 to 145 *Pet1* transcripts/cell (*n* = 54 cells across 3 mice) Figure 2.1E). This finding validates that r2-*Pet1* neurons, indeed constituents of both subgroups, continue to express *Pet1* in adulthood. Quantitative analyses of puncta representing individual *Tph2* mRNA transcripts in these cells normalized to cell area showed that ~30% of EGFP-marked r2-*Pet1* neurons (16 of 54 cells) expressed high levels of *Tph2* (*Tph2* transcripts too numerous to count), while the remainder of cells (38) had few or no *Tph2* puncta (Figure 2.1E'). For cells with countable levels of *Tph2* puncta, area-normalized *Tph2* transcript levels exhibited a positive correlation with *Pet1* transcript counts (Spearman correlation, r=0.3413; n=38 cells, p=0.036). Overall, these findings are consistent with our prior r2-*Pet1* scRNAseq results (Okaty et al. 2015).

Next, we explored the relationship between *Tph2* and *Vglut3* transcript abundance in the *r2-Pet1* cells, using RNAscope FISH on tissue sections from a triple transgenic (*r2Hoxa2-cre, Pet1-Flpe, RC-FrePe*) mouse, but now visualizing the *r2-Pet1* cells by immunofluorescent detection of EGFP protein (Figure 2.1F,F'). We counted *Tph2* and *Vglut3* puncta per $EGFP^+$ cell (n=252 r2-*Pet1* cells) and calculated the base 2 logarithm of the *Vglut3:Tph2* transcript ratio. If 1 or greater, we classified those cells as belonging to the r2-$Pet1^{Vglut3\text{-high}}$ group, and if -1 or less, to the r2-$Pet1^{Tph2\text{-high}}$ group (Figure 2.1G-H), meaning that a ratio of at least 2:1 in transcript count is necessary to be classified as either cell type. By these criteria, we found 172 (68.3%) cells as r2-$Pet1^{Vglut3\text{-high}}$, and 65 (25.8%) cells as r2-$Pet1^{Tph2\text{-high}}$. We also examined transcript counts normalized to cell area for cells classified into these groups, finding r2-$Pet1^{Tph2\text{-high}}$ cells exhibited high *Tph2* expression (mean 0.9438 transcripts/μm^2, 95% CI [0.86,1.03]) and low *Vglut3* expression (mean 0.1096 transcripts/μm^2, 95% CI [0.084, 0.14]), while r2-$Pet1^{Vglut3\text{-high}}$ cells

expressed high *Vglut3* (mean 0.6308 transcripts/μm^2, 95% CI [0.58, 0.69]) and low *Tph2* (mean 0.06315 transcripts/μm^2, 95% CI [0.051, 0.075]). A small subset of *r2-Pet1* cells (5.9%) contained an intermediate *Vglut3:Tph2* transcript ratio or vice versa, i.e., a less than 2:1 comparative enrichment of either *Vglut3* or *Tph2*. For simplicity, the present study approximates the molecular heterogeneity of *r2-Pet1* neurons using the neuron subgroups descriptors of r2-*Pet1*$^{Vglut3\text{-high}}$ and r2-*Pet1*$^{Tph2\text{-high}}$ cells, with the caveat that a small minority of r2-*Pet1* neurons likely harbor an intermediate phenotype. Collectively, these RNAscope *in situ* hybridization findings are in line with the previously reported scRNAseq datasets (Okaty et al. 2015), confirming that the r2-*Pet1* neuron group shows a segregation of somata into two subgroups based on expression of neurochemical pathway genes.

*Segregation anatomically of r2-*Pet1 *boutons by serotonin$^+$ versus VGLUT3$^+$ neurochemical identity*

To visualize and subsequently explore the anatomical distribution and neurochemical identity of r2-*Pet1* neuron axonal boutons in the adult brain, we used the intersectional *RC-FPSit* allele (Niederkofler et al. 2016), which drives expression of a synaptophysin–GFP (synGFP) fusion protein selectively in cells with a history of both Cre and Flp expression. Synaptophysin, a synaptic vesicle protein, enriches the fused GFP signal in both axon terminal and *en passant* boutons (De Paola et al. 2003; Kelsch et al. 2008; Li et al. 2010; Tripodi et al. 2011); both types of boutons have been shown to participate in vesicle-mediated neurotransmission (Beaudet and Descarries 1981; Agnati et al. 1995; De-Miguel and Trueta 2005; Trueta and De-Miguel 2012). In triple-transgenic (*r2Hoxa2-cre, Pet1-Flpe, RC-FPSit*) mice, the synGFP robustly and selectively illuminated r2-*Pet1* neuron axonal boutons as compared to inter-bouton (i.e., intervaricose) axon

segments. We observed the densest r2-*Pet1* bouton distribution in the following brain areas: olfactory bulb (OB; glomerular layer), prelimbic cortex (superficial layers 1-3), suprachiasmatic nucleus of the hypothalamus (SCN), paraventricular nucleus of the thalamus (PVT), hippocampus (HP; present throughout many layers and highest at the stratum radiatum-stratum lacunosum moleculare (sr/slm) border), medial and lateral septal nuclei (MS and LS, respectively), and diagonal band of Broca (DB). This pattern of regions corroborates previous reports of fiber distribution from r2-*Pet1* neurons (Bang et al. 2012).

Next we probed synGFP-marked r2-*Pet1* boutons for co-immunolocalization with 5-HT and VGLUT3. Brain sections (every eighth 40 μm serial section from 5 male and 6 female P60 *r2Hoxa2-cre, Pet1-Flpe, RC-FPSit*) were immunostained, imaged on a confocal microscope, and resulting images analyzed using Imaris (Bitplane) to calculate the fraction of synGFP$^+$ boutons that were also immunopositive for 5-HT, VGLUT3, both, or neither, for four images per region per mouse (see Methods). We analyzed 66,435 synGFP$^+$ boutons across 13 forebrain subregions, for an average of 5,110 boutons per region and 465 boutons per region per mouse. Generally, we observed a segregation of bouton neurochemical identity by anatomical target site. In the glomerular layer of the olfactory bulb, the PVT, and the SCN, the r2-*Pet1* boutons were largely immunopositive for 5-HT but not VGLUT3 (Figure 2.2D–F). Furthermore, in the PVT, approximately half of the GFP-marked boutons lacked immunodetectable levels of even 5-HT. By contrast, dorsal cortical and hippocampal regions were largely innervated by VGLUT3-only r2-*Pet1* boutons (86.3 ± 0.94%, across the 7 regions) (Figure 2.3A–C). Few 5-HT$^+$ r2-*Pet1* boutons were observed (1.35 ± 0.51% of all boutons across these regions), and a modest proportion lacked staining for either (9.38 ± 0.68% across these regions). These regions harbored synGFP$^-$,

5-HT$^+$ fibers, suggesting that these areas are also innervated by other (non-r2-derived) subtypes of serotonergic neurons, which is not surprising given that r1- and r3-derived *Pet1* serotonergic neuron cell bodies are also present in the MR (Jensen et al. 2008), and that DR efferents also innervate these target regions (Azmitia and Segal 1978). These results show that r2-*Pet1* cells are in part responsible for the largely VGLUT3$^+$ innervation of the hippocampus and cortex previously observed as arising from the median raphe (Jackson et al. 2008; Szőnyi et al. 2016). In the dorsolateral and medial septum (DLS and MS, respectively) and caudal stratum radiatum of the CA3 hippocampal subfield (cCA3-SR), the r2-*Pet1* boutons were largely VGLUT3-only (66 ± 8.6%), but ~20% stained positive for both 5-HT and VGLUT3 (20.4 ± 5.2%; Figure 2.4A–C). Furthermore, in the DLS, we also found 5-HT$^+$-only r2-*Pet1* boutons (8.04 ± 1.6%), making the DLS unique among examined regions in harboring all four types of r2-*Pet1* boutons—5-HT-only, VGLUT3-only, co-positive, and negative 5-HT and VGLUT3. The DLS, and the septum more generally, also exhibited extensive non-r2-*Pet1* 5-HT$^+$ and VGLUT3$^+$ innervation, with many of these fibers immunopositive for both 5-HT and VGLUT3, suggesting another lineage of *Pet1* cells also innervates the septum and may be able to co-transmit 5-HT and glutamate.

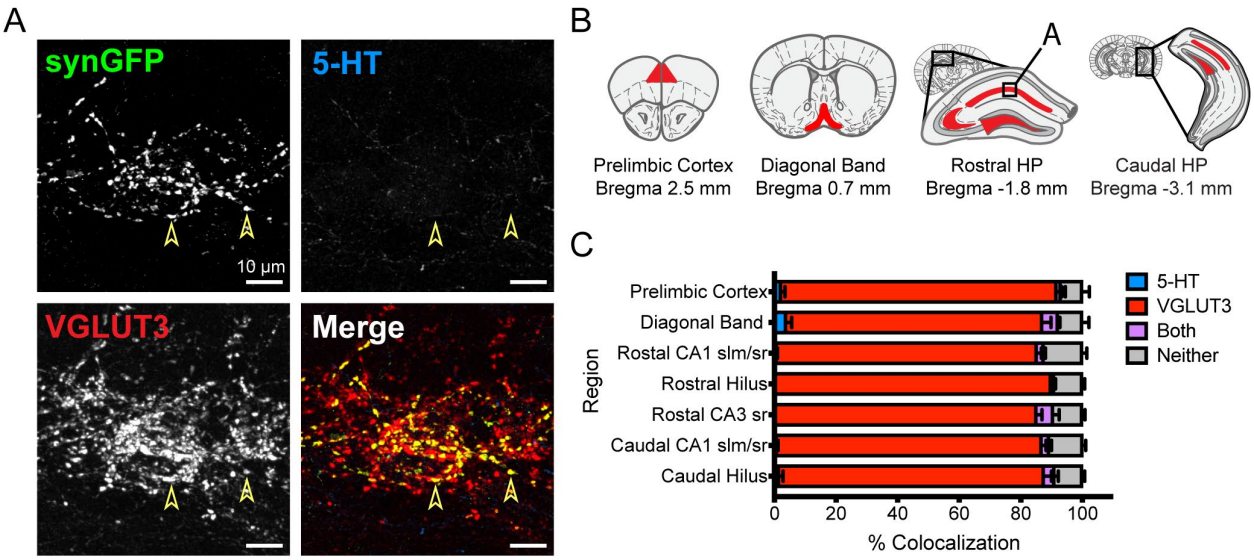

Figure 2.3. The cortex, hippocampus (HP), and diagonal band are innervated by VGLUT3$^+$ r2-*Pet1* boutons.

The cortex, hippocampus (HP), and diagonal band are innervated by VGLUT3$^+$ r2-*Pet1* boutons. Fluorescent photomicrograph from dorsal hippocampal CA1 stratum radiatum and stratum lacunosum moleculare (sr/slm) showing r2-*Pet1* boutons labeled by VGLUT3 but not 5-HT (arrowheads show examples; A). Coronal schematics with regions demonstrating this innervation pattern shown in red (B) and quantification of colocalization (C).

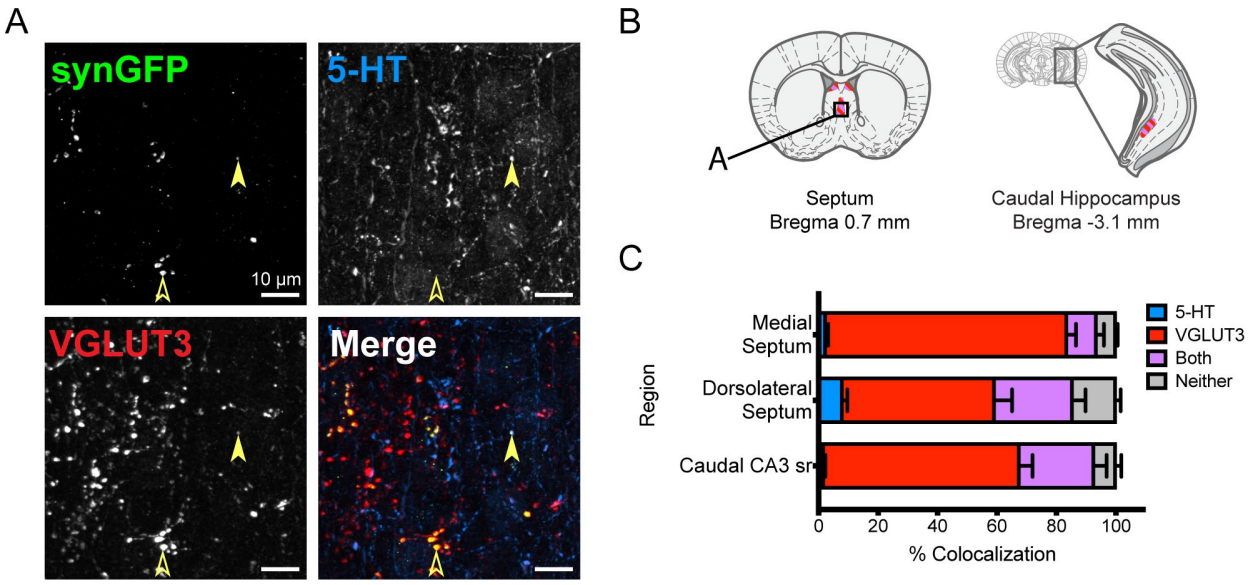

Figure 2.4. The medial and dorsolateral septum and caudal hippocampus are innervated by r2-*Pet1* boutons that are either labeled by VGLUT3 alone or are 5-HT and VGLUT3 co-positive.

Fluorescent photomicrograph from the medial septum showing VGLUT3+ r2-Pet1 boutons (open arrowheads as examples) and 5-HT+/VGLUT3+ r2-Pet1 boutons (filled arrowhead; A). Coronal schematics with regions demonstrating this innervation pattern in magenta (B) and quantification of colocalization (C).

Driver Piezo2-cre *coupled with* Pet1-Flpe *captured MR boutons positive for serotonin but not VGLUT3*

Given that the r2-Pet1 boutons found in the OB, SCN, and PVT were largely of the 5-HT-only class, we hypothesized that the source neuron subset was the r2-*Pet1*$^{Tph2\text{-high}}$ neuron subpopulation and not the r2-*Pet1*$^{Vglut3\text{-high}}$ subgroup. Alternatively, it is possible that a single r2-*Pet1* neuron projects both serotonergic and glutamatergic boutons, for example through differential axonal trafficking of mRNA and/or protein. To test our hypothesis, we devised means to intersectionally label the r2-*Pet1*$^{Tph2\text{-high}}$ neuron subpopulation. Single-cell transcriptomic analysis of *Pet1* MR neurons showed *Piezo2* transcripts selectively enriched in r2-*Pet1*$^{Tph2\text{-high}}$

neurons as compared to other *Pet1* neurons (Okaty et al. 2015). This was further supported in Ren et al., 2019 with the characterization of MR cluster 4, a *Piezo2*$^{+}$ *Tph2*-high MR population expressing similarly modest levels of *Vglut3* as the r2-*Pet1*$^{Tph2\text{-high}}$ group. Thus we generated triple transgenic *Piezo2-GFP-IRES-Cre, Pet1-Flpe, RC-Ai65* mice to illuminate somata and axons of r2-*Pet1*$^{Tph2\text{-high}}$ neurons selectively, which would also reveal the efferent target regions and allow neurochemical phenotyping for comparison with our generated bouton neurochemical maps for r2-*Pet1* cells.

Cell bodies labeled in *Piezo2-GFP-IRES-Cre, Pet1-Flpe, RC-Ai65* animals were restricted to the MR and were largely immunopositive for 5-HT (95.2 ± 4.76%), with a small fraction of cells co-positive for VGLUT3 and 5-HT (4.76 ± 4.76%) and no cells immunopositive for VGLUT3 in the absence of 5-HT (0.00 ± 0%; Figure 2.5A). We observed fewer *Piezo2-Pet1* neurons than would be expected of the entire r2-*Pet1*$^{Tph2\text{-high}}$ population, and cell bodies were restricted to the midline, suggesting that they are a subset of the r2-*Pet1*$^{Tph2\text{-high}}$ group, or at least a subset accessible using this recombinase driver combination. We observed dense, 5-HT^{+} *Piezo2-Pet1* fibers within the SCN (73.2 ± 3.27% 5-HT^{+}) and the PVT (60.5 ± 3.16% 5-HT^{+}; Figure 2.5B-C). *Piezo2-Pet1* fibers were present, but less dense, in other regions where we observed 5-HT^{+} r2-*Pet1* innervation such as OB, DLS, and MS (Figure 2.5D-F). In these regions, the majority of *Piezo2-Pet1* fibers were immunopositive for 5-HT^{+} (OB: 74.7 ± 6.01% 5-HT^{+}, LS: 56.2 ± 4.97%, MS: 71.6 ± 1.90%) but negative for VGLUT3 (OB: 0.250 ± 0.126% VGLUT3^{+}, LS: 1.04 ± 0.536%, MS: 1.342 ± 0.514%). Across all regions, a small percentage of *Piezo2-Pet1* boutons were immunopositive for both VGLUT3 and 5-HT, highest in the OB (2.98 ± 0.201% VGLUT3^{+}/5-HT^{+}) and SCN (2.87 ± 0.437% VGLUT3^{+}/5-HT^{+}). Upon exploring the target areas harboring VGLUT3-

only boutons from r2-*Pet1* neurons, we failed to detect innervation by the *Piezo2-Pet1* neuron group (dorsal hippocampus shown, Figure 2.5G). Together, these findings suggest that *Piezo2-Pet1* neurons represent a r2-*Pet1*$^{Tph2\text{-high}}$ population with projections largely restricted to the 5-HT-only SCN, PVT, and OB.

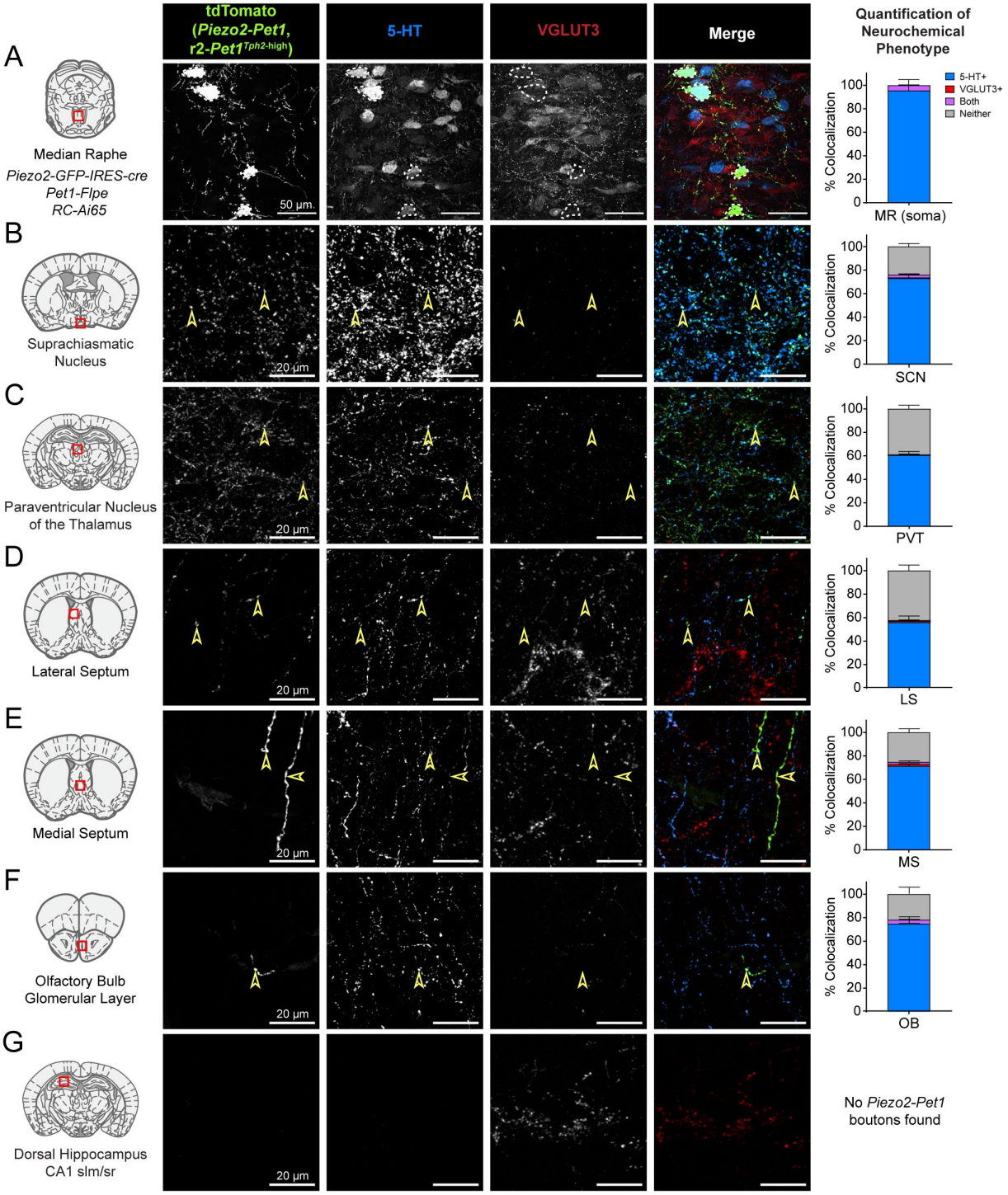

Figure 2.5. *Piezo2-Pet1* neurons are of the r2-*Pet1*$^{Tph2\text{-high}}$ subtype and harbor projections selectively to regions innervated by 5-HT-positive r2-*Pet1* boutons.

We previously identified *Piezo2* as a marker of the r2-*Pet1*$^{Tph2\text{-high}}$ subtype (Okaty et al. 2015). *Piezo2-Pet1* cell bodies in the MR are labeled by 5-HT but not VGLUT3 (A). Piezo2-*Pet1* neurons give rise to 5-HT^{+} projections (arrowheads) in the suprachiasmatic nucleus (SCN; B),

(Figure 2.15 continued)
paraventricular nucleus of the thalamus (PVT; C), lateral septum (D), medial septum (E), and olfactory bulb glomerular layer (F). By contrast, *Piezo2-Pet1* cells do not innervate the dorsal hippocampus, a region shown to have predominately VGLUT3+ r2-*Pet1* innervation (G).

*Retrograde viral tracing from the dorsal hippocampus highlighted r2-*Pet1 *somata positive for VGLUT3 but not serotonin*

Given that the r2-Pet1 boutons found in the dorsal hippocampus were of the VGLUT3-only class, we hypothesized that the source neuron subset was the r2-Pet1$^{Vglut3\text{-}high}$ neuron subpopulation and not the r2-Pet1$^{Tph2\text{-}high}$ subgroup. To test this, we injected into the dorsal hippocampus (AP -2.06, ML ± 2.06, DV -1.75 mm) of r2Hoxa2-cre, Pet1-Flpe, RC-FrePe mice (n=3) a retrogradely-transported, tdTomato-expressing AAV and analyzed the neurochemical phenotype (staining for either 5-HT or VGLUT3) of the tdTomato-labeled (and thus dorsal hippocampus-projecting) subset of r2-Pet1 (EGFP$^+$) somata (Figure 2.6). Worth noting, VGLUT3, in contrast to other VGLUTs, localizes both to axonal boutons and the somatodendritic compartment as well (Fremeau et al. 2004; Herzog et al. 2004), which we exploited here. To identify VGLUT3$^+$ cell bodies, we used a knockout mouse-verified antibody (Schallier et al. 2011) previously used to label VGLUT3$^+$ somata in the raphe (Sos et al. 2017; Okaty et al. 2020) and found a distribution of VGLUT3-immunolabeled cell bodies consistent with prior anatomical studies describing the colocalization of Vglut3 mRNA and its protein in MR neurons (Herzog et al. 2004). We examined 1804 neurons, with 1263 EGFP$^+$ neurons, 629 tdTomato$^+$ neurons, and 88 neurons co-labeled for tdTomato and EGFP; the latter indicating that our retrograde tracing conditions labeled a fraction of the r2-Pet1 cell group. Of the dual labeled (EGFP$^+$, tdTomato$^+$)

r2-Pet1 somata, 82.3 ± 1.46% stained immunopositive for VGLUT3 but only 2.0 ± 2.0% stained positive for 5-HT. Thus, the hippocampal-projecting r2-Pet1 somata were significantly more likely to be VGLUT3$^+$ than 5-HT$^+$ ($t = 106.6$, $df=2$, $p<0.0001$, paired t-test; Figure 2.6E). This finding is in line with the r2-Pet1 bouton immunophenotype of VGLUT3-only mapped to the dorsal hippocampus. Of all retrogradely labeled tdTomato$^+$ cells in the MR region, most were VGLUT3$^+$ (76.8 ± 6.6%) and few were 5-HT$^+$ (9.6 ± 3.86%), consistent with previous literature reporting a predominant VGLUT3$^+$ innervation of the hippocampus from the MR (Jackson et al., 2008; Szőnyi et al., 2016; Figure 2.6E′). In contrast, when sampling all r2-Pet1 cells (EGFP-labeled), a smaller fraction of cells was immunoreactive for VGLUT3 (52.0 ± 2.19%) and 28.74 ± 0.94% were 5-HT$^+$ (Figure 2.6E′′). These results demonstrate that the r2-Pet1 cells that project to the dorsal hippocampus overwhelmingly express VGLUT3 in the soma, consistent with the neurochemical phenotype of the mapped r2-Pet1 boutons, suggesting the source neurons are the r2-Pet1$^{\text{Vglut3-high}}$.

Figure 2.6. Hippocampal retrograde tracing shows that VGLUT3$^+$ boutons in this region preferentially arise from r2-*Pet1*$^{\textit{Vglut3}\text{-high}}$ neurons.

Schematic showing injection, in the dorsal hippocampus (bilaterally) at the CA1 slm/sr border, of a retrograde serotype AAV expressing tdTomato under a *CAG* promoter performed in *r2Hoxa2-cre, Pet1-Flpe, RC-FrePe* mice expressing EGFP in r2-*Pet1* cells (A). Fluorescent photomicrograph showing the general localization of retrogradely labeled cells (tdTomato$^+$) and r2-*Pet1* cells (EGFP$^+$) in the MR (B). r2-*Pet1* cells that project to the hippocampus (EGFP$^+$/tdTomato$^+$) have somata immunopositive for VGLUT3 (C) but not 5-HT (D). Hippocampus-projecting r2-*Pet1* cells were more likely to be VGLUT3$^+$ than 5-HT$^+$ ($t = 106.6$, $df=2$, $p<0.0001$, paired t-test). We also quantified VGLUT3 and 5-HT immunopositivity for all tdTomato+ cells in the MR (E′) or the entire population of r2-*Pet1* cells (E′′). Asterisks indicate statistically significant differences.

(Figure 2.6 continued)

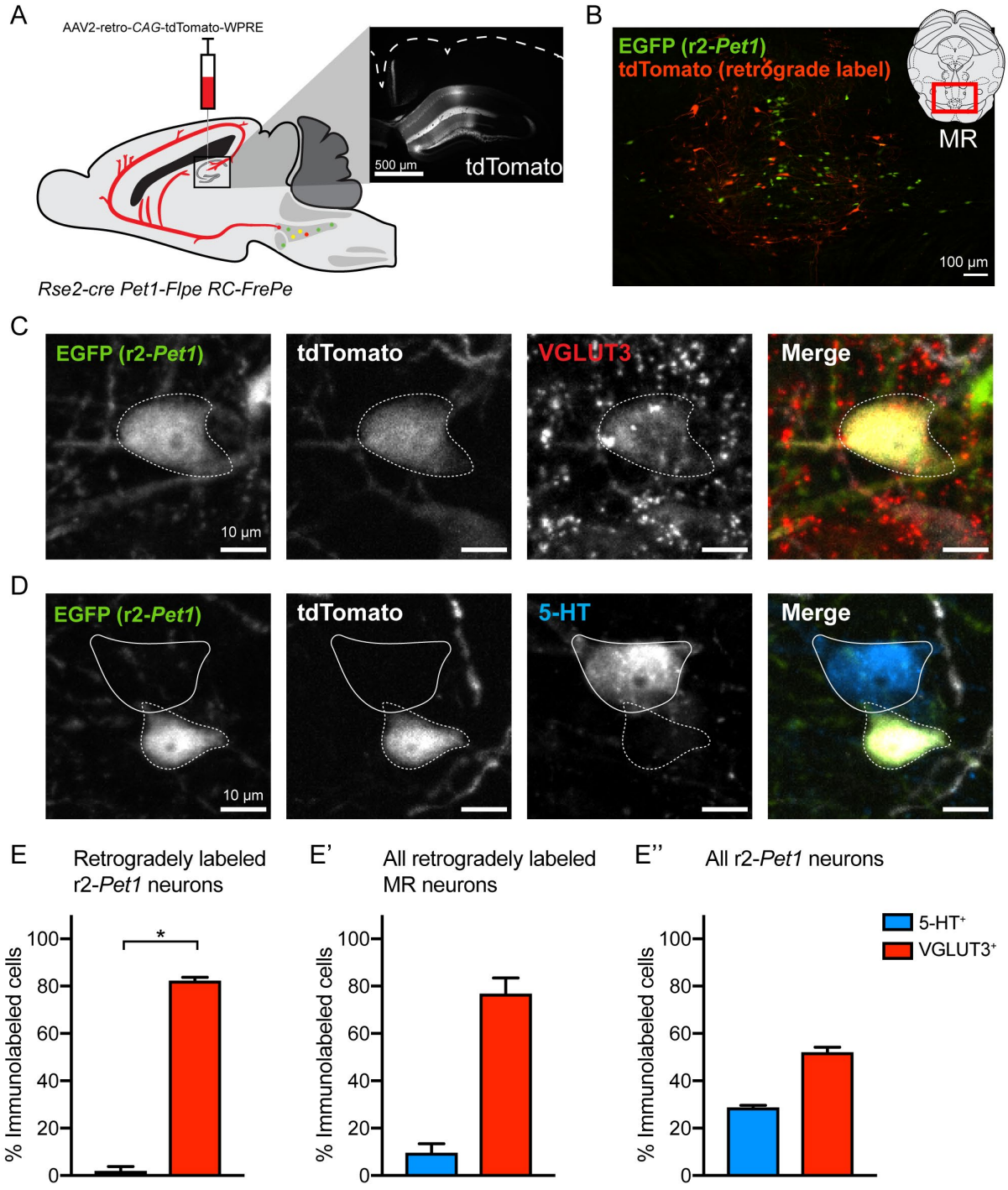

r2-Pet1 VGLUT3^{+} boutons comprise pericellular baskets in certain brain regions

In brain regions with r2-*Pet1* VGLUT3^{+} innervation, including the cortex (retrosplenial, cingulate, prelimbic, somatosensory, and motor cortex), hippocampus, and septal nuclei, we found r2-*Pet1* boutons in dense arrays surrounding a target cell body and proximal dendrites, akin to previously described "pericellular baskets" (Figure 2.7A-D; DeFelipe et al., 1991; Dinopoulos et al., 1993; Freund et al., 1990; Hioki et al., 2004; Hornung et al., 1990; Köhler et al., 1982; Riedel et al., 2008; Vu and Törk, 1992). Operationally, we defined r2-*Pet1* pericellular baskets when r2-*Pet1* axons wrapped around more than half of the soma perimeter (or when no cell stain was present, the nucleus perimeter) or when boutons were closely apposing the soma on multiple sides such that dividing the cell into quadrants would result in boutons apposing the cell in all quadrants. Such pericellular basket structures rarely characterized r2-*Pet1* boutons found in the OB and PVT and not at all in the SCN – all target regions harboring r2-*Pet1* boutons of the 5-HT-only class. Additionally, *Piezo2-Pet1* fibers representing a subset of the r2-*Pet1*$^{Tph2\text{-high}}$ subtype were not observed to make pericellular baskets. Thus, this specialized presynaptic basket structure may be feature specific to r2-*Pet1*$^{Vglut3\text{-high}}$ cells, but not r2-*Pet1*$^{Tph2\text{-high}}$ cells.

We show in Figure 2.4 that r2-*Pet1* boutons in the septum are either VGLUT3^{+} or co-positive for VGLUT3^{+} and 5-HT^{+}. We examined a subset of 11 medial septum images from *r2Hoxa2-cre, Pet1-Flpe, RC-FPSit* mice (n=7) quantified in Figures 2-4 and examined the neurochemical phenotypes of boutons belonging to baskets (manually defined as above) versus other boutons in the image innervating the same region but not contributing to baskets. Of the r2-*Pet1* boutons comprising pericellular baskets (473 boutons examined across all mice), 31.98% were co-positive, versus only 15.9% of boutons in non-basket configurations (1300 non-basket

boutons examined across all mice; Figure 2.7D'), showing that r2-*Pet1* boutons that contribute to baskets in the medial septum were significantly more likely to be co-positive for both VGLUT3 and 5-HT than non-basket boutons in the same region ($t=3.140$, $df=6$, $p=0.020$, paired t-test). These results indicate that in the septum, boutons that contribute to baskets may be more likely to co-transmit 5-HT and glutamate.

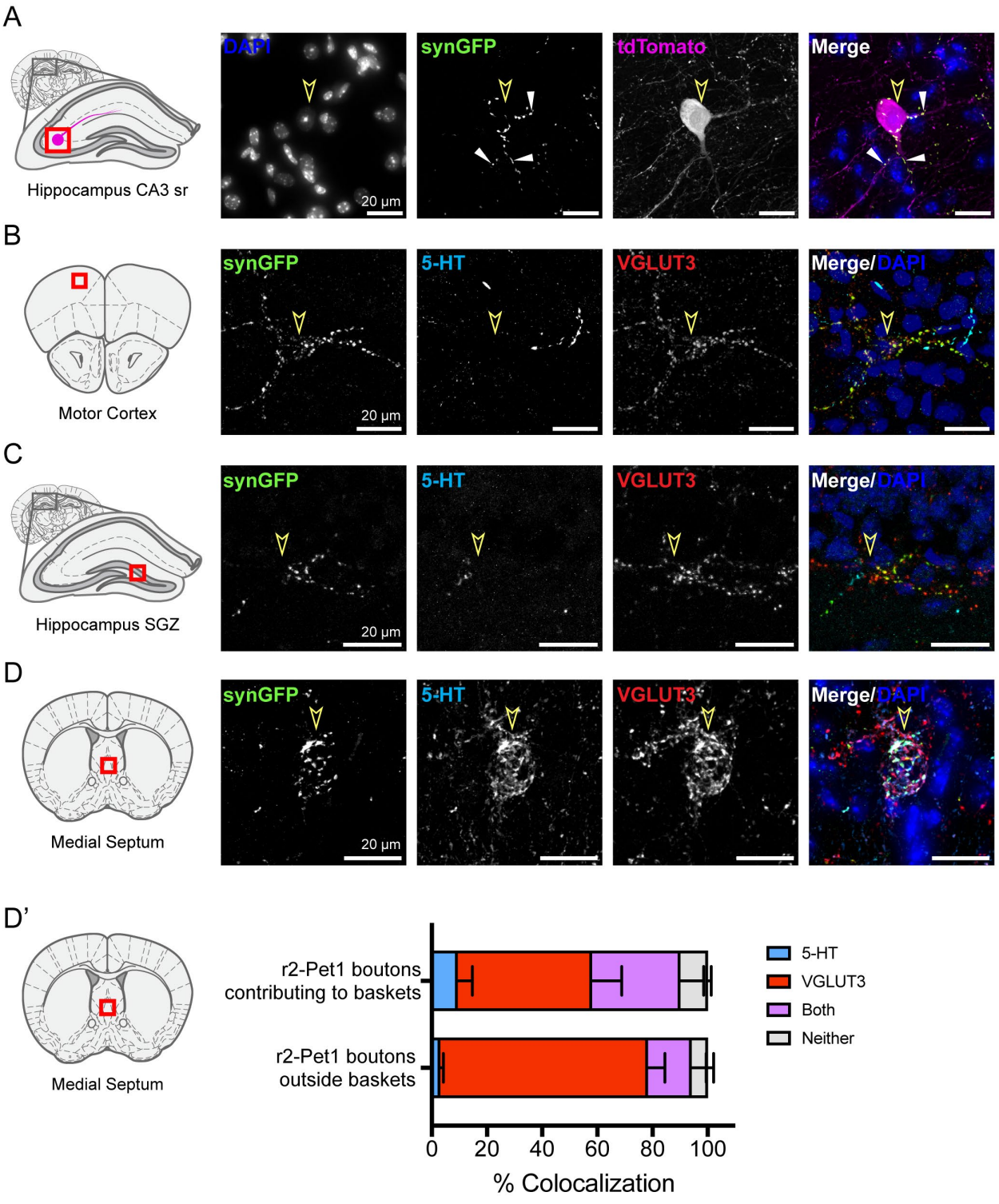

Figure 2.7. r2-*Pet1* neuron boutons contribute to pericellular basket arrays in the cortex, hippocampus, and septum.

(Figure 2.7 continued)
Fluorescent photomicrograph showing a basket comprising r2-*Pet1* boutons surrounding the soma and proximal dendrites of a hippocampal CA3 cell retrogradely labeled by injection of AAV2-retro-*CAG*-tdTomato-WPRE into CA1 (A). Fluorescent photomicrographs showing pericellular basket arrays in the prelimbic cortex (B) and hippocampal subgranular zone (C) comprising VGLUT3$^+$ r2-*Pet1* boutons. By contrast, r2-*Pet1* basket arrays in the medial septum (D) comprise boutons that are 5-HT$^-$/VGLUT3$^+$ as well as co-positive 5-HT$^+$/VGLUT3$^+$. In the medial septum, co-positive 5-HT$^+$/VGLUT3$^+$ boutons are enriched in pericellular baskets, ($t=3.140$, $df=6$, $p=0.020$, paired t-test; D'). Operationally, we defined r2-*Pet1* pericellular baskets as occurring when *r2-Pet1* axons surrounded >50% of the perimeter of the cell body or nucleus and/or *r2-Pet1* boutons closely apposed the target cell body in all four surrounding quadrants. Arrowheads are placed above the basket-targeted cell body.

Some pericellular baskets are comprised of boutons from multiple Pet1 *neuron subtypes exhibiting distinct neurochemical profiles*

In some cases, our 5-HT and synGFP staining revealed synGFP-negative, 5-HT$^+$ fibers converging on the same target cell as the synGFP$^+$ r2-Pet1 boutons comprising a basket (Figure 2.8A). This suggested that the former might arise from a non-r2-derived Pet1 serotonergic neuron (i.e., a different subtype of serotonergic neuron). Such composite baskets (r2-Pet1 VGLUT3$^+$ boutons and other 5-HT$^+$ boutons) were found to be most prevalent in the stratum radiatum of the hippocampal CA3 subfield (Figure 2.8A) and in the medial and lateral septal nuclei (Figure 2.8B). In line with the observation that the non-r2-Pet1 fibers in these composite baskets were found to be 5-HT$^+$ (or SERT$^+$), we discovered that some of the postsynaptic target cells in the cortex and dorsal hippocampus expressed 5-HT3A (Figure 2.8C), the ionotropic excitatory 5-HT receptor and thus could be capable of receiving the basket-derived 5-HT signal. Moreover, the nature of the 5-HT3A receptor suggests that 5-HT may evoke fast excitatory synaptic firing (Lee et al. 2010) in these specific target cells. In the lateral septum, some basket-

targeted cells were immunopositive for the slower signaling G-protein-coupled receptor (GPCR) 5-HT2C (Figure 2.8D); none were immunopositive for 5-HT3A (data not shown). Together, these findings suggest that 5-HT released from pericellular basket-associated boutons may act on distinct temporal scales across different brain regions.

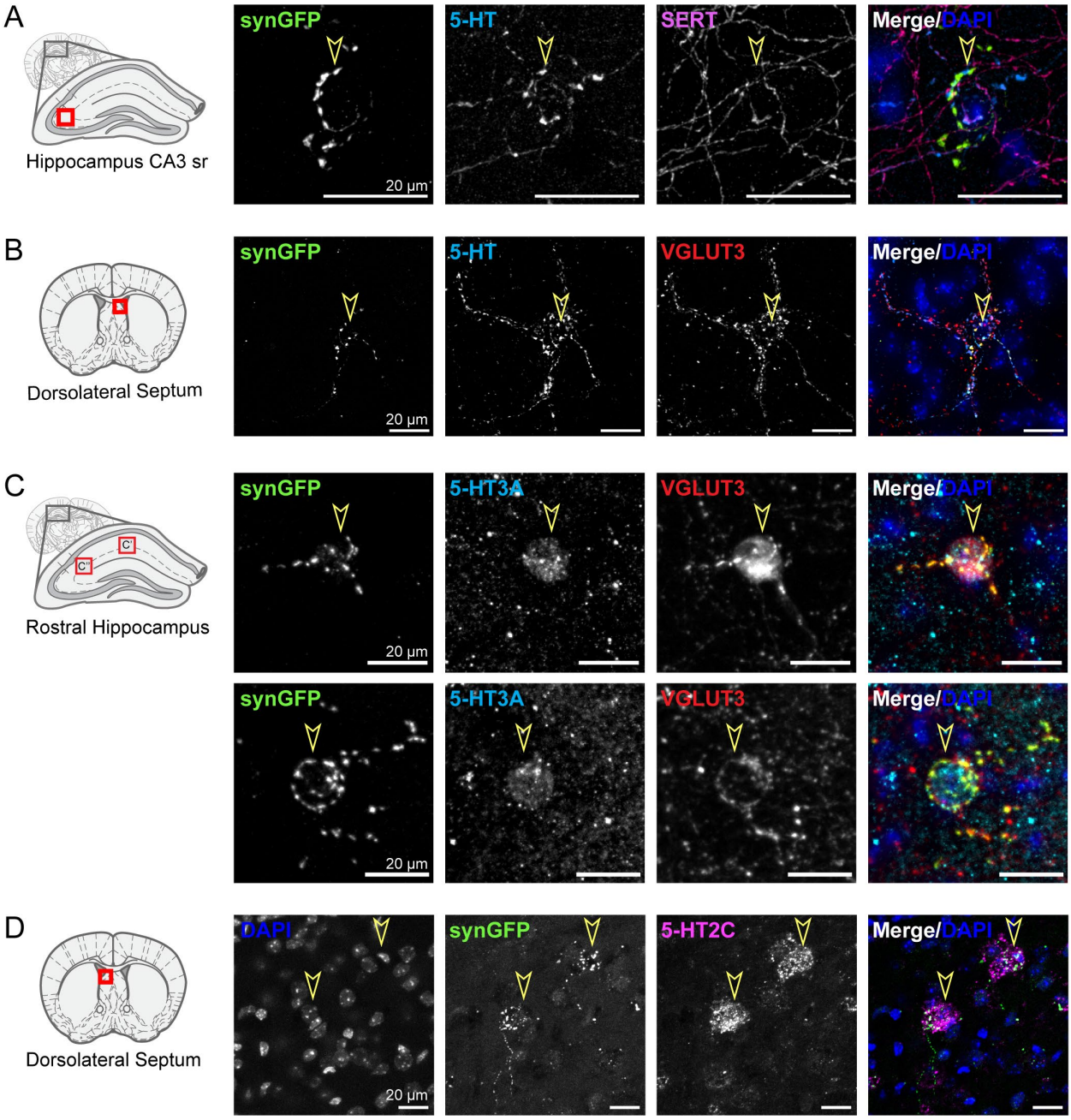

Figure 2.8. Cells targeted by r2-*Pet1* pericellular baskets also receive 5-HT input.

Fluorescent photomicrographs in hippocampus (A) and dorsolateral septum (B) showing baskets comprised of both synGFP$^+$ r2-*Pet1* boutons and non-synGFP-labeled 5-HT$^+$ boutons. Arrowheads placed above the nucleus targeted by the r2-*Pet1* pericellular basket. Consistent with the non-r2-*Pet1* serotonergic innervation, some basket target cells expressed the 5-HT receptors 5-HT3A (C-C'') and 5-HT2C (D).

To assess whether multiple *Pet1* neuron subtypes converge to form pericellular baskets around the same downstream cell, we labeled simultaneously r2-*Pet1* fibers versus other (non-r2) *Pet1* fibers with different fluorophores and examined basket composition in the septum, a region abundant in baskets. Triple transgenic *r2Hoxa2-cre, Pet1-Flpe, RC-FrePe* (n=4, 2 males, 2 females) mice and one *r2Hoxa2-cre, Pet1-Flpe, RC-FLTG* (n=1, male) mouse equally enabled this analysis, as each strain selectively marked r2-*Pet1* somata and fibers intersectionally with EGFP while simultaneously labeling other *Pet1* cells with mCherry or tdTomato, respectively as the subtractive population (Figure 2.9A-A'). We examined 163 r2-*Pet1* pericellular baskets, finding many with nearby subtractive *Pet1* boutons closely apposing the same cell (64.5 ± 3.95% of r2-*Pet1* baskets). Further, for 35.1 ± 3.10% of r2-*Pet1* baskets, this subtractive *Pet1* contribution also formed a pericellular basket (Figure 2.9B). For an additional third of r2-*Pet1* baskets, there was no other *Pet1* innervation closely apposing the targeted cell nucleus (35.5 ± 3.95% of baskets). These results demonstrate that r2-*Pet1* pericellular baskets are a heterogeneous group with a large portion converging with other *Pet1* neurons to form composite pericellular baskets on the same downstream cell.

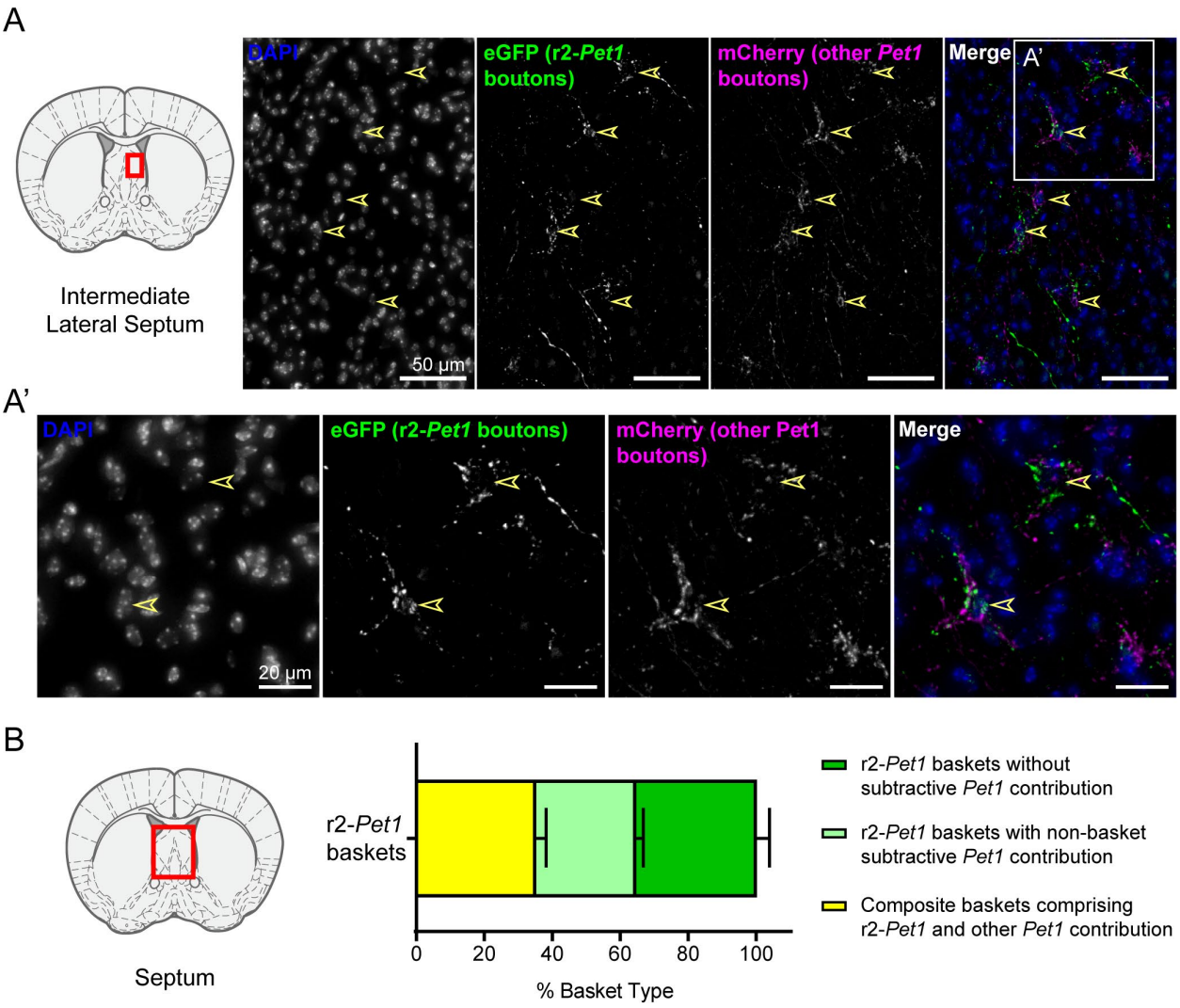

Figure 2.9. Multiple *Pet1* neuron lineages contribute to composite pericellular baskets in the septum.

Fluorescent photomicrographs showing composite baskets in the lateral septum in which r2-*Pet1* axons (green) and other non-r2 *Pet1* axons (red) converge onto the same targeted cell body, indicated by arrowheads (A-A'). Quantification of the proportion of r2-*Pet1* baskets that were composite with other *Pet1* axons (B).

We next queried whether r2-*Pet1* boutons in composite pericellular baskets differed neurochemically from other *Pet1* boutons contributing to the same baskets. We sampled 132 composite baskets (3,294 EGFP boutons and 2,672 mCherry boutons) of the lateral septum from

adult *r2Hoxa2-cre, Pet1-Flpe, RC-FrePe* (n=3, 2 male, 1 female) mice. In separate experiments, we immunodetected EGFP (r2-*Pet1* boutons), mCherry (other *Pet1* boutons), and either 5-HT (Figure 2.10A) or VGLUT3 (Figure 2.10B). Composite baskets showed no differences in amounts of r2-*Pet1* EGFP boutons (25.6 ± 1.40) versus other *Pet1* mCherry boutons (19.8 ± 1.52). Baskets also contained additional boutons immunopositive for 5-HT (31.4 ± 2.01) or VGLUT3 (32.2 ± 1.05) not captured using our transgenic fluorescent labeling approach. These boutons could be from *Pet1* neurons missed by our drivers or immunohistochemical methods or alternatively, could reflect boutons from non-*Pet1* neurons that form baskets around these same target cells (Figure 2.10C-D). With respect to the *Pet1*-captured basket-forming fibers, we found the non-r2 *Pet1* boutons were more likely to be 5-HT$^+$ (70.6 ± 2.67%) than the r2-*Pet1* boutons (45.9 ± 3.42%; t=12.7, df=2, p=0.0062, paired t-test; Figure 2.10E). Both populations contributing to composite baskets were similarly likely to be VGLUT3$^+$ (r2-*Pet1*: 65.1 ± 1.80%; other *Pet1*: 58.6 ± 4.61%; t=1.02, df=2, p=0.415, paired t-test; Figure 2.10F). Altogether, these findings demonstrate that 1) r2-*Pet1* and other *Pet1* neurons commonly form composite pericellular baskets around the same downstream target cells and 2) in the lateral septum, composite baskets are neurochemically diverse, with r2-*Pet1* boutons less likely to be 5-HT$^+$, but similarly likely to be VGLUT3$^+$ as other *Pet1* fibers contributing to the same baskets.

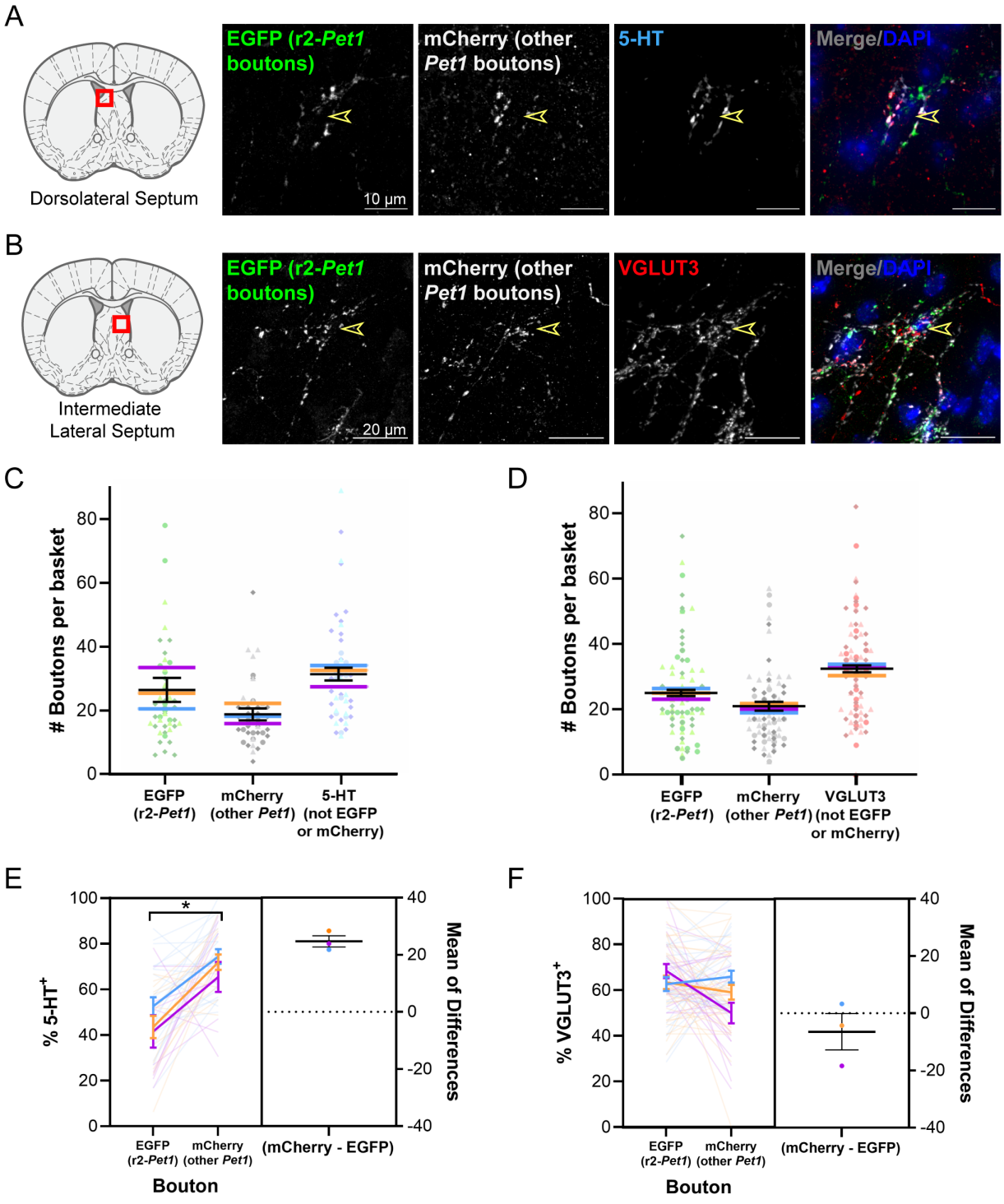

Figure 2.10. In pericellular baskets, r2-*Pet1* boutons (EGFP$^+$) and other *Pet1* boutons (mCherry$^+$) are neurochemically distinct.

Composite baskets with r2-*Pet1* boutons and other *Pet1* boutons in the lateral septum with co-labeling for 5-HT (A) and VGLUT3 (B). Arrowheads demarcate the location of the nucleus

(Figure 2.10 continued)
targeted by the pericellular basket. We found similar numbers of EGFP and mCherry boutons contributing to composite *Pet1* lateral septum pericellular baskets (C-D). However, r2-*Pet1* boutons were less likely to be 5-HT$^+$ (t=12.7, df=2, p=0.0062, paired t-test, E), but similarly likely to be VGLUT3$^+$ (t=1.02, df=2, p=0.415, paired t-test, F). The orange, purple, and blue lines indicate individual animal means and individual measurements of baskets are indicated by differently shaped points in C,D and lightly shaded orange, purple, and blue lines in E and F. Asterisks indicate statistically significant differences.

r2-Pet1 *pericellular baskets target specific GABAergic neuron subtypes*

Next we applied various cell subclass markers to further explore the identity of cells targeted by r2-*Pet1* pericellular baskets. We found that r2-*Pet1* pericellular baskets targeted GABA$^+$ neurons in both cortical regions and in the septum (Figure 2.11A-B), a finding consistent with previous literature on the pericellular baskets formed by median raphe 5-HT neurons (Halasy et al. 1992; Hornung and Celio 1992). Further, we found that target cells in the cortex and hippocampus as compared to the septum could be differentiated by labeling with markers of interneuron class. In the cortex and hippocampus, we observed r2-*Pet1* baskets around Reelin$^+$ and vasoactive intestinal peptide (VIP)$^+$ interneurons (Figure 2.11C-D) as well as VGLUT3$^+$ interneurons that were sometimes positive for neurokinin B (NKB) (Figure 2.11E). The latter group is likely to be the well described cholecystokinin (CCK)$^+$/VGLUT3$^+$ basket cell type, which in turn forms pericellular baskets targeting cortical pyramidal neurons (Somogyi et al. 2004; Fasano et al. 2017; Booker and Vida 2018; Harris et al. 2018). In contrast to the hippocampus and cortex, the targets of r2-*Pet1* pericellular baskets in the septum remain largely mysterious (Riedel et al. 2008), though some of these targeted cells express somatostatin (SST). In all regions, r2-*Pet1* fibers do not form baskets around parvalbumin (PV)-positive interneurons

(data not shown), consistent with previous studies from the MR (Freund et al. 1990; Hornung and Celio 1992; Papp et al. 1999) and suggesting the r2-*Pet1* pericellular basket regulates specific subtypes of interneurons and possibly GABAergic projection neurons in the septum.

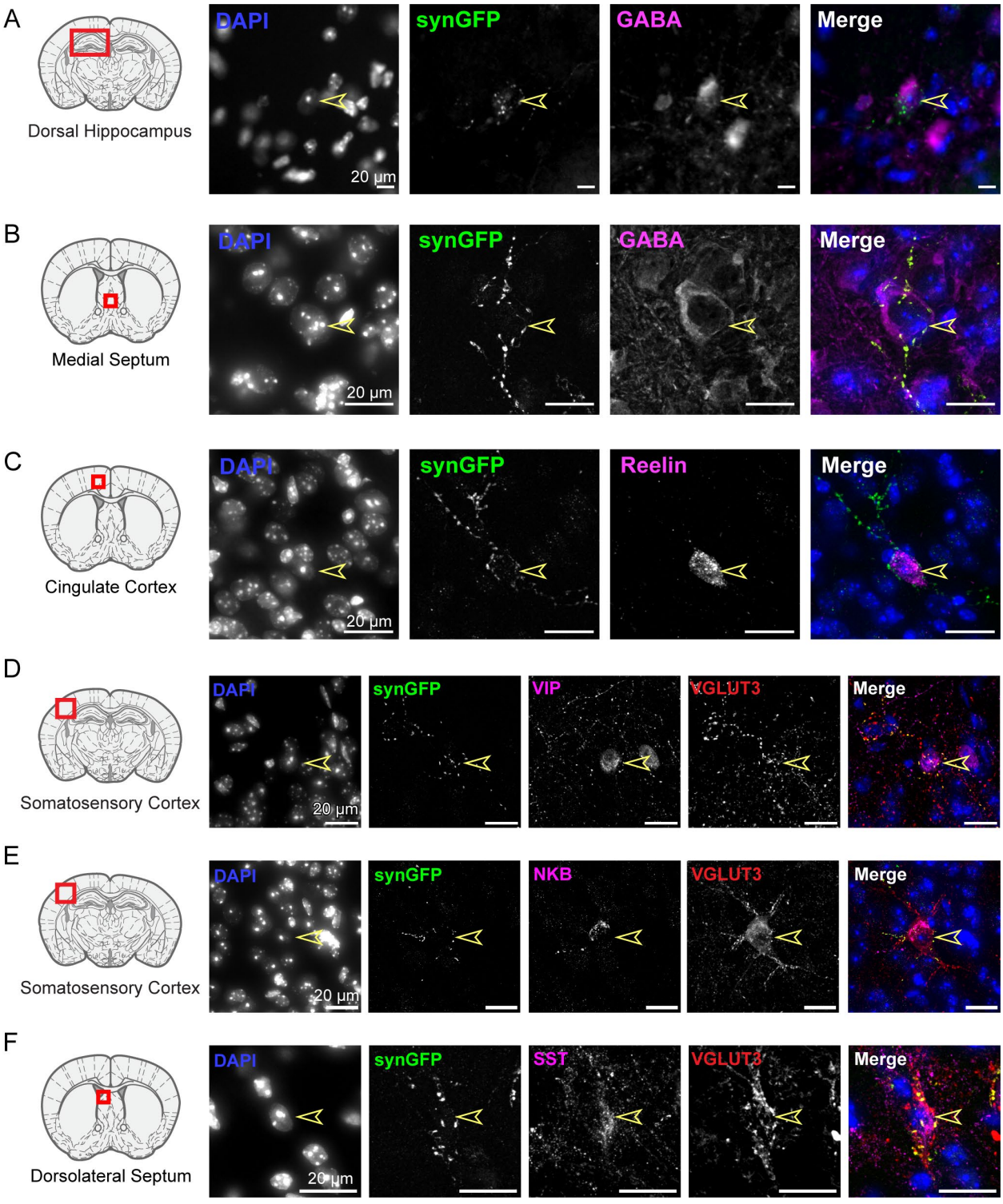

Figure 2.11. r2-*Pet1* pericellular baskets target interneurons.

Targets of pericellular baskets were overwhelmingly GABA^{+} in hippocampus (A), and (A-B). Cortical and hippocampal basket targets were often Reelin+ (C), Calbindin^{+}, VIP^{+} (D), or

(Figure 2.11 continued)
VGLUT3$^+$/NKB$^+$ (E), whereas subcortical septal basket targets were sometimes SST$^+$ (F). Arrowheads demarcate the cell body targeted by the r2-*Pet1* pericellular basket.

We then quantified the prevalence of r2-*Pet1* baskets on two interneuron classes in cortex, hippocampus, and septum: calbindin$^+$ and VGLUT3$^+$ somata. We examined sections containing dorsal hippocampus and septum in adult *r2Hoxa2-cre, Pet1-Flpe, RC-FPSit* mice (n=6, 3 male and 3 female). Using a combination of manual and automatic segmentation combined with automatic detection of baskets (see Methods), we quantified the proportion of calbindin$^+$ and VGLUT3$^+$ somata receiving a r2-*Pet1* basket. We observed VGLUT3$^+$ somata were most prevalent in layer 2 and layer 6 in cortex, and in the sr and sr/slm border region in hippocampus, in line with previous studies (Fremeau et al., 2004; Figure 2.12A). Calbindin$^+$ somata were highly abundant in cortical layer 2/3 and sporadically present in deeper layers, were distributed through the sr and sr/slm of the dorsal hippocampus (Figure 2.12B) and were enriched in the lateral septum (Figure 2.12C). We quantified the proportion of each cell type targeted by r2-*Pet1* baskets varied as a function of region. We observed a higher proportion of cortical VGLUT3$^+$ somata (31.2 ± 3.18%, 343 total cells examined) that were targeted by an r2-*Pet1* pericellular basket relative to hippocampal VGLUT3$^+$ somata (16.6 ± 4.12%; 329 cells examined; t=8.60, df=5, p=0.0004, paired t-test; Figure 2.12D). Examining subregions of cortex and hippocampus in which we observed an average of 10 cells per animal or greater, we found the greatest percent of VGLUT3$^+$ somata were targeted in secondary motor cortex (M2; 39.9 ± 4.29%) compared with other cortical subregions (primary motor cortex (M1): 26.6 ± 6.29; parietal association cortex (PtA): 31.2 ± 7.93%) and without appreciable difference between the two

hippocampal subregions analyzed (CA1 sr/slm: 16.3 ± 4.87%; CA3 sr/slm: 19.4 ± 3.90%; Figure 2.12D'). Regional targeting of calbindin$^+$ interneurons exhibited the opposite pattern: cortical calbindin$^+$ neurons were rarer targets (0.771 ± 0.127%, 15,331 total cells examined) compared with dorsal hippocampal calbindin$^+$ neurons (21.2 ± 2.71%, 225 total cells examined; t=7.65, df=5, p=0.0006, paired t-test Figure 2.12E). In the septum, there were no VGLUT3$^+$ somata and calbindin$^+$ somata were rarely targeted by r2-*Pet1* baskets (0.229 ± 0.170% of cells targeted, 2919 total cells examined). These results demonstrate target specificity of r2-*Pet1* baskets wherein different neuron types were preferentially targeted in different regions.

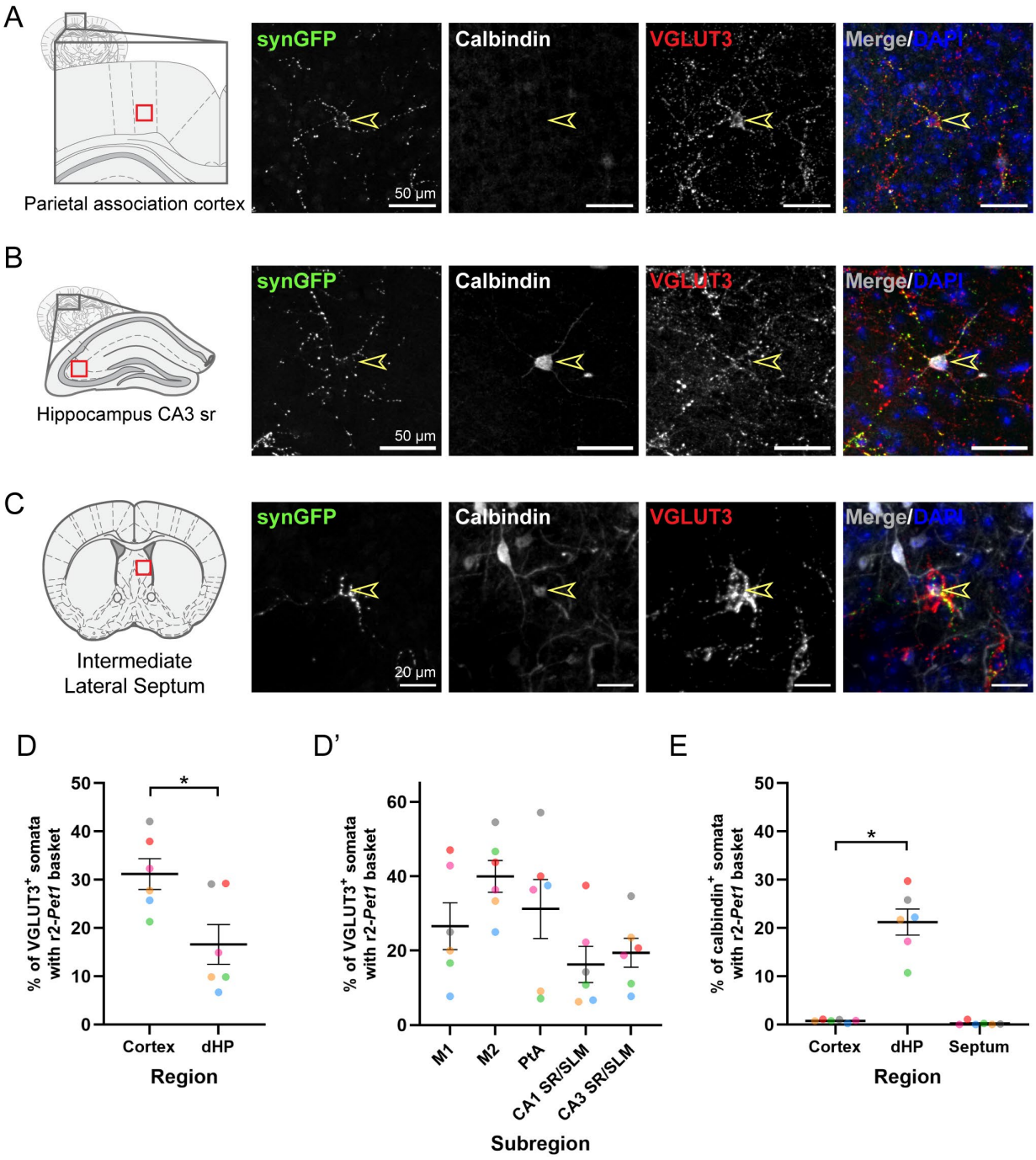

Figure 2.12. r2-*Pet1* pericellular baskets exhibit regional target cell-type specificity.

Examples of r2-*Pet1* pericellular baskets targeting VGLUT3$^+$ somata in cortex (A) and calbindin$^+$ somata in dorsal hippocampus (B). Rarely, calbindin$^+$ cells are targeted by r2-*Pet1* baskets in the lateral septum (C). Arrowheads indicate the cell body targeted by the r2-*Pet1* basket. VGLUT3$^+$ somata were more likely to be targeted by r2-*Pet1* baskets in cortex than hippocampus t=8.60, df=5, p=0.0004, paired t-test (D), with some variation across the primary motor cortex (M1),

(Figure 2.12 continued)
secondary motor cortex (M2), parietal association cortex (PtA), hippocampal CA1 and CA3 stratum radiatum and stratum lacunosum moleculare (SR/SLM, D'). In contrast, a higher proportion of calbindin^{+} neurons were targeted by r2-*Pet1* baskets in the dorsal hippocampus (dHP) than the cortex or septum, t=7.65, df=5, p=0.0006, paired t-test (E). Asterisks indicate statistically significant differences.

DISCUSSION

Strategy

The r2-*Pet1* neuron group is hodologically, functionally, and molecularly distinct from other *Pet1*$^{+}$ neurons and itself is comprised of two subgroups—the r2-*Pet1*$^{Tph2\text{-high}}$ group being serotonergic and the r2-*Pet1*$^{Vglut3\text{-high}}$ subgroup being largely VGLUT3^{+} and glutamatergic. We proposed that the cognate axonal boutons would likely show a matching neurochemical phenotype (5-HT^{+} or VGLUT3^{+}) and thus might be used to resolve downstream circuitry specific to each of these subtypes of r2-*Pet1* neurons.

Main Findings

Significant findings include the following: (1) r2-*Pet1* boutons were found distributed anatomically by neurochemical phenotype. 5-HT^{+}/VGLUT3^{-} boutons were found in the SCN PVT, and OB. The reciprocal bouton identity of VGLUT3^{+}, 5-HT^{-} was found in the hippocampus, prelimbic cortex, and septum. Rarely observed were co-positive boutons or a mix of each single-positive bouton type, the exception being in the septum. (2) *Piezo2-Pet1* neurons reside within the r2-*Pet1*$^{Tph2\text{-high}}$ group and exhibited axonal projections to the SCN, PVT, and OB. (3) Retrograde labeling from the hippocampus illuminated somata of r2-*Pet1*$^{Vglut3\text{-high}}$, but not r2-*Pet1*$^{Tph2\text{-high}}$ cells. Findings 2 and 3 substantiate the bouton-to-neuron-subtype match up of

finding 1 and suggest that the r2-*Pet1* neuronal group is comprised of two distinct neuronal subsystems that modulate different brain regions using different neurotransmitters. They likewise suggest that the majority of r2-*Pet1*$^{Vglut3\text{-high}}$ neurons are excitatory, potentially releasing glutamate as their sole transmitter, even with the expression of *Pet1* and having arisen from the same progenitor cell compartment as the classically serotonergic *Pet1*$^{Tph2\text{-high}}$ cells. (4) Some VGLUT3^{+} r2-*Pet1* boutons composed pericellular baskets encasing the post-synaptic neuron soma. (5) Some basket-forming boutons in the septum were both 5-HT^{+} and VGLUT3^{+}, suggestive of possible co-transmission of 5-HT and glutamate (Amilhon et al. 2010). (6) The r2-*Pet1* baskets often encased GABAergic interneurons of the Reelin^{+}, VIP^{+}, or VGLUT3^{+} classes, in some cases as composites containing fibers from different *Pet1* neuron subtypes. (7) Some basket-encased, postsynaptic targets in the septum expressed the metabotropic 5-HT2C receptor, and others in the cortex and hippocampus expressed the ionotropic 5-HT3A receptor, suggesting that the basket-released 5-HT may act on distinct temporal scales in different target brain regions.

*Separable neuronal subsystems comprise the r2-*Pet1 *neuron population of the median raphe*

A simple interpretation of our r2-*Pet1* bouton neurochemical mapping is a divergent circuitry model whereby the r2-*Pet1*$^{Tph2\text{-high}}$ and r2-*Pet1*$^{Vglut3\text{-high}}$ neuron subgroups innervate different brain regions and deploy different neurotransmitters (Figure 2.13). While the specific functions of each subgroup have yet to be determined, this divergent circuitry model supports certain predictions. The first is that the midline subcortical projections characterizing the r2-

Pet1$^{Tph2\text{-high}}$ subgroup may regulate sensory modulation of circadian behavior. The SCN and PVT targets are each implicated in regulating circadian rhythm and themselves are reciprocally connected structures (Weber et al. 1998; Morin and Meyer-Bernstein 1999). Loss of MR 5-HT input to the SCN has been shown to alter circadian rhythm and increase the sensitivity to light-induced circadian phase-shifting (Bradbury et al. 1997; Morin and Meyer-Bernstein 1999) Similarly, lesions of the PVT suggest that it too may mediate circadian rhythm shifts in response to light (Salazar-Juárez et al. 2002). Thus, r2-*Pet1*$^{Tph2\text{-high}}$ projections to these regions may suppress changes in circadian rhythm by modulating regional responsiveness to deviations from the expected pattern of illumination.

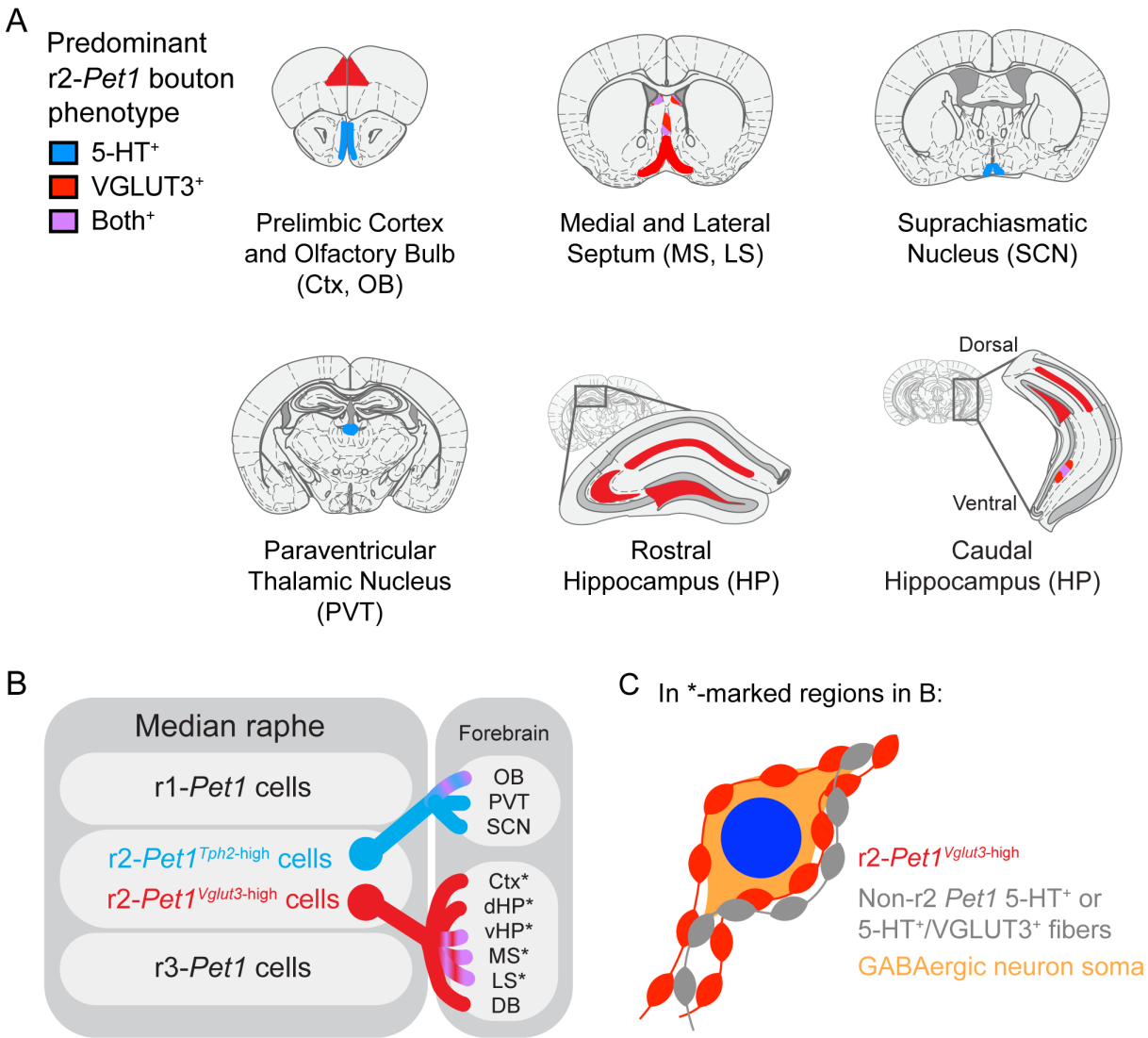

Figure 2.13. Summary of findings.

r2-*Pet1* VGLUT3$^+$ and 5-HT$^+$ boutons are spatially segregated across the forebrain (A), with cortical and hippocampal areas innervated by VGLUT3$^+$ r2-*Pet1* boutons, midline structures such as the SCN, OB, and PVT innervated by 5-HT$^+$ r2-*Pet1* boutons, and septal areas innervated by a mix of VGLUT3$^+$ and co-positive 5-HT$^+$/VGLUT3$^+$ boutons. These results suggest functionally separable subtypes of r2-*Pet1* cells (B). In the septum, cortex, and hippocampus, regions targeted by the r2-*Pet1*$^{Vglut3\text{-high}}$ subtype, r2-*Pet1* boutons formed pericellular baskets targeting inhibitory interneurons, suggesting additional functional specialization of this r2-*Pet1* subset (C).

VGLUT3^{+} r2-*Pet1* boutons, by contrast, were found in limbic regions such as the septum, hippocampus, and prelimbic cortex, suggesting r2-*Pet1*$^{Vglut3\text{-high}}$ neurons may modulate memory and sensorimotor gating. The medial septum and hippocampus are involved in generating theta rhythm, an oscillating pattern of brain activity that contributes to spatial and episodic memory formation (Buzsáki 2002; Hasselmo 2005; Munn et al. 2015) Stimulation of the MR has been shown to desynchronize theta (Vertes 1981; Vinogradova et al. 1999; Jackson et al. 2008; Wang et al. 2015). Though this effect has previously been attributed to 5-HT release (Assaf and Miller 1978; Kinney et al. 1996), recent work has suggested there also exists a non-serotonergic mechanism (Jackson et al. 2008). If r2-*Pet1*$^{Vglut3\text{-high}}$ neurons desynchronize theta, their activity may perturb memory formation (Vertes 2005). Indeed, in line with this hypothesis, recent experiments acutely inhibiting r2-*Pet1* neurons *en masse* during conditioned learning led to a later failure in the normal extinction of that conditioned place preference (Baskin et al. 2020). Finally, chronic silencing of r2-*Pet1* neurons has been shown to enhance prepulse inhibition (PPI), a measure of sensorimotor gating (Okaty et al. 2015). Given the extensive VGLUT3^{+} r2-*Pet1* innervation of regions that modulate PPI such as the prelimbic cortex and hippocampus (Bakshi and Geyer 1998; Rohleder et al. 2016) and sensitivity of VGLUT3^{+} MR neurons to sensory stimulation (Domonkos et al. 2016), we suggest this effect may have been driven by loss of neurotransmission from the r2-*Pet1*$^{Vglut3\text{-high}}$ neuron subtype. Thus, we predict r2-*Pet1*$^{Vglut3\text{-high}}$ neurons may regulate sensorimotor gating and modulate theta to affect memory.

*Pericellular baskets characterize some r2-*Pet1$^{\text{Vglut3-}high}$ *axonal collaterals*

We observed VGLUT3$^+$ r2-*Pet1* boutons in pericellular baskets in hippocampus, cortex, and septum, with baskets of the latter region also containing 5-HT$^+$/VGLUT3$^+$ co-positive r2-*Pet1* boutons. We propose that these co-positive boutons derive from r2-*Pet1*$^{Vglut3\text{-high}}$ collaterals because our analyses of *Piezo2-Pet1* fibers from the r2-*Pet1*$^{Tph2\text{-high}}$ subgroup failed to reveal baskets. This would further suggest that a fraction of r2-*Pet1*$^{Vglut3\text{-high}}$ cells express sufficient, even though low, levels of TPH2 or the 5-HT re-uptake transporter SLC6A4 to generate 5-HT$^+$ boutons. Pericellular baskets formed by 5-HT$^+$ fibers (Köhler et al. 1982; Freund et al. 1990; Hornung et al. 1990; Dinopoulos et al. 1993; Leger et al. 2001) and VGLUT3$^+$ fibers (Hioki et al. 2004; Riedel et al. 2008; Amilhon et al. 2010) have been reported previously; we suggest that fibers from r2-*Pet1*$^{Vglut3\text{-high}}$ cells may be reflected, in part, in the latter.

Also revealed here are composite baskets, where axons from multiple *Pet1* neuron subtypes converge on a single targeted cell in cortex, hippocampus and septum. In lateral septum composite baskets, r2-*Pet1* varicosities were less likely to be 5-HT$^+$ while both r2-*Pet1* and other *Pet1* varicosities were similarly likely to be VGLUT3$^+$, suggesting these subtypes of *Pet1* neurons may release different neurotransmitter onto the basket-targeted cell. The commonality of VGLUT3 in baskets suggests it may play a role in basket function, possibly by synergizing co-transmission of 5-HT and glutamate (Amilhon et al. 2010). Given previous retrograde tracing studies identified inputs from both the DR and MR to the LS (Köhler et al. 1982; Deng et al. 2019), we suggest that the other source of non-r2 *Pet1* 5-HT$^+$ input to pericellular baskets is from *En1-Pet1* neurons arising embryonically from r1 and/or r0 (Jensen et al. 2008). These results suggest that pericellular baskets are complex, potentially releasing either

5-HT or glutamate or both depending on which set of *Pet1* neurons and associated axonal terminals are excited.

In the cortex, we observed r2-*Pet1* VGLUT3^{+} pericellular baskets around subtypes of GABAergic interneurons. A particularly intriguing target was a set of inhibitory neurons that themselves were also VGLUT3^{+} and which likely correspond to a subset of cholecystokinin (CCK)-expressing interneurons referred to as "basket cells" (Somogyi et al. 2004; Fasano et al. 2017; Harris et al. 2018). Previous work proposed that the source of these presynaptic basket structures encasing these VGLUT3^{+} basket interneurons was intracortical rather than long-range from the raphe, because the baskets persisted after pharmacological ablation of serotonin neurons with 5,7-DHT (Hioki et al. 2004). It is possible that r2-*Pet1*$^{Vglut3\text{-high}}$ neurons are poorly killed by 5,7-DHT, due to their reduced expression of SLC6A4, MAOA, and/or MAOB (Okaty et al. 2015), which may be important for the uptake and toxicity of 5,7-DHT (Finnegan et al. 1989; Paterak and Stefański 2014). Additionally, there are likely multiple sources for these VGLUT3^{+} presynaptic baskets, such that loss of those composed of fibers from the MR goes undetected. Our work then clarifies the existence of a long-range pericellular basket-forming projection from *Pet1* MR cells to a specific subgroup of cortical interneurons.

An analogous projection from r2-*Pet1* neurons to VGLUT3^{+} putative basket cell interneurons in the hippocampus was also observed. As in the cortex, many of the postsynaptic cells were immunopositive for 5-HT3A, the ionotropic 5-HT receptor. It has been suggested that an MR glutamatergic input to 5-HT3A-expressing hippocampal interneurons "pre-potentiates" them to be responsive to subsequent presentation of 5-HT (Jackson et al. 2009). We suggest the r2-*Pet1*$^{Vglut3\text{-high}}$ subtype is well-positioned for this role, as it targets 5-HT3A-expressing

interneurons and, by forming pericellular baskets around these cells, could deliver strong, temporally precise excitation immediately prior to 5-HT release. This circuit could allow r2-*Pet1*$^{Vglut3\text{-high}}$ neurons to control the activity of basket cell interneurons that then each have highly collateralized axons extending to many principal cells, giving the r2-*Pet1* neuron a privileged position for tuning overall cortical and hippocampal network activity.

Conclusion

We describe neurochemically divergent groups of r2-*Pet1* neurons, one largely serotonergic and one largely glutamatergic, each arising from the same embryonic progenitor zone, rhombomere 2. We propose that the anatomical segregation of their collective ascending boutons by neurochemical phenotype reflects two separate, largely non-overlapping neuronal subsystems that may each mediate distinct functions of the median raphe. The work described here uncovers a new level of structural organization within the median raphe.

CHAPTER III.

NEURONAL PERICELLULAR BASKETS: NEUROTRANSMITTER CONVERGENCE AND REGULATION OF NETWORK EXCITABILITY

I wrote this chapter with input from my advisor, Dr. Susan M. Dymecki. Figure 1 was made by Mallory Rice with input from me. I would also like to thank Drs. Benjamin Okaty and Yasmin Escobedo Lozoya for discussions and feedback on the manuscript.

ABSTRACT

A pericellular basket is a presynaptic configuration of numerous axonal boutons decorating, indeed outlining, a target neuron soma and its proximal dendrites. Recent studies show neurochemical diversity of pericellular baskets and suggest that neurotransmitter usage together with the dense, soma-proximal boutons may permit strong input effects on different time scales. Here we review the development, distribution, neurochemical phenotypes, and possible functions of pericellular baskets, focusing on those formed by projections of certain *Pet1/Fev* neurons of the serotonergic raphe nuclei. We propose that pericellular baskets represent convergence sites of competition or facilitation between neurotransmitter systems on downstream circuitry, especially in limbic brain regions, where pericellular baskets are widespread. Study of these baskets may enhance our understanding of monoamine regulation of emotional behavior and memory.

PRESYNAPTIC PERICELLULAR BASKETS – WHAT AND WHERE ARE THEY?

The strength and temporal dynamics of neuronal input are determined in part by the spatial arrangement – location and density – of presynaptic axonal boutons on the postsynaptic cell. One particularly striking bouton arrangement comprises what is called a pericellular basket, a presynaptic organization of boutons from one or multiple axons that surround the postsynaptic cell body and proximal dendrites. This innervation is dense that the shape of the

postsynaptic soma is revealed, like climbing vines around the trunk and limbs of a tree (Köhler et al. 1982; Riedel et al. 2008). Historically, this configuration has also been referred to as a pericellular nest or pericellular array (Marin-Padilla 1974; Gall and Moore 1984; Hornung et al. 1990). Pericellular baskets are thought to confer privileged control over the targeted cell via the high number of boutons and their location proximal to the soma and axon hillock, potentially overriding the effects of more distal inputs (Strüber et al. 2015).

Pericellular baskets were originally described by Ramon y Cajal in the cerebellum, hippocampus, and cortex by axons later determined to be GABAergic (Curtis et al. 1970). Since this seminal work, it has been uncovered that diverse neuron types configure pericellular baskets at their axon termini, including certain monoaminergic neuron subtypes (Aznar et al. 2004; Riedel et al. 2008), some neuropeptide-releasing neurons (Gall and Moore 1984; Olucha-Bordonau et al. 2012), some glutamatergic projection neurons (Szőnyi et al. 2019a), and cells themselves called basket cells found in the cerebellum (Zhou et al. 2020), cerebral cortex, and hippocampus (Acsády et al. 2000; Pelkey et al. 2017). These basket-extending neurons have cell soma residing in regions such as the median raphe (MR) nucleus (Köhler et al. 1982; Aznar et al. 2004; Szőnyi et al. 2019a; Senft et al. 2021), cerebral cortex (Armstrong and Soltesz 2012), hypothalamus (Szeidemann et al. 1995), hippocampus (Pelkey et al. 2017), and cerebellum (Zhou et al. 2020). While basket cell interneurons project locally to excitatory principal cells (Armstrong and Soltesz 2012), other basket-extending monoaminergic neurons send long-range projections to target primarily GABAergic cells (Hornung and Celio 1992; Szőnyi et al. 2019a; Senft et al. 2021). The presence of pericellular baskets is phylogenetically widespread, being found in reptiles, songbirds, rodents, non-human primates, and humans (Marin-Padilla 1969, 1974; Font

et al. 1997; Goodson et al. 2004; Raghanti et al. 2008; Riedel et al. 2008). Even with their prevalence across organisms and brain regions and their likely gate-keeper role in controlling target neuron activity, little is known about the development, electrophysiology, and specific functions of pericellular baskets.

In this chapter, we review pericellular baskets, focusing on those formed by projection neurons of the serotonergic brainstem raphe nuclei. We discuss pericellular baskets as sites of convergence of neurotransmitter systems, suggesting that their privileged control over postsynaptic neuron excitability is complex and may span different time scales if the different neurotransmitters released signal ionotropically (e.g., "fast" glutamatergic signaling) versus metabotropically (e.g., "slow" serotonergic signaling). We consider functional roles for pericellular baskets, for example, in the regulation of target neuron activity in the hippocampus and septum shaping brain theta rhythm and memory formation. We close with a set of questions, intending to stimulate advances in this exciting area.

NEUROCHEMICAL AND STRUCTURAL DIVERSITY OF PERICELLULAR BASKETS

A diverse set of neurotransmitters have been detected singly or co-expressed in boutons comprising pericellular baskets. These include serotonin (5-hydroxytryptamine, 5-HT), dopamine, noradrenaline, acetylcholine, glutamate, gamma-amino-butyric acid (GABA), enkephalin (Met- and Leu-), substance P, somatostatin, neuropeptide Y (NPY), and cocaine- and amphetamine-regulated transcript (CART) peptide (Gall and Moore 1984; Wähle et al. 1986; Pickavance et al. 1992; Paspalas and Papadopoulos 1999; Riedel et al. 2008; Janzsó et al. 2010; Senft et al. 2021). Precedent for co-transmission deploying glutamate has been reported in monoaminergic,

cholinergic, and GABAergic neurons (Trudeau and El Mestikawy 2018), perhaps applying to pericellular basket terminals as well.

Architectural features of pericellular baskets

Pericellular baskets, even of different neurotransmitter phenotypes, share certain cytoarchitectural features. Boutons are characteristically large and typically 20-30 decorate the target soma (Acsády et al. 2000; Senft et al. 2021). The contained synapses are typically symmetric, as revealed in electron micrographs of septal and hippocampal pericellular baskets (Beauvillain et al. 1991; Dinopoulos et al. 1993; Hioki et al. 2004; Fasano et al. 2017). In these cases, the immunodetected neurotransmitters have included GABA, 5-HT, and/or Met-Enkephalin. Collectively, these features predict inhibitory postsynaptic effects, albeit still to be discerned electrophysiologically in most cases. Smaller boutons in baskets have been found to deploy CART peptide and to harbor asymmetric synapses (Janzsó et al. 2010), suggesting postsynaptic excitation. Excitatory control also seems possible by some pericellular baskets using glutamate and/or 5-HT to trigger excitatory postsynaptic receptors such as ionotropic and metabotropic glutamate receptors (Trudeau and El Mestikawy 2018; Crupi et al. 2019) or the excitatory ionotropic 5-HT receptor 3A (5-HT3aR) (Koyama et al. 2017) and the metabotropic 5-HT receptors 2A (Li et al. 2015; Zhang and Stackman 2015) and 2C (Palacios et al. 2017), as examples. Additionally, 5-HT neurons in culture have been found to release glutamate at asymmetric synapses (Johnson 1994), suggesting in cases of co-transmission of glutamate and serotonin, asymmetric synapses may be more common than symmetric.

Pericellular baskets as sites of neurotransmitter convergence

The degree to which neurochemically distinct pericellular baskets target the same soma is largely unknown. In the septum, different neurotransmitter systems form pericellular baskets in broadly similar distributions (Köhler et al. 1982; Gall and Moore 1984; Riedel et al. 2008), raising the possibility that different basket systems interact by projecting to the same downstream target neurons or by axo-axonic synapses onto other baskets. A convergence-organization model suggests that different neurotransmitter systems may compete against or facilitate modulation of the targeted cell, either by affecting postsynaptic cellular processes or by inhibiting or exciting other basket terminals. Indeed, multiple neurochemically distinct (serotonergic vs. non-serotonergic) fibers have been observed as making baskets on the same septal cells (Aznar et al. 2004; Senft et al. 2021), supporting the idea of basket convergence (Figure 3.1). An alternative possibility is that separate basket systems "tile" innervated regions, targeting largely distinct postsynaptic cells. A distributed, non-overlapping pattern of basket systems would suggest high target specificity for postsynaptic cell types, and possibly even repulsive or non-permissive environments underlying the development of basket stratification. In the septum, glutamatergic (expressing vesicular glutamate transporter 3 [VGLUT3]) pericellular baskets rarely overlap topographically with baskets immunopositive for parvalbumin (PV), tryptophan hydroxylase 2 (TPH2, the rate-limiting enzyme for 5-HT synthesis), calretinin, or choline acetyltransferase (Riedel et al. 2008). However, they do occasionally target the same somata as do separate, tyrosine hydroxylase^{+} (presumably dopaminergic) baskets (Riedel et al. 2008; Figure 3.1A). The extent of pericellular basket convergence may vary between different basket systems or as a function of region.

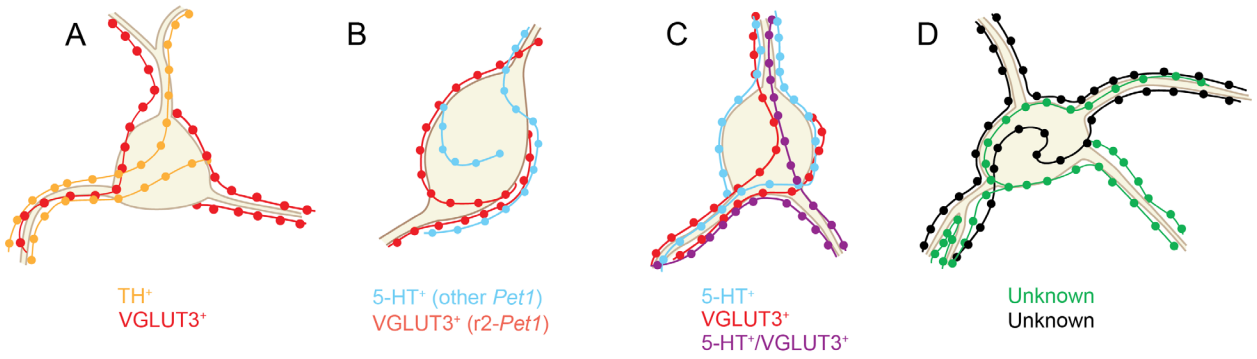

Figure 3.1. Neurochemically distinct pericellular baskets sometimes target the same cell soma.

Reported convergence of TH^+ and $VGLUT3^+$ pericellular baskets (A) in the lateral septum (Riedel et al. 2008). Observed 5-HT^+ and $VGLUT3^+$ baskets from separate *Pet1* neuron lineages (B) converging on the same targets in the cortex, hippocampus, and septum (Senft et al. 2021), baskets comprised of 5-HT^+, $VGLUT3^+$, and $VGLUT3^+$/5-HT^+ fibers (C) in the septum. Additional potential convergence of other axons known to form pericellular baskets (labeled 'unknown', D) are an exciting next step for characterizing pericellular basket inputs.

PET1 NEURONAL SUBSYSTEMS FORM SEROTONERGIC AND GLUTAMATERGIC BASKETS

Brainstem raphe neurons defined molecularly by developmental and adult expression of the *Pet1* (aka *Fev*) gene are referred to as *Pet1* neurons (Jensen et al. 2008; Okaty et al. 2015, 2019, 2020) and include a neuron subset that collectively forms pericellular baskets in the septum, hippocampus, and cerebral cortex (Senft et al. 2021). *Pet1* encodes for a transcription factor master regulator of differentiation of the serotonergic fate (Liu et al. 2010; Wyler et al. 2016; Deneris and Gaspar 2018). Recent findings, however, show that a substantial subset of basket-forming *Pet1* neurons express low or undetectable levels of serotonergic pathway genes such as *Tph2* and *Slc6a4,* the latter encoding the serotonin re-uptake transporter. Rather, these *Pet1* neurons express high levels of VGLUT3, enabling glutamate release (Amilhon et al. 2010; Trudeau and El Mestikawy 2018). This pattern contrasts some other *Pet1* neurons, which co-

express serotonergic and glutamatergic identity genes, permitting glutamate and serotonin co-transmission (Okaty et al. 2015). The soma of these putative glutamatergic *Pet1* neurons reside in the MR (Jensen et al. 2008; Okaty et al. 2015) and derive developmentally from the hindbrain compartment referred to as rhombomere 2 (r2). They can be accessed genetically by exploiting the overlap (intersection) of expression of two driver transgenics – the r2-specific *r2Hoxa2-cre* (Awatramani et al. 2003) and the *Pet1*-specific *Pet1-Flpe* (Jensen et al. 2008). The shorthand descriptor for these neurons is 'r2-*Pet1*' (Bang et al. 2012). Pericellular baskets are characteristic of a subgroup within the r2-*Pet1* neuron population – the VGLUT3-positive, TPH2-low-or-negative subset of r2-*Pet1* neurons referred to as r2-*Pet1*$^{Vglut3\text{-high}}$. The more classical, serotonergic subgroup of r2-*Pet1* neurons, referred to as r2-*Pet1*$^{Tph2\text{-high}}$, expresses high levels of TPH2, 5-HT, and SLC6A4 and are low-or-negative for VGLUT3. This group does not form pericellular baskets, and projects to brain regions different from the basket-forming r2-*Pet1*$^{Vglut3\text{-high}}$ cells (Senft et al. 2021).

The majority of baskets from r2-*Pet1*$^{Vglut3\text{-high}}$ cells are immunoreactive for VGLUT3 but not 5-HT, perhaps unsurprisingly given their soma transcriptome just mentioned (Okaty et al. 2015). Interestingly, some of the r2-*Pet1*$^{Vglut3\text{-high}}$-targeted postsynaptic cells are ensheathed by additional baskets that are serotonergic and derive from non-r2 *Pet1* neurons (Figure 3.1B). These baskets are likely formed by other MR serotonergic neuron subgroups referred to as *r1En1-Pet1* or *r3Egr2-Pet1* neurons (Bang et al. 2012). Thus, in some cases, axons from developmentally distinct subsets of *Pet1* neurons (derived from different hindbrain rhombomeres) converge and ensheath the same target cell with one deploying glutamate and the other 5-HT. Such 'composite' pericellular baskets are prevalent in the septum (Senft et al.

2021; Figure 3.1C) and likely explain at least a portion of the baskets formed by serotonergic and non-serotonergic fibers reported decades ago (Aznar et al. 2004).

We propose different models for composite baskets based on existing data on serotonin and glutamate postsynaptic effects. A cooperative model describes fast glutamatergic input as pre-potentiating the target cell, setting up enhanced responsiveness to subsequent excitatory serotonergic receptor signaling (Jackson et al. 2009). Also possible is that neuromodulatory input from 5-HT^{+} pericellular basket terminals may prime synapses to be more or less inducible to plasticity, as has been reported with cholinergic, dopaminergic, and adrenergic fibers (Ruan et al. 2014; Brzosko et al. 2019). An alternative oppositional model involves postsynaptic inhibitory 5-HT receptors, such that serotonergic signaling would oppose that of excitatory glutamate (Hannon and Hoyer 2008). Relevant to both cooperative and oppositional models, serotonergic and glutamatergic signaling typically operate at different timescales. Glutamate typically elicits fast synaptic responses through ionotropic receptors while serotonin typically operates with slower dynamics usually through metabotropic receptors (Jackson et al. 2009; Vaaga et al. 2014). Resolving the functional impact of these basket complexities is an exciting next step.

In addition to composite pericellular baskets formed by multiple *Pet1* neuron subtypes, some individual *r2-Pet1* neuron baskets co-localize VGLUT3 and 5-HT to the same boutons, raising the possibility for co-transmission (Varga et al. 2009; Amilhon et al. 2010; Trudeau and El Mestikawy 2018; Belmer et al. 2019). This is especially prevalent for r2-*Pet1* basket boutons in the septum, as compared to non-basket *Pet1* boutons (Senft et al. 2021). Thus, septal pericellular baskets from *Pet1* neurons may be centers for co-transmission that offer concurrent yet kinetically different control of the postsynaptic neuron and its embedded network via glutamate

versus 5-HT signaling. It is possible that glutamate versus 5-HT may require different thresholds of excitation for release. Indeed, while not baskets, certain serotonergic fibers in the amygdala showed differential neurotransmitter release depending on stimulation frequency. Though low frequency stimulation was sufficient to evoke glutamate release, higher frequencies were needed to elicit 5-HT release (Sengupta et al. 2017). This suggests that 5-HT deployment is reserved for specific environmental or physiological circumstances. It also suggests that 5-HT and glutamate are packaged into separate synaptic vesicles. Pericellular baskets have yet to be probed for such graded transmission. Nor have they been investigated for the alternative possibility of co-release of 5-HT and glutamate from the same synaptic vesicle. Both options suggest the possibility for sophisticated and complex modes of target cell modulation and septal network control by r2-*Pet1* neuron baskets.

DEVELOPMENTAL ELABORATION OF BASKET STRUCTURE PARALLELS TARGET NEURON MATURATION

In rodents, septal pericellular baskets typically form in the early postnatal period. For example, it is during the first postnatal week of life that dopaminergic (TH^+) baskets and met-enkephalin$^+$ baskets are first detectable developmentally, increasing in abundance and complexity by week two (Verney et al. 1987). In addition to this temporal axis of septal basket development, there is also a significant spatial axis, with baskets elaborating first in the medial septum, and later in the lateral septum. Notably, this pattern matches that of septal neuron maturation including dendritic arborization (Iyer and Tole 2020). Similar temporal dynamics describe the formation of pericellular baskets in other brain regions, such as baskets that form

around Purkinje cells in the cerebellum (Ichikawa et al. 2011), and pericellular baskets formed by interneurons in the cortex and hippocampus (Chattopadhyaya et al. 2004; Doischer et al. 2008; Pelkey et al. 2020). It may be a common feature for pericellular baskets to form as the cytoarchitectonics of a region and its resident cells mature. The development of *Pet1* neuron pericellular baskets remains to be mapped, though in rat, 5-HT$^+$ fibers form baskets in the septum starting after postnatal day (P) 7 and increase in number and complexity throughout the early postnatal period (Dinopoulos et al. 1993). Serotonin axon arborization and morphology reach an adult-like pattern shortly after weaning, ~P28 (Lidov and Molliver 1982; Maddaloni et al. 2017). Also unknown is whether early life experiences, such as stress or sensory experiences, affect the formation of pericellular baskets. Indeed, a different pericellular structure comprised of secreted glycoproteins, called the perineuronal net (described in Box 3.1), is affected in its development by postnatal stressors (Fawcett et al. 2019).

The elaboration of septal pericellular baskets during the early postnatal period parallels the development of certain septum-dependent social behaviors. One example is kinship recognition. At ~two weeks postnatally, rat pups switch preference from siblings to non-siblings, which is blocked by lesioning the lateral septum (Clemens et al. 2020). Moreover, lateral septal neurons responsive to sibling versus non-sibling cues differentially localize across the intermediate lateral septum, a subregion rich in pericellular baskets, including *Pet1* neuron baskets (Aznar et al. 2004; Riedel et al. 2008; Senft et al. 2021), that elaborate their basket structure along a similar time course to behavioral preference switching. It is possible then that *Pet1* neuron baskets influence this social preference shift. Consistent with this notion, albeit in

the adult rodent, optogenetic stimulation of the MR reduced aggression to a novel (non-sibling) intruder mouse (Balázsfi et al. 2018).

Box 3.1. Pericellular baskets and perineuronal nets: the first, a presynaptic elaboration; the second, an extracellular matrix network; both regulate target cell function.

Pericellular baskets and perineuronal nets (PNNs) are sometimes mistaken for each other conceptually, and while they do share features related to ensheathing neuron soma, they are quite different structures. Pericellular baskets are a presynaptic neuronal specialization comprised of axonal boutons decorating the soma and proximal dendrites of the postsynaptic target cell. They are formed by multiple neuron types, including basket cell interneurons and monoaminergic neurons, among others (Gall and Moore 1984; Armstrong and Soltesz 2012). By contrast, PNNS are extracellular structures composed of secreted chondroitin sulfate proteoglycans that ensheath neuronal soma (Fawcett et al. 2019). The extracellular matrix components that form PNNs are expressed by both neurons and glia (Fawcett et al. 2019). Pericellular baskets have been observed targeting excitatory and inhibitory neurons (Marin-Padilla 1969; Hornung and Celio 1992; Aznar et al. 2004; Armstrong and Soltesz 2012; Senft et al. 2021). Similarly, PNNs most commonly target GABAergic interneurons, typically fast-spiking parvalbumin neurons, but have also been observed to surround excitatory neurons (Sorg et al. 2016; Morikawa et al. 2017).

In mice, pericellular baskets and PNNs form during early postnatal life when neurons in many brain regions are maturing and finalizing synaptic connectivity, suggesting roles in circuit maturation. PNN formation is dependent on experience and sensory input during critical periods, as PNNs fail to form in visual cortex without exposure to light (Kind et al. 2013). Whether early life experience shapes the formation of pericellular baskets remains an open question. Also unclear is whether or how often pericellular baskets and perineuronal nets overlap in cellular target. The gaps in perineuronal 'netting' are typically occupied by synaptic boutons (Fawcett et al. 2019), suggesting the PNN acts as a scaffold for highly specific synapse formation that also limits further plasticity (Sorg et al. 2016). Loss of PNNs around parvalbumin interneurons also reduced the perisomatic innervation targeting them, suggesting the PNN scaffolding may be necessary to stabilize perisomatic innervation (Carceller et al. 2020). The same study proposed that a threshold of perisomatic innervation may be necessary for PNNs to form and stabilize this connectivity. These results suggest a potential interplay between pericellular baskets and PNNs, though there are relatively few reports examining whether PNNs and pericellular baskets target the same neurons. In the lateral septum for example, PNNs and glutamatergic ($VGLUT3^{+}$) pericellular baskets are reported to rarely overlap (Riedel et al. 2008). Perhaps a limited view though, as only one type of PNN has been well characterized – that which binds the lectin *Wisteria floribunda* agglutinin (WFA). There exist other PNNs labeled by antibodies to aggrecan (Matthews et al. 2002; Fawcett et al. 2019). Additionally, a subset of serotonergic neurons forms pericellular baskets around

(Box 3.1 continued)

parvalbumin interneurons (Aznar et al. 2004), which as a population are common targets of PNNs (Fawcett et al. 2019). Also suggesting potential interaction between the serotonergic system and PNNs, Selective serotonin reuptake inhibitors (SSRIs) administered during the early postnatal period affect PNN formation, reducing their number in the hippocampus (Mukhopadhyay et al. 2021). Determining whether different pericellular basket systems target the same somata as PNNs and whether the formation of each structure affects the other is a compelling direction for future research.

Pet1 axon-derived pericellular baskets in the septohippocampal circuit may modulate memory

Based on functional anatomy, *Pet1*-derived pericellular baskets are predicted to influence memory and reinforcement of learned behaviors through modulating theta rhythm generation in the septohippocampal circuit. Theta rhythm describes sinusoidal (4-12 Hz) electroencephalographic oscillations related to activity in the hippocampus, neocortex, and amygdala during attentive wake and REM sleep (Hasselmo 2005; Buzsáki and Moser 2013). Hippocampal theta oscillations are important in memory encoding (Hasselmo 2005; Buzsáki and Moser 2013; Hutchison and Rathore 2015; Whissell et al. 2019) and abnormalities in theta rhythm are associated with attention and cognitive disorders such as schizophrenia (Adams et al. 2020) and attention deficit/hyperactivity disorder (Guo et al. 2020). Hippocampal theta rhythms are generated within a broader limbic septohippocampal system in which projections from the medial septum drive theta in the hippocampus. The hippocampus in turn sends reciprocal regulatory connections back to the septum including both medial and lateral subdivisions (Khakpai et al. 2013). This circuit is modulated by the MR, generally in a desynchronizing fashion (Jackson et al. 2008; Hsiao et al. 2013; Bland et al. 2016) driven by serotonergic (*Pet1*) neurons

residing therein (Olvera-Cortés et al. 2013; Gutiérrez-Guzmán et al. 2017). Serotonergic neurons show diversity in their activity during theta (Kocsis et al. 2006), suggesting some subpopulations are better positioned to interact with theta-generating circuits. Subsets of *Pet1* neurons form pericellular baskets in the hippocampus, medial septum, and lateral septum (Senft et al. 2021), positioning them to modulate hippocampal theta and memory at several key nodes.

Most directly, *Pet1* neuron pericellular baskets may modulate theta via hippocampal GABAergic neurons, which they preferentially innervate relative to excitatory principal cells (Hornung and Celio 1992). Theta oscillations can be generated by interactions between pyramidal neurons and specific classes of interneurons, referred to as basket cells. Basket cells send highly collateralized axons to form pericellular baskets on many pyramidal neurons, coordinating their activity (Armstrong and Soltesz 2012; Bartos and Elgueta 2012). Basket cell interneurons are divided into two classes: the fast-spiking parvalbumin-expressing (PV) basket cells (Klausberger et al. 2005; Amilhon et al. 2015) and the regular-spiking cholecystokinin-expressing (CCK) basket cells (Fasano et al. 2017). The latter express 5-HT3aR and are heavily innervated by 5-HT$^+$ and VGLUT3$^+$ MR fiber pericellular baskets, suggesting excitatory, fast responsiveness to 5-HT and glutamate (Férézou et al. 2002; Lee et al. 2010; Armstrong and Soltesz 2012; Fasano et al. 2017; Senft et al. 2021). 5-HT3aR antagonists promote theta (Staubli and Xu 1995), suggesting 5-HT signaling to CCK basket cells may desynchronize theta. It is possible that glutamate vs. 5-HT release from *Pet1* neuron pericellular baskets has differential effects on CCK basket cell firing and thus theta synchrony. Glutamate acting on CCK basket cells may promote inhibitory tone, theta, and thus memory formation (Buzsáki and Moser 2013; Whissell et al. 2019), while 5-HT inputs may desynchronize CCK basket cells, suppress theta

(Olvera-Cortés et al. 2013), and promote extinction of memories through 5-HT3 receptors (Buhot et al. 2000). CCK basket cells have a slow membrane time constant and high input resistance (Lee and Soltesz 2011; Bartos and Elgueta 2012). Thus it is possible they are especially desynchronized by coincident glutamatergic and serotonergic basket input, which may force adaptation (see Box 3.2).

In addition to targeting a subset of hippocampal interneurons expressing markers of CCK basket cells, r2-*Pet1* pericellular baskets also target hippocampal neurons that express calbindin (Senft et al. 2021), a population that sends inhibitory projections to the medial septum (Tóth and Freund 1992), a major generator of theta (Tsanov 2018). *Pet1* neuron pericellular baskets are also prevalent within the medial and lateral septum, where they innervate GABAergic neurons (possibly interneurons), some of which express the excitatory 5-HT2C receptor (Aznar et al. 2004; Senft et al. 2021). If *Pet1* pericellular basket input (glutamate, serotonin, or both) excites these cell types as predicted by the cognate receptor function, their subsequent release of GABA would increase inhibitory tone in the septum. We predict this suppression of activity would reduce theta (Sörman et al. 2011) and disrupt memory formation (Calandreau et al. 2007).

Based on the predicted effects of basket neurotransmission and identity of cellular targets, we propose *Pet1* neuron basket activation generally reduces memory durability and increases circuit plasticity. Consistent with this idea, chemogenetic inhibition of r2-*Pet1* neurons during the encoding of a cocaine conditioned place preference increased resistance to extinction of that behavioral preference in the cocaine-free state (Baskin et al. 2020). This suggests that diminished r2-*Pet1* neuron activity strengthens the durability of cocaine memory. Conversely, this predicts that r2-*Pet1* neuron activity normally functions to limit this durability,

allowing for plasticity or flexibility in learning and memory (Baskin et al. 2020). 5-HT3aRs, expressed by hippocampal neurons targeted by r2-*Pet1* pericellular baskets, seem particularly important in erasing stored memories. 5-HT3aR knockout mice are less able to extinguish fear memories (Kondo et al. 2013) and are express high levels of anxiety-related behaviors (Kelley et al. 2003). In line with these findings, 5-HT3aR antagonists have anti-amnesic effects in Alzheimer's disease patients (Meneses 2015). Exciting next steps will involve 5HT3aR manipulations specific to septohippocampal circuitry.

What value results from decreasing memory durability? Malleable memories are essential to behavioral flexibility. A foraging animal, for example, must update its internal map to reflect when a food source is depleted or it risks returning again and again to diminishing returns and enhanced predation risk. Unfruitful perseveration can be life threatening. This appears reflected in certain human neuropsychiatric conditions, including post-traumatic stress disorder (PTSD) where prolongation and intrusion of stressful memories is highly debilitating. Greater risk for PTSD is thought related to serotonin system abnormalities, and is commonly treated with serotonin-modulating drugs (Zhao et al. 2017; Liu et al. 2018). Thus, studies of *Pet1* pericellular baskets may offer circuit nodes and molecular pathways for conceptualizing new therapeutic strategies for PTSD and other psychiatric disorders.

Box 3.2. *Pet1* neuron pericellular baskets poised to modulate memory

> Hippocampal CCK basket cells deliver strong perisomatic inhibition to pyramidal cells. This inhibition is thought to gate circuit transmission such that only the strongest signals persist, creating sparse, precise encoding of memories with minimal overlap in circuit representation (Acsády et al. 2000; Klausberger et al. 2005; Klausberger and Somogyi 2008). The most highly recruited pyramidal cells are able to thwart CCK basket cell inhibition by depolarization-induced suppression of inhibition (DSI). In DSI, activity-dependent retrograde release of cannabinoids activates presynaptic CB1 receptors on

(Box 3.2 continued)

the CCK basket cell terminals, preventing additional release of GABA (Bartos and Elgueta 2012). r2-*Pet1* pericellular baskets might act to excite via glutamate these CCK basket cells and thereby promote a sparser neural code. When the pericellular basket is active presynaptically, the postsynaptic CCK basket cell is also likely excited. Subsequent stronger downstream inhibition of pyramidal cells would raise the threshold of circuit recruitment for a pyramidal cell to remain active. Alternatively, coincident glutamate and 5-HT release may greatly depolarize the CCK basket cell, causing adaptation that reduces CCK basket cell firing and acts to 'reset' this gain control and increase circuit plasticity.

CONCLUDING REMARKS

Pericellular baskets are complex structures configured to allow one or several axons privileged and even multi-modal control over the downstream postsynaptic target cell. Formed by many neuron types in different brain regions, their functions and physiology remain under-described. In this opinion article, we argue that pericellular baskets may be an intriguing neurochemically complex interaction point between many different systems. Clarifying the extent of convergence of pericellular baskets across different neurotransmitter systems as well as answering central questions about their development and neurotransmission (See 'Box 3.3. Outstanding Questions') is essential to understanding their circuit function. Localization of many baskets to the limbic system suggests functional roles in emotional processing and/or memory. Consideration of pericellular basket disruptions in neurological disorders could potentially pave the way for new therapeutic approaches.

Box 3.3. Outstanding Questions

How frequently do different pericellular baskets target the same neuron, forming a 'composite basket'? Does the prevalence of composite baskets vary with target region?

(Box 3.3 continued)

Do individual monoamine neurons, which often have highly collateralized axons, make baskets in multiple regions? For neurons forming multiple pericellular baskets, are the baskets of identical or heterogeneous neurochemical phenotypes?

For monoamine neurons, which commonly co-transmit multiple neurotransmitters, are baskets sites of co-transmission and if so, is co-transmission fixed or variable as a function of presynaptic excitation?

For composite baskets, how does the activation of one basket affect the target cell response to subsequent input from the other basket(s)? Do baskets formed by different neurons ever signal to each other via axo-axonic appositions?

How does modulating neurotransmitter release from *Pet1* pericellular baskets in target regions such as the septum and hippocampus affect memory formation? Given their often-different neurochemical profiles, do different developmental lineages of basket-forming *Pet1* neurons have differential effects on memory durability? Are effects of modulating hippocampal r2-*Pet1* baskets (putatively glutamatergic) distinct from modulating septal r2-*Pet1* baskets (mixed glutamatergic/serotonergic phenotype)?

Pet1 neuron pericellular baskets are formed in the early postnatal period and are commonplace in brain regions that exhibit neuroplasticity in response to early life stress, such as the hippocampus and septum. Is the formation of pericellular baskets also plastic in response to early life stress, and does this plasticity have functional consequences on later expression of stress coping behavior or memory?

Does disrupting postsynaptic cell maturation also disrupt basket formation? Conversely, does disrupting basket formation disrupt neuronal maturation?

How do pericellular baskets form around targeted cells? Are cell-cell adhesion proteins involved in guiding axons to specific downstream targets?

CHAPTER IV.

SPATIAL PATTERNING AND CELLULAR ORIGIN OF LATERAL SEPTUM R2-*PET1* PERICELLULAR BASKETS

*I wrote this chapter with input from my advisor, Dr. Susan M. Dymecki. I performed the immunohistochemical experiments, imaging, and analysis. Biocytin fills of cells targeted by r2-*Pet1 *pericellular baskets in the septum were performed by Dr. Yasmin Escobedo-Lozoya. She also wrote the section of the methods pertaining to electrophysiology and gave input on the chapter.*

INTRODUCTION

Pericellular baskets, presynaptic axonal arborizations decorating the soma and proximal dendrites of the postsynaptic neuron, are thought to convey privileged control over the excitability of the cell encased in the basket (Miles et al. 1996; Acsády et al. 2000; Veres et al. 2017). These baskets are abundant in the septum and are neurochemically diverse, being formed by serotonergic, glutamatergic, and catacholaminergic fibers, among others (Köhler et al. 1982; Dinopoulos et al. 1993; Riedel et al. 2008). However, despite their abundance and potential to exert strong control over septal circuit nodes, septal pericellular baskets, the cells they target, and the cells that form them remain undercharacterized.

One population of neurons forming numerous pericellular baskets in the septum are those expressing *Pet1*, a serotonergic regulator gene (Hendricks et al. 2003; Liu et al. 2010). *Pet1* neurons form serotonin$^+$ (5-hydroxytryptamine, 5-HT) pericellular baskets and can also form baskets that are co-positive for 5-HT and the vesicular glutamate transporter 3 (VGLUT3), indicative of glutamate co-transmission in monoamine neurons (Amilhon et al. 2010; Vaaga et al. 2014; Ren et al. 2018; Trudeau and El Mestikawy 2018). Further, some *Pet1* neurons form pericellular baskets immunoreactive for VGLUT3 and immunonegative for 5-HT, suggesting sole release of glutamate (Senft et al. 2021). Both VGLUT3$^+$/5-HT$^+$ and VGLUT3-only baskets are

made by r2-*Pet1* neurons, a subpopulation of *Pet1* neurons that arise from the rhombomere (r) 2 progenitor compartment (Jensen et al. 2008; Okaty et al. 2015; Senft et al. 2021). This group of cells is composed of two neurochemically distinct subtypes, one expressing a suite of serotonin neuron identity genes including *Tph2,* encoding the rate-limiting enzyme for serotonin synthesis, while the other subtype expresses an incomplete serotonergic neuron gene battery, including low levels of *Tph2,* and instead expresses high levels of *Vglut3*, suggesting this group signals primarily via glutamate.

Recent work has characterized the neurochemical phenotype of r2-*Pet1* boutons forming pericellular baskets (Senft et al. 2021). In some septal regions, r2-*Pet1* boutons forming baskets were primarily VGLUT3$^+$ or 5-HT$^+$/VGLUT3$^+$, contrasting other regions with r2-*Pet1* pericellular baskets such as the hippocampus and cortex, in which boutons were virtually exclusively VGLUT3$^+$-only. In the septum, 5-HT$^+$/VGLUT3$^+$ boutons were more abundant in baskets relative to nearby non-basket innervation, suggesting septal r2-*Pet1* baskets may represent sites specialized for glutamate/5-HT co-transmission. However, r2-*Pet1* neurons are known to exhibit an 'either/or' serotonergic or glutamatergic soma expression pattern, with high *Tph2* and low *Vglut3* or vice versa. An open question is then which of these subtypes of r2-*Pet1* neuron is forming the septal pericellular baskets abundant in 5-HT$^+$/VGLUT3$^+$ boutons? Identifying the somatic phenotype of the neurons making these baskets may reveal whether one (or both) r2-*Pet1* subtypes retain the ability to co-transmit despite low expression of genes related to either serotonin or glutamate neurotransmission.

Additional fundamental questions remain regarding the organization of r2-*Pet1* neuron pericellular baskets in the septum. It is unknown how these r2-*Pet1* baskets are distributed through the septal nuclei, whether they exhibit any regional topography in their distribution and whether this topography may differ for baskets of different neurochemical phenotypes. Lateral septum neurons exhibit topography in their responsiveness to multisensory external stimuli (Clemens et al. 2020) and inputs reflecting a similar topography could suggest roles regulating specific behaviors like kinship recognition or parenting behaviors. Additionally, combined with already characterized projection mapping and tracing experiments, this knowledge could help us identify potential circuitry downstream of the basket-encased neurons. Also undercharacterized is the morphology of cells targeted by r2-*Pet1* pericellular baskets in the septum, which has been previously used to characterize cell type (Phelan et al. 1993). It is possible that baskets exhibit a high degree of target specificity to a particular cell type, or alternatively, they may tile the septum and encase neurons with very distinct morphologies and efferent connectivity.

This chapter details preliminary findings we have made regarding the distribution of r2-*Pet1* pericellular baskets throughout the septum, the morphology of the cells targeted by these baskets, and the somatic neurochemical phenotype of r2-*Pet1* neurons projecting to the septum, as assessed through retrograde tracing experiments. Though provisional, these results suggest specificity in the topography of pericellular baskets distributed throughout the septum, the morphological types of neurons targeted by pericellular baskets, and in the somatic neurochemical phenotype of cells producing these baskets, raising exciting new directions for future research.

METHODS

Animals

All experimental procedures were approved by Harvard's Institutional Animal Care and Use Committee (IACUC). Mice were housed in a colony maintained on a 12 hr light-dark cycle. All transgenic strains described below have been previously backcrossed to the C57BL/6J inbred strain (The Jackson Laboratory, stock no. 000664) for at least nine generations. To visualize r2-*Pet1* neurons and their projections, we utilized the intersectional (Cre- and Flp-responsive) reporter allele *RC-Ai65* (B6;129S-*Gt(ROSA)26Sor*$^{tm65.1(CAG-tdTomato)Hze}$/J; Jax stock #021875; (Madisen et al. 2015), partnered with rhombomere 2 (r2)-specific Cre driver *Hoxa2-cre* (alias *r2Hoxa2-cre*); Awatramani et al., 2003) and the pan-serotonergic Flp driver *Pet1-Flpe*. In these triple transgenic mice, diffuse tdTomato labels fibers and somata of r2-*Pet1* neurons. *RC-Ai65* was selected over other available intersectional mouse lines because it is bright enough for fibers forming baskets in the septum to be visible in thick acute slices *ex vivo*. For retrograde tracing experiments, to be compatible with virally-expressed tdTomato, we utilized the *RC-FrePe* mouse line (Brust et al. 2014), expressing eGFP intersectionally in *r2Hoxa2-cre Pet1-Flpe RC-Frepe*$^{-/+}$ triple transgenic mice.

Mice used in experiments charting the distribution of r2-*Pet1* pericellular baskets throughout the septum (n=2 males) were postnatal day 40 (P40) in age, while mice used in the biocytin fills (n=3 females) experiments ranged in age from P60-P80. For retrograde tracing experiments, mice (n=2 males and 2 females) were aged P150-P200.

Ex vivo biocytin fills

In vitro septal slice preparations containing were obtained from mice aged P60-P80. After isofluorane anesthesia, mice were perfused transcardially with a solution of artificial NaHCO3-aCSF containing the following (in mM): 124 NaCl, 25 NaHCO3, 3 KCl, 2 CaCl2, 2 $MgCl_2$, 1.2, NaH2PO4 and 25 d-Glucose, equilibrated with 95% O2 and 5% CO2 adjusted to 310 ± 5 mOsm/L. The forebrain was dissected and mounted on the stage of a VT1200S vibratome while immersed in an ice slush solution aCSF containing the following (in mM): NMDG 93, HCl 93, KCL 2.5, NaH_2P0_4 1.2, $NaHCO_3$ 30, HEPES 20, d-Glucose 25, Na-Ascorbate 5, Thiourea 2, Na-Pyruvate 3, $MgSO_4$ 10, $CaCl_2$ 0.5 equilibrated with 95% O2 and 5% CO2 adjusted to 310 ± 5 mOsm/L. Coronal slices 300 µm thick containing the medial septum, lateral septum and diagonal band were recovered for 1h at 35-6 °C in aCSF equilibrated with 95% O2 and 5% CO2 adjusted to 310 ± 5 mOsm/L and then transferred to room temperature for the duration of the experiment. Individual slices were transferred to the recording chamber and superfused with NaHCO3-aCSF at 34ºC. Electrodes (5–7 MΩ) were pulled from borosilicate glass. Pipettes were filled with (in mM): 140 K-gluconate, HEPES 10, KCl 5, Na-ATP 2, $MgCl_2$ 2, EGTA 0.02, biocytin 0.1% Na_2GTP 0.5, Na_2-phosphocreatine 4, 20 mM Alexa Fluor 405 NHS-Ester pH 7.4 adjusted with KOH and adjusted to 285 ± 5 mOsm/L with sucrose.

Tissue Preparation for Immunohistochemistry

Experiments mapping the distribution of r2-*Pet1* pericellular baskets used brain sections from mice perfused transcardially with 0.1 M phosphate-buffered saline (PBS), followed by 4% paraformaldehyde (PFA) as previously published (Brust et al. 2014). Brains were fixed overnight in 4% PFA/PBS for 24 hours at 4ºC and then sectioned on a vibratome (Leica VT1000S) at 50-µm thickness and stored in 28% sucrose 30% ethylene glycol cryoprotectant at -30ºC. For

electrophysiological experiments, post-recording sections were post-fixed overnight in 4% PFA/PBS and then immediately stained or stored in the same manner as vibratome sections before immunodetection.

Immunohistochemistry for basket distribution and morphology

Immunohistochemistry (IHC) was performed similarly as reported previously (Senft et al. 2021). Briefly, floating sections were rinsed in PBS, incubated for 2 hrs at room temperature in a blocking solution of PBS containing 5% normal donkey serum (NDS; Jackson ImmunoResearch), 1% Bovine Serum Albumin (BSA, Sigma-Aldrich), and 0.1% triton-X-100 (Sigma-Aldrich). Sections were then transferred to a solution containing primary antibodies diluted in PBS with 2% NDS and 0.1% triton-X-100 and incubated for 48 hrs at 4°C on a nutator mixer (BD Clay Adams). We used the following antibodies and dilutions anti-DsRed (Takara, catalog no. 632496, rabbit polyclonal, 1:1000), anti-Fluoro-Gold (Millipore AB153-I rabbit polyclonal, 1:3000), anti-5-HT (Abcam, catalog no. ab66047, goat polyclonal, 1:500), anti-VGLUT3 (Synaptic Systems, catalog no. 135-204, guinea pig polyclonal, 1:500). After three PBS with 0.1% Triton-X-100 (PBST) washes, sections were transferred to a solution containing secondary antibodies diluted in PBST with 2% NDS and incubated in a light-protected chamber for 2 hr at room temperature. For detection of primary antibodies, species-matched Alexa 488, Alexa 546, Cy5, and Alexa 647-conjugated secondary antibodies (Jackson ImmunoResearch) were used at 1:500 dilution. For visualization of the biocytin-filled somata, we added streptavidin conjugated to Alexa fluor 647 (Life Technologies catalog no. S32357, 1:500). Sections were then washed three times in fresh PBST at room temperature as before, with 1 μg/ml DAPI (Life Technologies) added to the last wash step lasting 15 min. Sections were mounted onto No. 1.5 coverslips (Electron Microscopy

Sciences) and then attached to SuperFrost Plus histological slides (Fisher Scientific) using ProLong Glass anti-fade mountant (ThermoFisher).

Retrograde tracing experiment

To label r2-*Pet1* cells that project to the septum, we injected 4 adult (2 male, 2 female) *r2Hoxa2-cre, Pet1-Flpe, RC-FrePe*$^{-/+}$ mice with AAV2-retro-*CAG*-tdTomato-WPRE virus (Addgene 59462-AAVrg) and AAV-GFP (AAV2/1-CAG-GFP-WPRE made by the Boston Children's Hospital Viral Core; 3 mice) or Fluoro-Gold (FG, 4% in sterile phosphate-buffered saline) (1 mouse) into the septum. The retrograde serotype of the AAV2-retro-*CAG*-tdTomato virus allows infection of projection neurons that innervate the region targeted by viral injections and results in virus-induced marking of infected neurons by tdTomato. Similarly, Fluoro-Gold is a fluorescent dye that can also be used as a retrograde tracer (Morecraft et al. 2014). For 3 mice, we targeted the lateral septum bilaterally (coordinates ML: ±0.37 mm, AP +0.8 mm, Z: -3.6 mm), though expression was mostly targeted to one side (see Results). For one AAV-injected mouse, we targeted a single injection to the medial septum (coordinates ML: 0 mm, AP +0.8 mm, Z: -3.6 mm).

Post-surgery (3 weeks for AAV-injected mice and 1 week for the Fluoro-Gold-injected mouse), mice were perfused and tissue processed as above. Sections were stained for EGFP and VGLUT3 or 5-HT using a previously reported immunohistochemistry protocol (Senft et al. 2021). Briefly, sections were blocked in PBST with 5% NDS for two hours at room temperature, incubated with primary antibodies for 48 hours at 4°C, rinsed 3x in PBST and incubated with secondary antibodies in PBST with 2% NDS for two hours at room temperature. After rinsing in

PBST with a last 10 minute rinse with 1.5 ug/mL DAPI, sections were mounted on #1.5 thickness coverslips and then adhered to slides with Prolong Glass mounting media.

Confocal microscopy

For mapping the distribution of pericellular baskets, the cells that project to the septum, and for examining the morphology of filled neurons, we performed confocal imaging as reported previously (Senft et al. 2021). Briefly, we used a Nikon Ti inverted spinning disk microscope equipped with a Yokogawa CSU-W1 Spinning disk scanhead with 50 µm pinhole disk, a PI Z piezo stage insert, a TOPTICA iChrome MLE laser launch and Lumencor Sola 395 LED Light Engine (the latter used for imaging DAPI). Laser lines (and relevant power levels measured at the fiber tip) included 488 nm solid state (100mW), 561 nm DPSS (100 mW), 640 nm solid state (60mW). The microscope had a Nikon Motorized Stage with Physik Instrument Piezo Z motor used to acquire z-stacks in both experiments. A Plan Apo λ 20x/0.75 DIC I objective was used for basket mapping and retrograde tracing and a Plan Apo λ 60X 1.4 N.A. oil objective (Type 37 immersion oil) was used for imaging filled neurons. Images were captured using an Andor Zyla 4.2 Plus sCMOS monochrome camera with 12 bit gain. Nikon Elements Acquisition Software AR 5.02 was used for acquiring images and stitching tiles according to an "optimal path" stitching algorithm. In the basket distribution mapping experiment and retrograde tracing experiment, single-label controls were used to determine imaging settings to eliminate channel bleedthrough. Signal from the different channels was acquired sequentially using a Semrock Di01-T405/488/568/647 multi-band pass dichroic mirror and band pass emission filters for green (Chroma ET525/36m), red (Chroma ET 605/52m) and far read (Chroma ET 705/72m) channels. For all images, when brightness/contrast settings were adjusted using ImageJ,

identical settings were used for each channel applied uniformly across images within a given experiment. In the biocytin fill experiments, since some cells were deeper in the tissue than others, resulting in higher scattering and variable antibody penetration, brightness was set manually for each cell. Images are presented as maximum intensity z-stack projections generated using Fiji (NIH; Schneider et al., 2012).

Quantitation of pericellular baskets

Pericellular baskets were assessed manually using the Multi-point tool in Fiji (Schindelin et al. 2012) to mark baskets (fibers wrapping around a nucleus and typically having visible offshoots wrapping around dendrites (Köhler et al. 1982). Baskets were scored as being composed of only VGLUT3$^+$ fibers or as being composed of 5-HT$^+$ fibers and VGLUT3$^+$ fibers (only very rarely were any 5-HT$^+$ baskets observed without any VGLUT3$^+$ fiber contribution). After identifying baskets according to VGLUT3 and 5-HT immunoreactivity, the tdTomato signal (labeling r2-*Pet1* axons) was examined at each basket location for whether it contributed to each basket. We quantified a total of 519 baskets from 2 mice. After quantifying the basket types present in each section, images were manually aligned to a brain atlas (Franklin and Paxinos 2008) and presented for display using Adobe Illustrator software (Adobe 2019).

Quantitation of retrograde tracing

For retrograde tracing experiments, images were analyzed by manual counting of EGFP$^+$ and tdTomato$^+$ cells using the Multi-point tool in Fiji (NIH). We first selected display settings using single label controls and then quantified the percent of all cells expressing VGLUT3 or 5-HT for tdTomato$^+$/EGFP$^+$ and FG$^+$/EGFP$^+$ cells as well as for all tdTomato$^+$ cells and all EGFP$^+$

cells.

Statistics

Unless otherwise noted, results are presented as mean ± standard error of the mean (SEM). Statistical tests are reported where discussed.

RESULTS

Distribution of 5-HT$^+$ and VGLUT3$^+$ pericellular baskets throughout the septum

In line with previous studies of 5-HT$^+$ baskets (Köhler et al. 1982; Gall and Moore 1984; Dinopoulos et al. 1993) and VGLUT3$^+$ baskets (Riedel et al. 2008), we observed 5-HT$^+$ and VGLUT3$^+$ baskets populated the dorsolateral septum (dLS) in more rostral sections and the intermediate lateral septum (iLS), particularly at the border region of the iLS and medial septum (MS; Figure 4.1A-B). Of the 519 baskets studied, 68.8% (357) exhibited contributions from VGLUT3$^+$ and 5-HT$^+$ fibers. In many cases, these fibers appeared doubly labeled for both 5-HT and VGLUT3, though at the resolution of our microscopy we are not able to determine colocalization for individual axonal boutons or varicosities. We observed many 5-HT$^+$ and VGLUT3$^+$ baskets in the rostral dLS (Figure 4.1C), consistent with previous reports of 5-HT$^+$/VGLUT3$^+$ co-labeling (Shutoh et al. 2008). Our observations of baskets immunoreactive for VGLUT3 alone also generally aligned with previous studies (Riedel et al. 2008), including abundant baskets in the dLS and ventral lateral septum (vLS) at mid levels, noting that we did not proceed as caudally as Riedel et al., and therefore did not observe these baskets disappearing in the caudal vLS.

Figure 4.1. Regional patterning of VGLUT3$^+$ and 5-HT$^+$ pericellular baskets in the septum

Locations of somata surrounded by a pericellular basket are shown with symbols (A) indicating whether the basket was immunoreactive for VGLUT3 only (magenta circles), or for VGLUT3 and 5-HT (green triangles). Solid symbols indicate contribution from r2-*Pet1* boutons and empty boutons without r2-*Pet1* contribution. Insets show examples of regions enriched for 5-HT$^+$/VGLUT3$^+$ baskets, indicated by green arrowheads (B) and for VGLUT3$^+$-only baskets, indicated by pink arrowheads (C).In B and C, arrowheads are solid if r2-*Pet1* fibers contribute and outlines if the basket lacks r2-*Pet1* fibers. Scale bar is 100 μm. Abbreviations: cc: corpus callosum, dLS: dorsolateral septum, iLS: intermediate lateral septum, Ld: lamdoid septal zone, LV: lateral ventricle, MS: medial septum, SHi: septohippocampal nucleus, vLS: ventrolateral septum.

(Figure 4.1 continued)

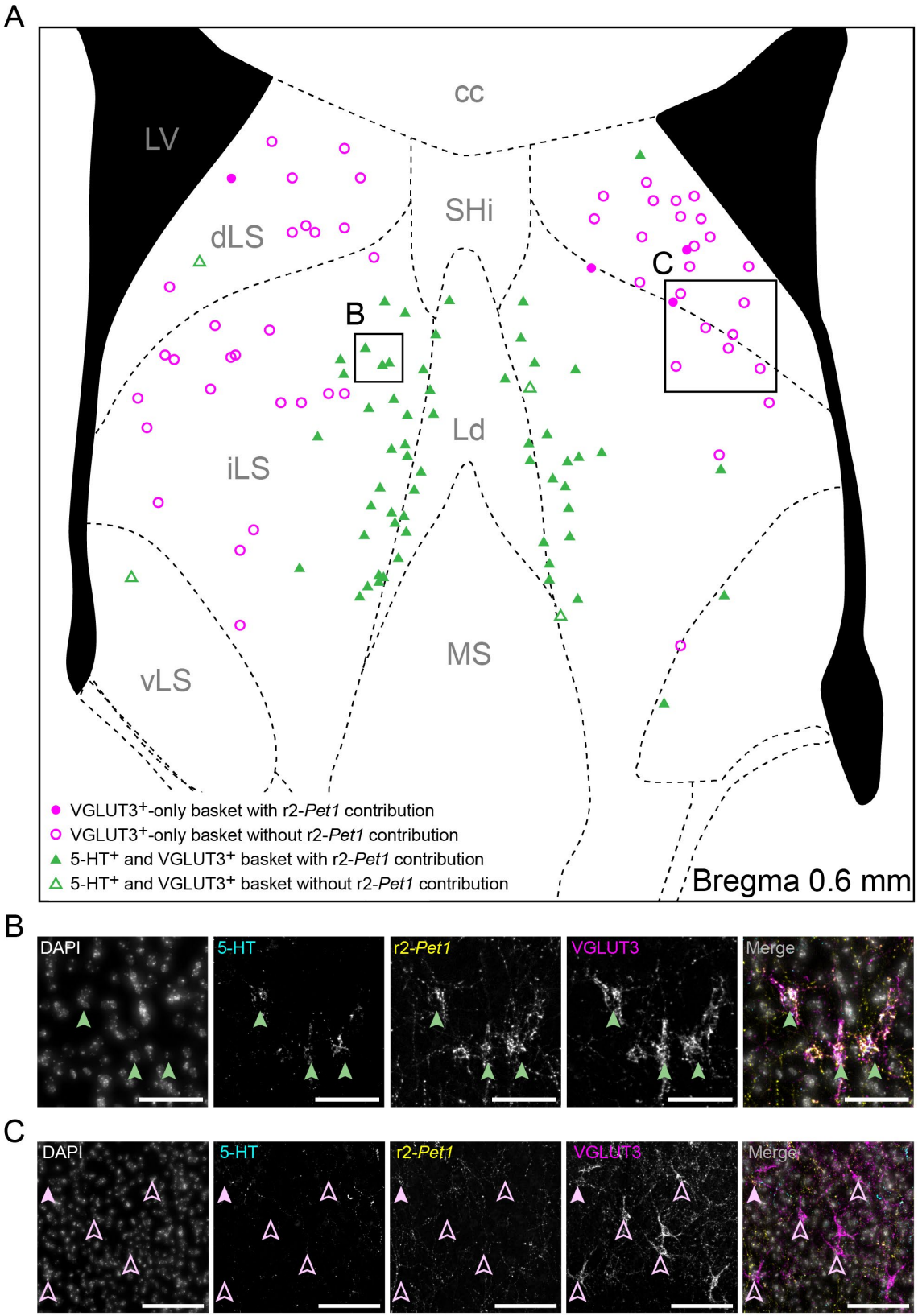

*Contribution of r2-*Pet1 *axons to 5-HT$^+$ and VGLUT3$^+$ septal pericellular baskets*

We observed r2-*Pet1* fibers contributed to most septal pericellular baskets labeled by VGLUT3 or 5-HT (on average, 62%; Figure 4.2). The distribution of these baskets largely matched the previously described 5-HT$^+$ and VGLUT3$^+$ basket pattern, noticeably absent from the VGLUT3$^+$-only baskets in the mid- to caudal- dLS and vLS. We observed baskets exhibiting 5-HT- and VGLUT3-immunoreactivity were more likely to also receive contribution from r2-*Pet1* projections (88.4 ± 2.7%) than baskets only labeled by VGLUT3 (14.8 ± 4.6%), though additional mice should be examined before pursuing statistical analysis (Figure 4.2F). At rostral levels where we observed a higher proportion of 5-HT$^+$ and VGLUT3$^+$ baskets, we correspondingly observed a higher percentage of baskets receiving r2-*Pet1* contribution (Figure 4.2G), though the percentage of baskets that received r2-*Pet1* fibers was relatively constant over the rostrocaudal extent of the septum for each basket type (Figure 4.2H).

Figure 4.2. Distribution of VGLUT3$^+$ and 5-HT$^+$ pericellular baskets through the rostrocaudal extent of the septum

Rostrocaudal position for each image indicated at top (A-E). Locations of somata surrounded by a pericellular basket are shown with symbols (legend below). Quantification of r2-*Pet1* contribution to septal VGLUT3$^+$ and VGLUT3$^+$ and 5-HT$^+$ baskets (F). More rostral positions were associated with higher proportions of 5-HT$^+$ and VGLUT3$^+$ baskets and a greater of fraction of baskets receiving contributions from r2-*Pet1* neurons (G). Overall, baskets with 5-HT$^+$ boutons and VGLUT3$^+$ boutons were more likely to also include r2-*Pet1* fibers than baskets with only VGLUT3$^+$ boutons. Atlas images were adapted from (Franklin and Paxinos 2008). Abbreviations: cc: corpus callosum, dLS: dorsolateral septum, f: fornix, iLS: intermediate lateral septum, Ld: lamdoid septal zone, LV: lateral ventricle, MS: medial septum, SFi: septofimbrial nucleus, SHi: septohippocampal nucleus, SHy: septohypothalamic nucleus, vLS: ventrolateral septum.

(Figure 4.2 continued)

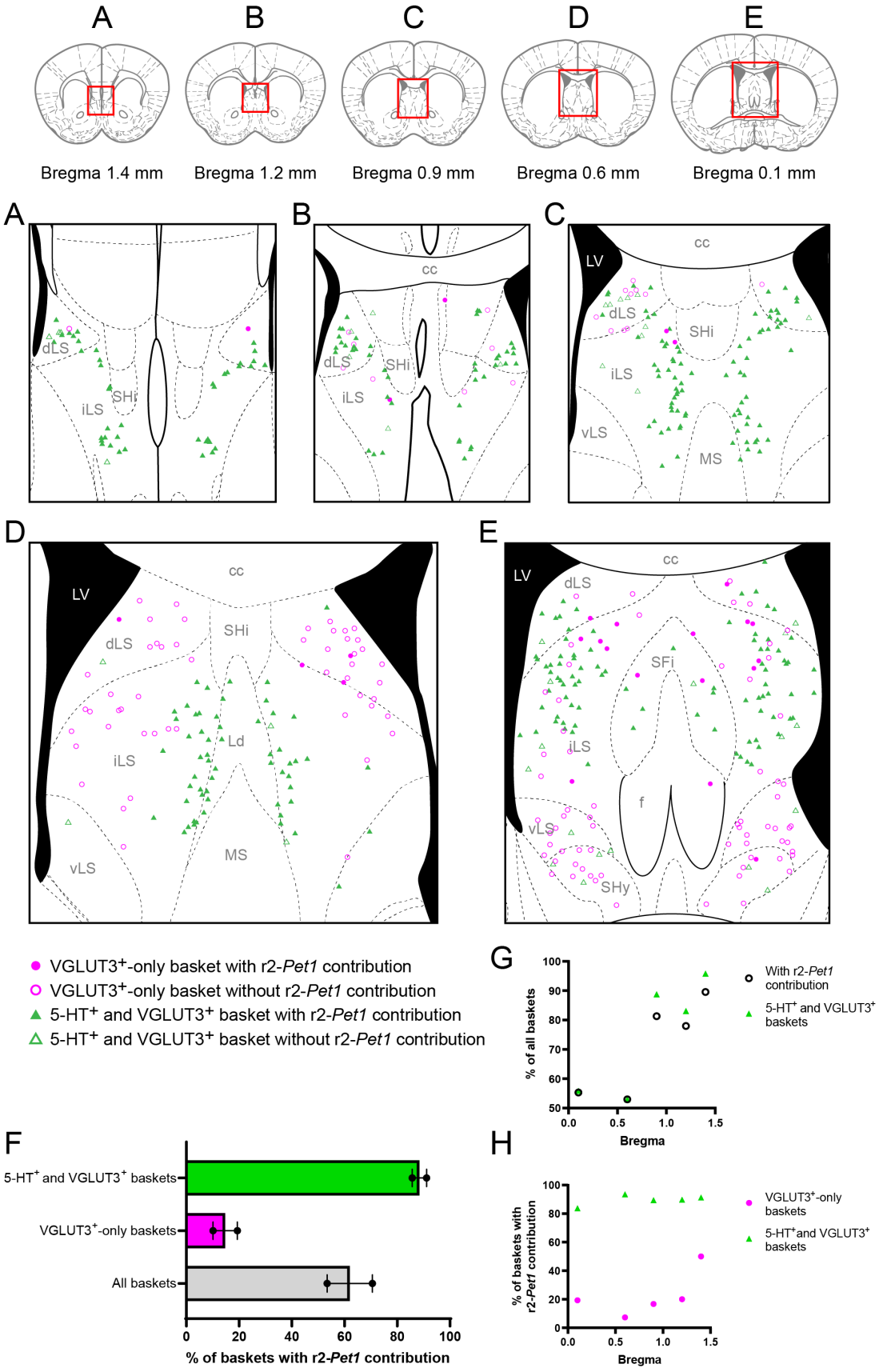

*Morphology of neurons targeted by r2-*Pet1 *pericellular baskets*

Preliminary biocytin fills of neurons targeted by pericellular baskets revealed several different morphologies (Figure 4.3A-A'') that are nonetheless consistent with a morphological type of lateral septum neuron previously described (Alonso and Frotscher 1989). The neurons examined thus far were distributed throughout the dorsoventral extent of the lateral septum (Figure 4.3B) and had 4-5 thin primary dendrites. Some cells exhibited round soma (Figure 4.3A, A'') while some exhibited a triangular soma (Figure 4.3A'). These cells exhibit some dendritic spines (Figure 4.3C'), though not on the soma or most proximal segments of dendrites. These characteristics are consistent with what have been termed Type II neurons of the dLS and iLS (Alonso and Frotscher 1989) and are distinct from Type I neurons, which are abundant in spines and display thick dendrites.

Sections with filled neurons were also labeled for 5-HT, which revealed many r2-*Pet1* varicosities forming pericellular baskets (Figure 4.3A) but not all (Figure 4.3A') exhibited a strong 5-HT-immunoreactivity. Additionally, non-r2-*Pet1* 5-HT$^+$ fibers were also observed to closely appose the basket-targeted neurons, suggesting the filled cells are the targets of composite baskets formed by multiple *Pet1* neurons from distinct rhombomeric lineages (Senft et al. 2021). We occasionally observed cells nearby the filled neuron that were also labeled by biocytin albeit not as brightly (Figure 4.3C). This observation suggests that biocytin diffused from the filled cell to these nearby neurons via a dendro-dendritic or dendro-somatic connection, as has been observed previously in the dLS (Phelan et al. 1993).

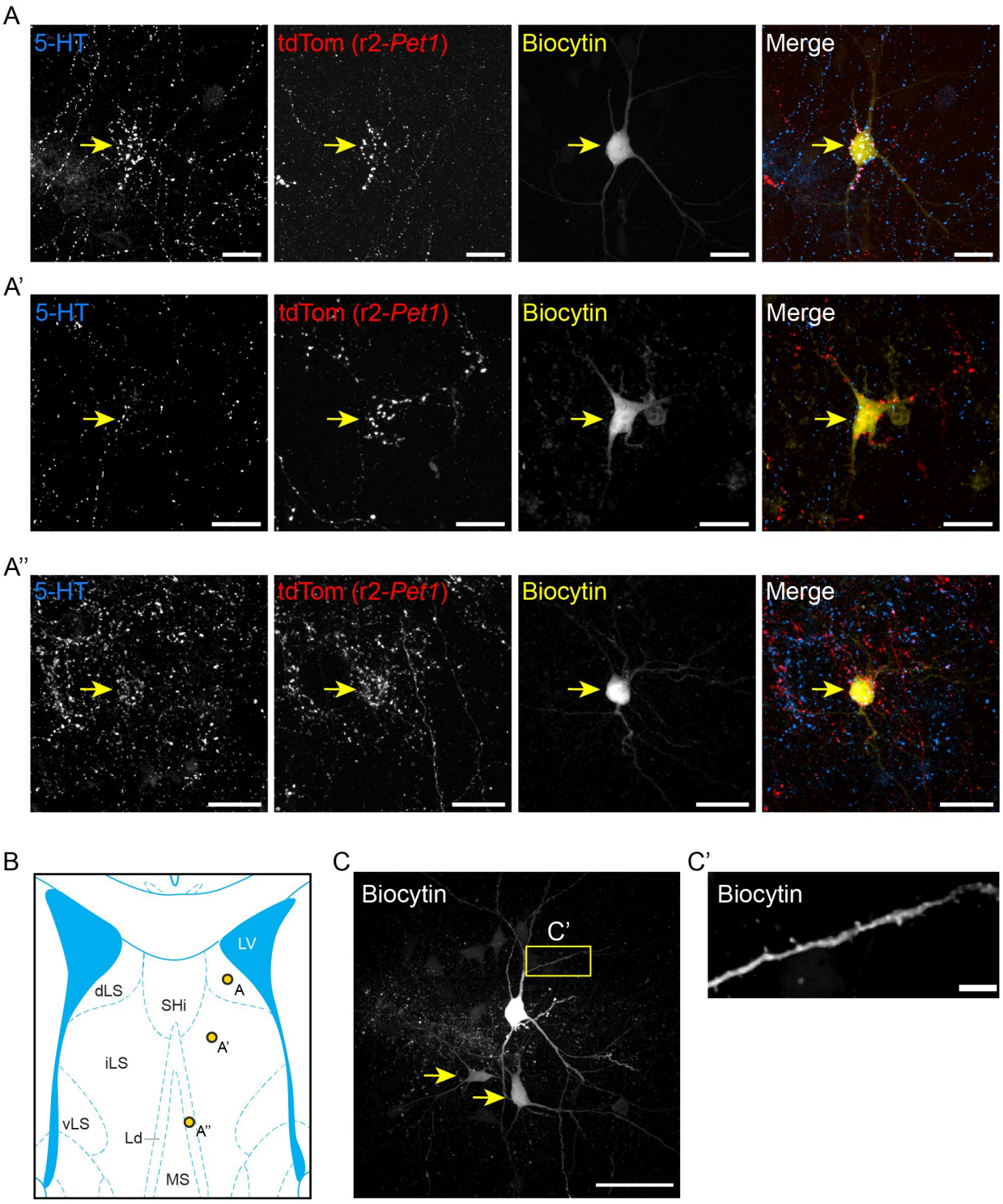

Figure 4.3 Morphology of septal neurons targeted by r2-*Pet1* pericellular baskets

Several examples of biocytin fills of neurons targeted by r2-*Pet1* pericellular baskets displaying different somatic morphologies consistent with Type II septal neurons (A-A''). Approximate locations of filled soma in A-A'' (B). Nearby some filled cells, such as the cell in A, we observed

(Figure 4.3 continued)
additional cells with biocytin labeling (C, arrows), suggesting cells may be coupled via dendro-somatic or dendro-dendritic connections. Inset showing spines on a thin dendrite from the cell in C (C'). Scale bars for panels A-A'' and C are 50 μm, scale bar for C' is 5 μm.

*Cellular origin of r2-*Pet1 *neurons making pericellular baskets in the septum*

Our retrograde tracing experiments (Figure 4.4A) identified the neurochemical phenotype of r2-*Pet1* and other MR neurons projecting to the septum (injection sites schematized in Figure 4.4B). We observed 56 r2-*Pet1* neurons from n=4 mice and quantified their immunoreactivity for either 5-HT or VGLUT3. In general, r2-*Pet1* neurons ($eGFP^+$) that were additionally labeled by either retrograde tracer (FG or retro-AAV-expressed tdTomato) were found to be often $VGLUT3^+$ (65.0 ± 19.3%; Figure 4.4C) and only rarely $5\text{-}HT^+$ (2.8 ± 2.8%; Figure 4.4D). Our quantification of the fraction of r2-*Pet1* neurons labeled by septal injections indicated that this technique captured a small subset of r2-*Pet1* neurons (2.8 ± 0.8%; Figure 4.4E) and these cells were anatomically intermingled with other r2-*Pet1* neurons that were not captured by retrograde tracer (see nearby $eGFP^+$ neurons in Figure 4.4C-D).

Quantification of VGLUT3- vs. 5-HT-immunoreactivity revealed that r2-*Pet1* neurons that project to the septum were more likely to be $VGLUT3^+$ than $5\text{-}HT^+$ ($t=3.769$, $df=5$ $p=0.013$, unpaired t-test; Figure 4.4F). In contrast, the entire population of r2-*Pet1* neurons, quantified for three of the four injected mice (in total, 909 cells), exhibited similar percentages of cells that were $5\text{-}HT^+$ (31.2 ± 1.8%) and $VGLUT3^+$ (37.4 ± 1.6%). However, it should be noted that while VGLUT3 is immunodetectable at the soma (Sos et al. 2017; Okaty et al. 2020), there is likely a range of VGLUT3 expression in which mRNA transcript levels are high at the soma, but protein

remains non-immuno-detectable, as would be suggested by the gap between percent of VGLUT3^{high} r2-*Pet1* neurons as measured by *in situ* hybridization vs. immunohistochemistry (Okaty et al. 2015; Senft et al. 2021). This suggests that some neurons unlabeled in our experiment may be of the r2-*Pet1*$^{Vglut3\text{-high}}$ neuronal subtype but are not detectable as VGLUT3^{+} with immunohistochemistry. We also examined all MR neurons labeled by retrograde tracer (in total, 621 cells), finding 14.1 ± 5.2% were 5-HT^{+} and 30.2 ± 8.3% were VGLUT3^{+} (Figure 4.4H), demonstrating that 5-HT neurons are capable of being labeled by these retrograde tracer injections, but within the r2-*Pet1* lineage, septum-projecting neurons are mostly of the VGLUT3^{high} subtype.

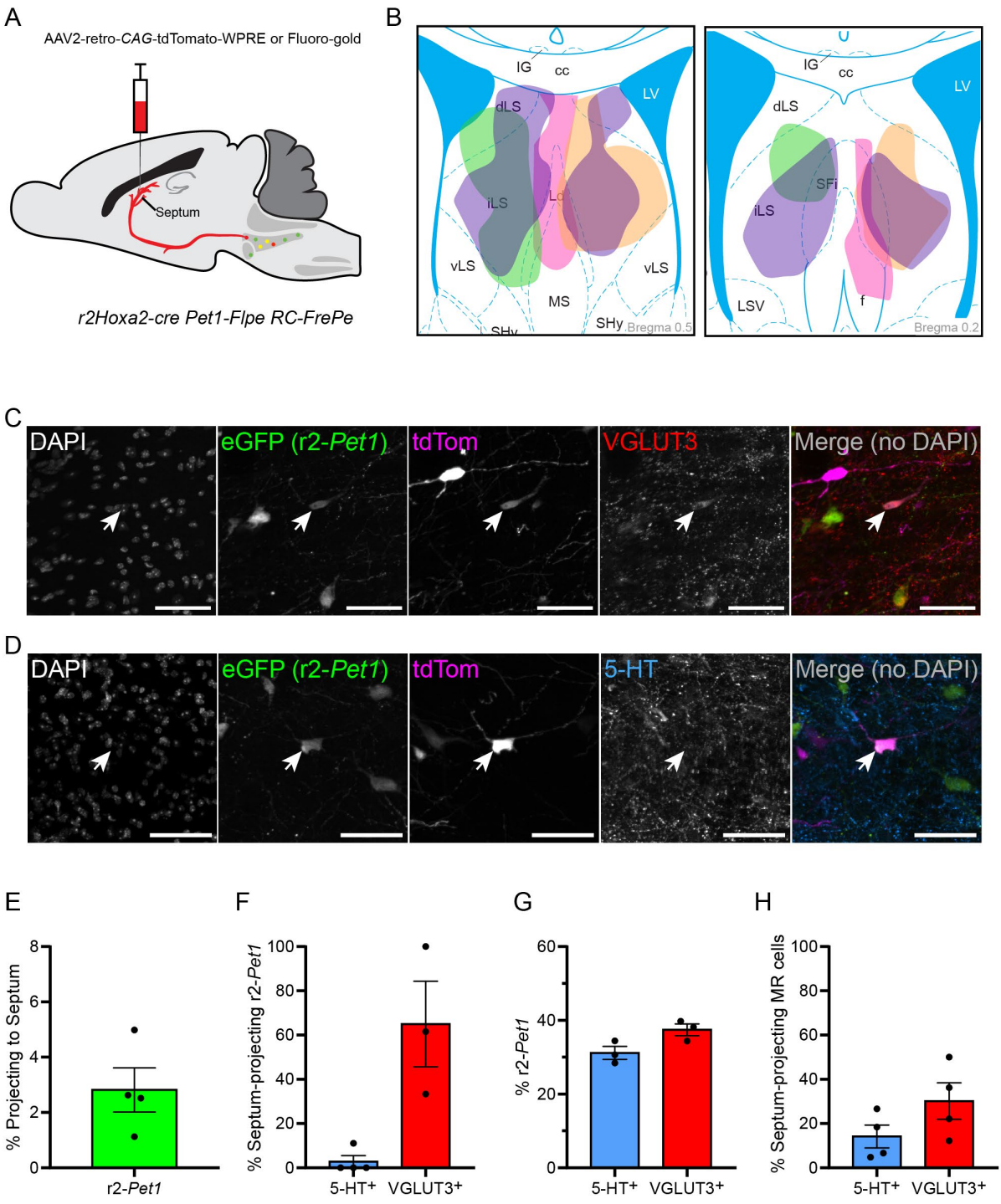

Figure 4.4. r2-*Pet1* neurons that target the septum express somatic VGLUT3 and not 5-HT

Schematic illustrating the experimental design for the retrograde tracing experiment (A) and injection areas in the lateral septum color-coded by mouse (B). r2-*Pet1* cells that project to the septum (i.e., eGFP$^+$/tdTomato$^+$ neurons) were often immunopositive for VGLUT3 (C), but rarely

(Figure 4.4 continued)
for 5-HT (D). Overall, a small percentage of r2-*Pet1* neurons were labeled using retrograde tracing from the septum (E), and these septum-projecting r2-*Pet1* neurons were generally VGLUT3$^+$ and 5-HT$^-$ (F), contrasting the entire population of r2-*Pet1* neurons (G) and the entire population of septum-projecting neurons (H), which both exhibited higher percentages of 5-HT-immunoreactivity. Scale bars in C, D are 50 µm. Atlas schematic in B is adapted from (Franklin and Paxinos 2008).

DISCUSSION

In the present study, we characterized the contribution of r2-*Pet1* neurons to septal pericellular baskets. Our main findings are as follows: 1) Septal pericellular baskets of different neurochemical phenotypes (5-HT$^+$/VGLUT3$^+$ vs VGLUT3$^+$-only) exhibit regional topography in the septum, and r2-*Pet1* perisomatic innervation maps closely onto the topography of 5-HT$^+$/VGLUT3$^+$ baskets, 2) Lateral septum neurons targeted by r2-*Pet1* pericellular baskets are morphologically consistent with previously described "Type II" neurons and these cells sometimes appear to exhibit connections to nearby lateral septum cells likely facilitated by gap junctions, and 3) the subtype of r2-*Pet1* neuron giving rise to septal pericellular baskets is likely the *Vglut3*^{high} group, suggesting this group may be capable of rapidly and selectively trafficking mRNA or proteins necessary for 5-HT release to a subset of collaterals despite low cell body expression of *Tph2*. These results inform our understanding of the organization of afferents to the septum and suggest functional roles for r2-*Pet1* neurons.

In our mapping of pericellular baskets, we noted a large proportion of VGLUT3$^+$-only pericellular baskets, which often did not receive any contribution from r2-*Pet1* fibers. We have previously observed additional 5-HT$^-$, VGLUT3$^+$ boutons contributing to *Pet1* neuron pericellular baskets in the septum (Senft et al. 2021). A remaining question to be answered is the source of

these VGLUT3$^+$ septal pericellular baskets. The septum receives pericellular baskets from many deep brain structures, including the hypothalamus, substantia nigra, and raphe nuclei (Jakab and Leranth 1995). These baskets are typically considered a feature most commonly found in modulatory neuron systems (Riedel et al. 2008). In addition to the VGLUT3$^+$ *Pet1* neuron populations, there are additional *Vglut3*-expressing neurons in the dorsal and median raphe (Sos et al. 2017) that send non-serotonergic projections to forebrain target regions (Jackson et al. 2009; Hioki et al. 2010). These non-*Pet1* VGLUT3$^+$ neurons are likely candidates for producing the baskets observed here and by others (Riedel et al. 2008). An additional possible candidate based on projections to the lateral septum (Luiten et al. 1982) and expression of *Vglut3* is the nucleus of the solitary tract (Schäfer et al. 2002). Anterograde tracing experiments from these regions can be used to test whether they give rise to the VGLUT3$^+$-only septal baskets observed in the mid-dLS and vLS. This approach can also be utilized to find the source of the non-*Pet1* VGLUT3$^+$ boutons found converging on the same neurons as *Pet1* pericellular baskets.

In our biocytin fill experiments, we sometimes observed neurons nearby the filled cell that were also labeled with biocytin, suggestive of intercellular transfer mediated by gap junctions, a phenomenon previously observed in the lateral septum (among other regions) that is also referred to as 'dye-coupling' (Phelan et al. 1993). This coupling is believed to be important for electrophysiological synchronization of neurons during oscillatory activity, such as during theta (Bennett and Zukin 2004; Bocian et al. 2011; Belousov and Fontes 2013). The presence of a basket on a cell electrotonically coupled to other neurons suggests the r2-*Pet1* neuron forming the basket may be poised to regulate not only the directly postsynaptic neuron, but through these connections, a larger circuit of potentially synchronized downstream neurons.

Similar to previous studies (Phelan et al. 1993), we observed labeled neurons were not somatically apposed, suggesting dendro-dendritic or dendro-somatic connection points. Further, their observed morphology of the coupled cells matched our neuron, including few spines except on more distal dendrites. Of course, additional neurons need to be examined to rule out the possibility of labeling caused by damage to nearby cells from the slicing process or from moving the recording pipette. Preliminary recordings suggest these cells exhibit electrophysiological characteristics such as narrow action potential and tonic spiking upon depolarization, consistent with the firing type denoted as 'tonic' (Wang, Simms, et al. 2019) and 'fast spiking' (Manseau et al. 2008; Huh et al. 2010).

The distribution of r2-*Pet1* baskets we observed suggests they may encase cells that regulate parenting and defensive/aggressive behaviors. The lateral septum is implicated in nurturing parental behaviors such as licking and grooming (Curley et al. 2012; Dulac et al. 2014) as well as defensive behaviors such as maternal aggression and territorial male-male aggression (Hasen and Gammie 2005; Nelson and Trainor 2007). This distribution of *Pet1* pericellular baskets is similar to that of cells expressing estrogen receptor α (ERα; Mitra et al. 2003) which are activated (as measured by c-fos expression) in lactating female rats exposed to pups (Lonstein et al. 2000). The number of ERα-expressing neurons in the lateral septum is also positively correlated with individual differences in aggressive behavior, suggesting these cells may be important in sensing and responding to a threats (Nelson and Trainor 2007). Based on their distribution, *Pet1* pericellular baskets are well-positioned to regulate these or other nearby neurons that modulate parenting and aggression.

There are several potential circuits through which *Pet1* neurons making pericellular baskets in the lateral septum may modulate parental behaviors and aggression. Previous work (Risold and Swanson 1997) identified a group of lateral septum neurons that project to the anterior hypothalamus, a brain region important in regulating parental behavior and aggression (Nelson and Trainor 2007; Dulac et al. 2014) and responding defensively to environmental threats (Hakvoort Schwerdtfeger and Menard 2008). These cells also broadly match the distribution of rostral 5-HT$^+$/VGLUT3$^+$ baskets receiving r2-*Pet1* input, suggesting a potential circuit of median raphe projections making pericellular baskets on LS cells that in turn project to the AHN to regulate parental behaviors and aggression. The lateral septum also exhibits projections to the periaqueductal grey (PAG) to regulate maternal and male-male aggression, another potential pathway through which median raphe projections to the lateral septum might influence parenting behaviors (Nelson and Trainor 2007).

Evidence from studies manipulating the raphe also supports a role for *Pet1* neurons in regulating aggression and parenting behavior. Median raphe (MR) lesions have been shown to reduce maternal behavior in postpartum rats (Yurino et al. 2001), and median raphe stimulation phasically reduces aggression (Balázsfi et al. 2018), supporting a role for the MR in regulating social and maternal behaviors. Additionally, serotonin neurons in the dorsal raphe (DR) have also been shown to be important in regulating parenting behavior and aggression (Niederkofler et al. 2016; Holschbach et al. 2018; Lyon et al. 2020; Muzerelle et al. 2021), though whether DR *Pet1* neurons form baskets is as yet unknown. We then predict that *Pet1* pericellular baskets in the lateral septum may play a role in promoting parenting behavior via release of 5-HT or glutamate onto lateral septal neurons. To further explore this possibility, baskets can be examined in

combination with c-fos immunodetection following exposure of an animal to pups to test whether neurons activated by cues from pups are also encased in pericellular baskets. Further, basket topology should be examined in both male and female mice at different reproductive states to determine if basket number or neurochemical phenotype is plastic and altered by different life history stages.

Chapter V.

Discussion and Future Directions

I wrote this chapter with input from my advisor, Dr. Susan M. Dymecki.

SUMMARY OF FINDINGS AND SIGNIFICANCE

Serotonergic *Pet1* neurons modulate numerous processes throughout the brain, enabled in part through highly collateralized axonal projections. This multiplicity of tasks appears to be divided across the *Pet1* neuronal system, with different kinds of *Pet1* neurons – defined hodologically, molecularly, and functionally – modulating distinct behavioral and physiological processes. Indeed, these subtypes of *Pet1* neurons can be viewed as comprising neuronal subsystems within the overall *Pet1* serotonergic neuronal system. One means that proved successful in identifying such constituent subsystems, at least at a gross level, involved subdividing the *Pet1* neuronal population based on progenitor cell compartment of origin, in other words, based on hindbrain rhombomere (r) of origin. This is perhaps not surprising given that distinctive gene expression programs are enacted in different rhombomeres during development that impact neuron differentiation and ultimately identity. Here we explored one rhombomeric lineage of *Pet1* neurons – specifically the r2-*Pet1* neuron group. Cell body gene expression data suggest this lineage is composed of two subgroups each equipped to release different neurotransmitters, serotonin (5-HT) vs. glutamate. We call these sub-subgroups r2-*Pet1*$^{Tph2\text{-high}}$ and r2-*Pet1*$^{Vglut3\text{-high}}$, respectively. We queried whether the divergent soma gene expression phenotypes of these neurons are reflected at the level of their axonal projections. Further, we probed the extent to which these two constituent subtypes exhibit hodological divergence.

Our findings suggest that the r2-*Pet1* neuronal lineage is made up of two major subsystems that are distinct neurochemically and hodologically, and by extension, likely also in the kinetic scales of neurotransmission. We discovered that the r2-*Pet1* subsystem comprised of *Vglut3*^{high} neurons forms presynaptic specializations termed pericellular baskets, found in cortical, hippocampal, and septal regions. Often, these basket structures were found to be composites formed by axons of r2-*Pet1* neurons and axons from other *Pet1* neurons (from different rhombomeric lineages) that converged to ensheath the same downstream neuron. This convergence of inputs, as well as the finding that basket inputs from different lineages may be neurochemically distinct (VGLUT3$^+$ vs. 5-HT$^+$), suggests complex regulation of the basket-targeted neuron. These composite pericellular baskets were found to be particularly common in the septum, where multiple neurotransmitter systems are known to send projections comprising pericellular baskets. In reviewing this literature, we propose that pericellular baskets should be further investigated as sites of potential neurotransmitter convergence, perhaps not only between lineages of *Pet1* neurons releasing different neurotransmitters, but also between wholly distinct neurotransmitter systems, such as the dopaminergic, serotonergic, and glutamatergic systems that each form pericellular baskets in the septum. As a first step toward mapping such interactions, we charted the distribution of r2-*Pet1* pericellular baskets relative to the baskets formed by 5-HT$^+$ and VGLUT3$^+$ fibers in the septum, finding a topology that spans several septal nuclei and suggests that pericellular baskets with r2-*Pet1* bouton contribution are sites of 5-HT and glutamate release onto the basketed cell. Preliminary exploration of the morphology of these cells suggests they are a previously described subtype of septal neuron called Type II neurons. The abundance of *Pet1* pericellular baskets in the septum, a major limbic relay station,

and our earlier findings implicating r2-*Pet1* neurons in the durability of reward-conditioned contextual memory suggests possible functional roles in emotional processing and spatial/sensory memory.

The remainder of this final chapter discusses implications of the research presented in this dissertation and proposes future questions to be explored regarding *Pet1* neurons and their hodology, physiology, and function.

IMPLICATIONS OF VGLUT3 AND SEROTONIN CO-LABELED R2-*PET1* BOUTONS

We found select regions, notably the septum and ventral hippocampus, that were innervated by 5-HT$^+$/VGLUT3$^+$ r2-*Pet1* boutons, suggestive of 5-HT/glutamate co-transmission. Release of glutamate and serotonin from the same neuron terminals has been reported previously (Amilhon et al. 2010; Vaaga et al. 2014; Trudeau and El Mestikawy 2018). However, we did not expect r2-*Pet1* boutons to be 5-HT$^+$/VGLUT3$^+$ given the largely divergent, either/or expression of *Vglut3* or *Tph2* at r2-*Pet1* somata. Retrograde tracing from the septum labeled r2-*Pet1*$^{Vglut3\text{-high}}$ neurons, suggesting they give rise to the 5-HT$^+$/VGLUT3$^+$ boutons in the septum, despite having somata that are 5-HT$^-$ and low in *Tph2* mRNA. One possible resolution for this discrepancy between somatic and bouton phenotypes would be if r2-*Pet1*$^{Vglut3\text{-high}}$ cells do not participate in somatodendritic release of 5-HT, wherein serotonin neurons extrasynaptically release 5-HT from their somata and dendrites in the raphe (Quentin et al. 2018). If r2-*Pet1*$^{Vglut3\text{-high}}$ neurons lack somatodendritic storage and release of 5-HT, they may be able to quickly transport *Tph2* transcripts to their axon terminals for translation and subsequent synthesis of serotonin (Hale et al. 2011). This proposed rapid trafficking might allow r2-*Pet1* neurons to

express low levels of *Tph2* mRNA at the soma but still release 5-HT in boutons. *Tph2* expression may also be low if it is selectively trafficked only to certain 5-HT-releasing axon collaterals. We predict that r2-*Pet1*$^{Vglut3\text{-high}}$ neurons do not extrasynaptically release 5-HT in the raphe, but are nonetheless sensitive to somatodendritic release of 5-HT by other neurons as the autoreceptor 5-HT1a is broadly expressed by r2-*Pet1* neurons (Okaty et al. 2015). Our findings suggest some r2-*Pet1* neurons are capable of co-transmitting glutamate and serotonin and we suggest they may selectively and rapidly transport *Tph2* mRNA to certain axon terminals, resulting in a discrepancy between their somatic and bouton neurochemical phenotypes.

Additional questions stemming from this work are 1) whether r2-*Pet1* neurons exhibiting 5-HT$^+$/VGLUT3$^+$ boutons in the septum send additional collaterals to other regions and 2) whether their boutons are always 5-HT$^+$/VGLUT3$^+$, or whether collaterals of these neurons may exhibit different neurochemical phenotypes. Segregation of neurotransmitters to different efferent pathways has been observed previously in spinal cord motor neurons, which release only acetylcholine onto some cell targets, but acetylcholine and glutamate on others (Nishimaru et al. 2005). If single r2-*Pet1* neurons produced neurochemically distinct collaterals, this would imply complex regulation of translation or trafficking of proteins/mRNA associated with 5-HT vs. glutamate release to different axons.

The question of whether single r2-*Pet1* neurons send neurochemically distinct projections to innervate different target regions could be assessed by several different experimental means. For example, injection of multiple different fluorescent retrograde tracers into regions with wholly distinct neurochemical phenotypes (such as the suprachiasmatic nucleus of the hypothalamus and hippocampus) could reveal if single r2-*Pet1* neurons send

collaterals to both regions. Analogous experiments have revealed ~11% of median raphe neurons send collaterals to both the medial septum and hippocampus (McKenna and Vertes 2001). Alternatively, retrogradely transported adeno-associated virus (AAV) expressing a fluorophore could be injected into a single region with homogenous r2-*Pet1* bouton neurochemical phenotype, such as VGLUT3$^+$-only cortical regions defined by work presented here. If injected into a transgenic mouse in which r2-*Pet1* boutons are labeled by a separate fluorophore, then the collaterals of r2-*Pet1* neurons that project to the AAV-injected region will be labeled with both fluorophores. This approach could be combined with neurochemical profiling to reveal if r2-*Pet1* neurons sending axonal projections to one region also send neurochemically distinct collaterals to other regions. Finally, sparse viral labeling of r2-*Pet1* neurons, accomplished via intersectional viral reporter injection, could be combined with whole-brain serial two-photon tomography (Oh et al. 2014; Feng et al. 2015) to view the projections of individual r2-*Pet1* neurons and chart whether collaterals are sent to regions previously characterized as having distinct neurochemical phenotypes. This latter approach could also be combined with immunohistochemistry of individual sections to query bouton phenotypes. Previous research has suggested that co-transmitting multiple neurotransmitters at specific synapses involved in recurrent feedback loops may stabilize their activity and promote signal integration (Nishimaru et al. 2005). Given the high interconnectivity of the septohippocampal system (Khakpai et al. 2013; Besnard et al. 2020), the 5-HT$^+$/VGLUT3$^+$ r2-*Pet1* boutons in the septum and ventral hippocampal CA3 may selectively stabilize this circuit's activity while other collaterals are deprioritized. Alternatively, segregation of different neurotransmitters to separate

collaterals may allow r2-*Pet1* neurons to simultaneously engage in multiple circuits each operating with different kinetics.

POTENTIAL FOR DIFFERENTIAL REGULATION OF R2-*PET1* NEURONS VS. OTHER *PET1* NEURONS BY 5-HT

Compared with other *Pet1* axons, r2-*Pet1* axons may represent 5-HT-insensitive super releasers of glutamate and/or 5-HT. The 5-HT autoreceptor 1b (5-HT1b, gene *Htr1b*) is expressed presynaptically on many 5-HT axon terminals and inhibits neurotransmitter release when extracellular 5-HT concentration is high (Tiger et al. 2018). However, our methods indicate that *Htr1b* is not expressed by r2-*Pet1* neurons (Okaty et al. 2015). Lacking 5-HT1b would suggest r2-*Pet1* neurons are less sensitive to 5-HT concentration near their axon terminals than other *Pet1* neurons. Lacking this feedback mechanism could permit r2-*Pet1* neurons to continue to release neurotransmitter even in a 5-HT-rich microenvironment that would typically prevent 5-HT release from many *Pet1* neurons. For example, at composite *Pet1* pericellular baskets, this differential sensitivity could allow r2-*Pet1* boutons to decouple their activity from that of nearby 5-HT-releasing *Pet1* axons, allowing for more independent regulation of each basket axon.

In regions like the septum and ventral CA3 within the hippocampus, the detection of r2-*Pet1* boutons co-positive for 5-HT and VGLUT3 suggests these boutons may possibly be 'super-releasers' of neurotransmitter via exploiting a vesicular filling synergy (Gras et al. 2008; Amilhon et al. 2010). The transporters VMAT2 and VGLUT3 that package 5-HT and glutamate into vesicles, respectively, act with complementary bioenergetics. Both utilize an electrochemical gradient produced by a proton pump to drive packing of neurotransmitter into vesicles (Eiden

and Weihe 2011; Herman et al. 2018). VGLUT3 depends on the positive membrane potential of the vesicle to pack negatively charged glutamate; as glutamate is added to the vesicle, this unequally dissipates the electrical component of the gradient more than the chemical (pH) component (Gras et al. 2008; Herman et al. 2018). Conversely, VMAT2 is an antiporter that sequesters positively charged 5-HT in vesicles by exchanging it for two protons (Parsons 2000; Eiden and Weihe 2011) thereby depleting the chemical (pH) gradient faster than the electrical gradient. VMAT2 and VGLUT3 then bioenergetically counterbalance each other, and action of both transporters on the same vesicles is thought to allow for packing more neurotransmitter molecules under a constant electrochemical gradient (Gras et al. 2008). In vesicles lacking VGLUT3 but having VMAT2, neurotransmitter packing is reduced as VMAT2 shifts vesicle pH to be more alkaline. Thus r2-*Pet1* boutons that are 5-HT$^+$/VGLUT3$^+$ may be capable of releasing more serotonin than serotonergic *Pet1* boutons lacking VGLUT3.

To fully understand neurotransmission at 5-HT$^+$/VGLUT3$^+$ r2-*Pet1* boutons, it will be important to examine boutons for the presence of the serotonin reuptake transporter SERT, which functions to remove extracellular 5-HT through active uptake (Baudry et al. 2019). *Sert* is expressed at low levels in r2-*Pet1*$^{Vglut3\text{-high}}$ neurons (Okaty et al. 2015), which we observe to project to the septum where many 5-HT$^+$/VGLUT3$^+$ r2-*Pet1* boutons comprise pericellular baskets (Senft et al. 2021). If SERT is absent from septal r2-*Pet1* 5-HT$^+$/VGLUT3$^+$ boutons, this would further promote and prolong high concentrations of 5-HT at the release site. However, this extracellular 5-HT could be taken up by nearby non-r2 *Pet1* boutons if they expressed SERT, which is common in the septum (Belmer et al. 2019). Internalized 5-HT could be added to intracellular neurotransmitter stores to increase the 5-HT available for release (Baudry et al.

2019). Suggesting potential far-ranging effects of 5-HT reuptake, studies have demonstrated retrograde transport of 5-HT from projection sites like the olfactory bulb back to the raphe (Azmitia 1999). 5-HT reuptake could be promoted further if the non-r2 *Pet1* axon terminals in composite baskets additionally express 5-HT1b, which can further enhance SERT function in conditions of high extracellular 5-HT (Hagan et al. 2012). Our prediction would be that while r2-*Pet1* septal pericellular baskets are likely $SERT^-$, in general other $5\text{-}HT^+$ or $5\text{-}HT^+/VGLUT3^+$ boutons contributing to baskets are likely $SERT^+$. *Pet1* neuron pericellular baskets may then be sites of convergence of axons with differential sensitivity to extracellular 5-HT and different neurotransmission properties.

TESTING INTERACTIONS BETWEEN NEURONAL PERICELLULAR BASKETS

We have described composite pericellular baskets comprised of *Pet1* neuron axons from different rhombomeric lineages. To determine how often *Pet1* neuronal pericellular baskets are a product of one vs. multiple *Pet1* neurons, a similar approach can be used to map the topology of *Pet1* neuron composite baskets throughout the septum as well as other regions, like the cortex and hippocampus. This mapping can be combined with neurochemical phenotyping to identify regions where individual cells likely receive complex input from *Pet1* neurons. Identifying regions with high numbers of composite pericellular baskets can also aid subsequent electrophysiological experiments investigating the effects of manipulating axons from different *Pet1* neuron lineages on the activity of the basket-targeted cell.

In composite pericellular baskets, it is possible that *Pet1* axons may interact with one another. For example, it is possible that neurotransmitters released from one *Pet1* axon terminal

bind receptors on a separate *Pet1* axon to modulate release probability in an axo-axonic manner. This could be accomplished via volume transmission of 5-HT that then binds presynaptic 5-HT receptors such as 5-HT1b (as described above) at axo-axonic appositions, which are relatively common for serotonin neuron terminals in regions like the striatum, cortex, and hippocampus (Cover and Mathur 2021). Alternatively, glutamate-releasing *Pet1* boutons could make axo-axonic synapses or appositions on serotonergic axons in baskets, releasing glutamate onto presynaptic NMDA receptors, which have been shown to facilitate neurotransmitter release in noradrenergic and dopaminergic synaptosomes (Duguid and Smart 2009). Whether multiple *Pet1* axons comprising a pericellular basket closely appose each other could be examined through electron microscopy or array tomography. These techniques could be used to generate high resolution images of pericellular baskets with *Pet1* neuron axons labeled differentially by rhombomeric lineage. These connections could be explored functionally via expression of fluorescent neurotransmitter sensors such as GluSnFR (Marvin et al. 2013) or $GRAB_{5\text{-}HT}$ (Wan et al. 2021) in the *Pet1* neuron type putatively receiving glutamate or 5-HT, respectively. The sensor-expressing terminals can then be imaged while stimulating the other, putative upstream *Pet1* neuron type (e.g., optogenetically). Increased fluorescence is indicative of stimulation-evoked neurotransmitter release onto the sensor-expressing *Pet1* neuron axons (Cover and Mathur 2021).

Similar experimental techniques can be used to test whether *Pet1* pericellular basket inputs exert opposing or synergistic effects on the basket-targeted neuron. Cells encased by baskets can be queried for their responsiveness to a battery of serotonin and glutamate receptor agonists and antagonists to establish what receptors are likely expressed and the

effects of their activation on postsynaptic cell excitability. Further, optogenetically stimulating different *Pet1* axons contributing to composite baskets can be accomplished via virally-mediated intersectional expression of channelrhodopsin (Fenno et al. 2014). This stimulation can be combined with *ex vivo* whole-cell patch clamp recording of basket-encased neurons to explore the effect of *Pet1* basket neurotransmission on the postsynaptic neuron. These experiments could be combined with various receptor blockers and micro-iontophoretic application of neurotransmitter to isolate the receptors and currents responsible for the observed effects.

Finally, it is possible that *Pet1* and non-*Pet1* septal pericellular baskets also interact with each other. This can be explored first by mapping their distributions relative to each other in the same tissue. Given their broadly similar distributions, likely candidates for overlap with *Pet1* pericellular baskets include dopaminergic, enkephalinergic, and VGLUT2-labeled baskets (Köhler et al. 1982; Gall and Moore 1984; Beauvillain et al. 1991; Riedel et al. 2008; Szőnyi et al. 2019b). Though the serotonergic *Pet1* and dopaminergic systems are known to bi-directionally interact (Niederkofler et al. 2015; Wang, Zhang, et al. 2019; Lyon et al. 2020), it is unknown whether pericellular baskets are convergence points between dopaminergic and serotonergic systems. It is also possible that *Pet1* neuron pericellular baskets across the septum encase different cells than other septal afferents forming pericellular baskets. This result would suggest a high degree of target specificity for each neurotransmitter system forming baskets, potentially correlated with molecular differences in their cellular targets.

GENERALIZING FINDINGS TO OTHER *PET1* CELLS WITH A 'PARTIAL' SEROTONERGIC PHENOTYPE

Rhombomere 2 is not the only progenitor compartment to give rise to a subset of *Pet1* neurons that are *Tph2*^{low} in the adult brainstem. scRNAseq and *in situ* hybridization data from our lab suggests such cells also arise from rhombomeres 4 and 5 (Okaty et al. 2015; Chang and Dymecki, unpublished data). Some of these cells also exhibit variable expression of other serotonin neuron identity genes in the adult brain and have mixed expression of *Vglut3*. Though the majority of r2-*Pet1* neurons appear putatively glutamatergic and not serotonergic, this is potentially not the case for all *Pet1* neurons with a 'partial' serotonergic phenotype. Some appear equipped to release GABA, as evidenced by expression of *Gad1* and *Gad2*, encoding enzymes synthesizing GABA, and *Vgat*, the vesicular GABA transporter (Okaty et al. 2015), though GABA/5-HT co-transmission has not yet been reported (Johnson 1994; Okaty et al. 2019). Other *Tph2*^{low} *Pet1* neurons express *Penk*, encoding enkephalin. It is thus likely that multiple other neurotransmitters besides glutamate may be utilized by *Pet1* neurons, either in addition to or instead of 5-HT. Future research profiling neurochemically and mapping the projections from these various *Tph2*^{low} groups will help to resolve how these other 'partial' serotonin neurons organize their projections and neurotransmission properties. It is possible that other putative glutamatergic *Pet1* neurons may exhibit similarities to r2-*Pet1* neurons, such as in targeted regions or the formation of pericellular baskets. Alternatively, they may form subsystems with more similarities to serotonergic neurons arising from their rhombomeric lineage or divergent subsystems altogether with wholly unique hodology. Resolving this circuitry

will inform our understanding of how the efferent pathways of the brainstem raphe nuclei are organized to perform many distinct functions.

Conclusion

We have demonstrated the presence of two hodologically and neurochemically distinct subsystems within the r2-*Pet1* rhombomeric lineage, each equipped to regulate different downstream circuitry. A *Tph2*^{high} group innervates the suprachiasmatic nucleus, olfactory bulb, and paraventricular nucleus of the thalamus, implying potential functional roles regulating circadian rhythm. In contrast, a *Vglut3*^{high} group innervates the hippocampus, cortex, and septum, suggesting they may modulate memory, emotional processing, and sensorimotor gating. Finally, this latter cell type also sends axons comprising pericellular baskets to certain target regions, implying them to be critical regulators of those targeted cells. This work is important because it extends our understanding of *Pet1* neuronal diversity and elucidates how median raphe *Pet1* neurons organize their axonal projections to subserve different functions. Given the conservation of the serotonergic system across mammals, and the presence of *Tph2*^{low} *Vglut3*^{high} *Pet1* neurons in the human brainstem (Chang and Dymecki, unpublished data), the circuitry and projection pathways described here likely also apply to humans. The modulation of r2-*Pet1* neurons and similar *Tph2*^{low} *Vglut3*^{high} *Pet1* neurons may then have implications for human health, such as in regulating emotional processing and memory.

APPENDIX 1.

BEST PRACTICES AND TOOLS FOR REPORTING REPRODUCIBLE FLUORESCENCE MICROSCOPY METHODS

Authors and Contributions

This appendix chapter includes work I collaborated on that was published in Nature Methods as Montero Llopis, Senft… et al., 2021 "Best practices and tools for reporting reproducible fluorescence microscopy methods" PMID: 34099930.

***Author contributions**: The manuscript was written by Drs. Paula Montero Llopis, Lisa A. Cameron, and Michelle S. Itano. I designed and made the MicCheck app described in the paper that suggests minimal fluorescence microscopy metadata for reporting in materials and methods sections based on the specifics of a user's microscope and experimental design. Drs. Guillermo Marqués, Mark A. Sanders and I contributed to editing the manuscript and I wrote a portion related to MicCheck. Ryan Stephansky, Drs. Tim J. Ross-Elliot, Daniel P. Keeley and Paula Montero-Llopis generated data and figures for the paper. Drs. Michelle S. Itano, Daniel P. Keeley, Preman Koshar, Thomas Pengo, Benjamin R. Carlson, and Ya-Sheng Gao contributed to formatting and organization.*

Abstract

Although fluorescence microscopy is ubiquitous in biomedical research, microscopy methods reporting is inconsistent and perhaps undervalued. We emphasize the importance of appropriate microscopy methods reporting and seek to educate researchers about how microscopy metadata impact data interpretation. We provide comprehensive guidelines and resources to enable accurate reporting for the most common fluorescence light microscopy modalities. We aim to improve microscopy reporting, thus improving the quality, rigor and reproducibility of image-based science.

MAIN

The development of new technologies and tools in light microscopy has had an important role in making biomedical research more quantitative and interdisciplinary. This allows researchers to tackle more challenging scientific questions and obtain a more in-depth understanding of complex biological systems. However, with the rapid deployment of many new technologies, it is difficult for researchers to maintain in-depth knowledge of their capabilities and limitations. In addition, it is not always clear to users of advanced imaging techniques how specific limitations in hardware and software configurations for each modality might lead to errors that could affect scientific conclusions and reproducibility. Accordingly, the methods section of a publication requires complete and accurate information on the imaging conditions used to allow experimental replication. However, Marqués et al. (Marqués et al. 2020) recently showed that lack of detail in describing image acquisition is a widespread problem in biomedical publications, especially when considering that imaging is critical in biomedical research.

Many publications focus on guidelines to successfully perform a microscopy experiment, including sample preparation, method validation and appropriate controls to ensure reproducibility (Jost and Waters 2019; Jonkman et al. 2020; Kiepas et al. 2020; Wait et al. 2020). However, there are still few resources to guide and assist researchers in writing rigorous and reproducible microscopy methods. This Perspective focuses on filling this need by proposing minimal guidelines to ensure rigor and reproducibility in fluorescence light microscopy.

SCOPE OF THE GUIDELINES

The scope of this Perspective is to emphasize the importance of appropriate microscopy methods reporting and help educate researchers about microscopy components and parameters that impact data and conclusions. We showcase examples to demonstrate and highlight errors that can arise from insufficient reporting and provide resources to assist researchers with this task: an educational poster (Extended Data Figure A1.1), comprehensive checklists (Supplementary Exhibits 1–4) and a customizable checklist-generating tool, MicCheck (Supplementary Exhibit 5). These guidelines are in line with the tier-based system developed in the OME-4DN project for metadata collection to ensure consistency across the microscopy community (Hammer et al. 2021).

The checklists and MicCheck enumerate and describe in detail the essential and recommended metadata for the most common fluorescence light microscopy applications: widefield, laser scanning (confocal and multiphoton) and spinning disk confocal experiments, for live and fixed samples. The essential, or minimally required, metadata are critical for the correct interpretation of microscopy data and must be reported to ensure rigor and reproducibility. The recommended metadata represent best practices, particularly when using custom-built microscopes and nonstandard image acquisition strategies, but these may not substantially impact the conclusions that may be drawn. Finally, we include a list of resources and initiatives to improve image-based reproducibility and a list of definitions for many of the terms discussed in this Perspective (Supplementary Tables A1.1 and A1.2) that can serve as a reference for more novice microscopy users.

We intend these materials to be generally appropriate for many of the most common light microscopy configurations and applications (Reigoto et al. 2021) but encourage researchers

to use their own discretion and apply the recommendations as appropriate for their specific application and imaging system.

Guidelines on reporting instrument metadata

Illumination, light collection and wavelength selection

Illumination is critical to assess (1) how efficiently a fluorophore will be excited, (2) the relative illumination intensity for each fluorophore, (3) how reproducible intensity measurements are over time, (4) the probability of excitation cross-talk and (5) the compatibility of excitation filters (Mubaid et al. 2019). How the excitation and collection of light from fluorophores is achieved can vary widely. Thus, the choice of hardware used to illuminate the sample and to collect the fluorescence signal emitted from the fluorophores will have a profound effect on data interpretation and the ability to make meaningful comparisons between datasets (Box A1.1). Specifically, the light source and the excitation and emission wavelength bandwidth and hardware (for example, the excitation filter and dichromatic mirror) used are essential metadata. The power density (irradiance) at the sample impacts the excitation efficiency of fluorophores, the photobleaching rate and the cumulative amount of light that can be collected from the sample during acquisition. While irradiance is critical for reproducibility and ideally should be carefully documented, it is challenging to measure, requiring dedicated tools and protocols (Box A1.1).

The signal that can be collected is determined by the hardware used. Well-matched filters produce brighter fluorescence at shorter exposures or lower excitation light intensities and improve overall detection, signal-to-noise ratio (SNR) and downstream data analysis. Under

otherwise identical imaging conditions, the SNR of the fluorescent foci and membrane localization of the fusion protein in Figure A1.1a are below the detection threshold using an emission filter that is not well matched to the fluorophore. This will lead to conflicting results if not well documented. Additionally, the sample requires higher illumination intensity to excite and detect the appropriate fluorescence signal to determine the localization pattern. This can impact photobleaching and affect the health of the sample, which in turn could affect the localization pattern, leading to irreproducibility.

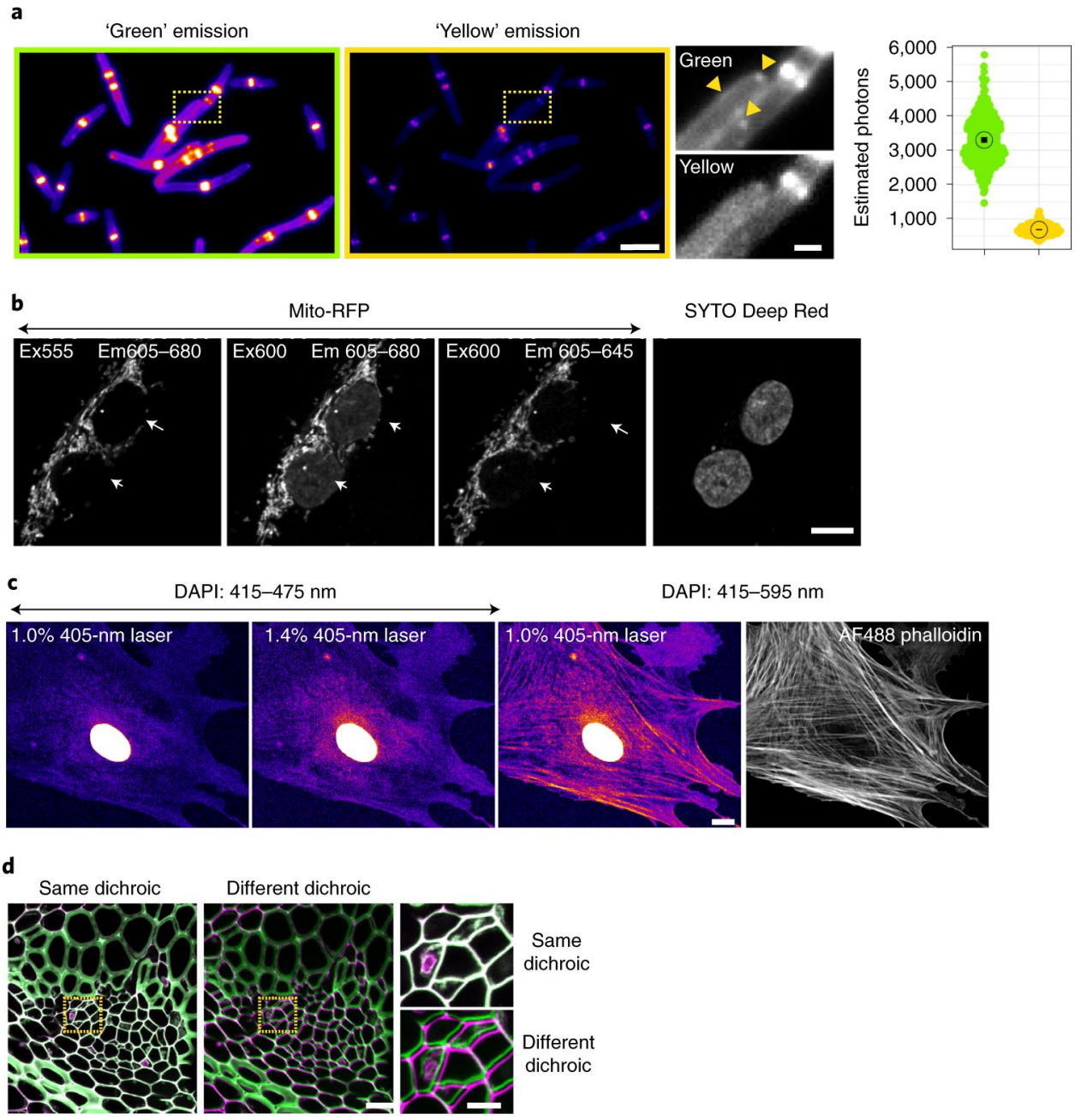

Figure A1.1. Illumination and wavelength selection impact signal detection, image quality and cross-talk between channels.

a, Fluorescence images (using Fire LUT) of *Escherichia coli* cells expressing ZipA–sfGFP acquired under identical acquisition settings and excitation wavelengths with different emission filters. Left, the emission filter is well matched to sfGFP ('green'; Semrock FF01-515/30). Center, the emission filter is less well matched to the fluorescence filter ('yellow'; Semrock FF01-544/24). The yellow arrowheads indicate localization at the membrane and discrete foci. Right, violin plots of the fluorescence intensity of individual images. Encircled dots indicate the population mean ('green', *n* = 432 cells; 'yellow', *n* = 432 cells). Scale bars, 5 µm and 1 µm (magnification). **b**,

(Figure A1.1 continued)
Fluorescence images (using a grayscale LUT) of U2OS cells expressing Mito-RFP and labeled with SYTO Deep Red (nuclei) acquired with excitation at 555 nm (left) or 600 nm (center left) and emission collected from 605–680 nm. White arrowheads indicate SYTO Deep Red nuclear emission signal collected. Center right, same as in center left but with emission collection adjusted down to 605–645 nm, which almost completely removes the SYTO Deep Red cross-talk, indicated by white arrowheads. Right, SYTO Deep Red image. Scale bar, 10 µm. **c**, Fluorescence images (using a Fire LUT) of BPAE cells stained with DAPI and Alexa Fluor 488 phalloidin (right) imaged using a narrow-bandpass emission range of 415–475 nm (left and center left) or a broad-bandpass emission range (center right). Center left, same as in left but with higher laser intensity. Scale bar, 10 µm. **d**, Two-color fluorescence imaging of *Convallaria* using a single multi-bandpass dichroic mirror for both channels (left) or a different dichroic mirror for each channel (center). Overlay images are pseudocolored green (488-nm excitation) and magenta (561-nm excitation). White indicates overlap between the two signals. Right, magnified views show the extent of *xy* shift between the two images using the same (top) or different (bottom) dichroic mirrors. Scale bars, 25 µm and 5 µm (magnification).

In multicolor imaging, in which the excitation and emission spectra of the different fluorophores may be partially overlapping, the appropriate selection and documentation of excitation and emission wavelengths (Supplementary Table 1) is critical to spectrally separate and quantify signals in different channels. In Figure A1.1b, the localization pattern and intensity of the Mito-RFP signal differ depending on the excitation wavelength used. Using 600-nm light to illuminate the sample results in an erroneous localization pattern and intensity levels, as they are partially due to cross-talk from a different fluorophore in the sample (nuclear SYTO Deep Red). This cross-talk can be minimized by illuminating the sample with 555-nm light. Figure A1.1c shows that using a narrow-bandpass emission range minimizes cross-talk between two channels (compare center right and left), even when the laser intensity is increased to improve SNR (center right). These examples highlight the need for appropriate controls to evaluate the extent of cross-talk between channels in multicolor experiments and how the lack of documentation of excitation and emission wavelengths may lead to irreproducibility.

Experiments in which multiple fluorophores need to be acquired simultaneously or with little temporal or spatial shift between channels (for example, ratiometric imaging and colocalization experiments) require the use and documentation of specific hardware to minimize chromatic shift (Box A1.2). This shift may be due to an improper angle of mounting for dichroic mirrors and imperfections on their thin-film interference coatings or to poor instrument calibration. Channel misregistration greatly impacts the conclusions from colocalization experiments and experiments aimed at quantifying distances between objects or intensity ratios between channels (Figure A1.1d). Controls are critical in assessing the extent of chromatic shift and correcting it (North, 2006; Stack et al., 2011; Waters, 2009; Box A1.2 and Supplementary Table 1).

Box A1.1. Irradiance and quantitative fluorescence

Irradiance, or illumination power density (W cm^{-2}) at the sample, determines the excitation efficiency of fluorophores and impacts the photobleaching rate and the cumulative amount of light that can be collected from the sample during acquisition. The total irradiance at the sample plane depends on the light source, the hardware to select excitation wavelengths, the objective lens and the modality (Patterson and Piston 2000; Wang et al. 2005).

If quantitative fluorescence intensity measurements are required, a more stable light source is advisable. Laser-based illumination usually results in higher irradiance than other types of illumination, as the light is coherent and typically has higher illumination power intensity than with other light sources. How modulation of the laser power is achieved also impacts irradiance. For example, a directly modulated laser with 100-mW power output at the optical fiber tip will have higher irradiance than the same power output in a laser modulated through an AOTF, as this tunable filter results in a loss of light of approximately 40–50% (P.M.L., unpublished observation). How focused the laser light is (objective numerical aperture) will also determine the irradiance at the sample. When comparing and choosing a laser power output configuration for an imaging system, it is important to note that different manufacturers report the laser output differently. Some report power output directly at the source, while others report it at the tip of the optical fiber just before light enters the confocal scanner or the microscope.

(Box A1.1. continued)

The light power can be adjusted in the acquisition software (often with a label indicating 'laser power'), but this adjustment may not be linear. The power should not be interpreted to indicate an exact percentage of the laser power output because of loss of light across optical surfaces on the way to the sample.

The importance of irradiance in reproducibility

Irradiance varies substantially with microscopy modality. In the case of single-point scanning confocal microscopy, the laser beam is focused into a single spot (whose size depends on the objective lens used) and therefore corresponds to higher irradiance than with other modalities such as spinning disk microscopy, where the laser is collimated and illuminates the entire field of view (Patterson and Piston 2000). Photobleaching, phototoxicity and fluorophore saturation (when most fluorophores in the sample are in the excited state and there are therefore no molecules to absorb new photons) are also greatly impacted by irradiance and are a source of variability and irreproducibility.

While irradiance influences fluorophore excitation efficiency and photobleaching, considering its impact on sample health is critical to obtaining reproducible and biologically meaningful results. Light can induce DNA damage and oxidation of cellular components (Icha et al. 2017; Kiepas et al. 2020). In addition to these damaging effects, fluorophore photobleaching further affects sample health by generating free radicals and other reactive species (Onukwufor et al. 2020). Together, these aspects will negatively impact cellular function and health. The extent of light-induced damage depends on the amount of light that the sample is subjected to, sometimes referred to as 'light overhead' (Schmidt et al. 2020). While breaks between consecutive periods of illumination may allow for partial recovery, the effects of photodamage are cumulative (Nishigaki et al. 2006; Hoebe et al. 2008). The effects of excess illumination before starting the image capture routine (for example, while navigating and focusing through the eyepiece of the microscope) or during a time-lapse experiment (excess illumination or illumination overhead) will vary between instruments and can contribute to variability in sample health and photobleaching, resulting in irreproducibility.

Every effort should be made to minimize fluorescence excitation exposure before the experiment is acquired and to limit it to the specific time of the image capture needed to collect data (Magidson and Khodjakov 2013). Other sources of illumination overhead include the time period of shutter opening and closing controlled by acquisition software, asynchronization between camera acquisition and illumination, stage movement during a *z*-stack acquisition and even environmental light exposure during sample storage.

The challenges of measuring irradiance

(Box A1.1 continued)

Thus, irradiance is a critical aspect and needs to be as consistent as possible between imaging sessions, especially when measuring intensity or when conducting live-cell imaging.

Providing information on the irradiance used in a particular experiment would greatly improve reproducibility. However, providing an accurate irradiance measurement at the sample presents several challenges. (1) This requires tools that most researchers or laboratories may not have available, such as optical power meters. Some power meters include a sensor area that fits on the stage, replacing the sample, thus enabling light intensity measurements at specific wavelengths at the sample plane. (2) Illumination overhead can be difficult to account for or to measure from the metadata. (3) There is a lack of standardization in the protocols used to collect irradiance measurements, leading to irreproducibility. Working group 1 of Quality Assessment and Reproducibility for Instruments & Images in Light Microscopy (QUAREP; Illumination Power) consists of an international team working on the development of standard procedures to measure and standardize irradiance measurements and will seek input and consensus from the global community (Nelson et al. 2021).

While irradiance measurements are challenging to perform properly, it is still advisable to routinely monitor light intensity in a particular instrument to evaluate potential sources of variability and imprecision.

To measure irradiance at the sample, the illuminated area needs to be measured. In widefield or spinning disk systems, this can be done by bleaching an area in a uniform sample and collecting an image with a lower-magnification lens to measure the bleached area. The sample can even be created using a fluorescent highlighter pen to mark the bottom of a sample carrier. In single-point scanning microscopes, the size of the laser spot can be measured using the reflection mode and a spot scan.

We encourage researchers to connect with core facilities or other imaging scientists at their institution for assistance, as these groups often have the tools and protocols to assist in measurement and monitoring of illumination intensity.

Box A1.2. Method validation considerations.

Validating the methodology used in an experiment is critical for reproducibility, as it ensures that the measurements obtained reflect the biological process under study and are not artifacts due to the performance of the microscope. Thus, a careful assessment of the capabilities, limitations and performance of a particular microscope is essential to ensure rigor and reproducibility. Here we describe some selected procedures and measurements that should be considered when designing microscopy experiments. Supplementary

(Box A1.2. continued)

Table A1.1 contains a list of selected reagents and resources to perform these tests, in addition to selected ongoing microscopy initiatives that are currently focusing on building resources.

Assessing microscope resolution. The point spread function (PSF) represents how a particular microscope affects light emitted from a single point. As light travels through the sample and the apertures within the microscope, including the objective, it diffracts, or spreads in space. The image of this point of light will consist of a central Gaussian spot surrounded by concentric diffraction rings of lower intensity. The PSF can be used to determine the resolving power of the system, in xy and z, and how sample preparation can affect the performance of the microscope as well as to anticipate limitations in the experimental design. A sample of fluorescent beads with a diameter of approximately 100 nm can be used to collect a PSF image with a high-NA lens, as the beads serve as a point source of light. Of note, however, these beads tend to clump together, and, because they are diffraction limited, it may not be obvious during imaging that the collected PSF corresponds to more than one bead, resulting in an underestimate of the system's resolution. Thus, the stock solution needs to be vortexed and sonicated, and the brightest spots in the images should be avoided during PSF analysis. The full width at half-maximum intensity (FWHM) of the PSF in xy and z from individual beads provides a quantitative measurement for the resolution achievable (Cole et al. 2011). PSFj is an excellent open-source tool to quantitatively evaluate many aspects of the PSF (Theer et al., 2014; https://github.com/cmongis/psfj). Additionally, study 3 from the Association of Biomolecular Resource Facilities (ABRF) Light Microscopy Research Group (LMRG) focuses on producing reliable and reproducible protocols for measuring the PSF (https://www.abrf.org/light-microscopy-lmrg-).

Adjusting a correction collar. Variation in coverslip thickness or mismatch in refractive index in the sample results in spherical aberration that compromises axial resolution and signal intensity. Some lenses are designed with a correction collar to make fine adjustments to minimize spherical aberration. Correction collar adjustment can be tricky and cumbersome, especially in inverted microscopes, as access to the objective and correction collar is limited to the space between the nosepiece and the stage. New advancements in this arena include motorization and software control of the correction collar to allow for more precise and reproducible adjustments of the settings. Any bright structures within the sample can be used to adjust the correction collar. The ideal shape of a PSFz is similar to an hourglass, with symmetrical diffraction patterns above and below the central focal plane. In the eyepiece, this would appear as concentric diffraction rings of similar size above and below the plane where a bead is in focus. In the case of spherical aberration, the shape of the PSFz would no longer be symmetrical and the diffraction rings would only be apparent when defocusing in one direction. Slowly rotating the correction collar in either direction

(Box A1.2. continued)

while examining the symmetry of the PSF with each change will help in adjusting the correction collar appropriately. Alternatively, the sharpness and overall intensity of an image can be examined before and after rotating the correction collar. The image will be sharpest and produce the brightest intensity when spherical aberration is minimized.

Assessing axial chromatic aberration. Chromatic aberration greatly impacts conclusions and measurements in 3D multicolor experiments. It can be due to the type of correction within the objective lens and/or to a mismatch in refractive index between the immersion medium and the sample mounting medium that results in different spherical aberration according to wavelength (for example, dispersion). Assessment of the extent of any axial shift between channels is essential to validate colocalization and distance measurements between objects, especially when their size is diffraction limited. TetraSpeck microspheres, which are stained with four different fluorescent dyes, gold beads, which are autofluorescent over a broad range of different wavelengths, or staining of the same target with two different fluorophores within a sample can be used to evaluate chromatic aberration. Ideally, these samples should be prepared in the same sample carrier, with the same coverslips and mounting/imaging media as for the sample and with the same image acquisition settings as in the multicolor experiment (for example, acquiring every wavelength in each focal plane). Image acquisition software may enable correction of chromatic aberration during acquisition if the mismatch in refractive index is known. Alternatively, this shift can be corrected after acquisition using different algorithms (Diel et al. 2020).

Assessing xy chromatic shift (channel registration). Registration or chromatic shift may be introduced by the optics, hardware selection (for example, multiple dichroic mirrors or filters not correctly set in the filter cube), relevant device precision (for example, stage movement), pinhole and collimator alignment, and the extent of instrument calibration (Waters 2009; Hodgson et al. 2010; Onukwufor et al. 2020). Of note, chromatic shift introduced by the optics may not be consistent across the field of view and the location of the objects/sample to measure could introduce bias and irreproducibility in the measurements. TetraSpeck beads and other fiducial markers, such as gold beads and commercial calibration slides (for example, ArgoLight, GATTAquant or DNA-PAINT 80R nanoruler slides), are useful to assess and correct for possible chromatic shift. There are a number of both open-source and proprietary algorithms that enable alignment and correction of this shift. Importantly, the algorithms used to correct this shift may also introduce image warping aberrations and require careful validation using a known sample before application to a raw image.

Assessing cross-talk. Even when fluorophores and filter sets are carefully chosen, cross-talk remains one of the main concerns in both single- and multicolor imaging because it can result in erroneous interpretation of the results (Frigault et al., 2009; Jost and Waters, 2019;

(Box A1.2. continued)

Kraus et al., 2007; Lee and Kitaoka, 2018). Unlabeled controls and singly labeled controls (in which the sample is labeled with each individual fluorophore or expresses each individual fluorescent protein) are used to determine the extent of excitation and emission cross-talk between channels. They serve to validate the selected hardware and acquisition settings to minimize cross-talk or can be used to calculate parameters to correct for any observed cross-talk.

Assessing and correcting evenness of illumination (flatfield). In most systems, illumination is not even across the field of view. This nonuniformity results in differences in fluorescence intensity that do not reflect the biology of the sample. Uneven illumination needs to be measured and, if necessary, corrected (shading or flatfield correction). Of note, errors can be introduced for subsequent measurements when applying a flatfield correction, so this processing step needs to be validated and evaluated. Slides containing high concentrations of quenchable fluorescent dyes such as fluorescein or Rose Bengal are ideal to determine the illumination pattern and collect a flatfield correction image (Model 2006; Model and Blank 2008). The quenching properties of these dyes ensure that a thin and even section is illuminated. This is critical in widefield systems because differences in the thickness of a fluorescent slide will result in an apparent change in intensity that is not due to the illumination pattern and can therefore introduce errors when correcting the raw data. In other modalities, fluorescent plastic slides (for example, Chroma) can be used. These slides are very bright, so it is recommended to use an illumination wavelength that is not optimal to minimize the intensity (for example, use a Red slide to assess the illumination pattern of the green channel). In most single-point scanning confocal microscopes, illumination uniformity can be maximized by carefully adjusting the alignment of the collimator and pinhole. While such adjustments may not be accessible to most researchers, talking with vendors and imaging scientists can ensure that the system is properly aligned to minimize field nonuniformity.

Calibrating distances. The final pixel size in a digital image acquired on a digital camera depends on the size of the photodiode in the camera and the total magnification (objective, optovar and relay lens). The final pixel size in a digital image acquired with a PMT is based on the magnification of the objective, the area of the field of view scanned by the laser and the sampling interval of the PMT signal by the pixel clock. Careful calibration of the pixel size of the digital image can be achieved by imaging a micrometer ruler slide. A slide with a ruler with 0.01-mm-scale resolution etched into the glass can be used with different magnifications to calibrate distances (Wolf et al. 2013).

Photobleaching. Intensity measurements over time will be affected by photobleaching, even in the case of fixed samples, as the signal intensity will decrease over time as a result of fluorophore destruction and not the biology of the sample. The rate of photobleaching

(Box A1.2. continued)

varies with the fluorophore used, illumination intensity and illumination mode. Minimizing photobleaching during the experiment is strongly advised, even for fixed samples. Correction can be applied by obtaining decay curves and correcting the decay function on fixed samples. Validation of this function is critical to avoid overcorrecting or introducing additional errors (Diaspro et al., 2006; Jost and Waters, 2019; Vicente et al., 2007; ImageJ plugin CorrectBleach 2.0.2; https://zenodo.org/record/30769#.XIflKyhKg2w).

Objective Lenses

Objective lenses are essential for image formation and impact all aspects of imaging; thus, they are one of the most critical components that need to be reported. Magnification is an important aspect of digital microscopy, as it contributes to the size of the field of view and, for camera-based microscopes, the pixel size (spatial sampling). Many researchers understand this, and in most cases this aspect is documented. However, objective lenses possess other characteristics that have an even greater impact on image formation and must be reported for others to reproduce an experiment.

Objective lenses contain spherical surfaces that focus the light into the sample and collect emitted fluorescence to form an image. These curved surfaces create different types of aberrations (Keller 2006; Goodwin 2013; Ross et al. 2014). Manufacturers design objective lenses applying different aberration corrections depending on the intended application. These corrections are made assuming specific conditions such as coverslip thickness, refractive index of the medium used, temperature and illumination wavelengths. Some objective lenses are designed with correction collars, which allow for fine-tuning of the performance of the objective lens to compensate for sample-induced aberrations (Cole et al. 2011, 2013). Of note, however,

these aberrations are not completely eliminated. High-quality sample preparation is essential to ensure the best performance of any objective lens, and appropriate controls and corrections need to be applied for best practices (Jost and Waters, 2019; Lee and Kitaoka, 2018; North, 2006; Wait et al., 2020; Box A1.2 and Supplementary Table 1).

The aberration corrections in an objective lens will have a profound effect on the interpretation of the microscopy data collected. Using a highly color-corrected lens will provide more precise measurements in experiments quantifying relative distance in multicolor three-dimensional (3D) imaging or colocalization (Figure A1.2a). In the example provided, the extent of colocalization between channels depends on the objective correction, which, if not reported, could result in irreproducibility.

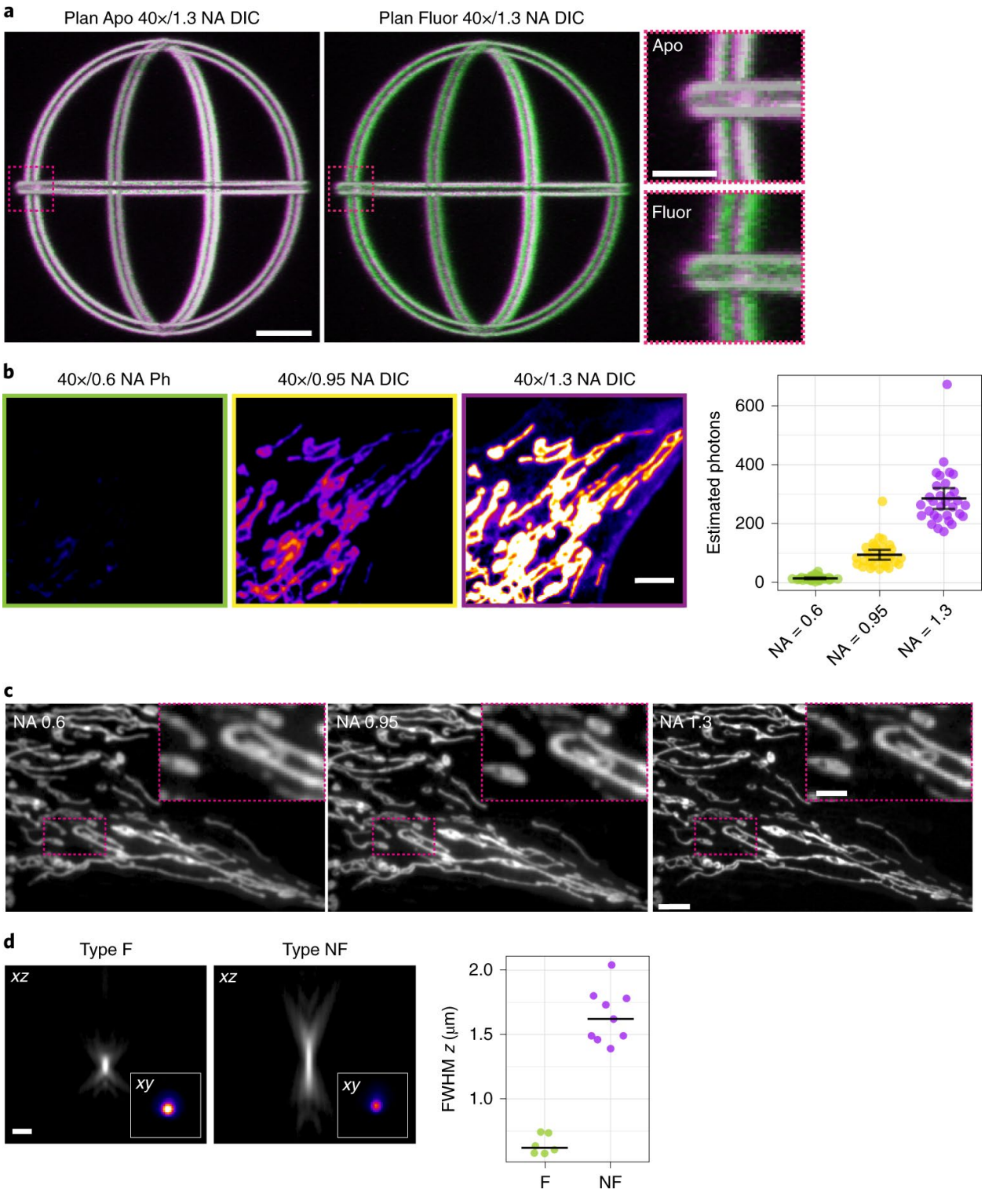

Figure A1.2. Objective lenses and immersion medium determine brightness and optical resolution and impact data interpretation.

(Figure A1.2 continued)
a, A 3D rendering of the 3D sphere pattern on the ArgoLight-SIM calibration slide acquired with two channels (488 nm, green; 561 nm, magenta) using either an Olympus Plan Apo 40×/1.3 NA DIC (left) or an Olympus Plan Fluor 40×/1.3 NA DIC (center) objective. Right, insets show the extent of overlap between signals (white). Overlay images are pseudocolored in green (488-nm excitation) and magenta (561-nm excitation). Scale bars, 5 µm. **b**, Fluorescence images (using a Fire LUT) of BPAE cells stained with MitoTracker Red CMXRos acquired under identical imaging conditions using a Plan Fluor ELWD 40×/0.6 NA Ph2 (left), a Plan Apo 40×/0.95 NA DIC (center left) or a Plan Fluor 40x/1.3 NA oil-immersion DIC (center right) objective. Images are displayed at the same brightness/intensity scale. Right, violin plots of fluorescence intensity quantification of individual regions of interest. Long black bars indicate the mean fluorescence intensity for each population, and vertical bars indicate the s.d. Scale bar, 5 µm. **c**, The same sample as in **b** imaged with the same objectives as in **b**. Acquisition was optimized for each objective to obtain high-SNR images. Insets in each panel demonstrate the difference in resolution obtained when using objectives with different NA. Scale bars, 5 µm (main panel) and 2 µm (magnification). **d**, Representative *xz* projections of *z* stacks obtained by imaging 100-nm fluorescent beads passively adhered to #1.5 HT coverslips and mounted with glycerol using a Nikon Plan Apo 100×/1.45 NA Ph3 objective with either Olympus Type F (left) or Nikon NF (center) immersion oil. Insets show the midplane displayed at the same scale using the Fire LUT. Right, dot plot illustrating the axial FWHM of individual beads quantified using the PSFj plugin when either the Type F or Type NF oil-immersion objective was used for imaging. The bars represent the population mean. Scale bar, 1 µm.

Numerical aperture (NA) is a critical characteristic of an objective lens because it indicates the amount of light that can be collected. Higher-NA lenses, under identical imaging conditions, produce brighter images than low-NA lenses (North, 2006; Waters, 2007, 2009; Figure A1.2b). A low-NA lens will require longer exposure times or higher excitation light intensities to detect the fluorescence signal, which will impact temporal resolution, photobleaching and/or phototoxicity, leading to irreproducibility. Most importantly, the NA, and not the magnification, determines the resolving power of the system. Consequently, the NA of the objective lens will determine whether two objects of interest can be resolved or even detected under certain conditions (Figure A1.2b,c). In the example, the high-NA objective lens

produces sharper and more resolved images, improving the detection and detail of individual mitochondria.

Objective lenses are designed to work with a specific immersion medium (for example, air, oil, silicone oil, water or glycerol). There are many types of immersion oil, which vary in viscosity, refractive index and dispersion under different conditions. The type of immersion medium affects the performance of an objective lens, by inducing or minimizing spherical aberration and sometimes introducing fluorescence background signal. Therefore, two different immersion oils may result in different axial resolution and overall brightness of the image, thus affecting the ability to resolve objects axially or to detect the object of interest (Figure A1.2d). The wrong immersion medium may also induce chromatic aberrations due to differences in dispersion (Diel et al. 2020). Even though the type of immersion medium is critical to performance of the objective lens, it is overlooked in most methods sections. This reporting is especially critical for multi-immersion objective lenses, which can be used with multiple immersion media.

Detector

The detector used is critical in all aspects of quantitative microscopy. It impacts the likelihood that the fluorescence signal will be detected (sensitivity and noise level), the temporal resolution (frame rate) and the spatial resolution (digital resolution) of the system (Murphy and Davidson 2012; Lambert and Waters 2014). As such, the choice of detector influences the capability to provide a conclusion faithful to the underlying biology. Thus, proper

documentation ensures that similar observations can be made and similar conclusions can be drawn in different systems or experimental replicates.

The digital resolution of the system determines the ability to resolve the object of interest and will influence the downstream analysis workflow. In camera-based systems, it is determined by the physical size of each photodiode (pixel) and the total magnification (Supplementary Exhibits 1-4). Data collected with two different cameras attached to the same microscope and acquired using the same objective lens can lead to fundamentally different interpretations of the results (Figure A1.3a). The camera with a large photodiode size (16 µm) cannot resolve the line pairs in the particular sample observed and instead creates a new pattern that does not correspond to the ground truth (aliasing). Pixel binning decreases the digital resolution and therefore must be reported (Murphy and Davidson 2012; Lambert and Waters 2014). Any additional magnification to the objective lens also needs to be reported to ensure measurement accuracy and precision, as this reduces light output (reduced SNR) and affects digital resolution (Supplementary Exhibits 1-4). In many cases, magnification changes are not accounted for in image calibrations and metadata, although not documenting them can lead to imprecision and irreproducibility in distance measurements (Box A1.2). This is true for any hardware component that is introduced manually into the lightpath, as it would not be recorded into the image metadata.

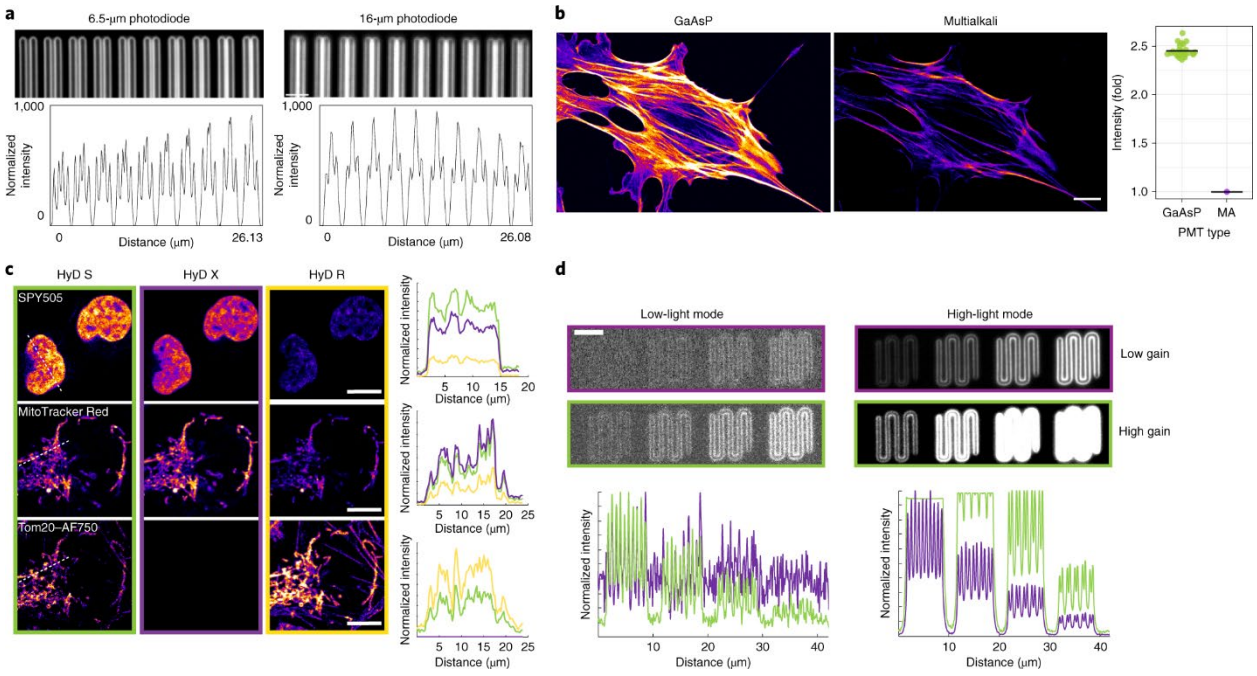

Figure A1.3. The sensitivity of detectors varies with wavelength and determines the digital resolution and image quality.

a, Fluorescence images of a pattern consisting of lines with incrementally increasing spacing on the ArgoLight-SIM calibration slide acquired with the same objective and a camera with either a 6.5-µm (left) or 16-µm (right) photodiode size. Lower row, line intensity profile plots. Scale bar, 2.5 µm. **b**, Fluorescence images (using a Fire LUT) of BPAE cells stained with Alexa Fluor 488 phalloidin acquired under identical imaging conditions with a single-point scanning confocal microscope using either a GaAsP (left) or multialkali PMT (MA; center) detector. Images are displayed with the same intensity scale. Right, fluorescence intensity quantification; bars represent the population mean. Scale bar, 10 µm. **c**, Fluorescence images (using a Fire LUT) of cultured cells prepared by Leica and imaged under identical conditions with a Leica Stellaris 8 Power HyD S (left column), Power HyD X (center-left column) or Power HyD R (center-right column) show a difference in intensity according to wavelength (right). Green, HyD S; purple, HyD X; yellow, HyD R. Scale bars, 10 µm. **d**, Fluorescence images of a pattern consisting of a repeating series of lines with progressively decreasing intensity (pattern C) on the ArgoLight-SIM calibration slide were acquired with an Andor Zyla sCMOS 4.2 plus camera under low-light conditions (left panels) or high-light conditions (right panels). Images were acquired under identical conditions in each case, with the exception of varying the amplifier gain amplification. Top left and top right, low gain; bottom left and bottom right, high gain. Bottom panels, plots of fluorescence intensities along a vertical line scan through the center of the pattern (purple, low gain amplification; green, high gain amplification). Scale bar, 5 µm.

Image quality and SNR are greatly impacted by the sensitivity (quantum efficiency, QE) and noise level of the detector. These specifications determine the probability of detection and minimal detectable signal. The peak QE of detectors varies widely22 (70–95% for cameras and 20–45% for photomultiplier tubes, PMTs). Under otherwise identical conditions, a more sensitive detector will detect more light, producing a brighter image (Figure A1.3b). Thus, the sensitivity and noise level of a particular detector will determine whether the signal can be detected at all and the dynamic range of the measurements, which in turn impacts their precision and accuracy. A less sensitive detector will require increased illumination intensity to detect the signal, which can induce photobleaching, fluorophore saturation and/or photodamage, leading to irreproducibility (Box A1.1).

Furthermore, the sensitivity of a detector varies with wavelength (Art 2006). Many systems are equipped with various types of detectors that offer different sensitivity at different wavelengths, such as in single-point scanning confocal and multiphoton microscopes. In the example provided in Figure A1.3c, a researcher using a HyD X detector (or another detector with similar specifications) to collect the emission of a near-infrared fluorophore would conclude that a protein of interest is not expressed in a particular cell type. Thus, the choice of detector in an experiment must be reported to ensure reproducibility.

The properties described above are inherent to a given detector; therefore, providing information on the specific manufacturer and model (for cameras) or the specific type of non-camera-based detector (for example, Multialkali PMT) will satisfy the minimal metadata requirements to ensure reproducibility. However, many detectors offer different acquisition settings that may affect the sensitivity, noise level and dynamic range of the detector, thus

impacting the ability to detect the signal of interest. These settings should be documented, as they will impact reproducibility.

The readout mode or digitizer of the detector and the bit depth are good examples of such settings that critically impact image acquisition. Many cameras and other detectors offer a choice of which digitizer (and associated gain) to use during acquisition, which can be optimized depending on the amount of light generated by the sample. Higher gain settings result in higher intensity levels per electron than lower gain settings. Under low-light conditions (that is, for dim samples), a high gain setting may improve signal detection in comparison to a low gain setting (Figure A1.3d). However, high gain settings also increase noise and reduce the dynamic range of the detector, so they are not ideal for bright samples as these samples will reach the saturation level sooner than when using low gain settings (Figure A1.3d). Some cameras enable charge amplification (electron-multiplied charge-coupled device, EM-CCD; (Lambert and Waters 2014), thereby improving the detection of very dim signals for applications including single-molecule fluorescence. Thus, researchers should specify the particular camera settings or readout modes used during acquisition.

Microscope stand and relevant motorized components

Microscopy experiments usually require the acquisition of multidimensional data (for example, multiple planes, positions, channels, time points, etc.). The microscope stand and peripheral motorized components required depend on the goals of the experiment and the sample used (Supplementary Exhibits 1-5). The precision of the motorized components and how the software manages the image acquisition workflow may significantly impact the conclusions

from the experiment, as they can introduce inaccuracies and limitations in measurements. Thus, knowledge of the hardware configuration and acquisition settings is required to collect precise, accurate and reproducible data. Consequently, the specifications of each component need to be verified as ideal for the application at hand, validated through appropriate controls (Box A1.2 and Supplementary Table 1) and accurately reported.

In multicolor experiments, the hardware used and whether the images are acquired sequentially or simultaneously will have a profound impact on several aspects of quantitative microscopy. Simultaneous acquisition will greatly increase the temporal resolution of the experiment but may also result in an increase in signal contamination between channels (Figure A1.4a). In this case, simultaneous acquisition would lead to erroneous results.

Figure A1.4. Data acquisition mode and instrument precision impact data reproducibility and interpretation.

a, Fluorescence images of BPAE cells stained with DAPI and Alexa Fluor 488 phalloidin acquired either simultaneously in the same track (center right and right) or sequentially in two different tracks (left and center left). Scale bar, 15 µm. **b**, Dot plots of the displacement between centroids of 1-µm beads imaged repetitively with two different translational precision settings of a Nikon linear-encoded motorized stage (green, open, lower precision setting; purple, precise, highest precision setting). Multiple *xy* positions were imaged repetitively over 15 loops. Bars represent the mean and s.e.m **c**, The *xyz* projections of TetraSpeck beads imaged by acquiring a *z* stack in each channel (left) or both channels in each focal plane of the *z* stack (center). Right, displacement plots of beads acquired using either the nosepiece Z drive (TiZ) or a PI piezo Z drive (piezo). Bars represent the mean and s.e.m. Scale bars, 2 µm. **d**, Fluorescence images of a *Convallaria* section showing the midplane (left) and *xz* and *yz* projections from *z* stacks acquired while varying the size of the *z* step (0.4 µm, 2 µm and 3 µm) (right). Scale bars, 10 µm. **e**, Same sample as in **a** imaged using a bidirectional scanning mode (left) or a unidirectional scanning mode (center). Inset images indicate a pronounced pixel shift in the image acquired using the bidirectional scanning mode when compared to the image acquired using the unidirectional scanning mode. Right, this shift can be corrected following calibration of the scanner. Scale bars, 5 µm (main panel) and 1 µm (magnification) . **f**, Same sample as in **a** acquired while varying the offset setting (top row, offset of 1.0 V (no offset); bottom row, offset of −118 V). Magnified views show processing steps to segment the mitochondria. Segmentation using images collected with improper offset settings results in identification of smaller objects (green arrowheads) and loss of objects (yellow arrowhead). Scale bars, 5 µm (main panel and magnification).

(Figure A1.4 continued)

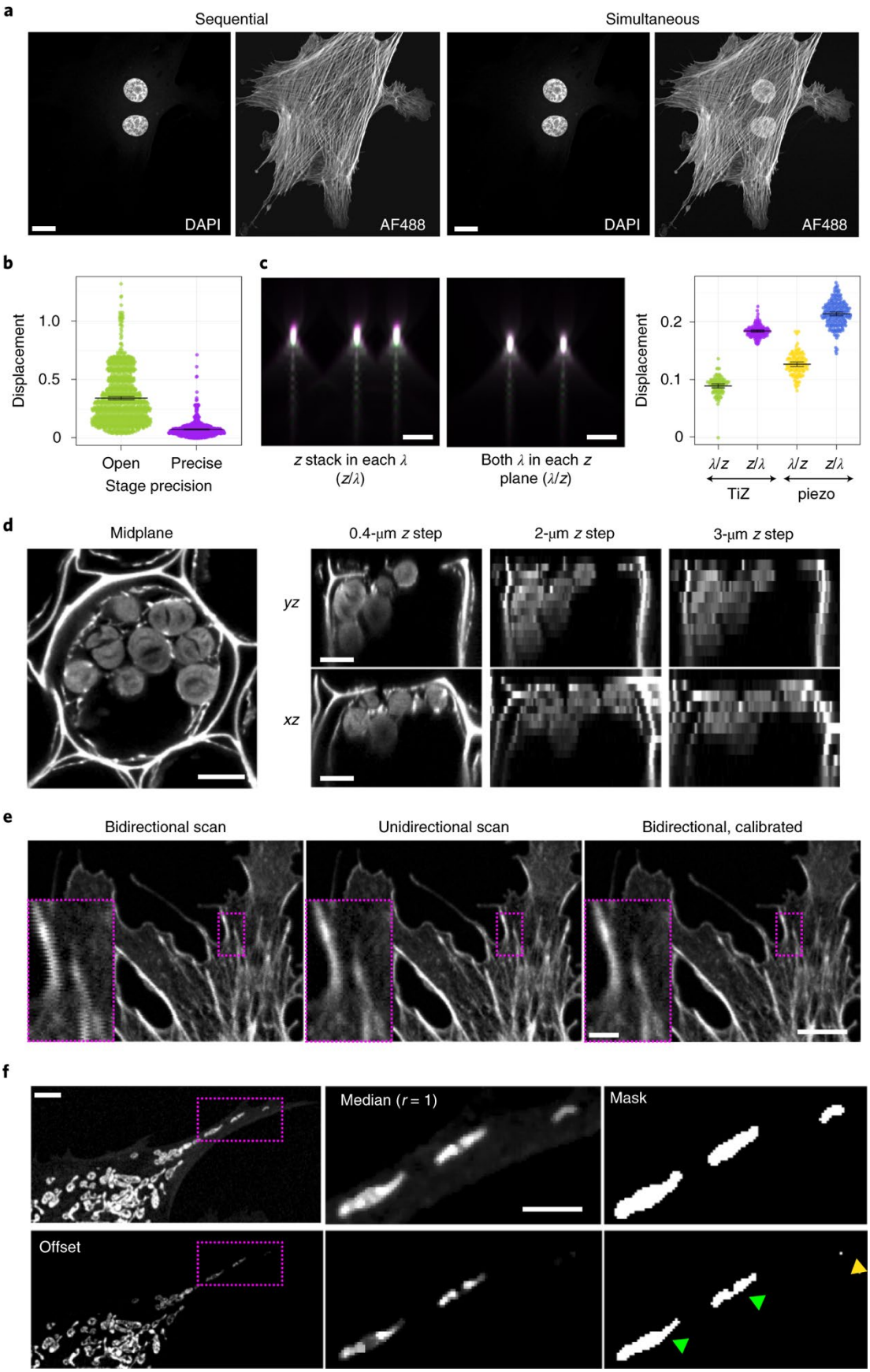

Experiments that rely on the repeatability of positions, such as those tracking moving objects in multiple positions over time, are greatly impacted by the speed and precision of the lateral movement of motorized stages. In some cases, these parameters can be changed in the software (Supplementary Materials) and overlooking and not documenting these settings will impact reproducibility. For example, the displacement between the centroids of stationary fluorescent beads imaged repeatedly in a multiple-position experiment can vary over fourfold depending on the precision settings of a motorized stage (Figure A1.4b). This also applies to the axial location of the beads when acquiring a *z* stack and will inevitably introduce error in the measurements (Figure A1.4c). Furthermore, the order in which the acquisition is performed in a multidimensional experiment (for example, multicolor and *z* stack) can also impact the results (Supplementary Materials). Acquiring a *z* stack of each wavelength instead of acquiring all the wavelengths at each *z* step can lead to higher imprecision. Therefore, consideration of the focusing device used and the order in which the data are collected is critical during experimental design and must be reported (Figure A1.4c and Box A1.2).

Furthermore, the *z*-step interval and total volume (and how it is selected) in a *z* stack are critical to resolve objects in the axial dimension and need to be specified and reported. Larger step intervals than required (undersampling) can result in insufficient axial resolution. This will compromise downstream analysis and the conclusions of the experiment (Diel et al., 2020; Figure A1.4d).

The success of a time-lapse imaging experiment depends on the ability to maintain focal and planar positioning and collect data at the appropriate temporal resolution and SNR to permit downstream image analysis without compromising the health of the sample. Irradiance is

one of the key factors that affect sample health, as it can induce phototoxicity (Box A1.1). The effects of phototoxicity tend to be underestimated or overlooked, even though they are critical to properly interpret the observations (Dixit and Cyr 2003; Magidson and Khodjakov 2013; Ettinger and Wittmann 2014; Icha et al. 2017; Kiepas et al. 2020). Implementing and reporting hardware and acquisition settings that reduce irradiance is critical to allow meaningful comparisons between experiments (Supplementary Exhibits 1-4). Notably, the nominal time interval set in the software may not be consistent with the actual acquisition time interval, which depends on the shutter speed, delays due to the electronics that drive the acquisition and the acquisition software used. However, the timestamp found in the image metadata is likely accurate and should be used for quantification. Additionally, the actual average time interval and standard deviation should be included in the methods reported in a publication.

GUIDELINES ON REPORTING ACQUISITION SOFTWARE

Modern microscope systems are connected to a computer and controlled by acquisition software, which can be commercially available (for example, NIS Elements) or open source (for example, μManager). Software programming allows advanced automated image acquisition. Flexibility and integration depend on the specific software, the version (including relevant hotfixes) and available modules. Often, in the case of commercial packages, additional modules and/or upgrades have to be purchased individually, and the software can therefore vary substantially over time and between systems with almost identical hardware. It is critical to report software, modules and versions used. Any custom acquisition code should be reported

and made available to the scientific community, including the URL or website that contains information on its source and capabilities.

Guidelines on reporting metadata specific to microscopy modality

Optical sectioning techniques, such as confocal and multiphoton, are designed to enhance the contrast of a wide variety of biological specimens, including tissue sections or whole organs and organisms. They use vendor-specific methods to configure the light path, which may vary by instrument. Consequently, each microscopy modality will have dedicated hardware and software acquisition configurations that will impact results. In this section, we describe the metadata specific to single-point scanning confocal, spinning disk confocal and multiphoton microscopy. The metadata applicable to widefield microscopy are described in "Guidelines on reporting instrument data" and Supplementary Exhibit 1. Other microscopy modalities, such as light-sheet and super-resolution microscopy, require separate and specific guidelines and considerations and are beyond the scope of this Perspective.

Single-point scanning confocal microscopy

The light path in a laser scanning confocal microscope is more complex than that in a conventional widefield microscope and entails additional hardware and settings that will impact acquisition and, ultimately, the interpretation of the results.

The hardware components required for optical sectioning (scanning mechanism, illumination and wavelength selection configuration, pinhole and detection) are usually integrated into a scan unit. The specific hardware components vary between different vendors

and even in models available from the same vendor. Reporting the scan unit model will specify the capabilities and limitations of each system, enabling other researchers to reproduce or interpret a particular experiment. Some scan units provide different options (for example, type of scanning mechanism and detectors) that can impact maximum acquisition frame rate, noise level and overall SNR and thus should be reported.

Although reporting the scan unit provides fixed information on the hardware configuration, there are many user-defined settings that contribute to image quality, quantification and conclusions and also need to be reported to ensure reproducibility (Supplementary Exhibit 2). Unfortunately, many of these settings are not well understood and are incorrectly applied and/or incompletely reported, which undoubtedly affects reproducibility. Below are some examples of the most commonly overlooked or misunderstood settings that have a great impact on the image and require reporting.

In a laser scanning confocal microscope, the digital resolution is not limited by a physical photodiode size. Instead, the detector analog signal is digitized at regular intervals by the pixel clock. The final pixel size is determined by the total magnification, the pixel clock or frame size (how many intervals/pixels the scan area can be divided into) and the size of the scanned area (zoom factor). This offers flexibility but results in increased complexity, leading to irreproducibility if not properly reported. In many cases, researchers provide the frame size (for example, 1,024 × 1,024) instead of the actual pixel dimensions. This can be due to how the information is displayed in the acquisition software or to a poor understanding of the instrument. Regardless, the frame size alone does not provide crucial or reproducible information on the digital resolution of the image.

Most commercial laser scanning confocal microscopes can be used in uni- or bidirectional scanning modes. While the acquisition time can be reduced by half, bidirectional scanning may induce a pixel shift, especially at faster scan rates and higher zoom factors. This shift may not be apparent in the whole image, but careful inspection will show an offset between adjacent lines (Figure A1.4e, left and inset, and Supplementary Materials). Often, the scan mirrors can be carefully calibrated to reduce this pixel shift (Figure A1.4e, right and inset), but reporting scanning directionality is still best practice.

A major setting that is often misused and under-reported is the offset. It may be tempting to adjust the offset to reduce fluorescence background and amplify the contrast for signal from the desired object. However, an improperly adjusted offset will lead to clipping of data intensities and removal of signal. If data clipping is substantial, entire structures within the sample can disappear from the image (Figure A1.4f). Not reporting the offset will produce imprecise and conflicting quantitative measurements, such as the number of mitochondria per area, the width and area of each mitochondria and the overall intensity.

Another critical parameter to report is the pinhole diameter. It determines the thickness of the optical section, axial resolution and overall brightness and contrast. This information is typically given in Airy units (AU; Box A1.2 and Supplementary Table 2). It is important to note that the thickness of the optical section obtained by setting the pinhole to 1 AU will vary with wavelength. The pinhole diameter (and wavelength, if stated in AU) should be reported.

The complexity in reporting the acquisition settings and configurations in a laser scanning confocal microscope is compounded by the lack of standardization of the

nomenclature utilized by different vendors. For example, the adjustable voltage of the detector, which modulates the amount of gain or amplification of signal, can be referred to as master gain, HV (high voltage) and gain or even displayed as the percentage of amplification (Supplementary Materials). In some acquisition software, adjustment of the scan rate (pixel dwell time) is provided on an arbitrary unit scale instead of in the appropriate units of microseconds per pixel or Hz. Caution is essential when reporting the scan rate/dwell time in these systems as inaccurate reporting would contribute to a lack of reproducibility (Supplementary Materials). Current important initiatives to improve metadata standardization are listed in Supplementary Table 1.

Multiphoton microscopy

Multiphoton microscopes share most of the hardware components of a laser-scanning electron microscope and therefore will be impacted by many of the same parameters. A notable difference is the absence of a pinhole, as optical sectioning is provided by the localized excitation produced by the nearly simultaneous absorption of multiple photons at the focal plane (Benninger and Piston 2013).

In this modality, a pulsed laser is necessary to achieve the high peak intensity required to excite fluorophores by nearly simultaneous absorption of multiple photons. The pulse length (femtosecond scale) and repetition frequency are important parameters as they determine the peak intensity (Denk et al. 2006). Oftentimes tunable lasers are used; the laser model, excitation wavelength, pulse length and repetition frequency should be reported to ensure reproducibility.

Many multiphoton systems have two light paths to collect and detect the emitted light. The first light path coincides with the traditional confocal light path (scan unit), whereas the second light path uses specialized detectors (non-descanned detectors, NDDs) that collect emitted light more efficiently than detectors within the scan unit. The image produced by the NDD will have higher SNR than that from a scan unit detector, other things being equal, and therefore the specific hardware and configurations need to be specified to ensure reproducibility (Supplementary Exhibit 3).

Spinning disk confocal microscopy

In spinning disk confocal microscopes, the sample is scanned simultaneously through multiple pinholes of fixed diameter on a disk. The spacing of these pinholes greatly impacts optical sectioning capabilities. Closely spaced pinholes reduce optical sectioning and contrast, whereas disks with pinholes spaced farther apart improve optical sectioning in thicker specimens but reduce sensitivity and frame rate and require longer integration times or higher illumination levels to generate images with high SNR.

The manufacturer and model of the scan unit determine the design of the disk, the diameter of the pinholes and the spacing between them. Some scan units provide multiple pinhole size and spacing options. Reporting the specific pinhole size and spacing used in the experiment is critical to ensure reproducibility (Supplementary Exhibit 4).

GUIDELINES ON REPORTING SAMPLE PREPARATION

Sample preparation is critical in fluorescence microscopy and will greatly influence the quality of the final image and its quantification (Burry 2010). There are many publications that

focus on troubleshooting sample preparation and appropriate controls required for the interpretation of microscopy data in both fixed and live specimens (Jerome 2001; Bacallao et al. 2006; North 2006; Burry 2010; Allen et al. 2013; Specht et al. 2017; Lee and Kitaoka 2018; Jost and Waters 2019; Wait et al. 2020). Detailed sample preparation methods including fixation, permeabilization, labeling and mounting of the sample (Supplementary Exhibits 1-4) and validation steps should be documented when writing a manuscript. Here we highlight some examples of sample-related metadata that are critical for image acquisition in both fixed and live samples.

Of particular importance to report is the specific fluorophore used in any given experiment. Not only will the fluorophore's properties heavily dictate the experimental design and the hardware required to accomplish a particular experiment (Shaner 2014; Heppert et al. 2016; Lambert 2019), but, notably, the fluorophore can also impact the outcome of the experiment itself. This is especially true for specific variants of a fluorescent protein. Even if spectral properties are similar, characteristics such as brightness, photostability, monomeric quality and maturation time are variant specific (Cranfill et al. 2016). The choice of fluorescent protein and how the fluorescent protein is attached to the target protein (C terminus, N terminus, or specific linker sequences and lengths) may alter the localization, concentration, lifetime and/or functionality of the protein of interest, leading to potentially erroneous measurements and different experimental outcomes (Landgraf et al. 2012; Montecinos-Franjola et al. 2020). Consequently, reporting GFP as the fluorophore (instead of sfGFP or mGFPmut3) does not provide sufficient information to reproduce a particular set of experiments and can

result in critically different results. The original papers describing the specific fluorescent protein's development should also be cited if possible.

Sample optical properties contribute to the performance of the optics in the microscope and need to be documented. Objective lens corrections are engineered with a specific coverslip thickness in mind (usually 0.17 mm or grade no. 1.5). Use of a coverslip with a different thickness/grade can therefore negate those corrections (Keller 2006). Coverslip thickness tolerance (for example, 0.17 ± 0.005 mm) can be quite variable. Reporting the coverslip vendor and reference number therefore supports experimental reproducibility.

The mounting medium serves to homogenize the refractive index across the sample and match it to the requirements for the objective lens. The specifications of mounting media vary widely (refractive index, compatible fluorophores, curing, etc.). Mounting media can therefore impact the overall brightness, axial resolution and, in some cases, the final thickness of the sample, which will affect many aspects of quantification. Additionally, the refractive index of a mounting medium may change with time, and imaging in the same general window of time after mounting is recommended. Understanding how the mounting medium affects the sample and reporting its specifications will improve reproducibility.

Live-cell imaging enables the study of biological processes as they occur in real time though time-lapse imaging. In this application, maintaining the health of the sample should be the top priority to ensure rigor and reproducibility (Supplementary Exhibits 1-4 and Box A1.1). Most biological samples require an optimal temperature range to carry out biological processes. Precise control of the environmental conditions is critical to ensure normal cell physiology and

function, including growth rate and molecular dynamics. The hardware used to maintain temperature, gas and humidity vary widely and will offer different stability and levels of control over these conditions. Thus, a description of the specific environmental conditions and how these are maintained will greatly improve accuracy, precision and reproducibility. The specific imaging medium and any additional components that may decrease phototoxicity or photobleaching (for example, antioxidants and reactive oxygen species scavengers) should be reported. Some components of the medium such as phenol red, fetal bovine serum, riboflavins and vitamins can produce substantial fluorescence background signal, limiting the ability to detect the signal of interest and impacting the accuracy and precision of quantitative measurements. Additionally, the concentration of a fluorescent dye and the solvent used or transfection reagents and expression of fluorescent protein fusions (Cranfill et al. 2016) in a live sample may affect cell function (Alford et al. 2009; Spracklen et al. 2014; Yang et al. 2020), induce synergistic effects with the conditions used (for example, drug treatments), and therefore impact reproducibility.

There is a wealth of publications offering insight on live-cell imaging that researchers can consult to better understand, optimize and troubleshoot aspects related specifically to this application (Brown 2007; Waters 2007; Frigault et al. 2009; Specht et al. 2017; Kiepas et al. 2020).

NOTES ON METHOD VALIDATION

Understanding the capabilities and limitations of the particular application is essential in designing a successful microscopy experiment, as it enables researchers to identify the sources of measurement imprecision and mitigate its effects. In addition to carefully reporting

microscopy methods, authors should aim to report critical steps for validation of the methodology. Box A1.2 describes some of the important validation steps that should be included in any experimental design and in the methods section, and Supplementary Table 1 lists selected resources for method validation. There are several outstanding publications that provide more information on method validation approaches and protocols (Lee and Kitaoka 2018; Jost and Waters 2019; Wait et al. 2020). Additionally, several initiatives in the microscopy field focus on the importance of quality control and instrument performance assessment to validate microscopy methods (Supplementary Table 1).

NOTES ON IMAGE FORMAT AND PROCESSING AND THEIR IMPACT ON METADATA

Image processing is used to enhance visualization and extract information from the digital image. While image processing is important for gleaning useful information (for example, during segmentation), it can irreversibly change the intensity levels and introduce nonlinear changes in shape and intensity across the image, compromising accurate quantification. Thus, all imaging processing steps and software settings must be reported (Aaron and Chew 2021; Miura and Nørrelykke 2021).

Most acquisition software options include image processing shortcuts to enhance image contrast (for example, haze reduction or smoothing) or other aspects of the image automatically or with a few convenient clicks of a button, often intended for presentation purposes while compromising the quantitative integrity of the image. Importantly, the resulting processed image is generally no longer faithful to the raw data collected, compromising reproducibility and accuracy in subsequent measurements, especially if the raw data are not saved alongside the

processed image. Researchers should pay careful attention to software controls/modules used and ask experts (vendors or core scientists) for guidance in image processing. Most critically, the raw data image should always be saved.

Another aspect to consider is the file format used to acquire and export/save the images. Most commercial software produces a raw, uncompressed proprietary image format that contains all accompanying metadata recorded by the system. However, images can be exported in other file formats that may compress or otherwise scale or filter the data, reduce bit depth, alter the intensity levels acquired by the detector and lose the metadata, often irreversibly (for example, jpeg, mov, AVI). Ensuring a copy of the raw image in its original suggested proprietary file format is saved and backed up before converting to or exporting as a different file format is absolutely critical for quantitative microscopy. No matter how tempting it is to work with small file sizes, a compromise, often significant, has been made, even if unintentionally.

RESOURCES FOR REPORTING MICROSCOPY METHODS

The examples provided in this Perspective serve as cautionary tales of how the lack of proper methods reporting can lead to conflicting data interpretation and thus irreproducibility. To facilitate proper microscopy methods reporting, we have assembled comprehensive checklists for the most common fluorescence light microscopy modalities (Supplementary Exhibits 1-4). Each checklist contains essential and recommended metadata to include in the methods section for any manuscript presenting data that were acquired using these modalities. Common examples are provided for each term, and a reference text example of a methods section write-up is also included after the checklist.

Additionally, to help researchers simplify and customize the essential metadata list according to their specific imaging and experimental design, we developed a microscopy metadata checklist generator tool (MicCheck). This tool guides researchers through simple questions related to their imaging choices and dynamically generates a checklist of essential and optional metadata that can then be copied and pasted into a text editor or downloaded in pdf format (Supplementary Exhibit 5). MicCheck is hosted online at https://rebecca-senft.shinyapps.io/MicCheck/, and relevant source files are available at the GitHub repository at https://github.com/rsenft1/MicCheck. In addition to online use, by downloading and modifying the example text file, core facilities or laboratories are also able to create their own versions of MicCheck with custom metadata examples specific to their microscope systems.

These checklists can also be used by researchers when designing imaging experiments to ensure that the relevant hardware and settings are properly identified and configured. They can also be used for reporting imaging methods, including during manuscript preparation or in the experimental design sections of funding proposals. Additionally, the checklists can be used by editors and reviewers to ensure sufficient detail is included to consider the experiments rigorous and reproducible.

Finally, for education and to help improve the adoption of these guidelines, we provide a visual infographic that can be printed and displayed in laboratories, core facilities or microscopy rooms to aid, remind and encourage researchers to compose detailed methods sections in their publications (Extended Data Figure A1.1). The poster summarizes the essential metadata described in the checklists and the figures, depicting examples of how these hardware and settings can impact image quality and reproducibility.

Recommendations to improve methods reporting

While the description of minimal microscopy reporting guidelines is an essential first step toward improving methods reporting, it is not sufficient to solve the microscopy reproducibility crisis. The imaging scientific community needs to work together in a coordinated effort to improve methods reporting and the overall quality and reproducibility of image-based research, including researchers, imaging scientists, institutions, granting agencies, scientific journals and vendors. More rigorous and reproducible science results in better use of resources, improved data integrity and, therefore, fewer retracted publications and the ability to extend research by mining published results. Thus, there is a need to establish standards and provide resources to educate, inform and improve microscopy methods metadata reporting. Greater awareness and education will improve how microscopy data are collected, shared, validated, analyzed and reported.

Role for researchers

Researchers can contribute to improvement in microscopy methods reporting by (1) improving their knowledge of the microscopy techniques and appropriate validation steps used throughout their research; (2) upholding and requiring guidelines and recommendations set by the imaging community when reviewing manuscripts and grant applications; (3) involving imaging scientists during all steps of the research process, from experimental setup to data interpretation and manuscript preparation; (4) acknowledging core facilities and imaging scientists or considering collaborations that lead to authorship, as a way to enable the critical role core facilities fulfill in support of the scientific community; and (5) using data repositories to

improve transparency and reproducibility and enhance data sharing (Ellenberg et al., 2018; Supplementary Table 1).

Role for imaging scientists and core staff

Imaging scientists, especially those in core facilities, have a key role by sharing their technical expertise and providing intellectual contributions in all aspects of image-based science. In addition, they serve an educational mission by disseminating resources and tools to improve image-based research. Educating researchers on the importance of appropriate methods reporting will encourage best practices and participation by everyone. While core staff and imaging scientists have a critical educational role, this is not a substitute for formal training of graduate students and other researchers in proper metadata collection and reporting. Such training can take place at home institutions and in summer or other intensive programs focused on microscopy methodology and will greatly improve education and awareness broadly.

Imaging scientists are encouraged to stay informed about resources on education, rigor and reproducibility and to contribute to the development of guidelines and standards by many initiatives in the imaging community (Mische et al. 2020; Hammer et al. 2021; Kunis et al. 2021; Nelson et al. 2021). These initiatives (including those in Supplementary Table 1, as well as many others) can help in this task by presenting the resources in conferences, workshops and other educational initiatives they support.

Role for scientific journals and funding agencies

Scientific journals are urged to update their instructions to authors and have them reviewed by the imaging community, to ensure that adequate microscopy metadata information

is included in the materials and methods. Removing word count limits from the methods section will allow authors to fully describe microscopy image collection and analysis, which should be written and reviewed with the same rigor as the entire paper. If space constraints cannot be adjusted, detailed methods descriptions can be included in supplementary information.

Encouraging or requiring proper recognition of the contribution of imaging scientists, as appropriate (acknowledgment or authorship), will facilitate researchers working closely with imaging scientists as standard practice. Incorporating imaging scientists in the peer review process, perhaps as technical experts, would help ensure that the experimental design, methodology and reporting of microscopy data support the conclusions of the manuscript.

Lastly, requiring appropriate analysis and quantification of imaging data (in addition to 'representative images') is long overdue. Quantification and validation of microscopy data will reduce bias and irreproducibility as well as the publication of artifactual results.

Conclusion

Rigorous and unbiased experimental design and analysis workflows are critical to provide accurate insight into the biological process under investigation (North 2006; Lee and Kitaoka 2018; Jost and Waters 2019; Wait et al. 2020). Sample preparation, choice of instrument and related hardware, and image acquisition parameters (that is, metadata) have a profound effect on the image data validity and interpretation and therefore must be reported in the methods section of a published manuscript. However, microscopy methods reporting is often overlooked throughout the peer review process. In this work, we describe specific examples that highlight how lack of reporting of comprehensive information can affect the integrity and

reproducibility of microscopy results. We present guidelines, checklists and resources to help researchers identify the critical metadata that should be included in their methods section, according to their specific experiment. The goal is not to put an unnecessary burden on researchers, but rather to help give readers of research papers enough information to assess the validity of biological findings and reproduce those findings independently. We hope that these reporting guidelines become second nature when carrying out microscopy experiments and reporting microscopy data and that implementing these guidelines will help improve the design of future experiments. We also hope that these guidelines provide a starting point for journal editors and peer reviewers when assessing microscopy data.

We recognize that addressing microscopy reproducibility is a complex, multifaceted issue that will require an ongoing and coordinated effort from everyone involved in scientific research. In particular, we recognize the contributions from core facilities and imaging scientists who are uniquely positioned to assist researchers in addressing these challenges by educating and supporting the scientific community (Aaron and Chew, 2021; Frigault et al., 2009; Hammer et al., 2021; Heddleston et al., 2021; Jost and Waters, 2019; Kunis et al., 2021; Lee and Kitaoka, 2018; Mische et al., 2020; Nelson et al., 2021; North, 2006; Wait et al., 2020; Waters, 2020; Supplementary Table 1). While this Perspective has focused on reporting of microscopy methodology, we emphasize that appropriate method validation and experimental design are critical to ensure the quality of quantitative microscopy data and the continued progress of feasible, rigorous and reproducible image-based science.

SUPPLEMENTARY MATERIALS AND EXTENDED DATA

Supplementary tables and extended data can be found online, at https://www.nature.com/articles/s41592-021-01156-w#Sec25.

APPENDIX 2.

EFFECT OF SEROTONERGIC NEURON SILENCING ON KAINIC ACID-INDUCED SEIZURE THRESHOLD AND ASSOCIATED HIPPOCAMPAL SEQUELAE

Authors and Contributions

This appendix chapter includes unpublished work I performed investigating the impact of preventing neurotransmission from Pet1 *neurons on seizure behavior and associated gliosis and cell death in the hippocampus. I wrote this appendix with input from my adviser Dr. Susan M. Dymecki. Components of this appendix are presented from my NIH grant T32 EY007110.*

Abstract

To understand how the brain copes with seizure-induced injury and develop targeted therapies for epilepsy, it is necessary to study the neural circuitry regulating seizures and resultant neuropathological changes in the brain. Previous work in human patients and rodent models has shown that serotonin and the neurons that produce and release it modulate susceptibility to seizures and seizure-induced neuropathological reorganization in the hippocampus. Work characterizing the serotonin neuron system into distinct subpopulations has shown these cells are diverse in their gene expression, patterns of axonal innervation, and neurotransmitter release. However, the specific serotonergic circuitry underlying the amelioratory effects of serotonin on seizures and associated sequelae are unknown. We silenced serotonergic neurons accessed by expression of the driver *Pet1-Flpe* and recorded behavior and hippocampal gliosis and neuron loss after triggering seizures with the chemoconvulsant kainic acid (KA). We found that neither silencing the entire *Pet1* neuron group nor the *r0/1En1-Pet1* serotonergic neuron subtype affected susceptibility to seizures nor seizure-induced gliosis and neuron loss. These results suggest developmental compensation or potentially opposing effects of different serotonergic subtypes on seizure susceptibility.

INTRODUCTION

Repetitive and severe seizures cause histological and organizational changes in the hippocampus that are associated with cognitive decline in patients with temporal lobe epilepsy (Bergen 2006; Marques et al. 2007; Dingledine et al. 2014; Cho et al. 2015). Preventing acute seizure events and precluding associated debilitating neuropathological changes remain important and unsolved problems in the study of epilepsy disorders. Though previous research has established a role of serotonin (5-hydroxytryptamine, 5-HT) neurotransmission in maintaining normal seizure resistance (Tripathi et al. 2008; Buchanan et al. 2014) and in preventing seizure-induced histological abnormalities (Clinckers et al. 2004; Jaako et al. 2009, 2011; Jin et al. 2009), the actual serotonergic circuitry involved in driving these effects is unknown.

Evidence from clinical studies and animal models suggests that diminished serotonergic neurotransmission may sensitize the brain to seizures and to seizure-induced hippocampal neuropathological changes. Among examples in mice, conditional deletion of the *Lmx1b* gene in developing 5-HT neurons embryonically results in the selective absence of virtually all 5-HT-producing neurons in the brain, as well as an increase in mortality, seizure frequency and severity, and reduction in latency to chemical or electroshock-induced seizures (Buchanan et al. 2014). Additionally, several studies have shown that depletion of central 5-HT in adult rodents using PCPA, which inhibits 5-HT synthesis, increases seizure severity, mortality, hippocampal cell loss and memory deficits (Buchanan et al. 2014; Maia et al. 2017). These studies demonstrate the necessity of 5-HT and 5-HT neurons in maintaining a seizure-resistant state.

Conversely, increasing extracellular 5-HT through administration of SSRIs has been shown to reduce seizure severity and prevent seizure-induced gliosis, altered differentiation, neurodegeneration, and memory deficits (Jaako et al. 2009, 2011; Jin et al. 2009; Choi et al. 2015). In preliminary trials, SSRIs have been shown to reduce seizures in patients with epilepsy with similar effectiveness to standard anticonvulsants (Favale et al. 2003; Richerson and Buchanan 2011), suggesting that modulating 5-HT neurotransmission may have therapeutic potential. Further, in rodent models, injection of PCPA inhibits the anticonvulsant effect of the SSRI fluoxetine (Yan et al. 1994), demonstrating the mechanism of SSRI effect is 5-HT-dependent rather than via an off-target effect. Also supporting a direct role of 5-HT in seizure resistance is the finding that intrahippocampal injection of 5-HT is able to prevent chemical induction of seizures in rodents (Clinckers et al. 2004). Finally, dramatically enhancing 5-HT neuron output in a genetic mouse model of 5-HT hyperinnervation prevents the induction of seizures with kainic acid (Tripathi et al. 2008), an effect reversible by treating animals with PCPA. There is thus strong evidence that serotonin and the neurons that produce it are required for normal seizure resistance and, further, that enhanced 5-HT neurotransmission can prevent acute seizures and epileptogenesis.

In the following experiments, we query the effects of pan-serotonergic silencing as well as subtype-specific silencing of *r1En1-Pet1* neurons on seizure behavior and seizure-associated hippocampal gliosis and neuron loss. The *r1En1-Pet1* lineage was of particular interest given the finding that a fate-shifting mutation to produce more 5-HT neurons and hyperinnervation from this domain greatly reduced seizure behaviors (Tripathi et al. 2008).

METHODS

Mice

We utilized mice expressing tetanus toxin light chain (tox) in either all *Pet1* neurons or r0/r1-derived *Pet1* neurons. We generated this mice by partnering either the broadly-expressed *Hbactin-cre* (Tmem163$^{Tg(ACTB-cre)2Mrt}$; Jax Stock No. 033984; Lewandoski et al. 1997) transgene or r0/1-specific *En1-cre* (En1$^{tm2(cre)Wrst}$/J; Jax Stock No. 007916; Kimmel et al. 2000) knock-in allele with the pan-serotonergic *Pet1-Flpe* transgene and the intersectional *RC-PFtox R26* knock-in effector (Kim et al. 2009). The resultant triple transgenic mice were called *Hbactin-Pet1-PFtox* for pan-serotonergic silencing and *En1-Pet1-PFtox* for r0/1-derived *Pet1* neuron silencing.

Seizure induction protocol

We utilized a repeated low dose (RLD) kainic acid (KA) administration model, which is advantaged over single high doses because it results in seizures more reliably and with less mortality (Tse et al. 2014; Umpierre et al. 2016). Briefly, mice were injected repeatedly with a low dose (5 mg/kg) of kainic acid dissolved in water. Behavior of mice was observed and animals were re-injected every 20 minutes until stage 4/5 seizures were observed (Figure A2.1A). Using this strategy, we were able to observe kainic acid-induced hippocampal neurodegeneration (Figure A2.1B-D). We quantified the number of doses required to reach stage 4/5 seizures for each mouse. We also examined video recordings of seizure behavior segmented into 5 minute epochs and scored seizure behavior on a modified racine scale (Umpierre et al. 2016).

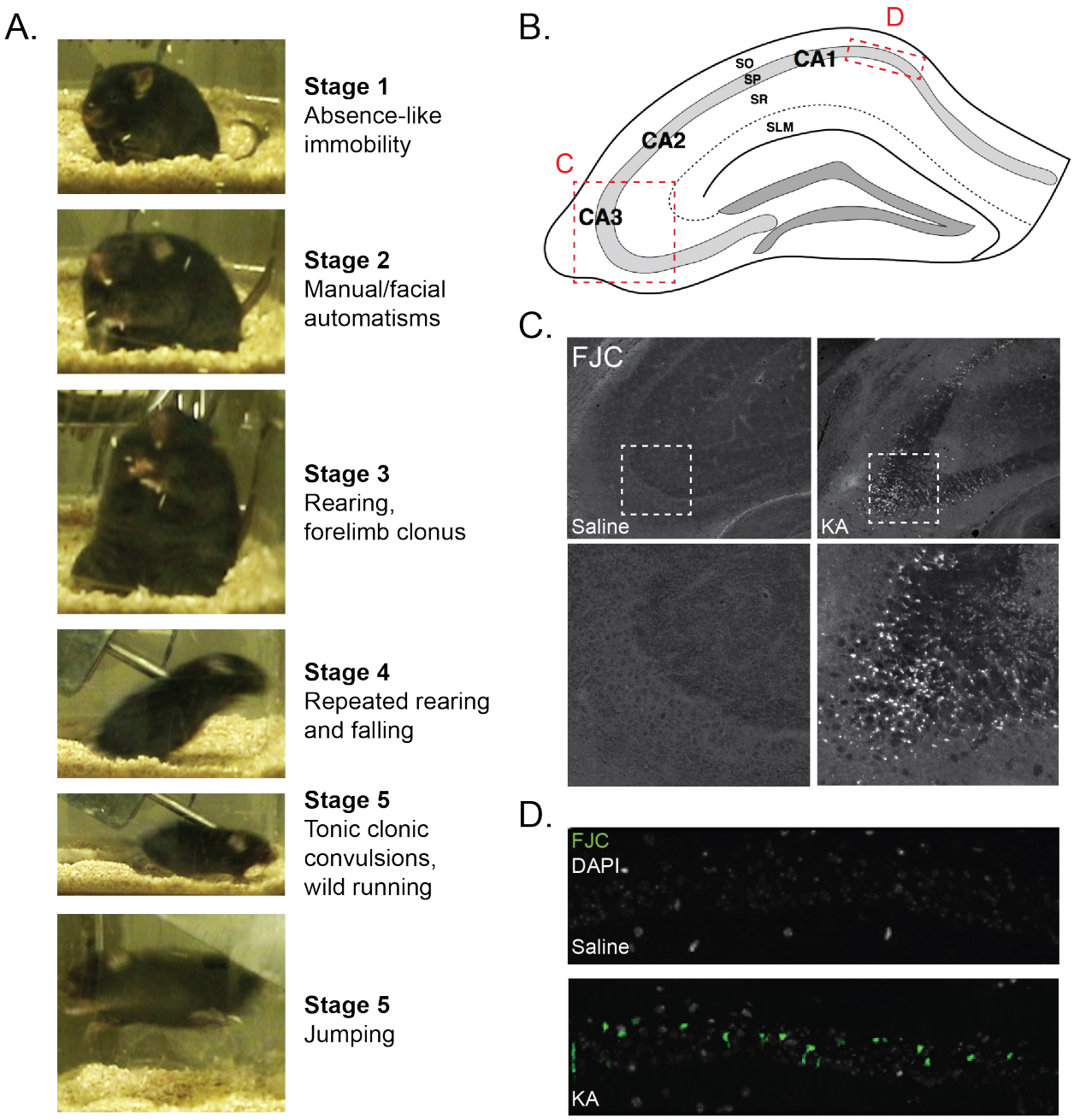

Figure A2.1. Kainic acid-induced seizure behavior and cell death

Animals were scored on a modified Racine scale (A, Umpierre et al. 2016) with 5 stages. Mice were dosed with repeated low doses (RLD) of kainic acid (KA) until stage 5 seizures with hole body convulsions were observed. Kainic acid-induced seizures were capable of inducing cell death in hippocampal subfields, as assessed through fluorojade C (FJC) staining (B-D).

Assess gliosis and neuron loss

We utilized immunohistochemical methods to assess the effect of constitutive serotonin neuron silencing on kainic acid-induced gliosis and neuron loss. We induced status epilepticus (long, repeating seizures; SE) in mice with pan-serotonergic silencing (*Hbactin-Pet1-PFtox*) or their control littermates (n=4 per group). All experimental and control mice received the same amount of kainic acid (5 doses of 5 mg/kg kainic acid for the experiment testing *Hbactin-Pet1-PFtox* mice and 3 doses for the *En1-Pet1-PFtox* experiment). Two days following SE, we perfused mice transcardially with ice cold phosphate-buffered saline (PBS) followed by 4% paraformaldehyde in PBS. Brains were embedded in tissue freezing media (TFM) and were cryosectioned at 40 µm thickness. Sections containing dorsal hippocampus were processed for free-floating immunohistochemistry (modified from Senft et al. 2021) to label neuronal nuclear protein (NeuN) to assess neuron loss and for Glial fibrillary acidic protein (GFAP) to assess gliosis.

Briefly, sections were rinsed in PBS then were incubated in block containing PBS with 0.1% triton-X-100 (PBST), 5% normal donkey serum (NDS, Jackson ImmunoResearch) 1% bovine serum albumin (Sigma) for three hours at room temperature. Primary antibodies (Rt-anti-GFAP (ThermoFisher catalog no. 13-0300) and Rb-anti-NeuN (Abcam catalog no. ab177487) were dissolved into PBST and sections were incubated in antibody solution overnight at 4 degrees C. Sections were then rinsed in PBST three times for five minutes each and then incubated at room temperature for two hours in PBST with 2% NDS and with fluorophore-conjugated species-matched secondary antibodies hosted in Donkey (Jackson ImmunoResearch Dk-anti-Rabbit-Cy2 and Dk-anti-Rat-Cy5). Sections were rinsed in PBST and incubated with DAPI (1:5000 dilution)

for 15 minutes before being mounted on #1.5 coverslips with Prolong glass anti-fade mounting media and attached to Fisher Superfrost plus slides.

Microscopy

Spinning disk confocal images were taken of several hippocampal subregions (CA3 stratum radiatum (SR), CA1 SR, CA1 stratum radiatum/stratum lacunosum moleculare border (SR-SLM), dentate gyrus (DG)). Confocal imaging was performed using a Nikon Ti inverted spinning disk microscope equipped with a Yokogawa CSU-W1 Spinning disk scanhead with 50 µm pinhole disk, a PI Z piezo stage insert, a TOPTICA iChrome MLE laser launch and a Plan Apo λ 20X 20x/0.75 DIC I air objective. Laser lines (and relevant power levels measured at the fiber tip) included 488 nm solid state (100mW), 561 nm DPSS (100 mW), 640 nm solid state (60mW). The microscope had a Nikon Motorized Stage with Physik Instrument Piezo Z motor. Images were captured using an Andor Zyla 4.2 Plus sCMOS monochrome camera and Nikon Elements Acquisition Software AR 5.02. Signal from the different channels was acquired sequentially using a Semrock Di01-T405/488/568/647 multi-band pass dichroic mirror and band pass emission filters for green (Chroma ET525/36m), red (Chroma ET 605/52m) and far read (Chroma ET 705/72m) channels.

Quantification of gliosis and neuron loss

A custom ImageJ macro was used to analyze NeuN and GFAP labeling. Briefly, this macro opened images and segmented cells based on autothreshold methods available in Fiji (Schindelin et al. 2012). The intensity of fluorescence within cells as well as the area taken up by labeling for NeuN or GFAP was measured and compared across genotypes.

Results and Discussion

Results will be presented as means plus or minus the standard error of the mean (SEM) unless otherwise noted. Statistical tests used are named when discussing the result of the test and were performed in Graphpad Prism software.

Constitutive silencing of r1En1-Pet1 cells does not alter seizure threshold nor the severity of kainic acid-induced seizures.

Contrary to our prediction, constitutively silencing *r1En1-Pet1* cells did not alter seizure threshold nor seizure severity. *En1-Pet1-PFtox* mice (4.7±0.49) did not differ from littermate controls (4.0 ± 0.58) in the total number of injections needed to reach stage 5 seizures (n=6 per group, t=0.8771, df=10, p=0.40, unpaired t-test). The number of 5 minute epochs that reached stage 5 seizures also did not differ between silenced mice (8.3 ± 2.3) and controls (4.5 ± 1.4; t=1.394, df=10, p=0.19, unpaired t-test). These results provide evidence that neurotransmitter release from *r1En1-Pet1* cells is not necessary for development of a normal seizure threshold. One possible explanation for these results is developmental compensation from other serotonin neurons or other neurotransmitter systems. It is also possible that serotonin neurons of other developmental domains, several of which project heavily to the hippocampus, may play a larger role in modulating seizures induced by chemoconvulsants.

Constitutive pan-serotonergic silencing does not alter seizure threshold nor the severity of kainic acid-induced seizures.

In similar seizure experiments with pan-serotonergic silencing, there was again no difference in the number of doses required to reach stage 5 seizures between silenced mice

(4.6±0.93) and their control littermates (5.8 ± 0.83; n=16 controls and 9 silenced mice, t=0.9610, df=23, p=0.35, unpaired t-test). Quantification of the number of stage 5 epochs in female mice revealed no difference between silenced mice (2 ± 0.41) and controls (5.7 ± 1.9; n=4 silenced and 7 controls, t=1.408, df=9; p=0.19, unpaired t-test). Based on these experiments, pan-serotonergic silencing does not appear to affect behavioral seizure threshold to kainic acid or seizure behavior after initiating status epilepticus. These results motivate exploring more acute alterations of serotonin neuron excitability, which may prove to be more illuminating that this chronic manipulation.

Constitutively silencing r0/1-derived serotonin neurons or all serotonin neurons does not affect gliosis or neuron loss in response to KA-induced SE relative to littermate controls.

We found no differences in the intensity or area of GFAP or NeuN labeling between controls and mice with chronic pan-serotonergic silencing (n=4 per group; multiple unpaired t-tests all p>0.05; Figure A2.2), suggesting that eliminating neurotransmitter release from all serotonin neurons does not affect kainic acid-induced gliosis and neuron loss. In a similar experiment, adult mice with r0/1-derived serotonin neuron silencing (*En1-Pet1-PFtox*) or control littermates (n=2 per group) were exposed each to 3 doses of 5 mg/kg kainic acid to induce SE. However, we observed no effect of genotype on gliosis or neuron loss (results not shown). One possible explanation for these results is that chronic silencing of *Pet1* neurons may allow for some compensation over the course of development. It is then still important to examine acute effects of inhibition or excitation on seizure behavior and associated sequaele. These results motivate experiments acutely manipulating serotonin neuron excitability prior to SE induction.

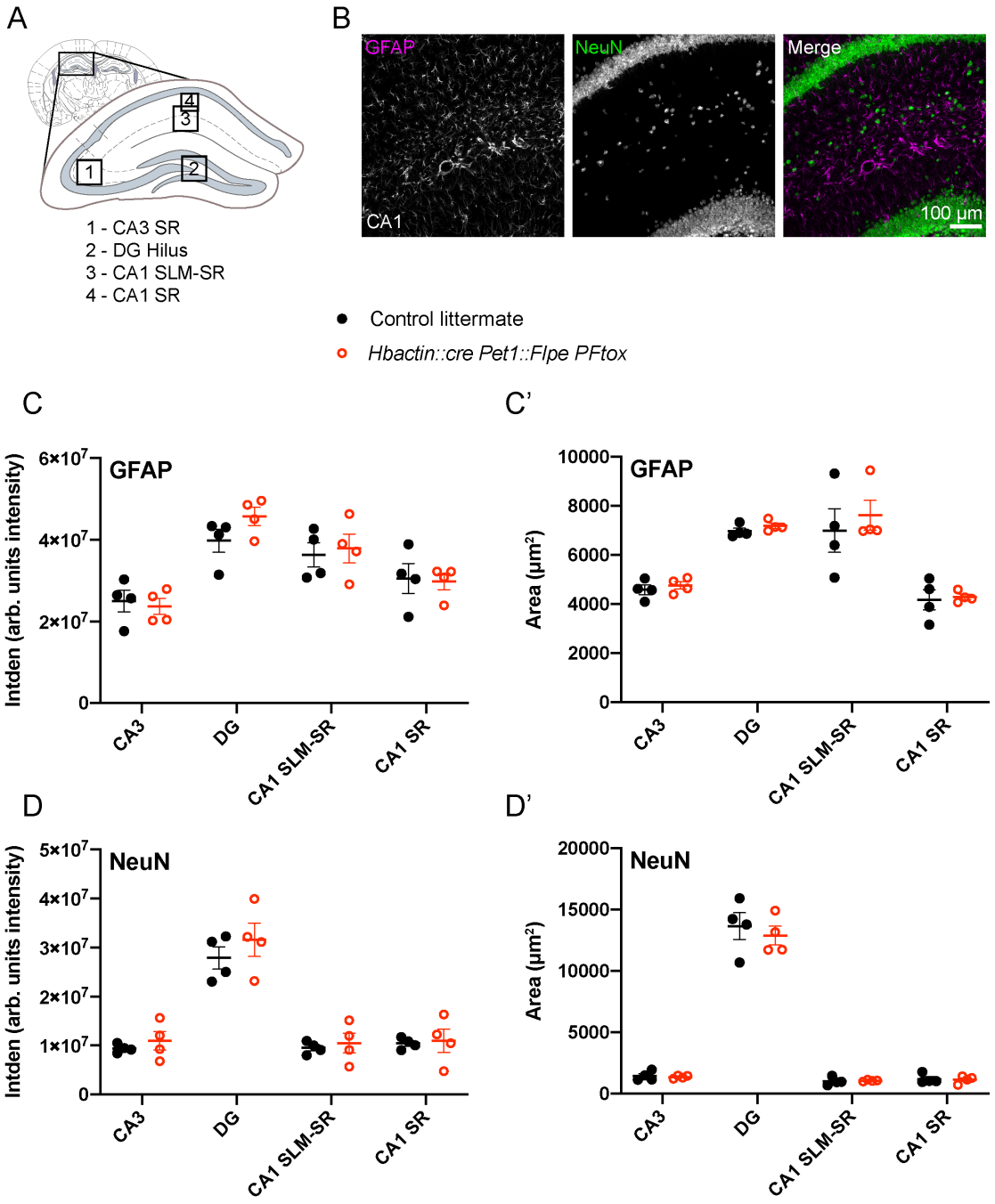

Figure A2.2. Preventing pan-serotonergic neurotransmission does not affect kainic acid status epilepticus-induced hippocampal sequelae

Hippocampal subfields (A) were labeled for neuronal marker NeuN and glial marker GFAP (B). Quantification of fluorescence intensity and area of GFAP (C-C') or NeuN (D-D') are presented and demonstrate no effect of pan-serotonergic silencing on these measures.

In conclusion, we observed no effects of pan-serotonergic silencing on seizure behavior nor on seizure-induced loss of hippocampal NeuN-labeled neurons nor increased area of GFAP-labeled glia. Our data suggest that any effects of ceasing serotonergic neurotransmission on seizure threshold or seizure-associated hippocampal sequelae are developmentally compensated in our chronically silenced mice. Alternatively, other, non-serotonergic circuitry may be more critical to regulating the brain's response to chemoconvulsants. Future studies should explore acute manipulations of serotonin neurons, such as chemogenetic or optogenetic manipulations of *Pet1* neuron activity.

APPENDIX 3.

ADDITIONAL IMAGE ANALYSIS CONTRIBUTIONS

A single-cell transcriptomic and anatomic atlas of mouse dorsal raphe *Pet1* neurons

Sex-specific role for dopamine receptor D2 in dorsal raphe serotonergic neuron modulation of defensive acoustic startle and dominance behavior

Authors and Contributions

This appendix chapter includes published work to which I contributed image analysis expertise, including writing custom macros in ImageJ to analyze RNAscope in situ *hybridization data and writing methods related to using the tools I developed. Full citations for the two papers are below. PDFs of the manuscripts follow.*

1. *Okaty BW, Sturrock N, Escobedo Lozoya Y, Chang Y, Senft RA, Lyon KA, Alekseyenko OV, Dymecki SM. 2020. A single-cell transcriptomic and anatomic atlas of mouse dorsal raphe Pet1 neurons. eLife. 2020;9:e55523*

2. *Lyon KA, Rood BD, Wu L, Senft RA, Goodrich LV, Dymecki SM. 2020. Sex-specific role for dopamine receptor D2 in dorsal raphe serotonergic neuron modulation of defensive acoustic startle and dominance behavior. eNeuro.*

RESEARCH ARTICLE

A single-cell transcriptomic and anatomic atlas of mouse dorsal raphe *Pet1* neurons

Benjamin W Okaty†*, Nikita Sturrock†, Yasmin Escobedo Lozoya, YoonJeung Chang, Rebecca A Senft, Krissy A Lyon, Olga V Alekseyenko, Susan M Dymecki*

Department of Genetics, Harvard Medical School, Boston, United States

Abstract Among the brainstem raphe nuclei, the dorsal raphe nucleus (DR) contains the greatest number of *Pet1*-lineage neurons, a predominantly serotonergic group distributed throughout DR subdomains. These neurons collectively regulate diverse physiology and behavior and are often therapeutically targeted to treat affective disorders. Characterizing *Pet1* neuron molecular heterogeneity and relating it to anatomy is vital for understanding DR functional organization, with potential to inform therapeutic separability. Here we use high-throughput and DR subdomain-targeted single-cell transcriptomics and intersectional genetic tools to map molecular and anatomical diversity of DR-*Pet1* neurons. We describe up to fourteen neuron subtypes, many showing biased cell body distributions across the DR. We further show that *P2ry1-Pet1* DR neurons – the most molecularly distinct subtype – possess unique efferent projections and electrophysiological properties. These data complement and extend previous DR characterizations, combining intersectional genetics with multiple transcriptomic modalities to achieve fine-scale molecular and anatomic identification of *Pet1* neuron subtypes.

***For correspondence:** bokaty@genetics.med.harvard.edu (BWO); dymecki@genetics.med.harvard.edu (SMD)

†These authors contributed equally to this work

Competing interests: The authors declare that no competing interests exist.

Funding: See page 33

Received: 27 January 2020
Accepted: 09 June 2020
Published: 22 June 2020

Reviewing editor: Anne E West, Duke University School of Medicine, United States

Introduction

Brainstem neurons that synthesize the monoamine neurotransmitter serotonin (5-hydroxytryptamine, 5-HT) (***Baker et al., 1991a***; ***Baker et al., 1991b***; ***Baker et al., 1990***; ***Dahlstroem and Fuxe, 1964***; ***Ishimura et al., 1988***; ***Steinbusch, 1981***; ***Steinbusch et al., 1978***) derive from embryonic precursors that express the transcription factor PET1 (alias FEV) upon terminal cell division (***Hendricks et al., 1999***). PET1 shapes the serotonergic identity of neurons by regulating expression of genes required for 5-HT biosynthesis, packaging in synaptic vesicles, reuptake, and metabolism (***Hendricks et al., 2003***; ***Krueger and Deneris, 2008***; ***Liu et al., 2010***; ***Wyler et al., 2015***; ***Wyler et al., 2016***), though some *Pet1*-lineage cells in the brain have ambiguous phenotypes with respect to their ability to synthesize and release 5-HT (***Alonso et al., 2013***; ***Barrett et al., 2016***; ***Okaty et al., 2015***; ***Pelosi et al., 2014***; ***Sos et al., 2017***). Aside from shared expression of 5-HT marker genes (to varying degrees), *Pet1*-lineage neurons display wide-ranging phenotypic heterogeneity, including diverse brainstem anatomy, hodology, and expression of neurotransmitters in addition to or other than 5-HT, suggestive of distinct *Pet1* neuron subtypes with divergent neural circuit functions (recently reviewed in ***Okaty et al., 2019***). We have previously shown that the mature molecular identities of *Pet1*-lineage neurons strongly correlate with both the embryonic progenitor domain (rhombomeric domain) from which they derive and with their mature anatomy (***Jensen et al., 2008***; ***Okaty et al., 2015***), largely consistent with (***Alonso et al., 2013***). However, even within a given *Pet1* rhombomeric sublineage and anatomical subdomain, *Pet1* neurons may display different molecular and cellular phenotypes (***Niederkofler et al., 2016***; ***Okaty et al., 2015***). *Pet1* neurons project widely throughout the brain and are functionally implicated in numerous life-sustaining biological processes and human pathologies. Thus, assembling a taxonomy of *Pet1* neuron subtypes based on molecular and cellular properties and linking identified *Pet1* neuron subtypes to specific biological functions is

important for basic neuroscience and human health, including the development of targeted therapeutics. Here we provide a high-resolution, single-cell transcriptomic atlas of dorsal raphe *Pet1*-lineage neurons revealing hierarchically and spatially organized molecular subtypes, each expressing unique repertoires of neurotransmitters, plasma membrane receptors, ion channels, cell adhesion molecules, and other gene categories important for specifying neuronal functions.

The dorsal raphe (DR) nucleus comprises the largest anatomically defined subgroup of *Pet1* expressing cells in the brain, and these cells are derived from embryonic progenitors in the isthmus and rhombomere 1 (**Alonso et al., 2013**; **Jensen et al., 2008**). Multiple studies have demonstrated neuronal diversity within the DR, in *Pet1*-expressing 5-HT neurons as well as other resident cell populations (**Calizo et al., 2011**; **Challis et al., 2013**; **Crawford et al., 2010**; **Fernandez et al., 2016**; **Huang et al., 2019**; **Kirby et al., 2003**; **Niederkofler et al., 2016**; **Prouty et al., 2017**; **Ren et al., 2018**; **Ren et al., 2019**; **Spaethling et al., 2014**; **Vasudeva and Waterhouse, 2014**; **Zeisel et al., 2018**). In the present study, we extend these findings by transcriptionally profiling *Pet1*-lineage marked DR neurons using microfluidic cell sorting and droplet-based single-cell RNA sequencing (scRNA-seq). Our particular experimental approach combining intersectional mouse genetics, high-throughput cell-type-specific purification (using the On-chip Sort), and newly improved scRNA-seq library construction chemistry (using the 10X Genomics Chromium Single Cell 3' v3 kit) allowed us to surpass prior resolution of DR *Pet1* neuron molecular diversity, both in terms of the number of DR *Pet1* cells profiled and the number of transcriptomically distinct *Pet1* neuron subtypes identified. To further characterize the anatomical organization of these molecularly defined *Pet1* neuron subtypes, we used intersectional mouse transgenic tools, crossing *Pet1-Flpe* mice with various subtype-relevant Cre-driver mice and dual Flpe- and Cre-responsive fluorescent reporter lines. In addition to performing histological analyses of these intersectionally defined *Pet1*-lineage neuron subpopulations, we further characterized them using manual cell-sorting from microdissected subdomains of the DR followed by scRNA-seq. Comparing this data with our high-throughput droplet-based scRNA-seq approach allowed us to map *Pet1* neuron molecular diversity onto DR anatomy. We found that DR *Pet1*-lineage neurons comprise as many as fourteen distinct molecularly defined subtypes, several of which we show are anatomically biased within rostral-caudal, dorsal-ventral, and medial-lateral axes. Additionally, by combining intersectional genetics with projection mapping and ex vivo slice electrophysiology we show examples of distinct *Pet1* neuron molecular subtypes that also differ in other cellular phenotypes important for function, such as hodology and electrophysiology.

Results

Droplet-based scRNA-seq of *Pet1* fate-mapped DR neurons reveals new molecularly defined neuron subtypes

To characterize the molecular diversity of *Pet1*-lineage DR neurons in a targeted, high-throughput, high-resolution manner we partnered recombinase-based genetic fate mapping, microfluidic fluorescence-based cell sorting, and droplet-based single-cell barcoding followed by RNA-seq library preparation and next-generation sequencing using the 10X Genomics Chromium Single Cell 3' v3 kit (**Figure 1A**; Materials and methods). Fluorescent labeling of *Pet1*-lineage DR neurons was achieved in mice of the following genotypes: (1) *Tg(Fev-flpe)1Dym* (referred to as *Pet1-Flpe*) (**Jensen et al., 2008**); *En1*$^{tm2(cre)wrst}$ (referred to as *En1-cre*) (**Kimmel et al., 2000**); *GT(ROSA)26Sor*$^{tm8(CAG-mCherry,-EGFP)Dym}$ (referred to as RC-FrePe, a dual Flpe- and Cre-dependent fluorescent reporter inserted into the *ROSA26* (*R26*) locus; **Brust et al., 2014**; **Dymecki et al., 2010**; **Okaty et al., 2015**), in which *Pet1*-lineage neurons derived from the *En1*$^{+}$ isthmus and rhombomere 1 (r1) embryonic progenitor domains are marked by EGFP expression or (2) *Pet1-Flpe; GT(ROSA)26Sor*$^{tm3.2(Cag-EGFP,CHRM3*/mCherry/Htr2a)Pjen}$ (referred to as RC-FL-hM3Dq) (**Sciolino et al., 2016**), in which all *Pet1* neurons are EGFP-labeled (Cre was not utilized in these experiments, thus only EGFP, not hM3Dq, was expressed).

Brains were acutely dissected from 6- to 10-week old mice of both genotypes (4 males and 6 females), and DR cells were dissociated as previously described (**Okaty et al., 2015**) (also see Materials and methods). EGFP-expressing neurons were selectively purified using the On-chip Sort (On-chip Biotechnologies Co., Ltd.), a recently developed technology that greatly reduces the pressure forces typically exerted on cells in conventional flow sorters, thereby achieving higher levels of

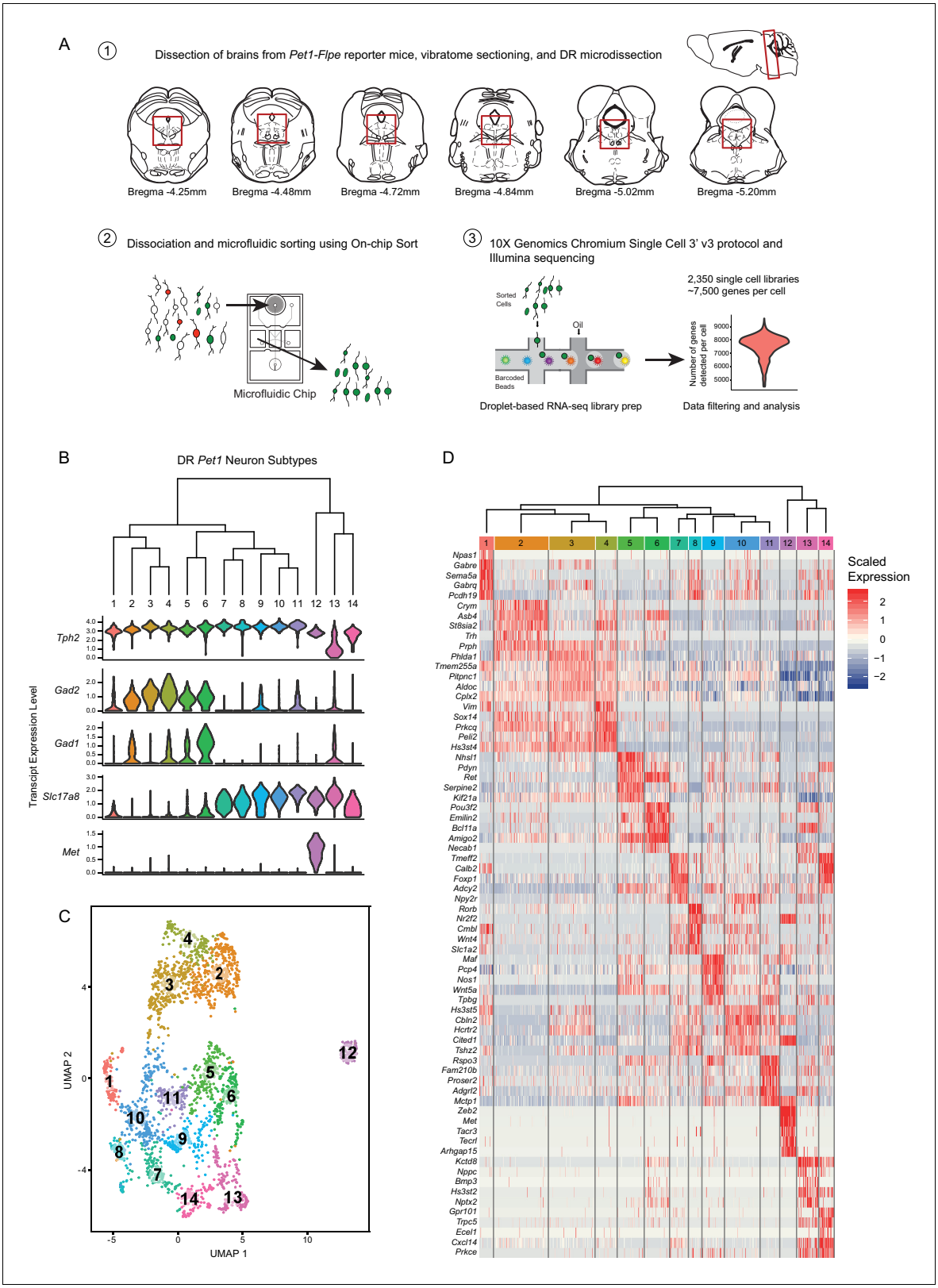

Figure 1. High throughput scRNA-seq and clustering analyses reveal as many as fourteen distinct molecularly-defined subtypes (clusters) of *Pet1* neurons in the mouse DR. (**A**) Schematic depicting the experimental and analytical workflow, specifically: (1) brain dissection and DR microdissection, (2) cellular dissociation and microfluidic fluorescence-based cell sorting using the On-chip Sort, and (3) library preparation, sequencing, and analysis using 10X genomics, Illumina sequencing, and the R package Seurat, respectively. (**B**) Hierarchical clustering of *Pet1* neuron subtypes identified by Louvain

Figure 1 continued on next page

Figure 1 continued

clustering (using the top two thousand genes with the highest variance, PCs = 1:5, 8:50, and resolution = 0.9), with violin plots depicting the log-normalized expression of a common set of genes (*Tph2, Gad2, Gad1, Slc17a8,* and *Met*) found useful for characterizing cluster structure across multiple resolutions (see ***Figure 1—figure supplement 2***). (**C**) UMAP visualization of single-neuron transcriptome community/similarity structure, with colors and numbers indicating discrete clusters (same clustering parameters as (**B**)). (**D**) Heatmap depicting the scaled expression of the top five marker genes for each cluster (ranked by p-value, or in some cases fold enrichment).

The online version of this article includes the following figure supplement(s) for figure 1:

Figure supplement 1. Systematic variation of key clustering parameters allows for exploration of the community structure of DR *Pet1* single neuron transcriptomes at variable resolutions.

Figure supplement 2. Analysis of clusters at successively increasing resolution values.

Figure supplement 3. Expression of serotonin-related genes across DR *Pet1* neuron subtypes.

Figure supplement 4. Correlation of 5-HT marker gene expression levels with *Fev* (*Pet1*) gene expression levels for clusters 13 and 14.

cell viability (***Watanabe et al., 2014***). Indeed, examination of sorted neurons revealed that many still had intact processes emanating from their somas. Cells were then run through the 10X Genomics Chromium Single Cell 3' v3 protocol, followed by Illumina NextSeq 500 sequencing. The Cell Ranger pipeline was used for transcript mapping and single-cell de-multiplexing, and all analyses of transcript counts were performed using the R package Seurat (***Butler et al., 2018***; ***Stuart et al., 2019***; also see Materials and methods). After stringently filtering out 'suspect' single-cell libraries (e.g. libraries with high levels of non-neuronal or mitochondrial genes, outlier library complexity, or absence/low levels of *Pet1* transcripts), we obtained 2,350 single cells for further analysis, with a mean of 7,521 genes detected per single cell library (mean of 57,678 UMIs per cell), and a total of 17,231 genes detected in aggregate (after filtering out genes that were expressed in fewer than ten cells).

As the principal goal of our scRNA-seq experiments was to characterize molecular diversity of *Pet1*-lineage neurons, our analyses were aimed at identifying genes with significantly variable transcript expression across single neurons, and using these gene expression differences to classify *Pet1*-lineage neuron subtypes. Typical clustering approaches used to classify cell types (or cell states) based on scRNA-seq data are largely unsupervised, but do require supervised input regarding a number of parameters that have the potential to significantly alter the resulting cluster assignments. These parameters include the data reduction used prior to clustering (such as principal components analysis), the number of components included in the reduction, and a resolution or granularity parameter that determines the 'community' size of clusters (i.e. whether cluster boundaries are more or less inclusive; coarse-grained or fine-grained). Rather than arbitrarily choosing a set of parameters for our *Pet1*-lineage neuron subtype classification, we chose a more exploratory approach by systematically varying key parameters and examining how sensitive the resulting clusters were to these combinations of parameters.

First, single-cell transcript counts were log-normalized, and we carried out principal components analysis (PCA) on the scaled and centered expression values of the top two thousand genes with the highest variance (after applying a variance-stabilizing transform, see Materials and methods) in order to reduce the dimensionality of the data onto a smaller set of composite variables that represent the most salient gene expression differences. Plotting the variance explained by each principal component we observed an inflection point, or 'elbow', around the fiftieth component suggesting a drop-off in the information content of subsequent components (***Figure 1—figure supplement 1A***), and found that roughly forty percent of the total variance was explained by these first fifty components. Further examination of the gene loadings of each component revealed that components six and seven were heavily weighted towards sex-specific transcripts and transcripts that largely correlated with batch. As our experiments were not designed to explicitly compare sex as a variable, and given the difficulties of interpreting batch-correlated gene expression differences (e.g. these could stem from population sampling biases of the different cell sorts, different genotypes used, different balance of sexes, or any number of idiosyncratic biological and technical differences) we ultimately chose to remove components six and seven from downstream analyses (though we found that their inclusion had only modest effects on data clustering).

Next, we varied: (1) the number of PCs included in the data reduction (from one to fifty, excluding PCs six and seven) used as input to the Seurat FindNeighbors function, and (2) the resolution

parameter in the Seurat FindClusters function (from 0.1 to 2.0, in intervals of 0.1, using the Louvain algorithm). The results of this analysis are summarized in the heatmap in ***Figure 1—figure supplement 1B***. Including only the first few principal components led to highly variable numbers of clusters depending on the resolution parameter (resulting in as many as 40 clusters at the highest resolution). However, for all resolutions the number of clusters mostly stabilized after including the first thirty PCs. In this regime of parameter space the number of clusters was, for the most part, bounded between five and twenty depending on the resolution. As a first pass at homing in on the 'optimum' number of clusters (strictly in a heuristic sense), we calculated the frequency of obtaining a given number of clusters over all combinations of parameters, reasoning that cluster numbers that are less sensitive to precise tuning of parameters would appear more frequently, and the 'robustness' of these cluster numbers might more faithfully reflect biologically meaningful subgroup structure in the data. The cluster number frequency plot in ***Figure 1—figure supplement 1C*** shows that there are four local maxima and one global maximum corresponding to five, eight, eleven, fourteen, and seventeen clusters respectively. Given the high frequency of these cluster numbers, we chose to examine their composition more carefully. As multiple combinations of parameters lead to the same number of clusters (***Figure 1—figure supplement 1D***), in some cases leading to differences in cluster composition (generally subtle), we decided to err on the side of including more data and thus fixed the number of PCs at one to fifty, excluding PCs six and seven, and varied the resolution to obtain five, eight, eleven, fourteen, and seventeen clusters.

We characterized cluster structure through hierarchical dendrograms, uniform manifold approximation and projection for dimension reduction (UMAP) (a technique recently developed by McInes, Healy, and Melville as described in a manuscript available at arXiv.org, and implemented in Seurat), and differential expression analysis using Wilcoxon rank-sum tests to identify transcripts that are significantly enriched or depleted among clusters (***Figure 1—figure supplement 2A–I***, ***Figure 1B–D***). We ultimately judged seventeen clusters (resolution = 1.5) to be excessive, due to the inclusion of clusters with very few enriched genes as well as clusters that appeared somewhat intermixed in UMAP space (analysis not shown). We thus focused our analyses on lower resolution clusters. Across all resolutions analyzed (0.1, 0.3, 0.7, and 0.9), we found a common set of genes that was useful in characterizing cluster structure, namely *Tph2, Gad2, Gad1, Slc17a8* (alias Vglut3), and *Met*. The *Tph2* gene encodes for tryptophan hydroxylase 2, the rate-limiting enzyme involved in 5-HT biosynthesis in the central nervous system (***Walther and Bader, 2003***; ***Walther, 2003***), and all but one cluster showed consistently high *Tph2* transcript expression. In the five- and eight-cluster-number analyses (resolution = 0.1 and 0.3, respectively), one cluster displayed a strikingly bi-modal distribution of *Tph2* transcript expression (***Figure 1—figure supplement 2A,D***, clusters four and six, respectively), however increasing the resolution further divided this group into a *Tph2*-low group (***Figure 1—figure supplement 2G*** and ***Figure 1B***, clusters eight and thirteen, respectively, corresponding to resolutions of 0.7 and 0.9) and a *Tph2*- 'variable' group, displaying a broader distribution of single-cell expression than other clusters (***Figure 1—figure supplement 2G*** and ***Figure 1B***, clusters ten and fourteen, respectively). Beyond *Tph2* expression, cluster thirteen (and to a lesser extent cluster fourteen) displayed lower and more variable expression of several 5-HT neuron marker genes (***Figure 1—figure supplement 3***). Interestingly, we found that expression of these genes was significantly correlated with the level of *Pet1* expression in these cells (***Figure 1—figure supplement 4***), consistent with demonstrated transcriptional regulation of 5-HT terminal identity markers by PET1 (***Hendricks et al., 2003***; ***Krueger and Deneris, 2008***; ***Liu and Deneris, 2011***; ***Spencer and Deneris, 2017***; ***Wyler et al., 2015***; ***Wyler et al., 2016***).

Gad1 and *Gad2* are paralogous genes that encode two distinct forms of the gamma-aminobutyric acid (GABA) synthetic enzyme glutamate decarboxylase (***Erlander et al., 1991***), and we found a sizable group of *Pet1* neurons (~50%) that express high levels of *Tph2* and *Gad2*, and to a lesser extent *Gad1* (generally detected in fewer cells than *Gad2*) (***Figure 1—figure supplement 2A,B***, clusters one and two), which could be further subdivided into five sub-clusters at finer resolution (***Figure 1B, C***, clusters two-six). One of these clusters, cluster six (***Figure 1B,C***), contained *Pet1* neurons additionally expressing intermediate levels of transcripts for *Slc17a8,* encoding the vesicular glutamate transporter 3 (***Fremeau et al., 2002***; ***Gras et al., 2002***). Notably, this group of neurons also had the highest expression of *Gad1* relative to other groups. High expression levels of *Slc17a8* transcripts were detected in ~46% of profiled *Pet1* neurons, comprising eight clusters at finer resolution (***Figure 1B,C***, clusters seven to fourteen), including the *Tph2*-low and *Tph2*-variable clusters

(*Figure 1B,C*, clusters thirteen and fourteen). The most striking outlier group of *Pet1* neurons (cluster twelve in *Figure 1B,C*) is characterized by high transcript expression of *Tph2*, *Slc17a8,* and *Met,* the latter encoding the MET proto-oncogene (also known as hepatocyte growth factor receptor) (*Iyer et al., 1990*). This group of cells consistently clustered separately from all other groups at all resolutions analyzed (*Figure 1—figure supplement 2*). At the finest resolution of 0.9, the remaining 4% of *Pet1* neurons, comprising cluster one, expressed high levels of *Tph2* transcripts but only sporadically expressed transcripts for *Gad2*, *Gad1*, or *Slc17a8* (*Figure 1B,C*).

Examination of the dendrogram in *Figure 1B* and the UMAP plot in *Figure 1C* (as well as examining the successively parcelled UMAP clusters in *Figure 1—figure supplement 2B,E and H* with increasing resolution) gives a sense of 'relatedness' among clusters. For example, *Gad1/2-Tph2* clusters two to four are more similar to each other than to *Slc17a8-Tph2* clusters, while cluster six, the *Gad1/2-Slc17a8-Tph2* cluster, and cluster five are situated between the other *Gad1/2-Tph2* and *Slc17a8-Tph2* groups. Like cluster twelve, clusters thirteen and fourteen appear as outliers from the other clusters in the dendrogram (*Figure 1B*), but despite showing low and variable expression of the 5-HT neuron marker gene *Tph2*, respectively, they nonetheless cluster more closely to other *Pet1* neurons than do *Met-Slc17a8-Tph2-Pet1* neurons (cluster twelve) in the UMAP plot (*Figure 1C*).

Met-expressing *Pet1* neurons have been previously reported in mice, both at the transcript and protein levels, specifically in the caudal DR and the median raphe (MR) (*Kast et al., 2017*; *Okaty et al., 2015*; *Wu and Levitt, 2013*) and more recently (*Huang et al., 2019*; *Ren et al., 2019*). Likewise, *Slc17a8*- and *Gad1/2*-expressing DR *Pet1* neurons have been previously reported in mice and rats, as demonstrated by mRNA in situ, immunocytochemistry, and RNA-seq (*Amilhon et al., 2010*; *Commons, 2009*; *Fu et al., 2010*; *Gagnon and Parent, 2014*; *Gras et al., 2002*; *Herzog et al., 2004*; *Hioki, 2004*; *Hioki et al., 2010*; *Huang et al., 2019*; *Okaty et al., 2015*; *Ren et al., 2018*; *Ren et al., 2019*; *Rood et al., 2014*; *Shikanai et al., 2012*; *Spaethling et al., 2014*; *Voisin et al., 2016*). Consistent with functional expression of VGLUT3 protein (encoded by the gene *Slc17a8*), which allows for filling of synaptic vesicles with the excitatory neurotransmitter glutamate, depolarization-induced glutamate release by DR *Pet1*/5-HT neurons has been demonstrated by a number of groups (*Johnson, 1994*; *Kapoor et al., 2016*; *Liu et al., 2014*; *Sengupta et al., 2017*; *Wang et al., 2019*). Additionally, VGLUT3 is thought to interact with vesicular monoamine transporter two (encoded by *Slc18a2,* alias Vmat2; *Erickson et al., 1992*) to enhance the loading of 5-HT into synaptic vesicles by increasing the pH gradient across vesicular membranes, a process referred to as 'vesicle-filling synergy' (*Amilhon et al., 2010*; *El Mestikawy et al., 2011*; *Münster-Wandowski et al., 2016*). GABA-release by *Pet1* DR neurons, on the other hand, has not been reported, thus the functional consequences of *Gad1* and *Gad2* transcript expression are presently unknown.

Differentially expressed genes span functional categories relevant to neuronal identity

Scaled expression of the top five marker genes for each cluster (ranked by Bonferroni corrected p-value or in some cases fold enrichment) are represented in the heatmaps in *Figure 1—figure supplement 2C,F,I*, and *Figure 1D*, depending on the cluster resolution. For all further analyses, we chose to focus on the 0.9 resolution clustering, as we felt that these fourteen clusters did the best job of parcellating UMAP space. For example, visually-distinguishable groups of cells, like clusters five and six, clusters ten and eight, and clusters seven and fourteen, are each consolidated into a single cluster at resolution = 0.7. While sharing some similarities, these groups differ in the expression of many genes, to an extent that we felt constituted separate classification as supported by the resolution = 0.9 analysis. To aid interpretation of the functional significance of differentially expressed genes, expression patterns of a subset of significantly variable genes and cluster markers are represented in the dot plots in *Figure 2*, organized by categories of biological function (identified by Gene Ontology annotations and literature searches). These gene categories were selected based on general importance for shaping neuronal functional identity – for example genes that encode transcription factors which broadly regulate molecular phenotypes, as well as genes that encode ion channels, plasma membrane receptors, calcium-binding proteins, kinases, and cell adhesion and axon guidance molecules, which collectively govern neuronal electrophysiology, signal transduction, and synaptic connectivity.

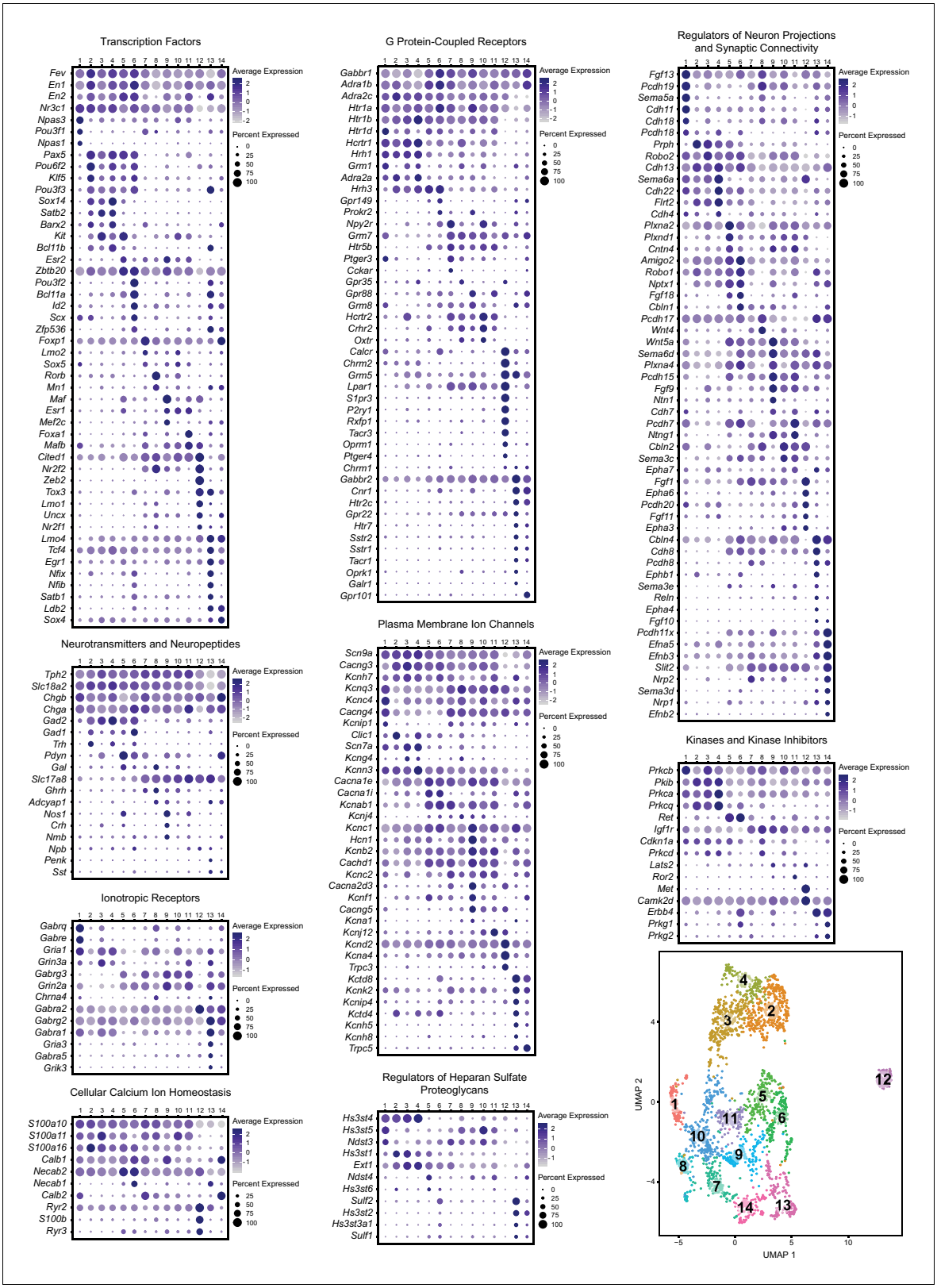

Figure 2. Expression patterns of a subset of highly variable genes classified by biological function. Dot plots show the expression of a gene (Y-axis) in each cluster (X-axis), separated by biological function. The size of the dot represents the percentage of cells expressing the gene and saturation of color represents average normalized expression level (scaled and centered). For convenience, the UMAP plot from ***Figure 1C*** is re-displayed at the bottom right to help link gene expression patterns to overall cluster structure. Minimum inclusion criteria for genes was that they were among the top

Figure 2 continued on next page

Figure 2 continued

2000 highest variance genes and/or they were found to be significantly enriched or 'de-enriched' in at least one subtype cluster (see Materials and methods).

Transcription factors

History of expression of *Pet1/Fev,* encoding the FEV transcription factor, ETS family member (**Fyodorov et al., 1998**; **Hendricks et al., 1999**) defines the *Pet1* neuronal lineage. As can be observed from the transcription factor dot plot in **Figure 2** (as well as the violin plot in **Figure 1—figure supplement 3**), *Pet1/Fev* displays broad expression across clusters but is expressed at significantly lower levels in cluster thirteen *Pet1* neurons. Several genes known to be directly regulated by *Pet1* (**Hendricks et al., 2003**; **Liu et al., 2010**; **Wyler et al., 2015**; **Wyler et al., 2016**), such as *Tph2*, *Slc6a4* (Sert) (encoding the serotonin transporter; **Hoffman et al., 1991**; **Lesch et al., 1993**), and *Slc18a2* likewise show reduced expression in cluster thirteen. The transcription factor engrailed 1 (encoded by *En1*) (**Joyner et al., 1985**), in its expression overlap with *Pet1,* is a marker of having derived from progenitors in the isthmus and r1 (**Alonso et al., 2013**; **Jensen et al., 2008**; **Okaty et al., 2015**), and, as expected, *En1* transcripts are detected broadly across all DR clusters. The paralogous gene engrailed 2 (*En2*) (**Joyner and Martin, 1987**), shows a more variable expression profile across *Pet1* DR neurons, being largely absent in cluster eight and twelve, and significantly lower in cluster seven. *En1* and *En2* are required for normal development of DR *Pet1* neuron cytoarchitecture and for perinatal maintenance of serotonergic identity (**Fox and Deneris, 2012**). *Nr3c1*, encoding the nuclear receptor subfamily 3, group C, member 1, aka the glucocorticoid receptor, which binds the stress hormone corticosterone (cortisol in humans), is expressed broadly across clusters one through eleven, but is de-enriched in cluster twelve, and to a lesser extent clusters thirteen and fourteen, suggesting differential sensitivity to corticosterone across different *Pet1* neuron molecular subtypes. Numerous studies have highlighted the functional importance of DR glucocorticoid signaling for 5-HT neuron activity and behavioral modulation (**Bellido et al., 2004**; **Evrard et al., 2006**; **Judge et al., 2004**; **Laaris et al., 1995**; **Vincent et al., 2018**; **Vincent and Jacobson, 2014**).

Other transcription factor encoding genes show more striking expression specificity. Transcripts for neuronal pas domain 1 and 3 (encoded by *Npas1* and *Npas3*) and POU class 3 homeobox 1 (*Pou3f1*) are significantly enriched in cluster one *Pet1* neurons. From mouse genetic studies, both NPAS1 and NPAS3 are associated with regulation of genes and behavioral endophenotypes implicated in psychiatric disorders, such as schizophrenia, though NPAS1/3 are also expressed by other cell types in the brain, such as cortical interneurons, which may contribute to observed behavioral effects of *Npas1/3* loss of function (**Erbel-Sieler et al., 2004**; **Michaelson et al., 2017**; **Stanco et al., 2014**).

Pax5, encoding paired box 5 (**Asano and Gruss, 1992**), a transcription factor involved in the regulation of isthmic organizer activity during development (**Funahashi et al., 1999**; **Ye et al., 2001**) is significantly enriched in clusters two, four, and five, and highly expressed in clusters three and six as well. *Pou6f2* (POU class 6 homeobox 2) and *Klf5* (Kruppel like factor 5) show a similar pattern of expression. *Sox14* (SRY-box transcription factor 14) and *Satb2* (SATB homeobox 2) show an even more restricted expression profile, limited to clusters two through four. Notably, clusters two through six are also enriched for expression of *Gad2*, which, like *Sox14*, is most highly expressed in cluster four. *Sox14* expression has been shown to regulate GABAergic cell identity in the dorsal midbrain (**Makrides et al., 2018**), and *Pax5* expression has been implicated in GABAergic neurotransmitter specification in the dorsal horn of the spinal cord (**Pillai et al., 2007**), suggesting that these genes may play similar roles in DR *Pet1* neurons. Interestingly, *Nr2f2* (encoding nuclear receptor subfamily 2, group F, member 2, alias COUP-TFII) shows an expression profile that is complementary to *En2* and *Pax5,* enriched in cluster eight, nine, and twelve, all of which are enriched for *Slc17a8* transcripts, and are largely devoid of *Gad1/2* expression.

Overall, each of the fourteen transcriptome-defined clusters of DR *Pet1* neurons can largely be classified by the combinatorial expression of two to three transcription factors. For example, *Pou3f2* (POU class three homeobox 2), *Bcl11a* (B cell CLL/lymphoma 11A zinc finger protein), and *Id2* (inhibitor of DNA binding 2) show enriched expression in cluster six, and to a lesser extent cluster thirteen.

Other notable transcription factor markers of *Pet1* neuron subgroups include *Foxp1* (forkhead box P1), enriched in clusters seven and fourteen, *Rorβ* (RAR-related orphan receptor beta), enriched in cluster eight, *Maf* (avian musculoaponeurotic fibrosarcoma oncogene homolog), enriched in cluster nine, *Foxa1* (forkhead box A1), enriched in cluster eleven, *Zeb2* (zinc finger E-box binding homeobox 2) enriched in cluster twelve, *Zfp536* (zinc finger protein 536), *Nfix* (nuclear factor I/X), and *Nfib* (nuclear factor I/B), enriched in cluster thirteen (detected in cluster six as well), and *Ldb2* (LIM domain binding 2), enriched in clusters thirteen and fourteen.

Neurotransmitters and neuropeptides

Pet1 neuron subtypes defined by transcriptomic clustering also show differential expression of a number of neurotransmitter-related and neuropeptide-encoding genes (***Figure 2*** Neurotransmitters and Neuropeptides dot plot). Transcript profiles related to classic neurotransmitter production, including *Tph2, Gad2, Gad1,* and *Slc17a8,* have already been described above (see also ***Figure 1B***). Transcript expression of *Trh*, encoding thyrotropin-releasing hormone, is significantly enriched in cluster two *Pet1* neurons and detected in clusters four and six (***Figure 1D*** and ***Figure 2***). Another gene involved in thyroid hormone signaling, *Crym*, encoding crystalline mu, also known as NADP-regulated thyroid-hormone-binding protein shows a similar expression profile (***Figure 1D***). *Pdyn*, encoding the preprohormone prodynorphin is enriched in clusters five, six, and fourteen. Prodynorphin is the precursor protein to the opioid polypeptide dynorphin, which predominately binds the kappa-opioid receptor to produce a variety of effects, such as analgesia and dysphoria (***Bruchas et al., 2010***; ***Chavkin et al., 1982***; ***Land et al., 2008***; ***Land et al., 2009***). Expression of *Nos1*, encoding nitric oxide synthase 1, is significantly enriched in cluster five, nine, and eleven. The anatomical distribution of nitric oxide expressing DR 5-HT neurons in rodents has been characterized previously as being predominately midline in the DR (***Fu et al., 2010***; ***Prouty et al., 2017***; ***Vasudeva et al., 2011***; ***Vasudeva and Waterhouse, 2014***). Cluster nine also shows enriched expression of *Crh*, encoding corticotropin-releasing hormone. Several other neuropeptide encoding genes show sporadic, significantly variable expression among different clusters, including growth hormone-releasing hormone (*Ghrh),* neuromedin B (*Nmb),* neuropeptide B (*Npb),* proenkephalin (*Penk),* and somatostatin (*Sst).*

Ionotropic and G protein-coupled receptors

Cluster one and cluster thirteen *Pet1* neurons show the most prominent specificity with respect to ionotropic receptor markers (***Figure 2*** Ionotropic Receptors), though in general we found relatively few *Pet1* neuron subtype-specific ionotropic gene markers relative to other categories of gene function. *Gabrq* and *Gabre*, encoding GABA type A receptor subunits theta and epsilon, respectively, are significantly enriched in cluster one, as well as *Gria1,* encoding glutamate ionotropic receptor AMPA type subunit 1. GABA type A receptor subunit gamma3 (*Gabrg3*) and glutamate ionotropic receptor NMDA type subunit 2A (*Grin2a*) transcripts are largely de-enriched in clusters two through four and twelve, are significantly enriched in cluster nine, and variably expressed in other clusters. GABA A receptor subunit alpha 2 (*Gabra2*) is expressed in all clusters but is significantly enriched in cluster twelve, and GABA A receptor subunit alpha 1 (*Gabra1*) and glutamate ionotropic receptor AMPA type subunit 3 (*Gria3*) transcripts both show significant enrichment in cluster thirteen.

Transcripts encoding G protein-coupled receptors (GPCRs) show patterns of enrichment largely across blocks of clusters (e.g. *Slc17a8*-expressing versus non-*Slc17a8*-expressing *Tph2-Pet1* neurons), or highly specific enrichment in either cluster twelve or clusters thirteen and fourteen (***Figure 2*** G Protein-Coupled Receptors). For example, cluster twelve neurons show strong enrichment for opioid receptor mu (*Oprm1*), purine receptor y1 (*P2ry1),* relaxin family peptide receptor 1 (*Rxfp1),* sphingosine-1-phosphate receptor *3* (*S1pr3*), and tachykinin receptor 3 (*Tacr3)* transcripts. Moreover, they lack expression of transcripts for many GPCRs expressed by the majority of other *Pet1* neurons, such as presynaptic 5-HT autoreceptors, encoded by *Htr1b* and *Htr1d*, as well as orexin and histamine receptors (e.g. *Hcrtr1*, *Hcrtr2*, *Hrh1*, *Hrh3*), whose protein products are involved in the regulation of arousal. We found that histamine receptor 1 (*Hrh1*) and hypocretin (alias orexin) receptor 1 (*Hcrtr1*) transcripts were the most abundant in clusters one through four, and histamine receptor 3 (*Hrh3*) transcripts were the most abundant in clusters two through six. Hypocretin receptor 2 (*Hcrtr2*) transcripts showed a somewhat complementary expression pattern, with the highest levels in clusters

seven through eleven, as well as cluster three. Other GPCR transcripts with notable expression patterns are neuropeptide Y receptor Y2 (*Npy2r*), enriched in clusters seven and ten, cannabinoid receptor 1 (*Cnr1*) and 5-HT receptor 2C (*Htr2c*), enriched in clusters thirteen and fourteen, and *Gpr101*, an 'orphan' GPCR thought to play a role in the growth hormone releasing-growth hormone signaling axis (GHRH-GH axis) (**Trivellin et al., 2016**; **Trivellin et al., 2018**), enriched in cluster fourteen.

Regulators of neuron projections, synaptic connectivity, and heparan sulfate proteoglycans

Similar to transcription factor expression patterns, most DR *Pet1* neuron subgroups can be classified by combinatorial enrichment of transcripts for genes encoding regulators of neuron projections and synaptic connectivity (**Figure 2** Regulators of Neuron Projections and Synaptic Connectivity). Differential expression of these genes likely contributes to differential innervation patterns of distinct DR *Pet1* neuron subgroups, such as reported by various studies (**Fernandez et al., 2016**; **Huang et al., 2019**; **Kast et al., 2017**; **Muzerelle et al., 2016**; **Niederkofler et al., 2016**; **Ren et al., 2018**; **Ren et al., 2019**; **Teng et al., 2017**). Genes encoding regulators of heparan sulfate proteoglycans may also play a role in projection specificity and synaptic organization (**Condomitti and de Wit, 2018**; **Di Donato et al., 2018**; **Lázaro-Peña et al., 2018**; **Minge et al., 2017**; **Zhang et al., 2018**), and likewise show patterns of enrichment across different *Pet1* neuron clusters (**Figure 2** Regulators of Heparan Sulfate Proteoglycans). For example, transcript expression of heparan sulfate-glucosamine 3-sulfotransferase 4 (*Hs3st4*) is enriched across clusters one through four, heparan sulfate-glucosamine 3-sulfotransferase 5 (*Hs3st5*) expression is significantly enriched in cluster ten (and expressed at high levels in clusters one, eight, nine, and eleven), and sulfatase 2 (*Sulf2*) and heparan sulfate-glucosamine 3-sulfotransferase 2 (*Hs3st2*) transcripts are enriched in cluster thirteen.

Intersectional genetic labeling of *Pet1* neuron subgroups in combination with histology and manual scRNA-seq reveals spatial distributions of DR *Pet1* neuron subtypes

Having identified transcriptomically distinct DR *Pet1* neuron subtypes in a largely unsupervised manner, we next sought to determine whether the cell bodies of these molecularly defined *Pet1* neuron subtypes show differential distributions within anatomical subfields of the DR. Using intersectional genetics to fluorescently label *Pet1* neuron subgroups defined by pairwise expression of *Pet1* and one of an assortment of identified subtype marker genes, we iteratively mapped molecular subtypes to anatomy in two ways – (1) using histology and microscopy to directly characterize cell body locations in fixed brain sections (**Figure 3**), and (2) performing manual scRNA-seq on labeled cells dissociated and hand sorted from microdissected anatomical subdomains of the DR, and comparing these expression profiles to our above described high-throughput scRNA-seq data (which we will refer to as our 10X scRNA-seq data) (**Figure 4**). We iteratively bred triple transgenic mice harboring (1) our *Pet1-Flpe* transgene, (2) one of two dual Flpe- and Cre- responsive reporter constructs (RC-FrePe or RC-FL-hM3Dq), and (3) one of five Cre-encoding transgenes (*Tg(Slc6a4-cre)*ET33Gsat (referred to as *Slc6a4-cre*), $Slc17a8^{tm1.1(cre)Hz}$ (referred to as *Slc17a8-cre*), $Npy2r^{tm1.1(cre)Lbrl}$ (referred to as *Npy2r-cre*), *Tg(Crh-cre)KN282Gsat/Mmucd* (referred to as *Crh-cre*), or $P2ry1^{tm1.1(cre)Lbrl}$ (referred to as *P2ry1-cre*), where *cre* expression is driven by either the endogenous promoter of the marker gene or by a gene-specific bacterial artificial chromosome (BAC). In selecting candidate markers from our list of differentially expressed genes, we sought gene drivers that could potentially divide *Pet1* neurons into subgroups at varying resolutions and were available as *cre* lines. Representative images for each triple transgenic genotype are given in **Figure 3** (organized by marker genes, columns A-E, at different rostrocaudal levels of the DR, rows 1–6). For each genotype, the intersectionally defined subpopulation of neurons is labeled in green (i.e. history of Flpe and Cre expression) whereas the 'subtractive' subpopulation is labeled in red (i.e. history of Flpe but not Cre expression).

Histology of *Pet1*-Intersectionally defined neuron populations

High *Slc6a4* expression, like high *Tph2* expression, defines *Pet1* neuron clusters one through eleven. Cluster twelve shows consistently lower mean expression of *Slc6a4* transcripts (and to a lesser extent *Tph2* transcripts) than clusters one through eleven (**Figure 3A**), cluster fourteen shows a broader

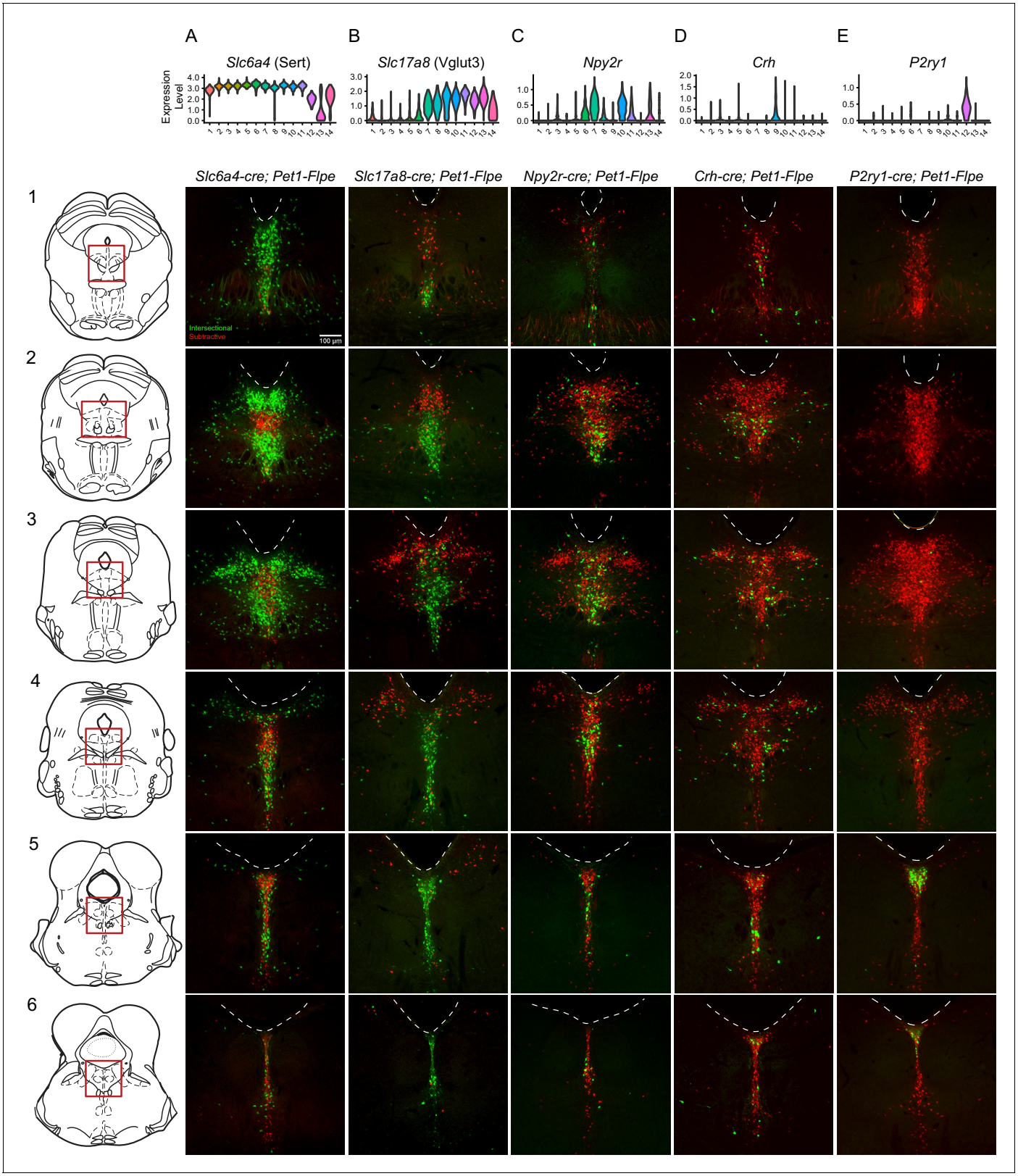

Figure 3. Intersectionally targeted *Pet1* neuron subtypes have different anatomical distributions in subregions of the DR. (**A–E**) Low magnification view of 40 µm coronal sections showing the DR from rostral to caudal (1-6) in triple transgenic animals. Cell bodies are labeled by the intersectional expression of a Cre driver of interest, *Pet1-Flpe*, and the intersectional allele RC-FrePe (green EGFP marked cells expressing both Cre and Flpe and red mCherry expressing *Pet1-Flpe* subtractive population) unless otherwise noted. (**A**) *Slc6a4-cre; Pet1-Flpe;* RC-FrePe, (**B**) *Slc17a8-cre; Pet1-Flpe;* RC-FL-

Figure 3 continued on next page

Figure 3 continued

hM3Dq (green mCherry-hM3Dq marked cells expressing Cre and Flpe and red EGFP expressing *Pet1-Flpe* subtractive population), (**C**) *Npy2r-cre; Pet1-Flpe;* RC-FrePe, (**D**) *P2ry1-cre; Pet1-Flpe;* RC-FrePe. Top row shows violin plots depicting transcript expression (10X scRNA-seq data) of the respective gene corresponding with each Cre driver. Scale bar (**A1**) equals 100 μm. The expression of TPH2 and VGLUT3 was further investigated in ***Figure 3—figure supplements 1*** and ***2***, respectively.

The online version of this article includes the following figure supplement(s) for figure 3:

Figure supplement 1. Diversity of *Tph2* RNA transcripts and protein expression in dorsal raphe *Pet1* neurons.

Figure supplement 2. VGLUT3 antibody staining of *Pet1* neurons is anatomically biased within different DR subdomains.

distribution of *Slc6a4* transcript levels (***Figure 3A***) and many 5-HT markers (***Figure 1—figure supplement 3***), and cluster thirteen shows very low levels of *Slc6a4* transcripts (***Figure 3A***) and other 5-HT markers (***Figure 1—figure supplement 3***). Consistent with the majority of profiled *Pet1* neurons expressing high levels of *Slc6a4* and *Pet1* transcripts, we detected intersectional *Slc6a4-cre; Pet1-Flpe* fluorescently marked neurons throughout the full rostrocaudal and dorsoventral extent of the DR (***Figure 3A1–A6***), however the subtractive population (presumably cluster thirteen and perhaps some cluster twelve and fourteen *Pet1* neurons) showed a more limited distribution. These subtractive (Flpe+ but Cre-) neurons were most conspicuously concentrated in the rostromedial DR (***Figure 3A2***), where only a few *Slc6a4-cre; Pet1-Flpe* intersectional (Flpe+ and Cre+) neurons were intermingled. More caudally, the Flpe-only subtractive neurons remained largely midline, but became more intermixed with the double-positive *Slc6a4-cre; Pet1-Flpe* intersectionally marked cells. As another way of anatomically characterizing putative cluster thirteen *Pet1* neurons, we immunostained for TPH2 in *En1-cre; Pet1-Flpe;* RC-FrePe mice (the same genotype as used in some of our 10X scRNA-seq experiments), and found that the distribution of TPH2 immunonegative *Pet1* neuron cell bodies showed a very similar distribution to the subtractive neurons (Flpe-only) in *Slc6a4-cre; Pet1-Flpe;* RC-FrePe mice. (***Figure 3—figure supplement 1A***), further confirming the existence of *Pet1*-expressing neurons that do not express TPH2 protein (***Barrett et al., 2016***; ***Pelosi et al., 2014***). To explicitly examine the relationship of *Tph2* transcript level to presence or absence of TPH2 protein, we additionally performed concurrent TPH2 immunostaining and *Tph2* single molecule fluorescent in situ hybridization in DR-containing brain sections of an *En1-cre; Pet1-Flpe;* RC-FrePe mouse (***Figure 3—figure supplement 1B–G***). Similar to our 10X scRNA-seq data, we found a bimodal distribution of *Tph2* transcript abundance, with the majority of single cells distributing in the higher mode (***Figure 3—figure supplement 1D***). Across all subregions of the DR analyzed, we found that dual EGFP and TPH2 immunopositive cells contained significantly more *Tph2* transcripts than EGFP immunopositive TPH2 immunonegative cells (p-value<0.01, Wilcoxon Rank Sum tests with Benjamini and Hochberg correction for multiple comparisons, see Materials and methods, ***Figure 3—figure supplement 1E***). However, as the TPH2 immunopositive and negative *Tph2* transcript distributions showed some overlap, cells with low *Tph2* transcript counts occasionally expressed TPH2 protein and cells with higher transcript counts occasionally did not. In particular we found that the third and fourth deciles (the 'transition zone' between modes) of the *Tph2* transcript distribution displayed the greatest degree of intermixing of TPH2 positive and negative cells (***Figure 3—figure supplement 1D***). Intriguingly, we also found that the somata of EGFP positive TPH2 negative cells were significantly smaller than dual EGFP and TPH2 positive cells (p-value<0.01, Wilcoxon Rank Sum tests with Benjamini and Hochberg correction for multiple comparisons, ***Figure 3—figure supplement 1F,G***).

Slc17a8-Pet1 expression defines *Pet1* neuron clusters seven through fourteen, and to a lesser extent cluster six (***Figure 3B***). We observed that *Slc17a8-cre; Pet1-Flpe* intersectionally marked neurons show a strong ventromedial bias in rostral portions of the DR (***Figure 3B1–B3***), and are the predominant *Pet1* neuron subgroup in the more caudal midline DR (***Figure 3B3–B6***). By contrast, the subtractive *Pet1* neuron subgroup (presumably comprising *Pet1* neurons from clusters one through five and partly six) show a strong dorsal and lateral bias and are largely absent from the most caudal portions of the DR. We further characterized VGLUT3 protein expression in *Pet1* neurons by VGLUT3 immunohistology in *Slc17a8-cre; Pet1-Flpe;* RC-FL-hM3Dq mice. We found consistent overlap between intersectional recombination marked neurons and VGLUT3 protein expression, especially in medial, ventromedial, and caudal portions of the DR (***Figure 3—figure supplement 1C–J***). In the

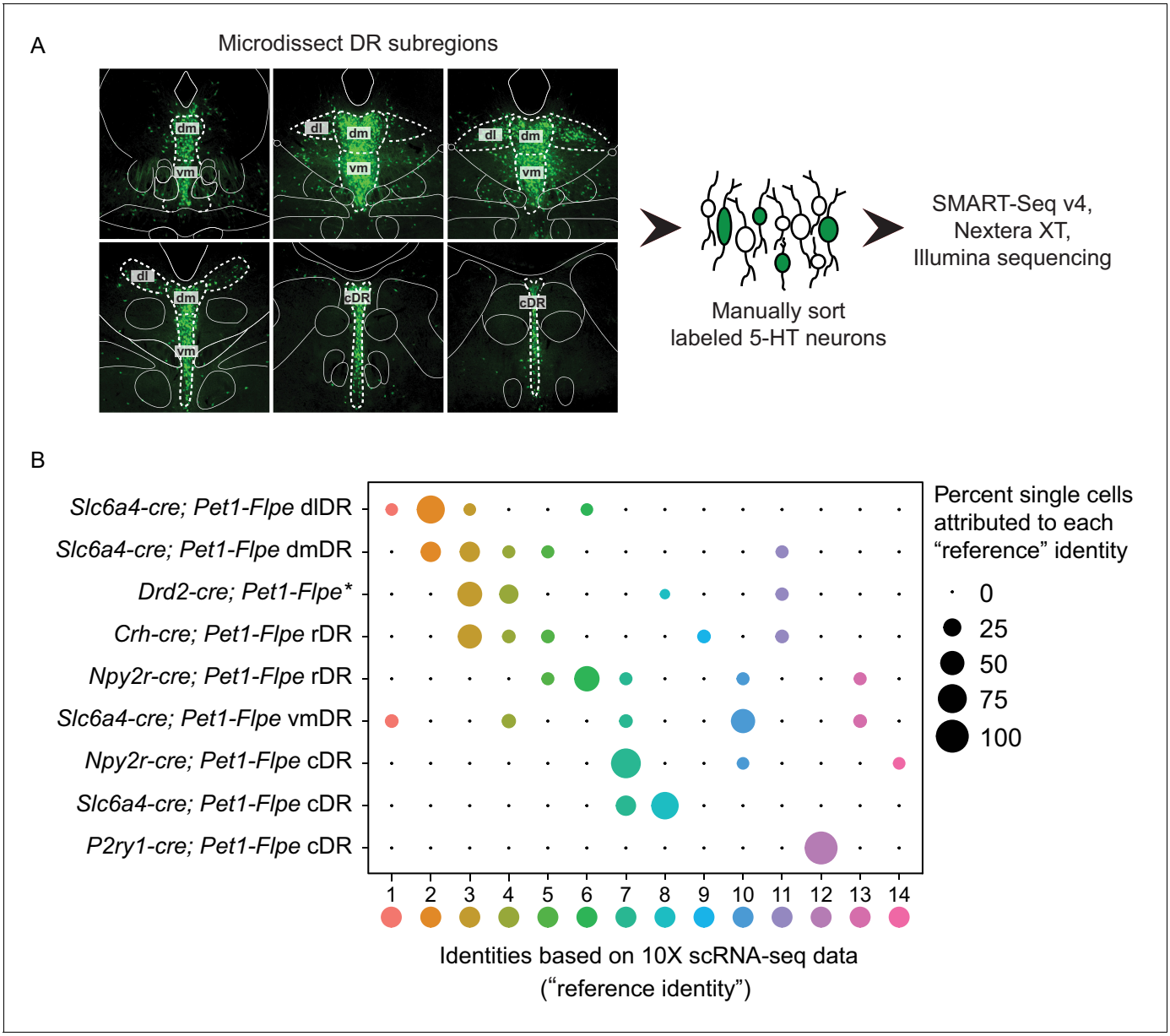

Figure 4. scRNA-seq of *Pet1* neurons manually sorted from anatomical subdomains map onto specific 10X scRNA-seq clusters. (**A**) Schematic of the pipeline used for manual sorting and sequencing, including referenced anatomical subdomains mapped onto representative images of the DR. *Pet1* neurons are in green. (**B**) Dot plot mapping manually sorted cells from a given genotype and anatomical subdomain (Y-axis) to the fourteen 10X clusters (X-axis). The size of the dot indicates the percentage of single cells from a genotype/anatomical region attributed to a reference cluster. Note, the asterisks after *Drd2-cre; Pet1-Flpe* is to denote that these data come from a previously published study (***Niederkofler et al., 2016***), and these particular single-cell libraries were prepared using the Nugen Ovation RNA-seq System v2 kit, rather than SMART-Seq v4. The expression of a selection of highly variable and cluster marker genes is depicted in ***Figure 4—figure supplement 1***.

The online version of this article includes the following figure supplement(s) for figure 4:

Figure supplement 1. Expression patterns of a selection of highly variable and cluster marker genes that show anatomical bias.

Figure supplement 2. PAX5 and SATB2 are expressed predominately in rostral dorsomedial and dorsolateral *Pet1* neurons while NR2F2 is expressed predominately in caudal *Pet1* neurons.

dorsal and lateral portions of the DR, however, where there are far fewer intersectionally labeled neurons, we observed a small number of *Slc17a8-cre; Pet1-Flpe* intersectionally marked neurons that were negative for VGLUT3 antibody staining, suggesting transient expression of *Slc17a8* (and

Slc17a8-cre) by these cells at an earlier time in their developmental history (or low *Slc17a8* expression sufficient to drive Cre expression, but not VGLUT3 immunodetection).

Transcripts for *Npy2r*, encoding the neuropeptide Y receptor Y2, are strongly enriched in clusters six, seven, and ten, with less consistent expression in clusters eleven, thirteen, and eight, and only sporadic expression elsewhere (**Figure 3C**). In mid-rostral portions of the DR, we found that *Npy2r-cre; Pet1-Flpe* intersectionally marked cell bodies show a largely midline bias, with a greater density of cells ventrally than dorsally, and the occasional labeled cell body appearing more laterally (**Figure 3C2–C3**). In more caudal extents of the DR, *Npy2r-cre; Pet1-Flpe* intersectionally marked cell bodies appear to be concentrated more medially (**Figure 3C4–C6**).

Transcripts for *Crh*, encoding corticotropin-releasing hormone, are most highly enriched in neurons comprising cluster nine and to a lesser extent cluster five, with sporadic expression in other clusters (**Figure 3D**). *Crh-cre; Pet1-Flpe* intersectionally labeled neurons do not show an obvious overall anatomical bias, distributing widely throughout the DR (**Figure 3D1–D6**). At the most rostral levels of the DR, they appear to be more consistently medially and ventrally localized (**Figure 3D1–D2**), but additionally appear in the dorsal and lateral DR at mid-rostral levels, and are preferentially localized off the midline more ventrally in these same sections (in regions sometimes referred to as the ventrolateral wings) (**Figure 2D3–D4**). At the most caudal levels they distribute dorsally and ventrally, with an apparent gap between these two domains (**Figure 3D5–D6**).

The most molecularly distinct *Pet1* neuron subtype we identified, cluster twelve *Met-Slc17a8-Tph2-Pet1* neurons, shows highly specific enrichment for a number of transcripts, including *P2ry1*, encoding purinergic receptor P2Y1, which is only sporadically expressed in other clusters (**Figure 3E**). *P2ry1-cre; Pet1-Flpe* intersectionally marked neurons likewise show a strikingly unique anatomical distribution from the other subgroups examined, being largely restricted to the caudal DR where they are densely clustered dorsally, just beneath the aqueduct (**Figure 3E5–E6**). This is consistent with previous characterizations of *Met*-expressing *Pet1*/5-HT neurons (**Okaty et al., 2015**; **Wu and Levitt, 2013**), as well as other more recent characterizations (**Huang et al., 2019**; **Kast et al., 2017**; **Ren et al., 2019**). Notably the distribution of *P2ry1-cre; Pet1-Flpe* intersectional neurons within the cDR is distinct from *Npy2r-cre; Pet1-Flpe* intersectional neurons, and only partially overlaps with where *Crh-cre; Pet1-Flpe* intersectional neurons are found, arguing for *Pet1*/5-HT neuron subtype diversity within the caudal DR, consistent with (**Kast et al., 2017**).

It should be noted that the precise anatomical boundaries of the caudal DR (cDR), also referred to as B6 (**Dahlstroem and Fuxe, 1964**; **Jacobs and Azmitia, 1992**), are variably described in the literature. Alonso and colleagues divide B6 into dorsal and ventral sub-compartments, referred to as r1DRd and r1DRv, respectively, where 'r1' designates the putative developmental domain of origin of *Pet1* neurons residing in this DR subregion (i.e. originating from r1, as opposed to isthmus) (**Alonso et al., 2013**). r1DRv likely corresponds to what others have described as the caudal portion of the 'interfascicular' DR (DRI), a medioventral band of DR cells flanked on either side by the medial longitudinal fasciculi. 5-HT neurons of the caudal DRI merge with the more dorsal B6 DR sub-nucleus roughly at the level of the DR where dorsolateral 5-HT neurons become sparse (coronal sections 5 and 6 in **Figure 3**; **Hale and Lowry, 2011**; **Jacobs and Azmitia, 1992**). Depending on the plane and angle of sectioning these caudal DRI cells also appear to merge with MR 5-HT neurons more ventrally, and it has been proposed that caudal DRI cells may be more similar to MR 5-HT neurons developmentally, morphologically, and hodologically than to DR 5-HT neurons (**Commons, 2015**; **Commons, 2016**; **Hale and Lowry, 2011**; **Jacobs and Azmitia, 1992**). In the present study, our designation of cDR is inclusive of r1DRd/r1DRv/caudal DRI/B6, as indicated in **Figure 4A**. Moreover, we do not discount the possibility that this region as drawn partially overlaps with what Alonso and colleagues would call the most dorsal portion of the caudal median raphe (MnRc), as the boundary between the MnRc and r1DRv is poorly defined. Thus, the territory between the cluster of *Met-Slc17a8-Tph2-Pet1* neurons beneath the aqueduct in the cDR and the MR is difficult to classify strictly based on cytoarchitecture, underscoring the importance of alternative classification schemes, such as offered by transcriptomics.

Manual scRNA-seq of *Pet1*-Intersectionally defined neuron populations

Having mapped the spatial distributions of intersectionally labeled *Pet1* neuron subgroups, next we wanted to explore the correspondence of molecular subtype identity with DR subregions more comprehensively. To do this, we microdissected subdomains of the DR in a subset of the intersectional

mouse lines just described, dissociated and sorted fluorescently labeled neurons, harvested mRNA from single cells, and prepared scRNA-seq libraries (n = 70 single-cell libraries in total) using the SMART-Seq v4 kit, followed by Illumina sequencing (**Figure 4A**). Specifically, we separately microdissected and manually sorted *Slc6a4-cre; Pet1-Flpe* intersectionally labeled neurons from the dorsolateral DR (dl or dlDR, n = 10 cells), dorsomedial DR (dm or dmDR, n = 9 cells) ventromedial DR (vm or vmDR, n = 8 cells), and caudal DR (cDR, n = 6 cells), as schematized in **Figure 4A**. Additionally, we separately microdissected and manually sorted *Npy2r-cre; Pet1-Flpe* intersectional neurons from the rostral (rDR, n = 9 cells) versus caudal (n = 10 cells) DR, *P2ry1-cre; Pet1-Flpe* intersectional neurons from the cDR (n = 10 cells), and *Crh-cre; Pet1-Flpe* intersectional neurons from the rostromedial DR (n = 8 cells). We then used the fourteen *Pet1* neuron subtype identities derived from our 10X scRNA-seq data as a reference to 'query' the corresponding identities of our manually sorted and transcriptomically profiled single cells (using the Seurat functions FindTransferAnchors and TransferData as described in **Stuart et al., 2019**). A summary of this analysis is shown in the dot plot in **Figure 4B**. We found that the majority of *Slc6a4-cre; Pet1-Flpe* dlDR neurons mapped to cluster two, with a smaller percentage of single cells mapping to clusters one, three, and six. *Slc6a4-cre; Pet1-Flpe* dmDR neurons were split between clusters two and three, and to a lesser extent four, five, and nine. *Slc6a4-cre; Pet1-Flpe* vmDR neurons mostly corresponded to cluster ten, and were additionally mapped to clusters one, four, seven, and thirteen (note, this may suggest that some *Pet1* neurons expressing little or no *Slc6a4* nor *Tph2* in the adult may yet express the *Slc6a4-cre* transgene). Finally, *Slc6a4-cre; Pet1-Flpe* cDR neurons mapped exclusively to clusters eight and seven (note, cluster twelve neurons do not appear to be well marked by *Slc6a4-cre; Pet1-Flpe;* RC-FrePe EGFP expression – see **Figure 3A5** compared with **Figure 3E5** – perhaps reflecting the lower levels of *Slc6a4* transcripts detected in these neurons).

The majority of *Npy2r-cre; Pet1-Flpe* neurons in the rDR were found to correspond to cluster six, with additional mapping to clusters five, seven, ten, and thirteen (consistent with the expression profile of *Npy2r* transcripts in the 10X scRNA-seq data) whereas the majority of *Npy2r-cre; Pet1-Flpe* neurons from the cDR were found to correspond to cluster seven, with a smaller percentage corresponding to clusters ten and fourteen. *P2ry1-cre; Pet1-Flpe* cDR manually sorted and profiled neurons were mapped exclusively to cluster twelve as expected. *Crh-cre; Pet1-Flpe* profiled neurons were split across clusters in a manner consistent with sporadic *Crh* expression in our 10X scRNA-seq data, however, we found more cluster three than cluster nine *Crh-cre; Pet1-Flpe* neurons, perhaps reflecting that our sampling of this population was biased towards rostromedial DR (or a potential discrepancy between endogenous *Crh* expression and *Crh-cre* expression). Finally, we also included *Drd2-cre; Pet1-Flpe* intersectional scRNA-seq data (n = 17 cells) associated with a previous study from our lab (**Niederkofler et al., 2016**). *Drd2-cre; Pet1-Flpe* intersectional neurons show a largely dorsolateral and dorsomedial bias within the DR. The majority of these neurons map to clusters three and four, with a much smaller percentage mapping to clusters eight and eleven.

Thus combining intersectional genetics, histological analyses, and precisely targeted manual scRNA-seq we were able to infer the anatomical distributions of our fourteen clusters to varying degrees of specificity. Clusters one through six appear to be rostrally and dorsally biased, with cluster two showing a strong dorsolateral bias as well. Clusters seven, eight, and twelve appear to be caudally and medially biased, with cluster twelve showing a clear dorsal bias and clusters seven and eight showing more ventral bias based on **Figures 3** A5-6, C5-6 (though a nontrivial degree of intermixing of different genetically defined *Pet1* neuron subpopulations in the dorsal cDR is apparent from these images). *Pet1-Tph2*^{low} neurons (comprising cluster thirteen and to a lesser extent cluster fourteen neurons) show a prominent enrichment in the dorsomedial and medial-rostral DR, though they are also scattered throughout the DR (but very rarely found dorsolaterally). The remaining clusters appear to be more ventromedially biased in the more rostral DR. Expression patterns of cluster marker genes showing strong anatomical biases in our manual scRNA-seq data are depicted in the dot plot in **Figure 4—figure supplement 1** in comparison with our 10X scRNA-seq data.

These inferred anatomical distributions of molecularly distinct *Pet1* neuron populations shed further light on the potential developmental significance of transcription factor expression patterns described above. As noted, *Pax5*, a gene associated with isthmic organizer activity during embryonic development (**Funahashi et al., 1999**; **Ye et al., 2001**), shows a complementary expression pattern to *Nr2f2*, which encodes a transcription factor that appears to be excluded from the isthmus, but is expressed in r1 and other rhombomeres during development, at least in zebrafish (**Love and Prince,**

2012). We further validated the anatomical expression profile of these genes, as well as *Satb2* (expressed by cluster two through four), at the level of protein expression by performing immunohistology in tissue sections prepared from *Slc17a8-cre; Pet1-Flpe;* RC-FL-hM3Dq mice (***Figure 4—figure supplement 2A–E***). Consistent with our anatomically-targeted, manual scRNA-seq data, PAX5 and SATB2 display a rostrodorsal bias in predominately non-*Slc17a8*-expressing DR *Pet1* neurons (***Figure 4—figure supplement 2B–C,E***), whereas NR2F2 has a ventromedial and caudal expression bias in predominately *Slc17a8*-expressing DR *Pet1* neurons (***Figure 4—figure supplement 2D,E***). Alonso and colleagues have proposed that cDR *Pet1* neurons are derived from r1 progenitors, whereas more rostral *Pet1* neurons are derived from isthmus (***Alonso et al., 2013***), however further fate-mapping experiments would be helpful to clarify isthmic versus r1-derived *Pet1* neuron populations (***Okaty et al., 2019***). Moreover, while rostral DR *Pet1* neurons may derive from isthmus and cDR *Pet1* neurons may derive from r1, our scRNA-seq data nonetheless show substantial *Pet1* neuron molecular heterogeneity within both DR domains, suggesting factors beyond isthmus and r1-lineage driving molecular diversity.

cDR *P2ry1-cre; Pet1-Flpe* neurons display unique hodological and electrophysiological properties

Having established correlations between DR *Pet1* neuron molecular expression profiles and anatomical distribution of cell bodies, we next wanted to explore corresponding differences in other cellular phenotypes. We chose to focus on cluster twelve *Met-Slc17a8-Tph2 Pet1* neurons, captured intersectionally by *P2ry1-cre; Pet1-Flpe,* as they are the most distinct from other *Pet1* neurons molecularly. To determine if these neurons are likewise unique from other DR *Pet1* neurons with respect to other features we explored the hodological and electrophysiology properties of *P2ry1-cre; Pet1-Flpe* neurons using the intersectional expression of TdTomato (*GT(ROSA)26Sor*$^{tm65.1(CAG\text{-}tdTomato)Hze}$, referred to as RC-Ai65). The anatomical location of cell somata labeled in *P2ry1-cre; Pet1-Flpe;* RC-Ai65 animals was similar to that found in the previously characterized *P2ry1-cre; Pet1-Flpe;* RC-FrePe mice, with a dense population of neurons directly under the aqueduct in the cDR. In addition, there were slightly higher numbers of intersectionally labeled cells in the rostral part of the dorsal raphe as well as scattered cells in the median raphe, consistent with the sporadic expression of *P2ry1* revealed by the present RNA-seq data and the scRNA-seq data of *Pet1* neurons from the MR (***Okaty et al., 2015***; ***Ren et al., 2019***). Strikingly, most fibers from *P2ry1-cre; Pet1-Flpe;* RC-Ai65 neurons were supra-ependymal and were found throughout the third, lateral, and fourth ventricles, a property previously attributed to 5-HT neurons within the cDR (***Kast et al., 2017***; ***Mikkelsen et al., 1997***; ***Tong et al., 2014***). Sparser fibers were found in regions such as the lateral hypothalamus, medial and lateral septum, hippocampus, olfactory bulb, lateral parabrachial nucleus, and the amygdala. To gain a better perspective of the extent of *P2ry1-cre; Pet1-Flpe;* RC-Ai65 fibers in the lateral ventricle we stained for *P2ry1-cre; Pet1-Flpe;* RC-Ai65 fibers on a flat mount of the lateral wall as previously described (***Mirzadeh et al., 2010***). *P2ry1-cre; Pet1-Flpe;* RC-Ai65 fibers were found on all aspects of the wall except for the adhesion area, including regions that contain proliferating cells and migrating neuroblasts from the subventricular zone (***Mirzadeh et al., 2010***; ***Figure 5***). Further, *P2ry1-cre; Pet1-Flpe;* RC-Ai65 fibers were closely apposed to proliferating cells (Ki67+) and migrating neuroblasts (doublecortin, DCX+) within the subventricular zone (SVZ) and within the rostral migratory stream (RMS) (***Figure 5***). The proximity of *P2ry1-cre; Pet1-Flpe;* RC-Ai65 fibers to adult neural stem cells suggests that they may constitute a serotonergic population of neurons that regulate SVZ proliferation, a process known to be regulated by 5-HT levels and that has previously been associated with the cDR (***Aghajanian and Gallager, 1975***; ***Banasr et al., 2004***; ***Brezun and Daszuta, 1999***; ***Hitoshi et al., 2007***; ***Kast et al., 2017***; ***Lorez and Richards, 1982***; ***Mirzadeh et al., 2010***; ***Negoias et al., 2010***; ***Siopi et al., 2016***; ***Soumier et al., 2010***; ***Tong et al., 2014***).

To determine if supra-ependymal projections are unique to *Pet1* neurons in the caudal dorsal raphe, we injected a retrograde AAV virus leading to expression of Cre under the synapsin promoter (pENN.AAV.hSyn.Cre.WPRE.hGH) unilaterally into the lateral ventricle of double transgenic *Pet1-Flpe;* RC-FrePe or *Pet1-Flpe;* RC-Ai65 mice, where expression of both Cre and Flpe leads to cell labeling by EGFP or TdTomato respectively (***Figure 5—figure supplement 1A***). The predominant labeled population in both genotypes was in the cDR, just under the aqueduct, suggesting that *P2ry1-cre; Pet1-Flpe* neurons constitute the major supraependymal projecting group of *Pet1* neurons (***Figure 5—figure supplement 1B,C***). However, in agreement with other studies that have included

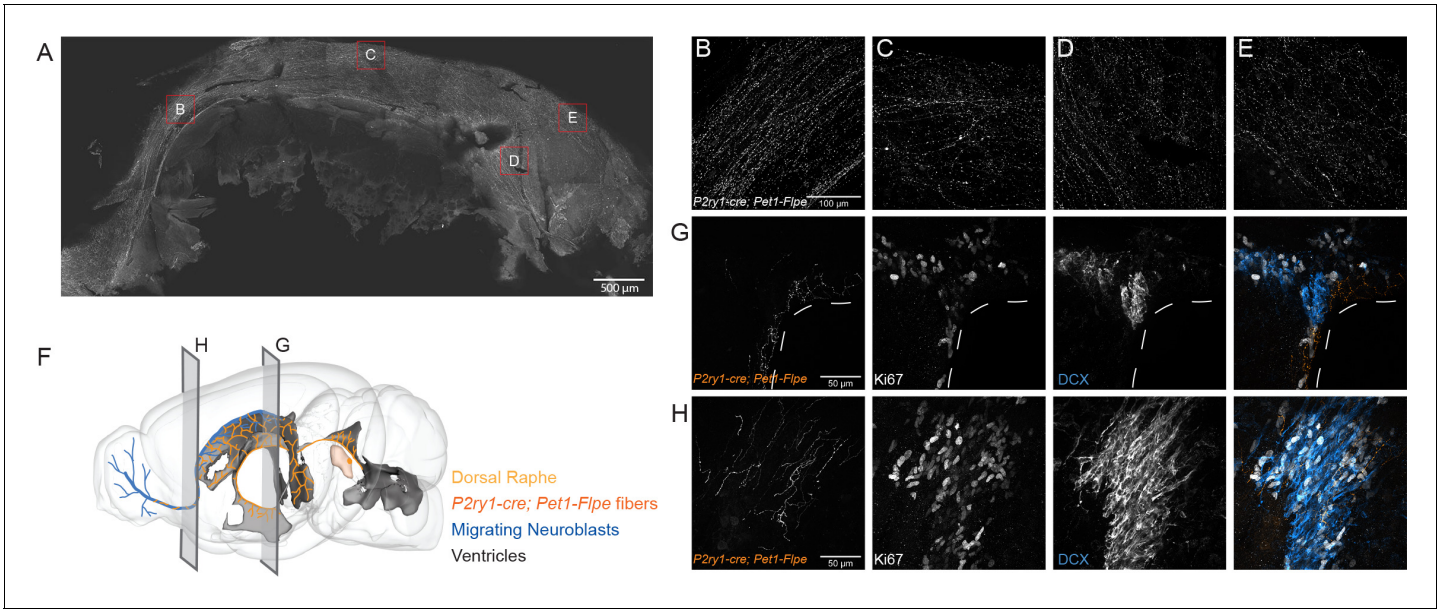

Figure 5. *P2ry1-cre; Pet1-Flpe* neurons project throughout the ventricles and their fibers are in close apposition to proliferating cells in the SVZ and RMS. (**A**) Flat mount of the lateral wall of the lateral ventricle of a *P2ry1-cre; Pet1-Flpe;* RC-Ai65 animal, where *P2ry1-cre; Pet1-Flpe* fibers are in grey. Scale bar = 100 µm. (**B–E**) High magnification confocal images from regions of the lateral wall represented in red boxes in A. Scale bar (**B**) = 100 µm. (**F**) 3D brain schematic showing the *P2ry1-cre; Pet1-Flpe* cell bodies (dark orange) in the caudal part of the DR (light orange) and fibers (dark orange) projecting through the ventricles (grey) and along the migrating neuroblasts of the rostral migratory stream (RMS, blue). (**G–H**) Coronal confocal images depicting *P2ry1-cre; Pet1-Flpe* fibers (orange) from *P2ry1-cre; Pet1-Flpe;* RC-Ai65 animals in the SVZ (**G**) and RMS (**H**). Proliferating cells labeled with Ki67 (grey) and migrating neuroblasts labeled with doublecortin (DCX, blue). Scale bar (**G, H**) = 50 µm.
The online version of this article includes the following figure supplement(s) for figure 5:

Figure supplement 1. The caudal dorsal raphe is the major *Pet1* neuron source of supra-ependymal fibers.

retrograde labeling via the lateral ventricle, some cell bodies were also found in the median raphe (***Kast et al., 2017***; ***Tong et al., 2014***). Thus, supra-ependymal projections, while predominantly originating from the cDR, are not entirely unique to this region.

We next characterized electrophysiological properties of *P2ry1-cre; Pet1-Flpe;* RC-Ai65 neurons in comparison with other more broadly defined *Pet1* neuron subpopulations using whole-cell patch clamp in acute slice preparations. As comparison groups we chose: (1) 'subtractive' *P2ry1-cre; Pet1-Flpe;* RC-FL-hM3Dq neurons in the cDR (i.e. cDR neurons with a history of *Pet1-Flpe* expression but not *P2ry1-cre* expression; we chose to use RC-FL-hM3Dq as opposed to RC-Ai65 or RC-FrePe because the subtractive population is identifiable in acute brain slices by EGFP fluorescence without the need for secondary staining), and (2) *Pet1* neurons from the more rostral and mostly dorsal DR using labeled intersectional expression of *Gad2*$^{tm2(cre)Zjh}$ (referred to as *Gad2-cre*) with *Pet1-Flpe;* RC-Ai65 (***Figure 6***). Recording from *P2ry1-cre; Pet1-Flpe;* RC-FL-hM3Dq subtractive cDR neurons allowed us to assess the degree to which electrophysiology may differ within a given DR subdomain depending on molecularly-defined neuron subtype, whereas *Gad2-cre; Pet1-Flpe;* RC-Ai65 neuron recordings provided a comparison group that is both anatomically and molecularly distinct. As demonstrated in the frequency-current (F-I) curves in ***Figure 6A***, we found that *P2ry1-cre; Pet1-Flpe;* RC-Ai65 neurons have dramatically lower excitability than the two comparison populations, requiring substantially more injected current to reach action potential threshold, and showing a roughly three-fold lower maximum firing rate. Even within the regime of current injection that *P2ry1-cre; Pet1-Flpe;* RC-Ai65 neurons are excitable, we found that they displayed very different spiking characteristics from other *Pet1* neuron groups (***Figure 6B,C***), specifically showing a longer latency to first action potential (AP, ***Figures 6B*** and ***3***). Altogether, we observed four distinct firing types exemplified by the voltage traces displayed in ***Figure 6B***: short-latency to first AP (regular spiking/non-adapting) (***Figures 6B*** and ***1***), mid-latency to first AP (***Figures 6B*** and ***2***), long-latency to first AP (***Figures 6B*** and ***3***), and short-latency to first AP with spike frequency adaptation (***Figures 6B*** and ***4***). The

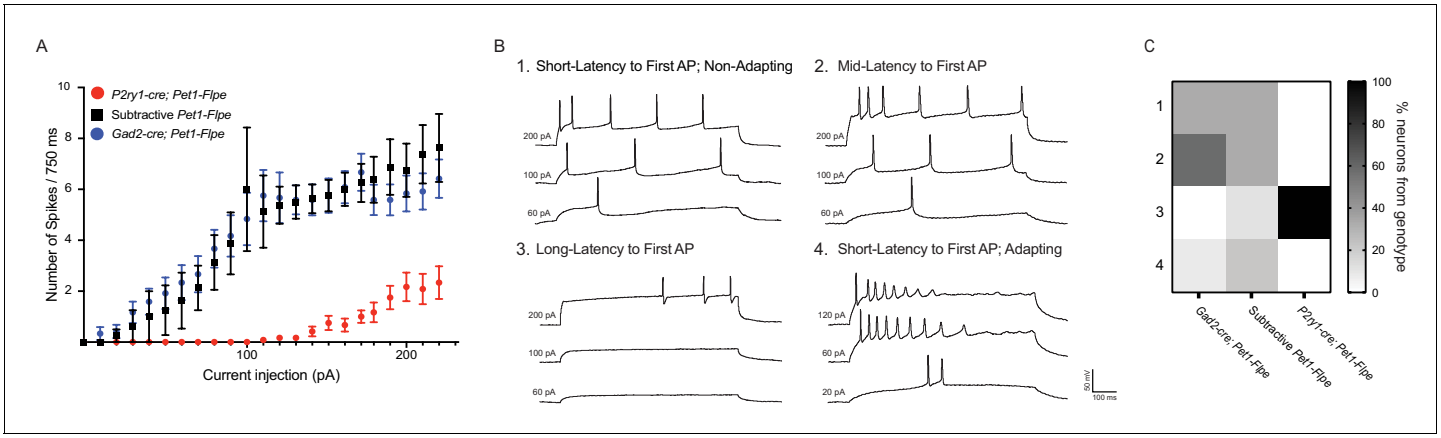

Figure 6. *P2ry1-cre; Pet1-Flpe* neurons have a distinct firing phenotype. (**A**) Frequency-Current (**F–I**) curves show *P2ry1-cre; Pet1-Flpe* neurons (tdTomato$^+$ *P2ry1-cre; Pet1-Flpe;* RC-Ai65, n = 12; three animals; red circles) are less excitable than nearby caudal dorsal raphe non-*P2ry1-cre; Pet1-Flpe* populations (EGFP$^+$ *P2ry1-cre; Pet1-Flpe;* RC-FL-hM3Dq, n = 8; three animals; black squares) or neurons from the dorsomedial and dorsolateral dorsal raphe *Gad2-cre; Pet1-Flpe* population (tdTomato$^+$ *Gad2-cre; Pet1-Flpe;* RC-Ai65, n = 12; two animals; blue circles) p<0.0001 Kruskal-Wallis test. (**B**) Example voltage traces from neuron patch-clamp recordings showing different firing types, specifically a neuron that started firing action potentials with (1) short latency (mean = 17.32 ms±6.61 at 200 pA), in response to 750 ms current pulses, (2) medium latency (mean = 64.18 ms±9.8 at 200 pA), (3) long latency (mean = 476.55 ms±223.64 at 200 pA), or (4) short latency (mean = 12.6 ms±5.9 at 200 pA) with spike-frequency adaptation. (**C**) Heat map shows the percentage of cells recorded from each genotype corresponding to each firing type, note all recorded *P2ry1-cre; Pet1-Flpe* neurons belong to type 3.

The online version of this article includes the following figure supplement(s) for figure 6:

Figure supplement 1. Key membrane properties distinguish serotonergic neuron firing types.

heatmap in ***Figure 6C*** shows the percentage of single-neuron recordings from each genotype that correspond to a given firing type. ***Figure 6—figure supplement 1*** displays differences in measured electrophysiological properties when cells are grouped by firing type, as opposed to genotype. All *P2ry1-cre; Pet1-Flpe;* RC-Ai65 neurons recorded (twelve neurons from three animals) showed long latency to first AP, whereas only one out of nine subtractive neurons in the *P2ry1-cre; Pet1-Flpe;* RC-FL-hM3Dq cDR (from three animals) showed this phenotype and none of the *Gad2-cre; Pet1-Flpe;* RC-Ai65 neurons (twelve neurons from two animals). These latter two groups of neurons showed greater heterogeneity with respect to firing characteristics, as might be expected given that labeled cells from both genotypes comprise multiple molecular subtypes identified by our scRNA-seq experiments. While the full extent of electrophysiological heterogeneity of these populations is likely under-sampled by the present dataset, the uniqueness of *P2ry1-cre; Pet1-Flpe;* RC-Ai65 neurons nonetheless stands out.

Comparison to other DR scRNA-seq datasets

Recent scRNA-seq studies of mouse DR cell types have been published (***Huang et al., 2019***; ***Ren et al., 2019***), reporting using either the InDrops platform to profile dissociated DR neurons (***Huang et al., 2019***) or fluorescence-activated cell sorting to purify dissociated Cre-dependent tdTomato-expressing *Slc6a4-cre* neurons from mouse DR and MR, followed by SMART-Seq v2 library preparation and sequencing (***Ren et al., 2019***). Huang and colleagues identified six distinct *Pet1*-expressing DR neuron subtypes – five serotonergic and one glutamatergic – while Ren and colleagues identified seven *Pet1*-expressing serotonergic DR neuron subtypes (note they did not identify a glutamatergic *Tph2*^{low} group, presumably because these neurons do not typically express *Slc6a4-cre*). To directly compare our subtype classifications, we used the fourteen *Pet1* neuron subtype identities derived from our 10X scRNA-seq data as a reference to query the corresponding identities of the Huang and Ren datasets (using the Seurat functions FindTransferAnchors and TransferData, as described above for comparison with our manual scRNA-seq data). The results of this analysis are shown in the dot plot in ***Figure 7***. Some *Pet1* neuron subgroup classifications were highly consistent across studies. For example, one hundred percent of single neurons making up the

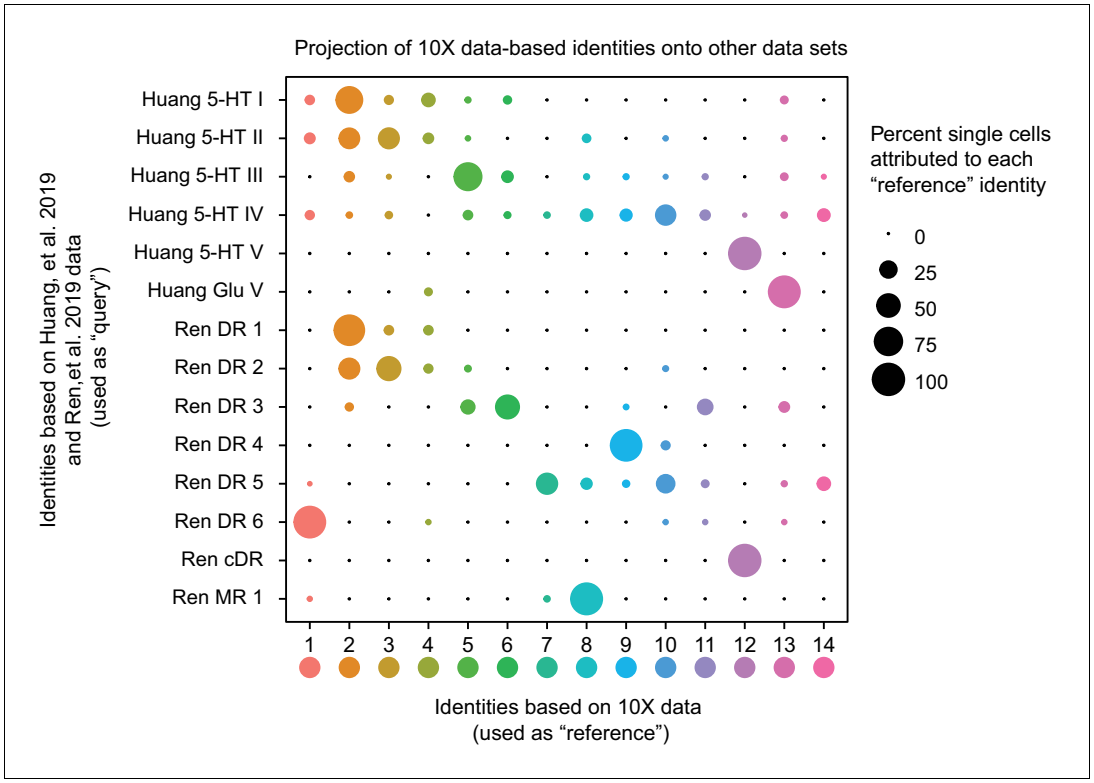

Figure 7. Correspondence of serotonin subtypes identified in previous studies (Y-axis) to the fourteen 10X scRNA-seq clusters identified in this study (X-axis). The size of the dot indicates the percentage of single cells from the original cluster that are attributed to a given reference cluster.

The online version of this article includes the following figure supplement(s) for figure 7:

Figure supplement 1. The number of cells sampled and the max UMIs per cell influence the number of clusters found in the dataset.

Huang 5-HT V and Ren cDR subgroups map to our cluster twelve *Pet1* neuron subgroup (*Met-Slc17a8-Tph2-Pet1* neurons, corresponding to neurons intersectionally captured by *P2ry1-cre; Pet1-Flpe* expression in the cDR shown in ***Figure 3E***). Likewise, there is high correspondence between Huang 5-HT I, Ren DR 1, and our cluster two *Pet1*-neuron subgroup (dorsolateral DR *Gad2-Trh-Tph2-Pet1* neurons). Huang 5-HT II and Ren 2 subgroups are largely split between our cluster two and cluster three subgroups, with a smaller portion of each mapping to our cluster four subgroup (which also corresponds to a small subset of Huang 5-HT I and Ren DR 1 neurons). Huang 5-HT III and Ren DR 3 correspond to our cluster five and six subgroups, with a larger percentage of Huang 5-HT III neurons mapping to cluster five and a larger percentage of Ren DR 3 neurons mapping to cluster six.

In other cases, there is better correspondence between our identified *Pet1* neuron subgroups and one or the other study, likely due in part to technological differences between studies. For example, Huang Glu V corresponds well with our cluster thirteen *Pet1* neuron subgroup (*Slc17a8-Tph2^{low}-Pet1* neurons) but very few neurons profiled in the Ren study map to cluster thirteen. As mentioned above, the absence of a prominent glutamatergic *Tph2^{low}* group of neurons in the Ren study likely stems from the fact that the low level of *Slc6a4* transcription in these neurons does not reliably drive *Slc6a4-cre* transgene expression and thus reporter expression for their cell sorting. However, the fact that a small number of *Slc6a4-cre* expressing neurons from the Ren study do map to our cluster thirteen subgroup indicates that there may be exceptions (moreover, these cells may more specifically map to cluster thirteen neurons at the higher end of the distribution of *Slc6a4* and *Tph2* transcript levels ***Figure 1—figure supplement 3***).

On the other hand, Ren DR 6 corresponds well with our cluster one subgroup (*Npas1/3-Tph2-Pet1* neurons) and Ren DR 4 corresponds well with our cluster nine subgroup (*Maf-Nos1-Tph2-Pet1*

neurons), but there is no such one-to-one correspondence between these groups and the neuron groups identified in the Huang study. Rather, cluster one and cluster nine neurons get 'pulled' from other groups identified by Huang. This likely reflects the different sensitivities of the various approaches. Specifically, our study and the Ren study achieved more than three-fold higher gene detection per single cell library on average than the Huang study, thus allowing for finer-scale molecular subgroup classification. However our higher single-cell sampling resolution – we profiled 2,350 DR *Pet1* neurons, whereas Huang and Ren profiled roughly 700 and 600 DR *Pet1* neurons, respectively – likely allowed us to resolve more subgroups. Huang 5-HT IV and Ren DR 5 show the greatest degree of dispersion into different clusters identified in our study. Ren DR 5 is split predominately between clusters seven, ten, and fourteen, while Huang 5-HT IV is split into clusters ten and fourteen, as well as across several other clusters. Lastly, we also found that Ren MR 1 (identified as being a median raphe 5-HT neuron subtype in that study) shows similarity to our cluster eight subgroup, which we have mapped to the cDR based on histology and our manual scRNA-seq data. As described above, the boundary between the cDR and the MR, specifically the portion of the MR attributed to r1-derived neurons (***Alonso et al., 2013***; ***Okaty et al., 2015***), is poorly defined, thus Ren MR 1 and our cluster eight neurons may indeed partially overlap anatomically. Notably, some Huang 5-HT IV neurons (microdissected from what was considered the DR in that study) also map to our cluster eight subgroup.

Importantly, our higher number of identified clusters does not appear to stem from analytic differences between studies per se, given that we identified more clusters using a lower resolution parameter in our clustering analysis than the other two studies. Huang, et al. reported using a Seurat FindCluster resolution of 2.0, Ren, et al. used a resolution of 1.0, whereas the highest resolution we used was 0.9. In order to explicitly investigate how specific aspects of our experimental design may have led to identification of more DR *Pet1* neuron subgroups than the other two studies, we modeled how the number of cells sampled and the number of UMIs identified per cell influence the number of identified clusters in our dataset. Specifically, we randomly sub-sampled variable numbers of cells (twenty times per iteration) and re-clustered the resulting data in the same manner described for the full dataset (using a Seurat FindClusters resolution of 0.9), varying the number of sampled cells from 200 to 2,300 (***Figure 7—figure supplement 1A***). As expected, we found that increasing the number of cells increased the number of clusters. Identification of fourteen clusters did not occur until at least 1,700 cells were included in the analysis, and this number of clusters began to stabilize as 2,100 or more cells were included. Similarly, we randomly sub-sampled UMIs, varying the maximum number of UMIs per cell from 500 to 100,000, and repeated our clustering analysis twenty times per sub-sampled max UMI (***Figure 7—figure supplement 1B***). In this case we found a much steeper relationship between max UMIs and number of clusters identified, with fourteen clusters being identified with as few as 4,500 max UMIs per cell, and completely stabilizing at roughly 60,000 max UMIs. With respect to our ability to resolve fine-scale DR *Pet1* neuron subgroup structure, these results indicate that while both variables are important, the number of cells sampled was more limiting than the number of UMIs in our dataset; that is, we could have uncovered a similar degree of overall cellular diversity (fourteen subtypes) with less 'complex' libraries (e.g. from more shallow sequencing), however we needed nearly 90% of the cells we sampled to consistently uncover fourteen molecular subgroups.

The results of these analyses shed light on the most likely reasons why we were able to achieve more fine-grained classification of DR *Pet1* neuron subtypes than the other two studies. For example, the Ren study had a similar degree of library complexity to ours (slightly higher, in fact), however as noted above they profiled fewer cells – 567 to our 2,350 cells (~2,200 excluding *Tph2-low* cells). When we sub-sample our data to a similar number of cells, we find between six and nine clusters, and similarly, Ren, et al. reported seven DR 5-HT neuron clusters. When we simultaneously sub-sample both the number of cells profiled and the maximum number of UMIs detected per single cell to levels similar to the Huang, et al. study (750 cells and 2,500 max UMIs, ***Figure 7—figure supplement 1C***), we uncover between four and seven subgroup clusters – Huang, et al. found six. Thus, all other methodological sources of variation between studies aside, these two parameters plausibly explain differences in the degree of diversity uncovered across studies.

Discussion

The dorsal raphe nucleus is likely one of the most extensively connected hubs in the mammalian brain. Efferent DR fibers, predominantly serotonergic (but also glutamatergic and GABAergic), collectively innervate much of the forebrain and midbrain, as well as some hindbrain nuclei (**Azmitia and Segal, 1978**; **Bang and Commons, 2012**; **Bang et al., 2012**; **Beaudet and Descarries, 1976**; **Fernandez et al., 2016**; **Gagnon and Parent, 2014**; **Hale and Lowry, 2011**; **Kast et al., 2017**; **Kosofsky and Molliver, 1987**; **Lidov et al., 1980**; **Lidov and Molliver, 1982**; **Maddaloni et al., 2017**; **McDevitt et al., 2014**; **Molliver, 1987**; **Muzerelle et al., 2016**; **O'Hearn and Molliver, 1984**; **Prouty et al., 2017**; **Ren et al., 2018**; **Steinbusch, 1981**; **Steinbusch et al., 1980**; **Vasudeva et al., 2011**; **Vertes, 1991**; **Vertes and Kocsis, 1994**), and DR afferents have been identified from as many as eighty distinct anatomical brain regions, including other brainstem raphe nuclei (**Celada et al., 2001**; **Commons, 2015**; **Gonçalves et al., 2009**; **Levine and Jacobs, 1992**; **Mosko et al., 1977**; **Ogawa et al., 2014**; **Peyron et al., 1997**; **Peyron et al., 2018**; **Pollak Dorocic et al., 2014**; **Weissbourd et al., 2014**). As such, the DR is hodologically poised to send and receive signals related to a wide range of sensory, motor, affective, and cognitive processes. Indeed, DR neuropathology is associated with several human disorders (or disease models thereof) with broad symptomatology, such as major depressive disorder, autism, and Alzheimer's disease (**Chen et al., 2000**; **Dengler-Crish et al., 2017**; **Autism Sequencing Consortium et al., 2019**; **Ellegood et al., 2015**; **Guo and Commons, 2017**; **Ji et al., 2020**; **Luo et al., 2017**; **Michelsen et al., 2008**; **Miyazaki et al., 2005**; **Šimić et al., 2017**; **Vakalopoulos, 2017**; **Wang et al., 2018**; **Zweig et al., 1988**). Outside of DR-specialist research, the DR has often been viewed by the wider neuroscience community as a 'black box' source of a single neurochemical, namely 5-HT. Accordingly, development of therapeutics for associated disorders has largely focused on modulating overall serotonergic tone. However, DR-focused research over several decades has revealed layers of functional complexity and compositional heterogeneity warranting a more nuanced view (reviewed in **Abrams et al., 2004**; **Andrade and Haj-Dahmane, 2013**; **Gaspar and Lillesaar, 2012**; **Hale and Lowry, 2011**; **Michelsen et al., 2007**; **Okaty et al., 2019**; **Vasudeva et al., 2011**). While these studies have reached into the black box of the DR and described a variety of features at different levels of observation, integration across levels to arrive at principles of DR organization has proved challenging. Elucidating how molecular, neurochemical, anatomical, hodological, electrophysiological, and functional descriptions of the DR overlap is essential to understanding the structure-function relationship of the DR and other raphe nuclei (**Brust et al., 2014**; **Fernandez et al., 2016**; **Huang et al., 2019**; **Kast et al., 2017**; **Niederkofler et al., 2016**; **Okaty et al., 2015**; **Prouty et al., 2017**; **Ren et al., 2018**; **Ren et al., 2019**), and will likely facilitate improved therapies for human disorders. Here we have focused on one broadly defined subgroup of DR cells – neurons that express the gene *Pet1/Fev* – and applied scRNA-seq, iterative intersectional genetics, histology, and slice electrophysiology to provide a transcriptomic and anatomic atlas of mouse DR *Pet1* neurons with examples of links between molecular, neurochemical, anatomical, hodological, and electrophysiological levels of description. We identify as many as fourteen distinct molecularly defined subtypes of *Pet1* neurons that show biased cell body distributions in DR subregions. We further characterize projections and electrophysiology of the most molecularly unique DR *Pet1* neuron subtype – *Met-Slc17a8-Tph2-Pet1* cDR neurons (cluster twelve), genetically accessed by intersectional *P2ry1-cre; Pet1-Flpe* expression. The present study complements other recent characterizations of DR cell types (**Huang et al., 2019**; **Ren et al., 2019**), increasing the sampling resolution of *Pet1* neurons in particular through our experimental approach to achieve fine-scale identification of *Pet1* neuron subtypes.

Molecular and anatomic organization of *Pet1* neuron subtypes

Our data and analysis highlight the hierarchical organization of DR *Pet1* neurons molecularly and anatomically, allowing for identification of features that organize *Pet1* neurons at different levels of granularity (**Figure 8**, **Figure 8—source data 1**). Neurochemistry has long served as a principal phenotypic axis for classifying neurons, and concordantly we found that distributions of transcripts associated with distinct neurotransmitters correspond with broad subgroup divisions. The majority of *Pet1* neurons (clusters one through twelve) express high levels of *Tph2* mRNA, encoding tryptophan hydroxylase two, the rate-limiting biosynthetic enzyme for 5-HT, as well as several other genes

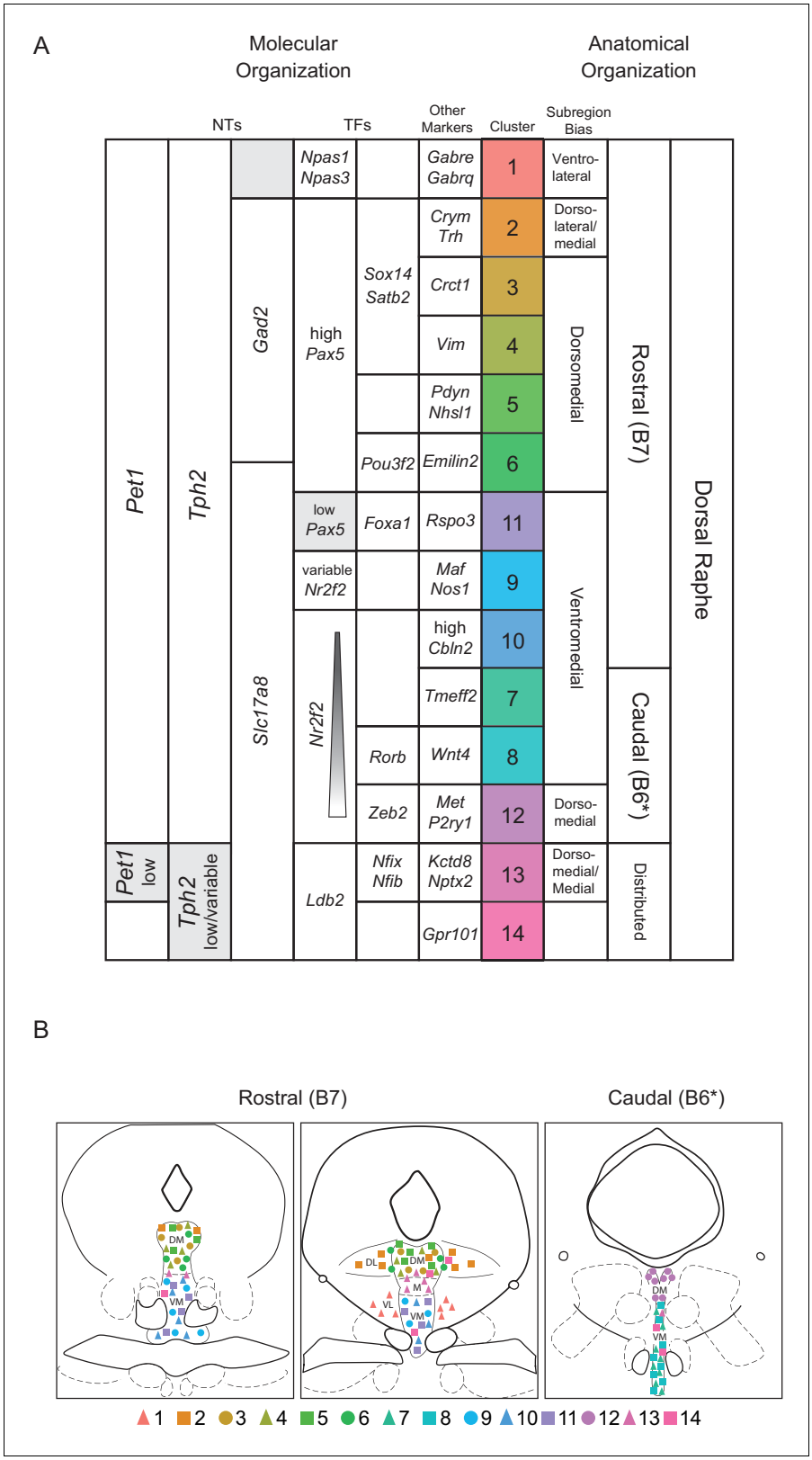

Figure 8. Fourteen *Pet1* subtypes in the DR can be defined by the combinatorial expression of transcription factors and other markers and have distinct anatomical organization. (**A**) Molecular markers (neurotransmitters (NTs), transcription factors (TFs), and other markers) on the left half of the table, with increasing specificity from left to right, that combinatorically define each identified *Pet1* subtype (colored column). Anatomical biases of each

Figure 8 continued on next page

Figure 8 continued

cluster are described on the right, with increasing specificity from right to left. ***Figure 8—source data 1*** outlines the combination of information used to inform the proposed anatomical bias. Note, cluster numbers have been re-ordered to highlight anatomical groupings. (**B**) Schematic depicting the anatomical distribution of each subtype based on the bias indicated in (**A**). B7 and B6 refer to the original Dahlström and Fuxe nomenclature for describing distinct anatomical clusters of 5-HT neurons. The asterisks after B6 in A and B are to indicate that some authors only consider B6 to encompass the dorsal part of what we refer to as the caudal DR.
The online version of this article includes the following source data for figure 8:

Source data 1. Anatomical bias of *Pet1* DR subtypes can be inferred by a combination of histology, single cell RNAseq, data from previously published papers, and Allen Mouse Brain atlas RNA in situ hybridization data.

indicative of a serotonergic phenotype, such as *Slc6a4* (Sert), *Slc18a2* (Vmat2), and *Maob*. However, we also identified two subgroups of *Pet1* neurons with 5-HT marker gene profiles that differ from the majority (clusters thirteen and fourteen). One subgroup (cluster thirteen) expresses very low transcript levels of 5-HT neuron marker genes, is mostly negative for TPH2 immunolabeling, and shows a biased cell body distribution in the rostromedial DR, as well as distributing sporadically throughout. The other subgroup (cluster fourteen) exhibits a much broader distribution of transcript levels for 5-HT marker genes than other groups. The functional significance of this variable expression can only be hypothesized at present; we speculate that it may reflect a capacity for neurotransmitter plasticity – that is experience-dependent induction or up-regulation of 5-HT phenotype, as hinted at by a recent study (***Prakash et al., 2020***). If this is the case, cluster fourteen neurons may be partially in transition, for example, from a predominately glutamatergic phenotype to a 5-HT phenotype or to a glutamate-5-HT co-transmitter phenotype. Both cluster thirteen and fourteen *Pet1* neuron subgroups express *Slc17a8* (alias Vglut3) transcripts, suggestive of a capacity for synaptic glutamate packaging and release, and show shared enrichment for several transcripts, including *Ldb2*, encoding the transcription factor LIM domain binding 2, and *Cnr1*, encoding cannabinoid receptor 1. Cluster fourteen is also uniquely distinguished by enrichment for *Gpr101* transcripts, encoding an orphan G protein-coupled receptor.

Among *Pet1* neurons expressing high levels of *Tph2* and other 5-HT gene markers, expression of genes related to GABA synthesis (*Gad1* and *Gad2*) or glutamatergic synaptic vesicle packaging (*Slc17a8*) correlate with major molecular and anatomical subdivisions (evident in the dendrogram in ***Figure 1B***, the UMAP plot in ***Figure 1C***, and the histological image series in ***Figure 3*** B1–6 and ***Figure 3—figure supplement 1D–J***). We found that the cell bodies of non-*Slc17a8*, largely *Gad2*-expressing *Pet1* neurons are preferentially distributed in the dorsal and lateral subregions of the rostral DR, and become exclusively lateral and ultimately absent at more caudal extents of the DR. Conversely, *Slc17a8-Tph2-Pet1* neuron bodies show a ventromedial bias rostrally and predominate the entire cDR. *Gad2-Tph2-Pet1* neurons and *Slc17a8-Tph2-Pet1* neurons show differential enrichment of hundreds of transcripts, including *Pax5* and *Nr2f2*. Both genes encode transcription factors, the expression of which we examined through immunohistology and found a similar distribution of cell body staining as revealed by intersectional genetic labeling of *Slc17a8-cre; Pet1-Flpe* neurons – *Pax5* expression overlaps predominately with the non-*Slc17a8*-expressing population, whereas *Nr2f2* overlaps with the *Slc17a8*-expressing population (***Figure 4—figure supplement 2***). We also found one *Pet1* neuron subgroup (cluster six) that expresses *Gad1*, *Gad2*, and 'intermediate' levels of *Slc17a8* transcripts (relative to other *Slc17a8+* clusters). These neurons correspond with the rostral population of neurons labeled by intersectional *Npy2r-cre; Pet1-Flpe* expression (***Figure 3C***), which we characterized by manual scRNA-seq (***Figure 4***).

Altogether we identified five *Pet1* neuron subgroups that express *Gad1* or *Gad2* transcripts (clusters two through six), and found *Gad2* to be expressed more consistently and at higher levels than *Gad1* (with the exception of cluster six). *Gad1* and *Gad2* encode two distinct isoforms of glutamate decarboxylase, referred to as GAD67 and GAD65, respectively. In many neuron types, these proteins are often co-expressed, but localize to different subcellular compartments and differ in their interaction with the co-factor pyridoxol phosphate (***Chen et al., 2003***; ***Erlander et al., 1991***; ***Soghomonian and Martin, 1998***). GAD65 (encoded by *Gad2*) is typically found in axon terminals where it is thought to play a role in GABA synthesis specifically for synaptic vesicular release, whereas GAD67 is typically localized to the soma and may be more involved with non-vesicular

GABA release. While we did not reliably detect transcripts for the vesicular GABA transporter (*Slc32a1*), we did detect expression of transcripts encoding VMAT2 which has been shown to package GABA into synaptic vesicles in dopaminergic neurons, allowing for monoaminergic-GABAergic co-transmission (**Tritsch et al., 2012**). Thus it is plausible that *Gad2-Tph2-Pet1* neurons may likewise co-release GABA, though it has yet to be reported in the literature.

Beyond classic neurotransmitters, we also found enrichment of various peptide hormone transmitters in different *Gad2-Tph2-Pet1* neuron subgroups. Cluster two shows enrichment for thyrotropin-releasing hormone transcripts (*Trh*), and clusters five and six show enrichment for prodynorphin (*Pdyn*) (as does cluster fourteen). As can be seen in the dendrogram in **Figure 1B** and UMAP plot in **Figure 1C**, there appears to be a major division between *Gad2-Tph2-Pet1* clusters two through four and clusters five and six, with clusters five and six also sharing many molecular similarities with *Slc17a8-Tph2-Pet1* subgroups. This may in part reflect differential expression of transcription factors that regulate divergent gene 'modules'. While all *Gad2-Tph2-Pet1* neurons express *Pax5*, clusters two through four also express *Sox14* and *Satb2*. Cluster six, on the other hand, shows enrichment for several transcription factor genes that are also enriched (or trend towards enrichment) in clusters thirteen and fourteen, such as *Pou3f2*, *Bcl11a*, and *Id2*. These molecularly distinct *Gad2-Tph2-Pet1* subgroups also show differences in anatomy. Based on manual scRNA-seq of sub-anatomically targeted *Pet1* neurons, we found that cluster two *Gad2-Trh-Tph2-Pet1* neuron cell bodies are found predominately in the dorsolateral DR, as well as the dorsomedial DR, whereas clusters three, four, and five appear to be more dorsomedially biased, consistent with recent reports (**Huang et al., 2019**; **Ren et al., 2019**). Cluster six neurons, as captured by *Npy2r-cre; Pet1-Flpe* expression, show a more diffuse distribution in the rostral DR, illustrating that not all *Pet1* neuron subtypes, as defined transcriptomically, correspond with clear-cut anatomical patterns. Indeed, while there are major differences between predominately dorsal versus ventral or rostral versus caudal DR *Pet1* neuron subtypes, different subtypes nonetheless intermix within these domains, emphasizing the importance of molecular-genetic targeting of *Pet1* neuron subtypes to gain specificity for functional characterization (a point also made by **Huang et al., 2019** and **Okaty et al., 2019**).

Slc17a8-Tph2-Pet1 neuron subgroups, as noted above, are found more ventrally than *Gad2-Tph2-Pet1* neurons in the rostral DR, and are the dominant neurotransmitter phenotype in the caudal DR (as inferred by transcript expression and VGLUT3 and TPH2 immunostaining). We found two *Slc17a8-Tph2-Pet1* neuron subtypes with cell bodies biased towards the rostral DR (clusters nine and ten) and three subtypes (clusters seven, eight, and twelve) biased towards the more caudal DR (as delineated in **Figure 4**, and see the discussion of varying nomenclature around the cDR in the Results section *Histology of Pet1-Intersectionally Defined Neuron Populations* above). Cluster twelve *Pet1* neurons, also marked by expression of the gene *Met*, we found to be the most different from all other *Pet1* neurons, both in terms of the number of differentially expressed genes and the magnitudes of enrichment/depletion compared to other *Pet1* neuron subtypes (as also observed by **Huang et al., 2019**; **Ren et al., 2019**). We show by histology of genetically marked neurons (intersectional *P2ry1-cre; Pet1-Flpe* expression) that the cell bodies of these *Met-Slc17a8-Tph2-Pet1* neurons are clustered beneath the aqueduct in the caudal DR (**Figure 3E**) and send extensive axonal projections throughout the ventricles (**Figure 5**). Based on our retrograde tracing experiments and other studies (**Kast et al., 2017**; **Tong et al., 2014**), it is likely that these neurons constitute the major source of 5-HT innervation to the ventricles. Furthermore, our demonstration that *P2ry1-cre; Pet1-Flpe* fibers are closely apposed with proliferating and migrating cells in the SVZ and rostral migratory stream (**Figure 5**), supports a proposed role for these neurons in regulating adult neural stem cell proliferation in the SVZ (**Tong et al., 2014**). Cluster twelve neuron transcript enrichment for several GPCRs implicated in modulation of adult neurogenesis, such as *P2ry1* (**Lin et al., 2007**), *Gipr* (found to be enriched in our *P2ry1-cre; Pet1-Flpe* manual scRNA-seq data) (**Nyberg, 2005**), *S1pr3* (**Alfonso et al., 2015**; **Ye et al., 2016**), and *Oprm1* (**Harburg et al., 2007**) lends further support to this hypothesis. Now, with intersectional access to this population of cDR 5-HT neurons provided by *P2ry1-cre* with *Pet1-Flpe,* the function of *Met-Slc17a8-Tph2-Pet1* cDR neurons in regulating SVZ proliferation can be tested directly in a cell type-specific manner using dual Cre- and Flpe-responsive chemo- or optogenetic approaches (**Brust et al., 2014**; **Hennessy et al., 2017**; **Kim et al., 2009**; **Madisen et al., 2015**; **Niederkofler et al., 2016**; **Okaty et al., 2015**; **Ray et al., 2011**; **Sciolino et al., 2016**; **Teissier et al., 2015**).

DR *Pet1* neuron subtypes have distinct electrophysiological properties

To further characterize correspondence of molecular identities with other cell phenotypes we performed whole-cell electrophysiological recordings in acute slices prepared from mice in which different *Pet1* neuron subsets were genetically labeled. We found that 5-HT neurons with different molecular identities also exhibit distinct electrophysiological properties likely to impact their circuit function. While we did not comprehensively sample all molecularly defined subtypes, our survey of cDR *Pet1* neurons and rostral dorsal raphe *Gad2-cre; Pet1-Flpe* neurons provides evidence for at least four distinct electrophysiological types based on four key properties: (1) rheobase (also known as current threshold), which reflects a neuron's sensitivity to input, (2) delay to first spike, which reflects the degree to which a neuron is able to activate phasically in response to input, (3) spike-frequency adaptation, which reflects the degree to which a neuron is able to continuously signal ongoing input, and (4) maximum firing rate, which determines the dynamic range of neuron responsiveness to graded inputs. As with molecular differences, cluster twelve *Met-Slc17a8-Tph2-Pet1* cDR neurons (*P2ry1-cre; Pet1-Flpe* intersectional expression) showed profound differences from other subtypes, including other cDR *Pet1* neurons. *P2ry1-cre; Pet1-Flpe* neurons consistently displayed a long latency to first action potential, required substantially more input to reach action potential threshold, and had a lower maximum firing rate (***Figure 6*** and ***Figure 6—figure supplement 1***). These differences, together with differential transcript expression of several GPCRs, suggest that *Met-Slc17a8-Tph2-Pet1* cDR neurons respond in a different way and to very different stimuli than other DR *Pet1* neuron types. For example, low excitability and long-latency to spike suggest that these neurons may only be recruited by very strong stimuli at relatively slower timescales than other *Pet1* neurons (to the extent that properties recorded in slice reflect in vivo properties). Notably, 5-HT neurons with this electrophysiological profile have not yet been reported in the literature. However, the two firing types that we have defined as 'Short-Latency to First AP; Non-Adapting' and 'Mid-Latency to First AP' (***Figure 6B***, 1 and 2) correspond well to those described by ***Fernandez et al., 2016*** in groups of *Pet1*-EGFP serotonergic neurons projecting to the mPFC and the BLA, respectively. Differential expression of ion channels and receptors identified here suggest molecular substrates of these different electrophysiological properties.

Technical aspects of our study allow for high-resolution transcriptome characterization of *Pet1* neurons

Due to the high-dimensional 'richness' of transcriptomic data, together with the capacity to propose explanations of cellular phenotypes in terms of molecular mechanisms – RNA-seq dissection of neural circuits has gained traction as a way to define and enumerate cell types in the brain (and other tissues). Single-cell RNA-sequencing, in particular, has become an indispensable approach, with different methods achieving different resolution of underlying cellular diversity (***Bakken et al., 2018***; ***Campbell et al., 2017***; ***Hodge et al., 2019***; ***Huang et al., 2019***; ***Lovatt et al., 2014***; ***Macosko et al., 2015***; ***Okaty et al., 2015***; ***Poulin et al., 2016***; ***Ren et al., 2019***; ***Rosenberg et al., 2018***; ***Saunders et al., 2018***; ***Spaethling et al., 2014***; ***Tasic, 2018***; ***Tasic et al., 2016***; ***Tasic et al., 2018***; ***Usoskin et al., 2015***; ***Zeisel et al., 2018***; ***Zeisel et al., 2015***). Droplet-based scRNA-seq approaches (without cell-type-specific purification) allow for unbiased classification of major cell types residing in a particular microdissected tissue region of interest, however lower abundance cell types, such as DR *Pet1* neurons profiled in the present study, are often insufficiently sampled to achieve high resolution of subtype molecular diversity. Moreover, different reaction chemistries employed in different droplet-based scRNA-seq approaches can lead to different gene detection sensitivity. Low cellular abundance compounded with low gene detection can greatly limit the power of a study to reveal fine-scale variation in molecular phenotypes that may be important for identifying neuronal subtypes and subtype 'states' (e.g. adaptive or pathological transcriptional variation). Where cell type-specific markers are available, cell sorting prior to scRNA-seq library preparation can greatly enhance the resolution of cellular diversity for less abundant cell classes. While manual sorting approaches combined with RNA-seq library preparation optimized for low amounts of input RNA achieve high single-cell gene detection and allow for sampling genetically and anatomically-defined neuron populations (***Niederkofler et al., 2016***; ***Okaty et al., 2015***), they are often limited in the number of cells profiled, and therefore may lack sufficient throughput to fully characterize subtype diversity. On the other hand, automated sorting approaches achieve greater throughput but

are less well suited to collecting low abundance cell types, such as defined by fine-scale anatomy or highly restricted marker gene expression. Our particular experimental approach to characterizing DR *Pet1*-lineage neuron diversity in the present study was informed by all of the above concerns. By combining intersectional genetic labeling of DR *Pet1* neurons with both high-throughput (microfluidic On-chip Sort) and targeted low-throughput (manual) sorting approaches, followed by high-sensitivity RNA-seq library preparation protocols (10X Genomics Chromium Single Cell 3' v3 and SMART-Seq v4 kits, respectively) we leveraged the strengths of multiple approaches to achieve high-resolution transcriptomic profiling of DR *Pet1* neurons.

Resource value of DR Pet1 neuron scRNA-seq data

While we have highlighted many salient experimental findings in the present report, the data no doubt have more to reveal, and we thus offer this dataset as a resource to be mined by the larger community. Towards this end, we have created an interactive web application allowing users to directly explore our scRNA-seq dataset (https://dymeckilab.hms.harvard.edu/RNAseq_database). With the web app, users can plot the expression of a gene or several genes of interest, and perform differential expression analysis. Newly identified *Pet1* neuron subtype marker genes may guide development of new recombinase driver lines allowing for subtype-specific genetic access and functional manipulation, and may potentially shape approaches for developing more targeted therapeutics. Moreover, we hope this work, together with other recent studies (***Huang et al., 2019***; ***Ren et al., 2019***), may lead to the development of a standardized DR *Pet1* neuron subtype nomenclature that allows for consolidation of experimental results across different labs and different data modalities.

Materials and methods

Key resources table

Reagent type (species) or resource	Designation	Source or reference	Identifiers	Additional information
Strain, strain background (*Mus musculus*)	C57BL/6J	The Jackson Laboratory	RRID:IMSR_JAX:000664	
Genetic reagent (*Mus musculus*)	*Tg(Fev-flpe)1Dym* Referred to as *Pet1-Flpe*	PMID:18344997	RRID:MGI:5004974	
Genetic reagent (*Mus musculus*)	*En1*$^{tm2(cre)Wrst}$ Referred to as *En1-cre*	PMID:10837030	RRID:IMSR_JAX:007916	
Genetic reagent (*Mus musculus*)	*Tg(Slc6a4-cre)ET33Gsat* Referred to as *Slc6a4*-cre	PMID:17855595	RRID:MGI:3836639	
Genetic reagent (*Mus musculus*)	*Npy2r*$^{tm1.1(cre)Lbrl}$ Referred to as *Npy2r-cre*	PMID:25892222	RRID:IMSR_JAX:029285	Lab of Steve Liberles
Genetic reagent (*Mus musculus*)	*P2ry1*$^{tm1.1(cre)Lbrl}$ Referred to as *P2ry1-cre*	PMID:25892222	RRID:IMSR_JAX:029284	Lab of Steve Liberles
Genetic reagent (*Mus musculus*)	*Tg(Crh-cre) KN282Gsat/Mmucd* Referred to as *Crh-cre*		RRID:MMRRC_030850-UCD	
Genetic reagent (*Mus musculus*)	*Gad2*$^{tm2(cre)Zjh}$ Referred to as *Gad2-cre*	PMID:21943598	RRID:IMSR_JAX:028867	
Genetic reagent (*Mus musculus*)	*Slc17a8*$^{tm1.1(cre)Hz}$ Referred to as *Slc17a8- cre*	MGI: J:146821	RRID:IMSR_JAX:028534	
Genetic reagent (*Mus musculus*)	*Gt(ROSA)26Sor*$^{tm8(CAG-mCherry,-EGFP)Dym}$ Referred to as RC-FrePe	PMID:22151329	RRID:IMSR_JAX:029486	
Genetic reagent (*Mus musculus*)	*Gt(ROSA)26Sor*$^{tm65.1(CAG-tdTomato)Hze}$ Referred to as RC-Ai65	PMID:25741722	RRID:IMSR_JAX:021875	

Continued on next page

Continued

Reagent type (species) or resource	Designation	Source or reference	Identifiers	Additional information
Genetic reagent (*Mus musculus*)	*GT(ROSA)26 Sor*$^{tm3.2(Cag-EGFP,CHRM3*/mCherry/Htr2a)Pjen}$ Referred to as RC-FL-hM3Dq	PMID:27264177	RRID:IMSR_JAX:026942	
Recombinant DNA reagent	pENN.AAV.hSyn. Cre.WPRE.hGH (AAVrg Viral prep)	Addgene	Cat# 10553-AAVrg RRID:Addgene_105553	
Antibody	anti-GFP (chicken polyclonal)	Aves Labs	Aves Labs Cat# GFP-1020, RRID:AB_10000240	IHC (1:3000)
Antibody	anti-DsRed (rabbit polyclonal)	Takara Bio	Takara Bio Cat# 632496, RRID:AB_10013483	IHC (1:1000)
Antibody	anti-PAX5 (goat polyclonal)	Santa Cruz	Santa Cruz Biotechnology Cat# sc-1974, RRID:AB_2159678	IHC (1:1000)
Antibody	anti-SATB2 (guinea pig polyclonal)	Synaptic Systems	Synaptic Systems Cat# 327 004, RRID:AB_2620070	IHC (1:1000)
Antibody	anti-COUP-TFII (anti-NR2F2, mouse monoclonal)	Perseus Proteomics	Perseus Proteomics Cat# PP-H7147-00, RRID:AB_2314222	IHC (1:1000)
Antibody	anti-VGLUT3 (guinea pig polyclonal)	Synaptic Systems	Synaptic Systems Cat# 135 204, RRID:AB_2619825	IHC (1:500)
Antibody	anti-RFP (rat monoclonal)	Chromotek	ChromoTek Cat# 5f8-100, RRID:AB_2336064	IHC (1:500)
Antibody	anti-DCX (goat polyclonal)	Santa Cruz	Santa Cruz Biotechnology Cat# sc-8066, RRID:AB_2088494	IHC (1:1000)
Antibody	anti-Ki67 (rat monoclonal)	Thermo Fisher Scientific	Thermo Fisher Scientific Cat# 14-5698-80, RRID:AB_10853185	IHC (1:1000)
Antibody	anti-TPH2 (rabbit polyclonal)	Novus Biologicals	Novus Cat# NB100-74555, RRID:AB_1049988	IHC (1:1000)
Antibody	Alexa Fluor 488 (donkey anti-chicken)	Jackson	Jackson ImmunoResearch Labs Cat# 703-545-155, RRID:AB_2340375	IHC (1:500)
Antibody	Alexa Fluor 546 (donkey anti-rabbit)	Thermo Fisher Scientific	Thermo Fisher Scientific Cat# A10040, RRID:AB_2534016	IHC (1:500)
Antibody	Alexa Fluor 647 (donkey anti-goat)	Thermo Fisher Scientific	Thermo Fisher Scientific Cat# A-21447, RRID:AB_2535864	IHC (1:500)

Continued on next page

Continued

Reagent type (species) or resource	Designation	Source or reference	Identifiers	Additional information
Antibody	Alexa Fluor 647 (donkey anti-mouse)	Jackson	Jackson ImmunoResearch Labs Cat# 715-605-151, RRID:AB_2340863	IHC (1:500)
Antibody	Alexa Fluor 647 (donkey anti-rabbit)	ThermoFisher Scientific	Thermo Fisher Scientific Cat# A-31573, RRID:AB_2536183	IHC (1:500)
Antibody	Cy5 (donkey anti-guinea pig)	Jackson	Jackson ImmunoResearch Labs Cat# 706-175-148, RRID:AB_2340462	IHC (1:500)
Commercial assay or kit	*Tph2*-C2 probe	ACDBio	ACDBio:318691-C2	
Commercial assay or kit	Chromium Single Cell v3 Reagent Kits	10X Genomics	10X Genomics :1000092/1000074	
Commercial assay or kit	SMARTseq V4 Ultra Low Input RNA Kit	Takara Bio	Takara Bio:634890	
Commercial assay or kit	Nextera XT DNA Library Preparation Kit	Illumina	Illumina: FC-131–1024	
Commercial assay or kit	RNAscope Fluorescent Multiplex Reagent Kit	ACDBio	ACDBio:320850	
Software, algorithm	R (Version 3.5.3, 3.6.3)	R Project for Statistical Computing	R Project for Statistical Computing, RRID:SCR_001905	https://cran.r-project.org/
Software, algorithm	Seurat (Versions 3.0.2, 3.1.1, 3.1.4)	PMID:29608179	Seurat, RRID:SCR_016341	https://satijalab.org/seurat/
Software, algorithm	Fiji (Version 2.0.0-rc-69/1.52 p)	PMID:22743772	Fiji, RRID:SCR_002285	https://imagej.net/Fiji

Intersectional genetic fate mapping

Triple transgenic mice were generated by crossing *Pet1-Flpe;* RC-FrePe (**Brust et al., 2014**; **Jensen et al., 2008**; **Okaty et al., 2015**) or *Pet1-Flpe;* RC-Ai65 (**Madisen et al., 2015**) mice with *Slc6a4-cre* (**Gong et al., 2007**), *Npy2r-cre* (**Chang et al., 2015**), *En1-cre* (**Kimmel et al., 2000**), *Crh-cre* (https://www.mmrrc.org/catalog/sds.php?mmrrc_id=30850), and *P2ry1-cre* (**Chang et al., 2015**) mice, or by crossing *Pet1-Flpe;* RC-FL-hM3Dq (**Sciolino et al., 2016**) mice with *Slc17a8-cre* mice (https://www.jax.org/strain/028534). All animals were group housed (five animals per ventilated cage) on a 12 hr light/dark cycle with access to food and water ad libitum and were handled and euthanized in accordance with Harvard's Institutional Animal Care and Use Committee Protocols.

Perfusion and immunohistochemistry

Anesthetized mice were transcardially perfused with cold phosphate-buffered saline (PBS) followed by 4% paraformaldehyde (PFA). Tissue was dissected and fixed in 4% PFA overnight followed by cryoprotection in 30% sucrose/PBS until equilibrated (~48 hr) before being frozen in tissue freezing medium (Triangle Biomedical Services). Tissue was cryosectioned in 40 um coronal sections and processed as floating sections.

For fluorescent staining, sections were washed with PBS and PBS with 0.1% Triton-X-100 (PBS-T), blocked in 5% normal donkey serum (NDS) and 1% bovine serum albumin (BSA) for 2 hr at room temperature (RT), and incubated with primary antibody at 4˚C for 48 hr: anti-GFP (1:3000, chicken polyclonal, Aves Labs, GFP-1020), anti-DsRed (1:1000, rabbit polyclonal, Takara, 632496), anti-TPH2 (1:1000, rabbit polyclonal, Novus Biologicals, NB100-74555), anti-Pax5 (1:1000, goat polyclonal, Santa Cruz, sc-1974), anti-SATB2 (1:1000, guinea pig polyclonal, Synaptic Systems, 327–004), anti-COUP-TFII (1:1000, mouse monoclonal, Perseus Proteomics, PP-H7 147–00), anti-ZEB2 (1:200, rabbit polyclonal, MyBioSource, MBS9601451), anti-VGLUT3 (1:500, guinea pig polyclonal, Synaptic Systems, 135–204), anti-RFP (1:500, rat monoclonal, Chromotek, 5f8-100), anti-Doublecortin (1:1000,

goat polyclonal, Santa Cruz, SC-8066), and anti-Ki-67(1:1000, rat monoclonal, Invitrogen, 14-5698-80). For fluorescent detection, sections were washed in PBS-T and incubated with species matched secondary antibodies- Alexa Fluor 488 (donkey anti-chicken, Jackson, 703-545-155), Alexa Fluor 546 (donkey anti-rabbit, Invitrogen, A10040), Alexa Fluor 647 (donkey anti-goat, Invitrogen, A21447 or donkey anti-mouse, Jackson, 715-605-151), and Cy5 (donkey anti-guinea pig, Jackson, 706-175-148)- at 1:500 dilution for two hours. Sections were washed in PBS and 1:3000 DAPI before rinsing and mounting onto slides.

Confocal and fluorescent microscopy and quantification

Overview images

Overview images of intersectional subtypes were acquired using a 5x objective on a Zeiss Axioplan2 fluorescence microscope equipped with an Axiocam digital camera and Axiovision software using 1 × 1 binning. Images were then cropped to a 1000 × 1000 pixel square containing the dorsal raphe. Images showing the distribution of PAX5, SATB2, and NR2F2 are 2 × 2 tiled maximum intensity images acquired using a Plan Apo λ 20x/0.75 DIC I objective on a spinning disk confocal. Images showing TPH2 and VGLUT3 staining are a single optical slice taken on a spinning disk confocal using a Plan Apo λ 20x/0.75 DIC I objective or Plan Fluor 40x/1.3 Oil DIC H/N2 objective respectively. Images were cropped to create a zoomed image of the region of interest.

Flat mount of lateral wall of lateral ventricle

P2ry1-cre; Pet1-Flpe; RC-Ai65 mice (n = 4) were transcardially perfused with cold PBS. Lateral wall dissection was completed as described in ***Mirzadeh et al., 2010***. Briefly, brains were dissected into PBS and split into two hemispheres. The hippocampus was removed, exposing the lateral wall, and the brain was fixed overnight in 4% PFA in PBS. The remainder of the microdissection of the lateral wall was then completed and immediately proceeded to immunohistochemistry as described above.

Quantification of immunofluorescence

Quantification of PAX5, NR2F2, and SATB2 was completed in *Slc17a8-cre; Pet1-Flpe;* RC-hM3Dq animals, where cells expressing both *Slc17a8-cre* and *Pet1-Flpe* express an hM3Dq-mCherry fusion and all other *Pet1+* cells express EGFP. Images were acquired as 2 × 2 tiles as a z-stack (0.9 um step) using a Plan Apo λ 20x/0.75 DIC I objective on a spinning disk confocal and cropped into equally sized non-overlapping subregions (1000 × 1000 pixel) spanning the rostral to caudal extent of the dorsal raphe. Cells were counted positive if antibody staining for the protein of interest overlapped with DAPI staining and was within a DsRed + cell (*Slc17a8-cre; Pet1-Flpe* lineage) or a GFP+ cell (subtractive *Pet1* lineage). All counts were completed in images taken from 2 to 4 animals depending on the brain region. Images used for the quantification of VGLUT3 antibody staining were acquired using a Plan Fluor 40x/1.3 Oil DIC H/N2 objective on a spinning disk confocal on non-overlapping anatomical subdivisions of the dorsal raphe. Cells were counted positive based on the overlap of VGLUT3 antibody staining with mCherry (*Slc17a8-cre; Pet1-Flpe* lineage) or a EGFP (subtractive *Pet1* lineage) staining. In the case of TPH2 quantification, *En1-cre; Pet1-Flpe;* RC-FrePe animals were used (EGFP+ *En1-cre; Pet1-Flpe* intersectional lineage cells). Images were acquired as 2 × 2 tiles as a z-stack (0.9 um step) using a Plan Apo λ 20x/0.75 DIC I objective on a spinning disk confocal and cropped into equally sized non-overlapping subregions (1000 × 1000 pixel) spanning the rostral to caudal extent of the dorsal raphe. Cells were counted positive based on colocalization of TPH2 antibody staining with EGFP. All quantification was performed by an experienced observer blinded to the anatomical region of the image in a minimum of two animals per region.

TPH2/*Tph2* dual immunofluorescence and RNAscope

Transgenic *En1-cre; Pet1-Flpe;* RC-FrePe mice were briefly anesthetized with isoflurane and immediately perfused intracardially with phosphate buffered saline (PBS) followed by 4% paraformaldehyde (PFA) in PBS. Brains were extracted and fixed for 16 hr in 4% PFA at 4 ˚C, and were then cryoprotected using 30% sucrose in PBS for 48 hr and subsequently embedded in OCT compound (Tissue-Tek). Coronal sections were cut on a cryostat into PBS at 20 µm thickness, rinsed three times with PBS for 10 min and frozen in cryo-storage solution at −30 ˚C. The day before RNAscope (ACDBio) procedure, the sections were mounted on slides and dried at room temperature (RT) overnight. Prior

to RNAscope, the slides were heated on a slide warmer at 50 ˚C for 30 min. Sections were re-fixed with 4% PFA for 15 min at RT, followed by Protease III treatment for 30 min at 40 ˚C. RNAscope was performed based on the manufacturer's protocol: mouse *Tph2*-C2 probe (ACDbio Cat# 318691-C2) and Amp4 AltA were used for hybridization. After the last wash of RNAscope, the slides were washed briefly with PBS followed by permeabilization and blocking with 0.3% TritonX-100% and 5% Normal Donkey Serum (NDS, Jackson ImmunoResearch) in PBS for 1 hr at RT. Then the sections were incubated with primary antibodies in 0.3% TritonX-100% and 3% NDS in PBS for 16 hr at 4 ˚C. Primary antibodies: chicken polyclonal anti-GFP (1:1000; GFP-1010; Aves Labs), rabbit polyclonal anti-Tph2 (1:1000; NB100-74555; Novus Biological). Sections were then washed with PBS three times for 10 min and incubated with secondary antibodies for 2 hr at RT. Secondary antibodies: donkey anti-chicken IgG-Alexa Fluor 488 (1:500, Jackson ImmunoResearch Laboratories, Inc), donkey anti-rabbit IgG-Alexa Fluor 647 (1:500, ThermoFisher Scientific.). DAPI (4', 6-diamidino-2-phenylindole) was used for nuclear counterstaining.

Image acquisition and analysis

Images were collected on a Nikon Ti2 inverted microscope with a Yokowaga CSU-W1 spinning disk with a 50 µm pinhole disk, using a Nikon Plan Apo λ 60x/1.4 NA oil-immersion objective and laser lines at 405, 488, 561, and 640 nm, and captured using an Andor Zyla 4.2 Plus sCMOS monochrome camera and Nikon Elements Acquisition Softwarre AR 5.02. Laser settings were adjusted for each sample but kept constant throughout image collection. A custom Fiji (***Schindelin et al., 2012***) macro script was used to process and analyze these images in a semi-automatic manner (***Senft, 2020***; copy archived at https://github.com/elifesciences-publications/RNAscope-IHC-Colocalization-in-ImageJ). Analysis was performed on maximum intensity projections of 5 µm thick z-stacks. To segment cells, the GFP and TPH2 channels were processed with a 100 pixel rolling ball background subtraction to remove uneven background fluorescence and a two pixel gaussian blur to aid in cell segmentation. Cells were segmented first by automatic thresholding using the 'Default' Fiji autothreshold method. Cells in the resulting binary images were separated using the Adjustable Watershed plugin (Michael Schmid, https://imagejdocu.tudor.lu/plugin/segmentation/adjustable_watershed/start), which allows the user to manually adjust the default ImageJ binary watershed tolerance. Next, cells were filtered for size (minimum area 70 μm^2) and circularity (minimum 0.3) using Fiji's 'Analyze Particles.' Segmented cells were checked manually by a user who could delete or redraw ROIs using the freehand tool and the ROI manager. After segmenting both channels sequentially, 2D overlap-based colocalization of the TPH2 and GFP-labeled cells was performed in which a cell was considered as 'colocalized' if area overlap was greater than 60% of the GFP area (determined empirically). To quantify *Tph2* RNAscope puncta within cells, a 50 pixel rolling ball background subtraction was applied before isolating puncta as local intensity maxima using the Fiji 'Find Maxima' function with a prominence level of 100. RNAscope puncta were then counted within each cell ROI and resulting data were output to a spreadsheet. For GFP^+ soma located close to $TPH2^+$ cells such that their outlines in the maximum projection partially overlapped with TPH2 signal but did not reach the colocalization criterion, RNAscope puncta were only counted in the $TPH2^-$ region of the cell soma to avoid including puncta belonging to the neighboring cell.

Stereotaxic surgery

Mice were anesthetized with 1.5–2.0% isofluorane and placed in a stereotaxic system (Kopf). Using a Micro4 injector (WPI) and Nanofil sytringe equipped with a metal 33 g beveled needle (WPI) 75 nL of pENN.AAV.hSyn.Cre.WPRE.hGH was injected at 50 nL/min into the lateral ventricle using using the following stereotaxic coordinates: −0.34 mm AP, + 1.00 mm LM, −2.25 mm DV (AP is relative to bregma). After surgery, mice recovered on a heated pad until ambulatory and returned to their home cage. pENN.AAV.hSyn.Cre.WPRE.hGH was a gift from James M. Wilson (Addgene viral prep #105553-AAVrg; http://n2t.net/addgene:105553; RRID:Addgene_105553).

Single-cell sorting and RNA sequencing

On-chip sort, 10X library preparation, and RNA sequencing

Data was derived from two different experiments composed of brain tissue harvested from *En1-cre; Pet1-Flpe;* RC-FrePe mice (n = 4) or *Pet1-Flpe;* RC-FL-hM3Dq mice (n = 6). Tissue was sectioned on

a vibratome and protease-digested in ACSF containing activity blockers as described in ***Hempel et al., 2007***. The dorsal raphe was micro-dissected under an upright dissection microscope with fluorescence optics and all tissue was combined in a 1.5 mL Eppendorf tube containing 500 ul of filtered ACSF/1%FBS. Tissue was then gently triturated using glass micropipettes of decreasing diameter until achieving a mostly homogeneous single-cell suspension without visible tissue chunks. One drop of NucBlue (Thermo Fisher Scientific) was added to the cell suspension and allowed to sit for 20 min (to aid in sorting and cell quantification). EGFP-marked, NucBlue-positive cells were sorted using the On-chip Sort (On-chip Biotechnologies Co., Ltd.). Final cell concentration was determined by counting the number of cells in 10 ul of the sorted output using a hemacytometer. Cells were then run through the 10X Genomics Chromium Single Cell 3' v3 protocol, and libraries were sequenced on an Illumina NextSeq 500 sequencer to a mean depth of ~115,000 reads per cell.

Manual sorting and RNA sequencing

Brain tissue was harvested from triple transgenic animals – *Slc6a4-cre; Pet1-Flpe;* RC-FrePe, *Npy2r-cre; Pet1-Flpe;* RC-FrePe, *Crh-cre; Pet1-Flpe;* RC-FrePe, and *P2ry1-cre; Pet1-Flpe;* RC-FrePe (p60-p120, a minimum of two mice per condition) and fluorescently labeled cells were sorted as described in ***Okaty et al., 2015***. Briefly, the brainstem was sectioned into 400 um coronal sections using a vibratome. Sections were bubbled in artificial cerebrospinal fluid (ACSF) containing activity blockers for at least 5 min before being transferred to ACSF containing 1 mg/ml pronase for 1 hr. Slices were then returned to protease-free ACSF for 15 min, before regions of interest were micro-dissected. Anatomical subdivisions of the dorsal raphe were made based on the shape of the dorsal raphe and landmarks including fiber tracts and the aqueduct (as indicated in ***Figure 4A***). Dissected chunks of tissue were transferred first to a clean 35 mm dish containing ACSF and then to a 1.5 mL Eppendorf tube containing 1 mL of filtered ACSF/1% FBS. Tissue was then gently triturated until without visible chunks. Dissociated cells were diluted and poured into a Petri dish. Fluorescently marked cells were aspirated using mouth aspiration and moved into three consecutive wash dishes. Each cell was then aspirated a final time and deposited into an individual 0.5 mL tube containing 9.5 ul of nuclease-free water and 1 ul of 10x Reaction Buffer (Smart-Seq V4 Ultra Low Input RNA kit, Takara Bio) and allowed to incubate at room temperature for 5 min before being stored at −80 deg until cDNA synthesis. Single cells were converted to cDNA and amplified using Smart-Seq V4 Ultra Low Input RNA Kit (Takara Bio). The cDNA output was then processed with Nextera XT DNA Library Preparation Kit. Quantification and quality control were assessed with TapeStation. Libraries were then sequenced on either an Illumina HiSeq 2500 (50 base-pair, single-end) or NextSeq 500 (75 bp, paired-end) to a mean depth of ~4,000,000 reads per cell.

scRNA-seq analysis

10x scRNA-seq data

Transcriptome mapping (using the mm10 genome assembly) and demultiplexing were performed using the 10X Genomics Cell Ranger software (version 3.0.2). Several data-filtering steps were performed on the matrix of transcript counts (using R version 3.5.3) prior to further analysis. First, we filtered out all genes detected in fewer than ten single-cell libraries, and filtered out all libraries with less than 4,500 detected genes. This threshold was selected based on the histogram of gene detection for all single-cell libraries as initially called by the Cell Ranger cell detection algorithm, which appeared to reflect two different distributions corresponding to low-complexity versus high-complexity libraries. The low-complexity distribution was right-skewed and had a mode of less than 1,000 detected genes, whereas the high-complexity distribution was left-skewed and had a mode of ~7,500 detected genes. 4,500 genes was roughly the boundary between the two distributions; that is the minima between the two modes, and also corresponded to a sharp inflection point in the Barcodes versus UMI counts plot in the web_summary.html file generated by Cell Ranger. While many of these low-complexity libraries may have been misidentified as cells by Cell Ranger (e.g. droplets containing transcripts from lysed cells, rather than intact cells) examination of genes enriched in lower-complexity libraries suggested that some of them reflected unhealthy cells (e.g. libraries with high mitochondrial gene expression) or contaminating non-neuronal cells (e.g. libraries enriched for glial marker genes). Notably, the number of cells with high-complexity libraries corresponded well with our estimated number of EGFP positive cells used as input to the 10X chip. We

further excluded libraries with: (1) evidence of glial contamination, based on high-outlier expression of glial marker genes, including *Plp1*, *Olig1*, and *Aqp4*, (2) absence or low-outlier levels of *Pet1/Fev* transcripts, (3) greater than fifteen percent of detected genes corresponding with mitochondrial genes, (4) less than two percent of detected genes corresponding with ribosomal genes (these appeared to be single-nuclei libraries, rather than single-cell), (5) high-outlier UMI counts, and (6) high-outlier gene detection. 2,350 single-cell libraries and 17,231 genes passed the above filtering criteria.

Next, we created a Seurat object using these filtered data (Seurat version 3.0.2). Data were log-normalized using the NormalizeData function (using the default scale factor of 1e4), and we identified the top two thousand genes (or in some cases non-coding RNAs) with the most highly variable transcript expression across single cells using the FindVariableFeatures function (selection.method = 'vst', nfeatures = 2000). We then scaled and centered the log-normalized data using the ScaleData function and carried out principal components analysis (PCA) on the scaled expression values of the two thousand most highly variable genes. This allowed us to reduce the dimensionality of the data onto a smaller set of composite variables representing the most salient gene expression differences across single neurons. The procedure for identifying meaningful *Pet1* neuron subtype clusters is thoroughly described in the Results section of the main text. Briefly, we systematically varied the number of principal components included and the resolution parameter in the functions FindNeighbors, FindClusters, and RunUMAP, Dendrograms were created using BuildClusterTree and PlotClusterTree, and cluster-enriched genes were identified using the FindAllMarkers function, with min.pct = 0.25 and logfc.threshold = 0.25, using Wilcoxon Rank Sum tests. This function adjusts p-values for multiple comparisons using the Bonferroni correction. All genes found to be significantly enriched or 'de-enriched' (i.e. expressed at a significantly lower level) in each cluster, as well as the top two thousand highest variance genes, can be found in ***Supplementary file 1***.

Manual scRNA-seq data

Transcript mapping to the mm10 genome assembly and feature counts were performed using STAR (version 2.5.4) (***Dobin and Gingeras, 2016***). Given the high purity of manual cell sorting and the high sensitivity of SMART-Seq v4 cDNA amplification, no data filtering was required; that is single-cell libraries showed no evidence for off-target contamination and showed consistently high gene detection (~9,000 genes per single-cell). Counts data were analyzed using Seurat as described for 10X scRNA-seq data.

Transfer of 10x cell type labels

In order to explore the correspondence between the fourteen 10X scRNA-seq data-defined *Pet1* neuron subtypes and other scRNA-seq data, including our manual scRNA-seq data, and the ***Huang et al., 2019*** and ***Ren et al., 2019*** datasets, we employed the strategy outlined in ***Stuart et al., 2019***. Specifically, we used the Seurat functions FindTransferAnchors and TransferData, using the 10X data as the 'reference' and the other datasets as the 'query' group.

Electrophysiology methods

In vitro brainstem slice preparations containing dorsal raphe serotonin neurons were obtained from 4 to 5 week old mice. After isofluorane anesthesia, mice were perfused transcardially with a solution of artificial CSF ($NaHCO_3$-aCSF) containing the following (in mM): 124 NaCl, 25 NaHCO3, 3 KCl, 2 CaCl2, 2 $MgCl_2$, 1.2, NaH2PO4 and 25 d-Glucose, equilibrated with 95% O2% and 5% CO2 adjusted to 310 ± 5 mOsm/L. The brainstem was dissected and mounted on the stage of a VT1200S vibratome while immersed in an ice slush solution aCSF containing the following (in mM): NMDG 93, HCl 93, KCL 2.5, NaH_2P0_4 1.2, $NaHCO_3$ 30, HEPES 20, d-Glucose 25, Na-Ascorbate 5, Thiourea 2, Na-Pyruvate 3, $MgSO_4$ 10, $CaCl_2$ 0.5 equilibrated with 95% O2% and 5% CO2 adjusted to 310 ± 5 mOsm/L. Coronal slices 200 µm thick containing the dorsal nucleus raphe were recovered for 1 hr at 35–6 C in HEPES-aCSF containing: NaCl 92, KCl 2.5, NaH_2P0_4 1.2, $NaHCO_3$ 30, HEPES 20, Glucose 25, Na-Ascorbate 5, Thiourea 2, NaPyruvate 3, $MgSO_4$ 10, $CaCl_2$ 0.5 equilibrated with 95% O2% and 5% CO2 adjusted to 310 ± 5 mOsm/L and placed at room temperature for storage. Individual slices were transferred to the recording chamber and superfused with NaHCO3-aCSF at 34˚C. Electrodes (5–7 MΩ) were pulled from borosilicate glass. Pipettes were filled with (in mM): 140

K-gluconate, HEPES 10, KCl 5, Na-ATP 2, $MgCl_2$ 2, EGTA 0.02, biocytin 0.1% Na_2GTP 0.5, Na_2-phosphocreatine 4, pH 7.4 adjusted with KOH and adjusted to 285 ± 5 mOsm/L with sucrose. Somatic whole-cell recordings were obtained with a Multiclamp 700B amplifier, signals were acquired and sampled at 100 kHz using Digidata 1440A digitizing board. Pipette capacitance was compensated ≈70% in current clamp (CC). Series resistance (*Rs*) was typically 9–15 MΩ. Cells with *Rs* >15 MΩ were discarded. A measured liquid junction potential of ≈10 mV was corrected online. Cells were held at V_h = −80 mV unless otherwise indicated. To create action potential frequency-current curves, a protocol that applies a series of 750 ms current pulses ranging from −100 pA to 220 pA was created using Molecular Devices Clampex 10.7 software running on Windows 7.

Acknowledgements

The authors thank the Biopolymers Facility at HMS for assistance with next-generation sequencing; the Microscopy Resources on the North Quad (MicRoN) core at Harvard Medical School for microscope use and training; Steve Liberles for providing *Npy2r-cre* and *P2ry1-cre* driver lines; ChangHee Lee and Jin Akagi for advice with the On-chip Sort; Kathryn Commons and the Dymecki lab for discussions and thoughtful comments on this manuscript; J.J Mai for reagents and animal husbandry. Grants supporting this work include NARSAD Young Investigator Grant (BWO), NIDA Grant RO1DA034022 (BWO, OVA, SMD), T32 HL 007901 (NS), NIH F31NS108406 (RAS), Howard Hughes Medical Institute Gilliam Fellowship (KAL), NIH F99-NS108515 (KAL), Harvard Brain Science Initiative Bipolar Disorder Seed Grant, supported by Kent and Liz Dauten (OVA), and the GVR Khodadad Fund for the Study of Genetic, Neurobiological, and Physiochemical Processes of EPS (OVA, BWO, SMD).

Additional information

Funding

Funder	Grant reference number	Author
NARSAD Young Investigator Grant	27594	Benjamin W Okaty
National Institute on Drug Abuse	RO1DA034022	Benjamin W Okaty Olga V Alekseyenko Susan M Dymecki
National Heart, Lung, and Blood Institute	T32HL007901	Nikita Sturrock
GVR Khodadad Fund for the Study of Genetic, Neurobiological, and Physiochemical Processes of EPS		Benjamin W Okaty Olga V Alekseyenko Susan M Dymecki
National Institute of Neurological Disorders and Stroke	NIH F31NS108406	Rebecca A Senft
Howard Hughes Medical Institute Gilliam Fellowship		Krissy A Lyon
Harvard Brain Science Initiative Bipolar Disorder Seed Grant, supported by Kent and Liz Dauten		Olga V Alekseyenko
NIH Blueprint for Neuroscience Research	F99 NS108515	Krissy A Lyon

The funders had no role in study design, data collection and interpretation, or the decision to submit the work for publication.

Author contributions

Benjamin W Okaty, Conceptualization, Data curation, Software, Formal analysis, Supervision, Funding acquisition, Validation, Investigation, Visualization, Methodology, Writing - original draft, Project

administration, Writing - review and editing; Nikita Sturrock, Conceptualization, Data curation, Formal analysis, Funding acquisition, Validation, Investigation, Visualization, Methodology, Writing - original draft, Project administration, Writing - review and editing; Yasmin Escobedo Lozoya, Formal analysis, Investigation, Visualization, Methodology, Writing - review and editing; YoonJeung Chang, Krissy A Lyon, Olga V Alekseyenko, Investigation; Rebecca A Senft, Software, Formal analysis, Methodology; Susan M Dymecki, Conceptualization, Supervision, Funding acquisition, Writing - original draft, Project administration, Writing - review and editing

Author ORCIDs
Benjamin W Okaty https://orcid.org/0000-0003-1281-2244
Nikita Sturrock https://orcid.org/0000-0002-1635-6760
Yasmin Escobedo Lozoya https://orcid.org/0000-0001-8197-770X
YoonJeung Chang https://orcid.org/0000-0001-9549-8208
Rebecca A Senft https://orcid.org/0000-0003-0081-4170
Krissy A Lyon https://orcid.org/0000-0002-4453-8406
Olga V Alekseyenko https://orcid.org/0000-0003-1645-5133
Susan M Dymecki https://orcid.org/0000-0003-0910-9881

Ethics
Animal experimentation: Procedures were in accordance with institutional animal care and use committee (IACUC) policies at Harvard Medical School, specifically as outlined and approved in IACUC protocol IS00000231.

Decision letter and Author response
Decision letter https://doi.org/10.7554/eLife.55523.sa1
Author response https://doi.org/10.7554/eLife.55523.sa2

Additional files
Supplementary files
- Supplementary file 1. The 'all_subgroup_markers' worksheet displays the output of the Seurat FindAllMarkers function. Column one is the gene symbol, column two is the p-value given by the Wilcoxon Rank Sum test, column three is the average 'log fold change' (i.e. log-fold difference in transcript abundance between the in-group and out-group), where a positive value indicates that a gene is expressed at a higher level in a given cluster relative to all other clusters, and a negative value indicates that a gene is expressed at a lower level. Column four is the percent of cells within a particular cluster in which the gene was detected, column five is the percent of cells within all other clusters in which a gene was detected, column six gives the Bonferroni-corrected p-value, and column seven indicates the cluster in which the given gene is a positive or negative marker. Note, not all enriched genes are unique to only one cluster, as more similar clusters will share subsets of enriched genes. The 'sig_var_genes' worksheet lists the top two thousand highest 'standardized variance' genes, that is genes that vary significantly more than expected based on mean expression.
- Transparent reporting form

Data availability
The RNA-seq dataset has been deposited to GEO under the accession number GSE144980.

The following dataset was generated:

Author(s)	Year	Dataset title	Dataset URL	Database and Identifier
Okaty BW, Sturrock N, Escobedo Lozoya Y, Chang Y, Senft RA, Lyon KA, Alekseyenko OV,	2020	A single-cell transcriptomic and anatomic atlas of mouse dorsal raphe Pet1 neurons	https://www.ncbi.nlm.nih.gov/geo/query/acc.cgi?acc=GSE144980	NCBI Gene Expression Omnibus, GSE144980

The following previously published datasets were used:

Author(s)	Year	Dataset title	Dataset URL	Database and Identifier
Niederkofler V, Asher TE, Okaty BW, Rood BD	2016	Intersectionally labeled Drd2-Pet1 single-neuron RNA-seq	https://www.ncbi.nlm.nih.gov/geo/query/acc.cgi?acc=GSE87758	NCBI Gene Expression Omnibus, GSE87758
Ren J, Isakova A, Friedmann D, Zeng J	2019	Single-Cell Transcriptomes and Whole-Brain Projections of Serotonin Neurons in the Mouse Dorsal and Median Raphe Nuclei	https://www.ncbi.nlm.nih.gov/geo/query/acc.cgi?acc=GSE135132	NCBI Gene Expression Omnibus, GSE135132
Huang KW, Ochandarena NE, Philson AC, Hyun M	2019	Molecular and anatomical organization of the dorsal raphe nucleus	https://www.ncbi.nlm.nih.gov/geo/query/acc.cgi?acc=GSE134163	NCBI Gene Expression Omnibus, GSE134163

References

Abrams JK, Johnson PL, Hollis JH, Lowry CA. 2004. Anatomic and functional topography of the dorsal raphe nucleus. *Annals of the New York Academy of Sciences* **1018**:46–57. DOI: https://doi.org/10.1196/annals.1296.005, PMID: 15240351

Aghajanian GK, Gallager DW. 1975. Raphe origin of serotonergic nerves terminating in the cerebral ventricles. *Brain Research* **88**:221–231. DOI: https://doi.org/10.1016/0006-8993(75)90386-8, PMID: 167906

Alfonso J, Penkert H, Duman C, Zuccotti A, Monyer H. 2015. Downregulation of sphingosine 1-Phosphate receptor 1 promotes the switch from tangential to radial migration in the OB. *The Journal of Neuroscience* **35**:13659–13672. DOI: https://doi.org/10.1523/JNEUROSCI.1353-15.2015, PMID: 26446219

Alonso A, Merchán P, Sandoval JE, Sánchez-Arrones L, Garcia-Cazorla A, Artuch R, Ferrán JL, Martínez-de-la-Torre M, Puelles L. 2013. Development of the serotonergic cells in murine raphe nuclei and their relations with rhombomeric domains. *Brain Structure and Function* **218**:1229–1277. DOI: https://doi.org/10.1007/s00429-012-0456-8, PMID: 23052546

Amilhon B, Lepicard E, Renoir T, Mongeau R, Popa D, Poirel O, Miot S, Gras C, Gardier AM, Gallego J, Hamon M, Lanfumey L, Gasnier B, Giros B, El Mestikawy S. 2010. VGLUT3 (vesicular glutamate transporter type 3) contribution to the regulation of serotonergic transmission and anxiety. *Journal of Neuroscience* **30**:2198–2210. DOI: https://doi.org/10.1523/JNEUROSCI.5196-09.2010, PMID: 20147547

Andrade R, Haj-Dahmane S. 2013. Serotonin neuron diversity in the dorsal raphe. *ACS Chemical Neuroscience* **4**:22–25. DOI: https://doi.org/10.1021/cn300224n, PMID: 23336040

Asano M, Gruss P. 1992. Pax-5 is expressed at the midbrain-hindbrain boundary during mouse development. *Mechanisms of Development* **39**:29–39. DOI: https://doi.org/10.1016/0925-4773(92)90023-D, PMID: 1283313

Autism Sequencing Consortium, Doan RN, Lim ET, De Rubeis S, Betancur C, Cutler DJ, Chiocchetti AG, Overman LM, Soucy A, Goetze S, Freitag CM, Daly MJ, Walsh CA, Buxbaum JD, Yu TW. 2019. Recessive gene disruptions in autism spectrum disorder. *Nature Genetics* **51**:1092–1098. DOI: https://doi.org/10.1038/s41588-019-0433-8, PMID: 31209396

Azmitia EC, Segal M. 1978. An autoradiographic analysis of the differential ascending projections of the dorsal and median raphe nuclei in the rat. *The Journal of Comparative Neurology* **179**:641–667. DOI: https://doi.org/10.1002/cne.901790311, PMID: 565370

Baker KG, Halliday GM, Törk I. 1990. Cytoarchitecture of the human dorsal raphe nucleus. *Journal of Comparative Neurology* **301**:147–161. DOI: https://doi.org/10.1002/cne.903010202, PMID: 2262589

Baker KG, Halliday GM, Halasz P, Hornung JP, Geffen LB, Cotton RG, Törk I. 1991a. Cytoarchitecture of serotonin-synthesizing neurons in the pontine tegmentum of the human brain. *Synapse* **7**:301–320. DOI: https://doi.org/10.1002/syn.890070407, PMID: 2042112

Baker KG, Halliday GM, Hornung JP, Geffen LB, Cotton RG, Törk I. 1991b. Distribution, morphology and number of monoamine-synthesizing and substance P-containing neurons in the human dorsal raphe nucleus. *Neuroscience* **42**:757–775. DOI: https://doi.org/10.1016/0306-4522(91)90043-N, PMID: 1720227

Bakken TE, Hodge RD, Miller JA, Yao Z, Nguyen TN, Aevermann B, Barkan E, Bertagnolli D, Casper T, Dee N, Garren E, Goldy J, Graybuck LT, Kroll M, Lasken RS, Lathia K, Parry S, Rimorin C, Scheuermann RH, Schork NJ, et al. 2018. Single-nucleus and single-cell transcriptomes compared in matched cortical cell types. *PLOS ONE* **13**:e0209648. DOI: https://doi.org/10.1371/journal.pone.0209648, PMID: 30586455

Banasr M, Hery M, Printemps R, Daszuta A. 2004. Serotonin-induced increases in adult cell proliferation and neurogenesis are mediated through different and common 5-HT receptor subtypes in the dentate gyrus and the subventricular zone. *Neuropsychopharmacology* **29**:450–460. DOI: https://doi.org/10.1038/sj.npp.1300320, PMID: 14872203

Bang SJ, Jensen P, Dymecki SM, Commons KG. 2012. Projections and interconnections of genetically defined serotonin neurons in mice. *European Journal of Neuroscience* **35**:85–96. DOI: https://doi.org/10.1111/j.1460-9568.2011.07936.x, PMID: 22151329

Bang SJ, Commons KG. 2012. Forebrain GABAergic projections from the dorsal raphe nucleus identified by using GAD67-GFP knock-in mice. *The Journal of Comparative Neurology* **520**:4157–4167. DOI: https://doi.org/10.1002/cne.23146, PMID: 22605640

Barrett KT, Dosumu-Johnson RT, Daubenspeck JA, Brust RD, Kreouzis V, Kim JC, Li A, Dymecki SM, Nattie EE. 2016. Partial raphe dysfunction in neurotransmission is sufficient to increase mortality after anoxic exposures in mice at a critical period in postnatal development. *The Journal of Neuroscience* **36**:3943–3953. DOI: https://doi.org/10.1523/JNEUROSCI.1796-15.2016, PMID: 27053202

Beaudet A, Descarries L. 1976. Quantitative data on serotonin nerve terminals in adult rat neocortex. *Brain Research* **111**:301–309. DOI: https://doi.org/10.1016/0006-8993(76)90775-7, PMID: 949604

Bellido I, Hansson AC, Gómez-Luque AJ, Andbjer B, Agnati LF, Fuxe K. 2004. Corticosterone strongly increases the affinity of dorsal raphe 5-HT1A receptors. *NeuroReport* **15**:1457–1459. DOI: https://doi.org/10.1097/01.wnr.0000130542.06764.7f, PMID: 15194873

Brezun JM, Daszuta A. 1999. Depletion in serotonin decreases neurogenesis in the dentate gyrus and the subventricular zone of adult rats. *Neuroscience* **89**:999–1002. DOI: https://doi.org/10.1016/S0306-4522(98)00693-9

Bruchas MR, Land BB, Chavkin C. 2010. The dynorphin/kappa opioid system as a modulator of stress-induced and pro-addictive behaviors. *Brain Research* **1314**:44–55. DOI: https://doi.org/10.1016/j.brainres.2009.08.062, PMID: 19716811

Brust RD, Corcoran AE, Richerson GB, Nattie E, Dymecki SM. 2014. Functional and developmental identification of a molecular subtype of brain serotonergic neuron specialized to regulate breathing dynamics. *Cell Reports* **9**:2152–2165. DOI: https://doi.org/10.1016/j.celrep.2014.11.027, PMID: 25497093

Butler A, Hoffman P, Smibert P, Papalexi E, Satija R. 2018. Integrating single-cell transcriptomic data across different conditions, technologies, and species. *Nature Biotechnology* **36**:411–420. DOI: https://doi.org/10.1038/nbt.4096, PMID: 29608179

Calizo LH, Akanwa A, Ma X, Pan YZ, Lemos JC, Craige C, Heemstra LA, Beck SG. 2011. Raphe serotonin neurons are not homogenous: electrophysiological, morphological and neurochemical evidence. *Neuropharmacology* **61**:524–543. DOI: https://doi.org/10.1016/j.neuropharm.2011.04.008, PMID: 21530552

Campbell JN, Macosko EZ, Fenselau H, Pers TH, Lyubetskaya A, Tenen D, Goldman M, Verstegen AM, Resch JM, McCarroll SA, Rosen ED, Lowell BB, Tsai LT. 2017. A molecular census of arcuate hypothalamus and median eminence cell types. *Nature Neuroscience* **20**:484–496. DOI: https://doi.org/10.1038/nn.4495, PMID: 28166221

Celada P, Puig MV, Casanovas JM, Guillazo G, Artigas F. 2001. Control of dorsal raphe serotonergic neurons by the medial prefrontal cortex: involvement of serotonin-1A, $_{GABA(A)}$, and glutamate receptors. *The Journal of Neuroscience* **21**:9917–9929. DOI: https://doi.org/10.1523/JNEUROSCI.21-24-09917.2001, PMID: 11739599

Challis C, Boulden J, Veerakumar A, Espallergues J, Vassoler FM, Pierce RC, Beck SG, Berton O. 2013. Raphe GABAergic neurons mediate the acquisition of avoidance after social defeat. *Journal of Neuroscience* **33**:13978–13988. DOI: https://doi.org/10.1523/JNEUROSCI.2383-13.2013, PMID: 23986235

Chang RB, Strochlic DE, Williams EK, Umans BD, Liberles SD. 2015. Vagal sensory neuron subtypes that differentially control breathing. *Cell* **161**:622–633. DOI: https://doi.org/10.1016/j.cell.2015.03.022

Chavkin C, James IF, Goldstein A. 1982. Dynorphin is a specific endogenous ligand of the kappa opioid receptor. *Science* **215**:413–415. DOI: https://doi.org/10.1126/science.6120570, PMID: 6120570

Chen CP, Eastwood SL, Hope T, McDonald B, Francis PT, Esiri MM. 2000. Immunocytochemical study of the dorsal and median raphe nuclei in patients with Alzheimer's disease prospectively assessed for behavioural changes. *Neuropathology and Applied Neurobiology* **26**:347–355. DOI: https://doi.org/10.1046/j.1365-2990.2000.00254.x, PMID: 10931368

Chen C-H, Battaglioli G, Martin DL, Hobart SA, Colón W. 2003. Distinctive interactions in the holoenzyme formation for two isoforms of glutamate decarboxylase. *Biochimica Et Biophysica Acta (BBA) - Proteins and Proteomics* **1645**:63–71. DOI: https://doi.org/10.1016/S1570-9639(02)00522-8

Commons KG. 2009. Locally collateralizing glutamate neurons in the dorsal raphe nucleus responsive to substance P contain vesicular glutamate transporter 3 (VGLUT3). *Journal of Chemical Neuroanatomy* **38**:273–281. DOI: https://doi.org/10.1016/j.jchemneu.2009.05.005, PMID: 19467322

Commons KG. 2015. Two major network domains in the dorsal raphe nucleus. *Journal of Comparative Neurology* **523**:1488–1504. DOI: https://doi.org/10.1002/cne.23748, PMID: 25652113

Commons KG. 2016. Ascending serotonin neuron diversity under two umbrellas. *Brain Structure and Function* **221**:3347–3360. DOI: https://doi.org/10.1007/s00429-015-1176-7

Condomitti G, de Wit J. 2018. Heparan sulfate proteoglycans as emerging players in synaptic specificity. *Frontiers in Molecular Neuroscience* **11**:14. DOI: https://doi.org/10.3389/fnmol.2018.00014, PMID: 29434536

Crawford LK, Craige CP, Beck SG. 2010. Increased intrinsic excitability of lateral wing serotonin neurons of the dorsal raphe: a mechanism for selective activation in stress circuits. *Journal of Neurophysiology* **103**:2652–2663. DOI: https://doi.org/10.1152/jn.01132.2009, PMID: 20237311

Dahlstroem A, Fuxe K. 1964. Evidence for the existence of Monoamine-Containing neurons in the central nervous system. I. demonstration of monoamines in the cell bodies of brain stem neurons. *Acta Physiologica Scandinavica. Supplementum* **232**:231–255.

Dengler-Crish CM, Smith MA, Wilson GN. 2017. Early evidence of low bone density and decreased serotonergic synthesis in the dorsal raphe of a Tauopathy Model of Alzheimer's Disease. *Journal of Alzheimer's Disease* **55**:1605–1619. DOI: https://doi.org/10.3233/JAD-160658, PMID: 27814296

Di Donato V, De Santis F, Albadri S, Auer TO, Duroure K, Charpentier M, Concordet JP, Gebhardt C, Del Bene F. 2018. An attractive reelin gradient establishes synaptic lamination in the vertebrate visual system. *Neuron* **97**:1049–1062. DOI: https://doi.org/10.1016/j.neuron.2018.01.030, PMID: 29429939

Dobin A, Gingeras TR. 2016. Optimizing RNA-Seq mapping with STAR. *Methods in Molecular Biology* **1415**:245–262. DOI: https://doi.org/10.1007/978-1-4939-3572-7_13, PMID: 27115637

Dymecki SM, Ray RS, Kim JC. 2010. Mapping cell fate and function using recombinase-based intersectional strategies. *Methods in Enzymology* **477**:183–213. DOI: https://doi.org/10.1016/S0076-6879(10)77011-7, PMID: 20699143

El Mestikawy S, Wallén-Mackenzie A, Fortin GM, Descarries L, Trudeau LE. 2011. From glutamate co-release to vesicular synergy: vesicular glutamate transporters. *Nature Reviews Neuroscience* **12**:204–216. DOI: https://doi.org/10.1038/nrn2969, PMID: 21415847

Ellegood J, Nakai N, Nakatani J, Henkelman M, Takumi T, Lerch J. 2015. Neuroanatomical phenotypes are consistent with Autism-Like behavioral phenotypes in the 15q11-13 duplication mouse model. *Autism Research* **8**:545–555. DOI: https://doi.org/10.1002/aur.1469, PMID: 25755142

Erbel-Sieler C, Dudley C, Zhou Y, Wu X, Estill SJ, Han T, Diaz-Arrastia R, Brunskill EW, Potter SS, McKnight SL. 2004. Behavioral and regulatory abnormalities in mice deficient in the NPAS1 and NPAS3 transcription factors. *PNAS* **101**:13648–13653. DOI: https://doi.org/10.1073/pnas.0405310101, PMID: 15347806

Erickson JD, Eiden LE, Hoffman BJ. 1992. Expression cloning of a reserpine-sensitive vesicular monoamine transporter. *PNAS* **89**:10993–10997. DOI: https://doi.org/10.1073/pnas.89.22.10993, PMID: 1438304

Erlander MG, Tillakaratne NJ, Feldblum S, Patel N, Tobin AJ. 1991. Two genes encode distinct glutamate decarboxylases. *Neuron* **7**:91–100. DOI: https://doi.org/10.1016/0896-6273(91)90077-D, PMID: 2069816

Evrard A, Barden N, Hamon M, Adrien J. 2006. Glucocorticoid receptor-dependent desensitization of 5-HT1A autoreceptors by sleep deprivation: studies in GR-i transgenic mice. *Sleep* **29**:31–36. DOI: https://doi.org/10.1093/sleep/29.1.31, PMID: 16453979

Fernandez SP, Cauli B, Cabezas C, Muzerelle A, Poncer JC, Gaspar P. 2016. Multiscale single-cell analysis reveals unique phenotypes of raphe 5-HT neurons projecting to the forebrain. *Brain Structure and Function* **221**:4007–4025. DOI: https://doi.org/10.1007/s00429-015-1142-4, PMID: 26608830

Fox SR, Deneris ES. 2012. Engrailed is required in maturing serotonin neurons to regulate the cytoarchitecture and survival of the dorsal raphe nucleus. *Journal of Neuroscience* **32**:7832–7842. DOI: https://doi.org/10.1523/JNEUROSCI.5829-11.2012, PMID: 22674259

Fremeau RT, Burman J, Qureshi T, Tran CH, Proctor J, Johnson J, Zhang H, Sulzer D, Copenhagen DR, Storm-Mathisen J, Reimer RJ, Chaudhry FA, Edwards RH. 2002. The identification of vesicular glutamate transporter 3 suggests novel modes of signaling by glutamate. *PNAS* **99**:14488–14493. DOI: https://doi.org/10.1073/pnas.222546799, PMID: 12388773

Fu W, Le Maître E, Fabre V, Bernard JF, David Xu ZQ, Hökfelt T. 2010. Chemical neuroanatomy of the dorsal raphe nucleus and adjacent structures of the mouse brain. *The Journal of Comparative Neurology* **518**:3464–3494. DOI: https://doi.org/10.1002/cne.22407, PMID: 20589909

Funahashi J, Okafuji T, Ohuchi H, Noji S, Tanaka H, Nakamura H. 1999. Role of Pax-5 in the regulation of a mid-hindbrain organizer's activity. *Development, Growth and Differentiation* **41**:59–72. DOI: https://doi.org/10.1046/j.1440-169x.1999.00401.x

Fyodorov D, Nelson T, Deneris E. 1998. Pet-1, a novel ETS domain factor that can activate neuronal nAchR gene transcription. *Journal of Neurobiology* **34**:151–163. DOI: https://doi.org/10.1002/(SICI)1097-4695(19980205)34:2<151::AID-NEU5>3.0.CO;2-1, PMID: 9468386

Gagnon D, Parent M. 2014. Distribution of VGLUT3 in highly collateralized axons from the rat dorsal raphe nucleus as revealed by single-neuron reconstructions. *PLOS ONE* **9**:e87709. DOI: https://doi.org/10.1371/journal.pone.0087709, PMID: 24504335

Gaspar P, Lillesaar C. 2012. Probing the diversity of serotonin neurons. *Philosophical Transactions of the Royal Society B: Biological Sciences* **367**:2382–2394. DOI: https://doi.org/10.1098/rstb.2011.0378

Gonçalves L, Nogueira MI, Shammah-Lagnado SJ, Metzger M. 2009. Prefrontal afferents to the dorsal raphe nucleus in the rat. *Brain Research Bulletin* **78**:240–247. DOI: https://doi.org/10.1016/j.brainresbull.2008.11.012, PMID: 19103268

Gong S, Doughty M, Harbaugh CR, Cummins A, Hatten ME, Heintz N, Gerfen CR. 2007. Targeting cre recombinase to specific neuron populations with bacterial artificial chromosome constructs. *Journal of Neuroscience* **27**:9817–9823. DOI: https://doi.org/10.1523/JNEUROSCI.2707-07.2007, PMID: 17855595

Gras C, Herzog E, Bellenchi GC, Bernard V, Ravassard P, Pohl M, Gasnier B, Giros B, El Mestikawy S. 2002. A third vesicular glutamate transporter expressed by cholinergic and serotoninergic neurons. *The Journal of Neuroscience* **22**:5442–5451. DOI: https://doi.org/10.1523/JNEUROSCI.22-13-05442.2002, PMID: 12097496

Guo YP, Commons KG. 2017. Serotonin neuron abnormalities in the BTBR mouse model of autism. *Autism Research* **10**:66–77. DOI: https://doi.org/10.1002/aur.1665, PMID: 27478061

Hale MW, Lowry CA. 2011. Functional topography of midbrain and pontine serotonergic systems: implications for synaptic regulation of serotonergic circuits. *Psychopharmacology* **213**:243–264. DOI: https://doi.org/10.1007/s00213-010-2089-z, PMID: 21088958

Harburg GC, Hall FS, Harrist AV, Sora I, Uhl GR, Eisch AJ. 2007. Knockout of the mu opioid receptor enhances the survival of adult-generated hippocampal granule cell neurons. *Neuroscience* **144**:77–87. DOI: https://doi.org/10.1016/j.neuroscience.2006.09.018, PMID: 17055658

Hempel CM, Sugino K, Nelson SB. 2007. A manual method for the purification of fluorescently labeled neurons from the mammalian brain. *Nature Protocols* **2**:2924–2929. DOI: https://doi.org/10.1038/nprot.2007.416, PMID: 18007629

Hendricks T, Francis N, Fyodorov D, Deneris ES. 1999. The ETS domain factor Pet-1 is an early and precise marker of central serotonin neurons and interacts with a conserved element in serotonergic genes. *The Journal of Neuroscience* **19**:10348–10356. DOI: https://doi.org/10.1523/JNEUROSCI.19-23-10348.1999, PMID: 10575032

Hendricks TJ, Fyodorov DV, Wegman LJ, Lelutiu NB, Pehek EA, Yamamoto B, Silver J, Weeber EJ, Sweatt JD, Deneris ES. 2003. Pet-1 ETS gene plays a critical role in 5-HT neuron development and is required for normal anxiety-like and aggressive behavior. *Neuron* **37**:233–247. DOI: https://doi.org/10.1016/S0896-6273(02)01167-4, PMID: 12546819

Hennessy ML, Corcoran AE, Brust RD, Chang Y, Nattie EE, Dymecki SM. 2017. Activity of *Tachykinin1*-Expressing *Pet1* Raphe Neurons Modulates the Respiratory Chemoreflex. *The Journal of Neuroscience* **37**:1807–1819. DOI: https://doi.org/10.1523/JNEUROSCI.2316-16.2016, PMID: 28073937

Herzog E, Gilchrist J, Gras C, Muzerelle A, Ravassard P, Giros B, Gaspar P, El Mestikawy S. 2004. Localization of VGLUT3, the vesicular glutamate transporter type 3, in the rat brain. *Neuroscience* **123**:983–1002. DOI: https://doi.org/10.1016/j.neuroscience.2003.10.039, PMID: 14751290

Hioki H. 2004. Chemically specific circuit composed of vesicular glutamate transporter 3- and preprotachykinin B-producing interneurons in the rat neocortex. *Cerebral Cortex* **14**:1266–1275. DOI: https://doi.org/10.1093/cercor/bhh088

Hioki H, Nakamura H, Ma YF, Konno M, Hayakawa T, Nakamura KC, Fujiyama F, Kaneko T. 2010. Vesicular glutamate transporter 3-expressing nonserotonergic projection neurons constitute a subregion in the rat midbrain raphe nuclei. *Journal of Comparative Neurology* **518**:668–686. DOI: https://doi.org/10.1002/cne.22237, PMID: 20034056

Hitoshi S, Maruta N, Higashi M, Kumar A, Kato N, Ikenaka K. 2007. Antidepressant drugs reverse the loss of adult neural stem cells following chronic stress. *Journal of Neuroscience Research* **85**:3574–3585. DOI: https://doi.org/10.1002/jnr.21455, PMID: 17668856

Hodge RD, Bakken TE, Miller JA, Smith KA, Barkan ER, Graybuck LT, Close JL, Long B, Johansen N, Penn O, Yao Z, Eggermont J, Höllt T, Levi BP, Shehata SI, Aevermann B, Beller A, Bertagnolli D, Brouner K, Casper T, et al. 2019. Conserved cell types with divergent features in human versus mouse cortex. *Nature* **573**:61–68. DOI: https://doi.org/10.1038/s41586-019-1506-7, PMID: 31435019

Hoffman B, Mezey E, Brownstein M. 1991. Cloning of a serotonin transporter affected by antidepressants. *Science* **254**:579–580. DOI: https://doi.org/10.1126/science.1948036

Huang KW, Ochandarena NE, Philson AC, Hyun M, Birnbaum JE, Cicconet M, Sabatini BL. 2019. Molecular and anatomical organization of the dorsal raphe nucleus. *eLife* **8**:e46464. DOI: https://doi.org/10.7554/eLife.46464, PMID: 31411560

Ishimura K, Takeuchi Y, Fujiwara K, Tominaga M, Yoshioka H, Sawada T. 1988. Quantitative analysis of the distribution of serotonin-immunoreactive cell bodies in the mouse brain. *Neuroscience Letters* **91**:265–270. DOI: https://doi.org/10.1016/0304-3940(88)90691-X, PMID: 3185964

Iyer A, Kmiecik TE, Park M, Daar I, Blair D, Dunn KJ, Sutrave P, Ihle JN, Bodescot M, Vande Woude GF. 1990. Structure, tissue-specific expression, and transforming activity of the mouse met protooncogene. *Cell Growth & Differentiation : The Molecular Biology Journal of the American Association for Cancer Research* **1**:87–95. PMID: 2085463

Jacobs BL, Azmitia EC. 1992. Structure and function of the brain serotonin system. *Physiological Reviews* **72**:165–229. DOI: https://doi.org/10.1152/physrev.1992.72.1.165, PMID: 1731370

Jensen P, Farago AF, Awatramani RB, Scott MM, Deneris ES, Dymecki SM. 2008. Redefining the serotonergic system by genetic lineage. *Nature Neuroscience* **11**:417–419. DOI: https://doi.org/10.1038/nn2050

Ji X, Wang H, Zhu M, He Y, Zhang H, Chen X, Gao W, Fu Y. 2020. Brainstem atrophy in the early stage of Alzheimer's disease: a voxel-based morphometry study. *Brain Imaging and Behavior* **11**:3. DOI: https://doi.org/10.1007/s11682-019-00231-3

Johnson MD. 1994. Synaptic glutamate release by postnatal rat serotonergic neurons in microculture. *Neuron* **12**:433–442. DOI: https://doi.org/10.1016/0896-6273(94)90283-6, PMID: 7906530

Joyner AL, Kornberg T, Coleman KG, Cox DR, Martin GR. 1985. Expression during embryogenesis of a mouse gene with sequence homology to the *Drosophila* engrailed gene. *Cell* **43**:29–37. DOI: https://doi.org/10.1016/0092-8674(85)90009-1, PMID: 2416459

Joyner AL, Martin GR. 1987. En-1 and En-2, two mouse genes with sequence homology to the *Drosophila* engrailed gene: expression during embryogenesis. *Genes Dev.* **1**:29–38. DOI: https://doi.org/10.1101/gad.1.1.29

Judge SJ, Ingram CD, Gartside SE. 2004. Moderate differences in circulating corticosterone alter receptor-mediated regulation of 5-hydroxytryptamine neuronal activity. *Journal of Psychopharmacology* **18**:475–483. DOI: https://doi.org/10.1177/0269881104018004004

Kapoor V, Provost AC, Agarwal P, Murthy VN. 2016. Activation of raphe nuclei triggers rapid and distinct effects on parallel olfactory bulb output channels. *Nature Neuroscience* **19**:271–282. DOI: https://doi.org/10.1038/nn.4219, PMID: 26752161

Kast RJ, Wu HH, Williams P, Gaspar P, Levitt P. 2017. Specific connectivity and unique molecular identity of MET receptor tyrosine kinase expressing serotonergic neurons in the caudal dorsal raphe nuclei. *ACS Chemical Neuroscience* **8**:1053–1064. DOI: https://doi.org/10.1021/acschemneuro.7b00020, PMID: 28375615

Kim JC, Cook MN, Carey MR, Shen C, Regehr WG, Dymecki SM. 2009. Linking genetically defined neurons to behavior through a broadly applicable silencing allele. *Neuron* **63**:305–315. DOI: https://doi.org/10.1016/j.neuron.2009.07.010, PMID: 19679071

Kimmel RA, Turnbull DH, Blanquet V, Wurst W, Loomis CA, Joyner AL. 2000. Two lineage boundaries coordinate vertebrate apical ectodermal ridge formation. *Genes & Development* **14**:1377–1389. PMID: 10837030

Kirby LG, Pernar L, Valentino RJ, Beck SG. 2003. Distinguishing characteristics of serotonin and non-serotonin-containing cells in the dorsal raphe nucleus: electrophysiological and immunohistochemical studies. *Neuroscience* **116**:669–683. DOI: https://doi.org/10.1016/S0306-4522(02)00584-5, PMID: 12573710

Kosofsky BE, Molliver ME. 1987. The serotoninergic innervation of cerebral cortex: different classes of axon terminals arise from dorsal and median raphe nuclei. *Synapse* **1**:153–168. DOI: https://doi.org/10.1002/syn.890010204

Krueger KC, Deneris ES. 2008. Serotonergic transcription of human FEV reveals direct GATA factor interactions and fate of Pet-1-deficient serotonin neuron precursors. *Journal of Neuroscience* **28**:12748–12758. DOI: https://doi.org/10.1523/JNEUROSCI.4349-08.2008, PMID: 19036967

Laaris N, Haj-Dahmane S, Hamon M, Lanfumey L. 1995. Glucocorticoid receptor-mediated inhibition by corticosterone of 5-HT1A autoreceptor functioning in the rat dorsal raphe nucleus. *Neuropharmacology* **34**:1201–1210. DOI: https://doi.org/10.1016/0028-3908(95)00095-N, PMID: 8532191

Land BB, Bruchas MR, Lemos JC, Xu M, Melief EJ, Chavkin C. 2008. The dysphoric component of stress is encoded by activation of the dynorphin kappa-opioid system. *Journal of Neuroscience* **28**:407–414. DOI: https://doi.org/10.1523/JNEUROSCI.4458-07.2008, PMID: 18184783

Land BB, Bruchas MR, Schattauer S, Giardino WJ, Aita M, Messinger D, Hnasko TS, Palmiter RD, Chavkin C. 2009. Activation of the kappa opioid receptor in the dorsal raphe nucleus mediates the aversive effects of stress and reinstates drug seeking. *PNAS* **106**:19168–19173. DOI: https://doi.org/10.1073/pnas.0910705106, PMID: 19864633

Lázaro-Peña MI, Díaz-Balzac CA, Bülow HE, Emmons SW. 2018. Synaptogenesis is modulated by heparan sulfate in *Caenorhabditis elegans*. *Genetics* **209**:195–208. DOI: https://doi.org/10.1534/genetics.118.300837, PMID: 29559501

Lesch K-P, Wolozin BL, Estler HC, Murphy DL, Riederer P. 1993. Isolation of a cDNA encoding the human brain serotonin transporter. *Journal of Neural Transmission* **91**:67–72. DOI: https://doi.org/10.1007/BF01244919

Levine ES, Jacobs BL. 1992. Neurochemical afferents controlling the activity of serotonergic neurons in the dorsal raphe nucleus: microiontophoretic studies in the awake cat. *The Journal of Neuroscience* **12**:4037–4044. DOI: https://doi.org/10.1523/JNEUROSCI.12-10-04037.1992, PMID: 1357117

Lidov HG, Grzanna R, Molliver ME. 1980. The serotonin innervation of the cerebral cortex in the rat–an immunohistochemical analysis. *Neuroscience* **5**:207–227. DOI: https://doi.org/10.1016/0306-4522(80)90099-8, PMID: 6990293

Lidov HG, Molliver ME. 1982. Immunohistochemical study of the development of serotonergic neurons in the rat CNS. *Brain Research Bulletin* **9**:559–604. DOI: https://doi.org/10.1016/0361-9230(82)90164-2, PMID: 6756556

Lin JH, Takano T, Arcuino G, Wang X, Hu F, Darzynkiewicz Z, Nunes M, Goldman SA, Nedergaard M. 2007. Purinergic signaling regulates neural progenitor cell expansion and neurogenesis. *Developmental Biology* **302**:356–366. DOI: https://doi.org/10.1016/j.ydbio.2006.09.017, PMID: 17188262

Liu C, Maejima T, Wyler SC, Casadesus G, Herlitze S, Deneris ES. 2010. Pet-1 is required across different stages of life to regulate serotonergic function. *Nature Neuroscience* **13**:1190–1198. DOI: https://doi.org/10.1038/nn.2623

Liu Z, Zhou J, Li Y, Hu F, Lu Y, Ma M, Feng Q, Zhang JE, Wang D, Zeng J, Bao J, Kim JY, Chen ZF, El Mestikawy S, Luo M. 2014. Dorsal raphe neurons signal reward through 5-HT and glutamate. *Neuron* **81**:1360–1374. DOI: https://doi.org/10.1016/j.neuron.2014.02.010, PMID: 24656254

Liu C, Deneris ES. 2011. Transcriptional control of serotonin-modulated behavior and physiology. *Neuropsychopharmacology* **36**:361–362. DOI: https://doi.org/10.1038/npp.2010.135, PMID: 21116255

Lorez HP, Richards JG. 1982. Supra-ependymal serotoninergic nerves in mammalian brain: morphological, pharmacological and functional studies. *Brain Research Bulletin* **9**:727–741. DOI: https://doi.org/10.1016/0361-9230(82)90179-4, PMID: 6184136

Lovatt D, Ruble BK, Lee J, Dueck H, Kim TK, Fisher S, Francis C, Spaethling JM, Wolf JA, Grady MS, Ulyanova AV, Yeldell SB, Griepenburg JC, Buckley PT, Kim J, Sul JY, Dmochowski IJ, Eberwine J. 2014. Transcriptome in vivo analysis (TIVA) of spatially defined single cells in live tissue. *Nature Methods* **11**:190–196. DOI: https://doi.org/10.1038/nmeth.2804, PMID: 24412976

Love CE, Prince VE. 2012. Expression and retinoic acid regulation of the zebrafish *nr2f* orphan nuclear receptor genes. *Developmental Dynamics* **241**:1603–1615. DOI: https://doi.org/10.1002/dvdy.23838, PMID: 22836912

Luo J, Feng Q, Wei L, Luo M. 2017. Optogenetic activation of dorsal raphe neurons rescues the autistic-like social deficits in Shank3 knockout mice. *Cell Research* **27**:950–953. DOI: https://doi.org/10.1038/cr.2017.52, PMID: 28374752

Macosko EZ, Basu A, Satija R, Nemesh J, Shekhar K, Goldman M, Tirosh I, Bialas AR, Kamitaki N, Martersteck EM, Trombetta JJ, Weitz DA, Sanes JR, Shalek AK, Regev A, McCarroll SA. 2015. Highly parallel Genome-wide expression profiling of individual cells using nanoliter droplets. *Cell* **161**:1202–1214. DOI: https://doi.org/10.1016/j.cell.2015.05.002, PMID: 26000488

Maddaloni G, Bertero A, Pratelli M, Barsotti N, Boonstra A, Giorgi A, Migliarini S, Pasqualetti M. 2017. Development of serotonergic fibers in the Post-Natal mouse brain. *Frontiers in Cellular Neuroscience* **11**:202. DOI: https://doi.org/10.3389/fncel.2017.00202, PMID: 28769763

Madisen L, Garner AR, Shimaoka D, Chuong AS, Klapoetke NC, Li L, van der Bourg A, Niino Y, Egolf L, Monetti C, Gu H, Mills M, Cheng A, Tasic B, Nguyen TN, Sunkin SM, Benucci A, Nagy A, Miyawaki A, Helmchen F, et al. 2015. Transgenic mice for intersectional targeting of neural sensors and effectors with high specificity and performance. *Neuron* **85**:942–958. DOI: https://doi.org/10.1016/j.neuron.2015.02.022, PMID: 25741722

Makrides N, Panayiotou E, Fanis P, Karaiskos C, Lapathitis G, Malas S. 2018. Sequential role of SOXB2 factors in GABAergic neuron specification of the dorsal midbrain. *Frontiers in Molecular Neuroscience* **11**:152. DOI: https://doi.org/10.3389/fnmol.2018.00152, PMID: 29867344

McDevitt RA, Tiran-Cappello A, Shen H, Balderas I, Britt JP, Marino RAM, Chung SL, Richie CT, Harvey BK, Bonci A. 2014. Serotonergic versus nonserotonergic dorsal raphe projection neurons: differential participation in reward circuitry. *Cell Reports* **8**:1857–1869. DOI: https://doi.org/10.1016/j.celrep.2014.08.037, PMID: 25242321

Michaelson JJ, Shin MK, Koh JY, Brueggeman L, Zhang A, Katzman A, McDaniel L, Fang M, Pufall M, Pieper AA. 2017. Neuronal PAS domain proteins 1 and 3 are master regulators of neuropsychiatric risk genes. *Biological Psychiatry* **82**:213–223. DOI: https://doi.org/10.1016/j.biopsych.2017.03.021, PMID: 28499489

Michelsen KA, Schmitz C, Steinbusch HWM. 2007. The dorsal raphe nucleus—From silver stainings to a role in depression. *Brain Research Reviews* **55**:329–342. DOI: https://doi.org/10.1016/j.brainresrev.2007.01.002

Michelsen KA, Prickaerts J, Steinbusch HW. 2008. The dorsal raphe nucleus and serotonin: implications for neuroplasticity linked to major depression and Alzheimer's disease. *Progress in Brain Research* **172**:233–264. DOI: https://doi.org/10.1016/S0079-6123(08)00912-6, PMID: 18772036

Mikkelsen JD, Hay-Schmidt A, Larsen PJ. 1997. Central innervation of the rat ependyma and subcommissural organ with special reference to ascending serotoninergic projections from the raphe nuclei. *The Journal of Comparative Neurology* **384**:556–568. DOI: https://doi.org/10.1002/(SICI)1096-9861(19970811)384:4<556::AID-CNE5>3.0.CO;2-1, PMID: 9259489

Minge D, Senkov O, Kaushik R, Herde MK, Tikhobrazova O, Wulff AB, Mironov A, van Kuppevelt TH, Oosterhof A, Kochlamazashvili G, Dityatev A, Henneberger C. 2017. Heparan sulfates support pyramidal cell excitability, synaptic plasticity, and context discrimination. *Cerebral Cortex* **17**:903–918. DOI: https://doi.org/10.1093/cercor/bhx003

Mirzadeh Z, Doetsch F, Sawamoto K, Wichterle H, Alvarez-Buylla A. 2010. The subventricular zone En-face: wholemount staining and ependymal flow. *Journal of Visualized Experiments* **6**:1938. DOI: https://doi.org/10.3791/1938

Miyazaki K, Narita N, Narita M. 2005. Maternal administration of thalidomide or valproic acid causes abnormal serotonergic neurons in the offspring: implication for pathogenesis of autism. *International Journal of Developmental Neuroscience* **23**:287–297. DOI: https://doi.org/10.1016/j.ijdevneu.2004.05.004, PMID: 15749253

Molliver ME. 1987. Serotonergic neuronal systems: what their anatomic organization tells us about function. *Journal of Clinical Psychopharmacology* **7**:3S–23. PMID: 3323265

Mosko SS, Haubrich D, Jacobs BL. 1977. Serotonergic afferents to the dorsal raphe nucleus: evdience from HRP and synaptosomal uptake studies. *Brain Research* **119**:269–290. DOI: https://doi.org/10.1016/0006-8993(77)90311-0, PMID: 830388

Münster-Wandowski A, Zander JF, Richter K, Ahnert-Hilger G. 2016. Co-existence of functionally different vesicular neurotransmitter transporters. *Frontiers in Synaptic Neuroscience* **8**:4. DOI: https://doi.org/10.3389/fnsyn.2016.00004, PMID: 26909036

Muzerelle A, Scotto-Lomassese S, Bernard JF, Soiza-Reilly M, Gaspar P. 2016. Conditional anterograde tracing reveals distinct targeting of individual serotonin cell groups (B5-B9) to the forebrain and brainstem. *Brain Structure and Function* **221**:535–561. DOI: https://doi.org/10.1007/s00429-014-0924-4, PMID: 25403254

Negoias S, Croy I, Gerber J, Puschmann S, Petrowski K, Joraschky P, Hummel T. 2010. Reduced olfactory bulb volume and olfactory sensitivity in patients with acute major depression. *Neuroscience* **169**:415–421. DOI: https://doi.org/10.1016/j.neuroscience.2010.05.012

Niederkofler V, Asher TE, Okaty BW, Rood BD, Narayan A, Hwa LS, Beck SG, Miczek KA, Dymecki SM. 2016. Identification of serotonergic neuronal modules that affect aggressive behavior. *Cell Reports* **17**:1934–1949. DOI: https://doi.org/10.1016/j.celrep.2016.10.063, PMID: 27851959

Nyberg J. 2005. Glucose-Dependent insulinotropic polypeptide is expressed in adult Hippocampus and induces progenitor cell proliferation. *Journal of Neuroscience* **25**:1816–1825. DOI: https://doi.org/10.1523/JNEUROSCI.4920-04.2005

O'Hearn E, Molliver ME. 1984. Organization of raphe-cortical projections in rat: a quantitative retrograde study. *Brain Research Bulletin* **13**:709–726. DOI: https://doi.org/10.1016/0361-9230(84)90232-6, PMID: 6099744

Ogawa SK, Cohen JY, Hwang D, Uchida N, Watabe-Uchida M. 2014. Organization of monosynaptic inputs to the serotonin and dopamine neuromodulatory systems. *Cell Reports* **8**:1105–1118. DOI: https://doi.org/10.1016/j.celrep.2014.06.042, PMID: 25108805

Okaty BW, Freret ME, Rood BD, Brust RD, Hennessy ML, deBairos D, Kim JC, Cook MN, Dymecki SM. 2015. Multi-Scale molecular deconstruction of the serotonin neuron system. *Neuron* **88**:774–791. DOI: https://doi.org/10.1016/j.neuron.2015.10.007, PMID: 26549332

Okaty BW, Commons KG, Dymecki SM. 2019. Embracing diversity in the 5-HT neuronal system. *Nature Reviews Neuroscience* **20**:397–424. DOI: https://doi.org/10.1038/s41583-019-0151-3, PMID: 30948838

Pelosi B, Migliarini S, Pacini G, Pratelli M, Pasqualetti M. 2014. Generation of Pet1210-Cre transgenic mouse line reveals non-serotonergic expression domains of Pet1 both in CNS and periphery. *PLOS ONE* **9**:e104318. DOI: https://doi.org/10.1371/journal.pone.0104318, PMID: 25098329

Peyron C, Petit J-M, Rampon C, Jouvet M, Luppi P-H. 1997. Forebrain afferents to the rat dorsal raphe nucleus demonstrated by retrograde and anterograde tracing methods. *Neuroscience* **82**:443–468. DOI: https://doi.org/10.1016/S0306-4522(97)00268-6

Peyron C, Rampon C, Petit JM, Luppi PH. 2018. Sub-regions of the dorsal raphé nucleus receive different inputs from the brainstem. *Sleep Medicine* **49**:53–63. DOI: https://doi.org/10.1016/j.sleep.2018.07.002, PMID: 30078667

Pillai A, Mansouri A, Behringer R, Westphal H, Goulding M. 2007. Lhx1 and Lhx5 maintain the inhibitory-neurotransmitter status of interneurons in the dorsal spinal cord. *Development* **134**:357–366. DOI: https://doi.org/10.1242/dev.02717, PMID: 17166926

Pollak Dorocic I, Fürth D, Xuan Y, Johansson Y, Pozzi L, Silberberg G, Carlén M, Meletis K. 2014. A whole-brain atlas of inputs to serotonergic neurons of the dorsal and median raphe nuclei. *Neuron* **83**:663–678. DOI: https://doi.org/10.1016/j.neuron.2014.07.002, PMID: 25102561

Poulin JF, Tasic B, Hjerling-Leffler J, Trimarchi JM, Awatramani R. 2016. Disentangling neural cell diversity using single-cell transcriptomics. *Nature Neuroscience* **19**:1131–1141. DOI: https://doi.org/10.1038/nn.4366, PMID: 27571192

Prakash N, Stark CJ, Keisler MN, Luo L, Der-Avakian A, Dulcis D. 2020. Serotonergic plasticity in the dorsal raphe nucleus characterizes susceptibility and resilience to anhedonia. *The Journal of Neuroscience* **40**:569–584. DOI: https://doi.org/10.1523/JNEUROSCI.1802-19.2019, PMID: 31792153

Prouty EW, Chandler DJ, Waterhouse BD. 2017. Neurochemical differences between target-specific populations of rat dorsal raphe projection neurons. *Brain Research* **1675**:28–40. DOI: https://doi.org/10.1016/j.brainres.2017.08.031, PMID: 28867482

Ray RS, Corcoran AE, Brust RD, Kim JC, Richerson GB, Nattie E, Dymecki SM. 2011. Impaired respiratory and body temperature control upon acute serotonergic neuron inhibition. *Science* **333**:637–642. DOI: https://doi.org/10.1126/science.1205295, PMID: 21798952

Ren J, Friedmann D, Xiong J, Liu CD, Ferguson BR, Weerakkody T, DeLoach KE, Ran C, Pun A, Sun Y, Weissbourd B, Neve RL, Huguenard J, Horowitz MA, Luo L. 2018. Anatomically defined and functionally distinct dorsal raphe serotonin Sub-systems. *Cell* **175**:472–487. DOI: https://doi.org/10.1016/j.cell.2018.07.043

Ren J, Isakova A, Friedmann D, Zeng J, Grutzner SM, Pun A, Zhao GQ, Kolluru SS, Wang R, Lin R, Li P, Li A, Raymond JL, Luo Q, Luo M, Quake SR, Luo L. 2019. Single-cell transcriptomes and whole-brain projections of serotonin neurons in the mouse dorsal and median raphe nuclei. *eLife* **8**:e49424. DOI: https://doi.org/10.7554/eLife.49424, PMID: 31647409

Rood BD, Calizo LH, Piel D, Spangler ZP, Campbell K, Beck SG. 2014. Dorsal Raphe Serotonin Neurons in Mice: Immature Hyperexcitability Transitions to Adult State during First Three Postnatal Weeks Suggesting Sensitive Period for Environmental Perturbation. *The Journal of Neuroscience* **34**:4809–4821. DOI: https://doi.org/10.1523/JNEUROSCI.1498-13.2014

Rosenberg AB, Roco CM, Muscat RA, Kuchina A, Sample P, Yao Z, Graybuck LT, Peeler DJ, Mukherjee S, Chen W, Pun SH, Sellers DL, Tasic B, Seelig G. 2018. Single-cell profiling of the developing mouse brain and spinal cord with split-pool barcoding. *Science* **360**:176–182. DOI: https://doi.org/10.1126/science.aam8999, PMID: 29545511

Saunders A, Macosko EZ, Wysoker A, Goldman M, Krienen FM, de Rivera H, Bien E, Baum M, Bortolin L, Wang S, Goeva A, Nemesh J, Kamitaki N, Brumbaugh S, Kulp D, McCarroll SA. 2018. Molecular diversity and specializations among the cells of the adult mouse brain. *Cell* **174**:1015–1030. DOI: https://doi.org/10.1016/j.cell.2018.07.028

Schindelin J, Arganda-Carreras I, Frise E, Kaynig V, Longair M, Pietzsch T, Preibisch S, Rueden C, Saalfeld S, Schmid B, Tinevez JY, White DJ, Hartenstein V, Eliceiri K, Tomancak P, Cardona A. 2012. Fiji: an open-source platform for biological-image analysis. *Nature Methods* **9**:676–682. DOI: https://doi.org/10.1038/nmeth.2019, PMID: 22743772

Sciolino NR, Plummer NW, Chen YW, Alexander GM, Robertson SD, Dudek SM, McElligott ZA, Jensen P. 2016. Recombinase-Dependent mouse lines for chemogenetic activation of genetically defined cell Types. *Cell Reports* **15**:2563–2573. DOI: https://doi.org/10.1016/j.celrep.2016.05.034, PMID: 27264177

Senft RA. 2020. RNAscope-IHC-Colocalization-in-ImageJ. *GitHub*. https://github.com/rsenft1/RNAscope-IHC-Colocalization-in-ImageJ

Sengupta A, Bocchio M, Bannerman DM, Sharp T, Capogna M. 2017. Control of amygdala circuits by 5-HT neurons via 5-HT and glutamate cotransmission. *The Journal of Neuroscience* **37**:1785–1796. DOI: https://doi.org/10.1523/JNEUROSCI.2238-16.2016, PMID: 28087766

Shikanai H, Yoshida T, Konno K, Yamasaki M, Izumi T, Ohmura Y, Watanabe M, Yoshioka M. 2012. Distinct neurochemical and functional properties of GAD67-containing 5-HT neurons in the rat dorsal raphe nucleus. *Journal of Neuroscience* **32**:14415–14426. DOI: https://doi.org/10.1523/JNEUROSCI.5929-11.2012, PMID: 23055511

Šimić G, Babić Leko M, Wray S, Harrington CR, Delalle I, Jovanov-Milošević N, Bažadona D, Buée L, de Silva R, Di Giovanni G, Wischik CM, Hof PR. 2017. Monoaminergic neuropathology in Alzheimer's disease. *Progress in Neurobiology* **151**:101–138. DOI: https://doi.org/10.1016/j.pneurobio.2016.04.001, PMID: 27084356

Siopi E, Denizet M, Gabellec MM, de Chaumont F, Olivo-Marin JC, Guilloux JP, Lledo PM, Lazarini F. 2016. Anxiety- and Depression-Like states lead to pronounced olfactory deficits and impaired adult neurogenesis in mice. *Journal of Neuroscience* **36**:518–531. DOI: https://doi.org/10.1523/JNEUROSCI.2817-15.2016, PMID: 26758842

Soghomonian JJ, Martin DL. 1998. Two isoforms of glutamate decarboxylase: why? *Trends in Pharmacological Sciences* **19**:500–505. DOI: https://doi.org/10.1016/S0165-6147(98)01270-X, PMID: 9871412

Sos KE, Mayer MI, Cserép C, Takács FS, Szőnyi A, Freund TF, Nyiri G. 2017. Cellular architecture and transmitter phenotypes of neurons of the mouse median raphe region. *Brain Structure and Function* **222**:287–299. DOI: https://doi.org/10.1007/s00429-016-1217-x, PMID: 27044051

Soumier A, Banasr M, Kerkerian-Le Goff L, Daszuta A. 2010. Region- and phase-dependent effects of 5-HT(1A) and 5-HT(2C) receptor activation on adult neurogenesis. *European Neuropsychopharmacology* **20**:336–345. DOI: https://doi.org/10.1016/j.euroneuro.2009.11.007, PMID: 20022222

Spaethling JM, Piel D, Dueck H, Buckley PT, Morris JF, Fisher SA, Lee J, Sul JY, Kim J, Bartfai T, Beck SG, Eberwine JH. 2014. Serotonergic neuron regulation informed by *in vivo* single-cell transcriptomics. *FASEB Journal : Official Publication of the Federation of American Societies for Experimental Biology* **28**:771–780. DOI: https://doi.org/10.1096/fj.13-240267, PMID: 24192459

Spencer WC, Deneris ES. 2017. Regulatory mechanisms controlling maturation of serotonin neuron identity and function. *Frontiers in Cellular Neuroscience* **11**:215. DOI: https://doi.org/10.3389/fncel.2017.00215, PMID: 28769770

Stanco A, Pla R, Vogt D, Chen Y, Mandal S, Walker J, Hunt RF, Lindtner S, Erdman CA, Pieper AA, Hamilton SP, Xu D, Baraban SC, Rubenstein JLR. 2014. NPAS1 represses the generation of specific subtypes of cortical interneurons. *Neuron* **84**:940–953. DOI: https://doi.org/10.1016/j.neuron.2014.10.040

Steinbusch HW, Verhofstad AA, Joosten HW. 1978. Localization of serotonin in the central nervous system by immunohistochemistry: description of a specific and sensitive technique and some applications. *Neuroscience* **3**:811–819. DOI: https://doi.org/10.1016/0306-4522(78)90033-7, PMID: 362232

Steinbusch HWM, Van der Kooy D, Verhofstad AAJ, Pellegrino A. 1980. Serotonergic and non-serotonergic projections from the nucleus raphe dorsalis to the caudate-putamen complex in the rat, studied by a combined immunofluorescence and fluorescent retrograde axonal labeling technique. *Neuroscience Letters* **19**:137–142. DOI: https://doi.org/10.1016/0304-3940(80)90184-6

Steinbusch HW. 1981. Distribution of serotonin-immunoreactivity in the central nervous system of the rat-cell bodies and terminals. *Neuroscience* **6**:557–618. DOI: https://doi.org/10.1016/0306-4522(81)90146-9, PMID: 7017455

Stuart T, Butler A, Hoffman P, Hafemeister C, Papalexi E, Mauck WM, Hao Y, Stoeckius M, Smibert P, Satija R. 2019. Comprehensive integration of Single-Cell data. *Cell* **177**:1888–1902. DOI: https://doi.org/10.1016/j.cell.2019.05.031, PMID: 31178118

Tasic B, Menon V, Nguyen TN, Kim TK, Jarsky T, Yao Z, Levi B, Gray LT, Sorensen SA, Dolbeare T, Bertagnolli D, Goldy J, Shapovalova N, Parry S, Lee C, Smith K, Bernard A, Madisen L, Sunkin SM, Hawrylycz M, et al. 2016. Adult mouse cortical cell taxonomy revealed by single cell transcriptomics. *Nature Neuroscience* **19**:335–346. DOI: https://doi.org/10.1038/nn.4216, PMID: 26727548

Tasic B. 2018. Single cell transcriptomics in neuroscience: cell classification and beyond. *Current Opinion in Neurobiology* **50**:242–249. DOI: https://doi.org/10.1016/j.conb.2018.04.021, PMID: 29738987

Tasic B, Yao Z, Graybuck LT, Smith KA, Nguyen TN, Bertagnolli D, Goldy J, Garren E, Economo MN, Viswanathan S, Penn O, Bakken T, Menon V, Miller J, Fong O, Hirokawa KE, Lathia K, Rimorin C, Tieu M, Larsen R, et al. 2018. Shared and distinct transcriptomic cell types across neocortical Areas. *Nature* **563**:72–78. DOI: https://doi.org/10.1038/s41586-018-0654-5, PMID: 30382198

Teissier A, Chemiakine A, Inbar B, Bagchi S, Ray RS, Palmiter RD, Dymecki SM, Moore H, Ansorge MS. 2015. Activity of raphé serotonergic neurons controls emotional behaviors. *Cell Reports* **13**:1965–1976. DOI: https://doi.org/10.1016/j.celrep.2015.10.061, PMID: 26655908

Teng T, Gaillard A, Muzerelle A, Gaspar P. 2017. EphrinA5 signaling is required for the distinctive targeting of raphe serotonin neurons in the forebrain. *Eneuro* **4**:ENEURO.0327-16.2017. DOI: https://doi.org/10.1523/ENEURO.0327-16.2017, PMID: 28197551

Tong CK, Chen J, Cebrián-Silla A, Mirzadeh Z, Obernier K, Guinto CD, Tecott LH, García-Verdugo JM, Kriegstein A, Alvarez-Buylla A. 2014. Axonal control of the adult neural stem cell niche. *Cell Stem Cell* **14**:500–511. DOI: https://doi.org/10.1016/j.stem.2014.01.014, PMID: 24561083

Tritsch NX, Ding JB, Sabatini BL. 2012. Dopaminergic neurons inhibit striatal output through non-canonical release of GABA. *Nature* **490**:262–266. DOI: https://doi.org/10.1038/nature11466, PMID: 23034651

Trivellin G, Bjelobaba I, Daly AF, Larco DO, Palmeira L, Faucz FR, Thiry A, Leal LF, Rostomyan L, Quezado M, Schernthaner-Reiter MH, Janjic MM, Villa C, Wu TJ, Stojilkovic SS, Beckers A, Feldman B, Stratakis CA. 2016. Characterization of GPR101 transcript structure and expression patterns. *Journal of Molecular Endocrinology* **57**:97–111. DOI: https://doi.org/10.1530/JME-16-0045, PMID: 27282544

Trivellin G, Hernández-Ramírez LC, Swan J, Stratakis CA. 2018. An orphan G-protein-coupled receptor causes human gigantism and/or acromegaly: molecular biology and clinical correlations. *Best Practice & Research Clinical Endocrinology & Metabolism* **32**:125–140. DOI: https://doi.org/10.1016/j.beem.2018.02.004, PMID: 29678281

Usoskin D, Furlan A, Islam S, Abdo H, Lönnerberg P, Lou D, Hjerling-Leffler J, Haeggström J, Kharchenko O, Kharchenko PV, Linnarsson S, Ernfors P. 2015. Unbiased classification of sensory neuron types by large-scale single-cell RNA sequencing. *Nature Neuroscience* **18**:145–153. DOI: https://doi.org/10.1038/nn.3881, PMID: 25420068

Vakalopoulos C. 2017. Alzheimer's Disease: The Alternative Serotonergic Hypothesis of Cognitive Decline. *Journal of Alzheimer's Disease* **60**:859–866. DOI: https://doi.org/10.3233/JAD-170364, PMID: 28984594

Vasudeva RK, Lin RC, Simpson KL, Waterhouse BD. 2011. Functional organization of the dorsal raphe efferent system with special consideration of nitrergic cell groups. *Journal of Chemical Neuroanatomy* **41**:281–293. DOI: https://doi.org/10.1016/j.jchemneu.2011.05.008, PMID: 21640185

Vasudeva RK, Waterhouse BD. 2014. Cellular profile of the dorsal raphe lateral wing sub-region: relationship to the lateral dorsal tegmental nucleus. *Journal of Chemical Neuroanatomy* **57-58**:15–23. DOI: https://doi.org/10.1016/j.jchemneu.2014.03.001, PMID: 24704911

Vertes RP. 1991. A PHA-L analysis of ascending projections of the dorsal raphe nucleus in the rat. *The Journal of Comparative Neurology* **313**:643–668. DOI: https://doi.org/10.1002/cne.903130409, PMID: 1783685

Vertes RP, Kocsis B. 1994. Projections of the dorsal raphe nucleus to the brainstem: pha-l analysis in the rat. *The Journal of Comparative Neurology* **340**:11–26. DOI: https://doi.org/10.1002/cne.903400103, PMID: 8176000

Vincent MY, Donner NC, Smith DG, Lowry CA, Jacobson L. 2018. Dorsal raphé nucleus glucocorticoid receptors inhibit tph2 gene expression in male C57BL/6J mice. *Neuroscience Letters* **665**:48–53. DOI: https://doi.org/10.1016/j.neulet.2017.11.041, PMID: 29174640

Vincent MY, Jacobson L. 2014. Glucocorticoid receptor deletion from the dorsal raphé nucleus of mice reduces dysphoria-like behavior and impairs hypothalamic-pituitary-adrenocortical Axis feedback inhibition. *European Journal of Neuroscience* **39**:1671–1681. DOI: https://doi.org/10.1111/ejn.12538

Voisin AN, Mnie-Filali O, Giguère N, Fortin GM, Vigneault E, El Mestikawy S, Descarries L, Trudeau L-É. 2016. Axonal segregation and role of the vesicular glutamate transporter VGLUT3 in serotonin neurons. *Frontiers in Neuroanatomy* **10**:39. DOI: https://doi.org/10.3389/fnana.2016.00039

Walther DJ. 2003. Synthesis of serotonin by a second tryptophan hydroxylase isoform. *Science* **299**:76. DOI: https://doi.org/10.1126/science.1078197

Walther DJ, Bader M. 2003. A unique central tryptophan hydroxylase isoform. *Biochemical Pharmacology* **66**:1673–1680. DOI: https://doi.org/10.1016/S0006-2952(03)00556-2, PMID: 14563478

Wang R, Hausknecht K, Shen RY, Haj-Dahmane S. 2018. Potentiation of glutamatergic synaptic transmission onto dorsal raphe serotonergic neurons in the valproic acid model of autism. *Frontiers in Pharmacology* **9**:1185. DOI: https://doi.org/10.3389/fphar.2018.01185, PMID: 30459605

Wang H-L, Zhang S, Qi J, Wang H, Cachope R, Mejias-Aponte CA, Gomez JA, Mateo-Semidey GE, Beaudoin GMJ, Paladini CA, Cheer JF, Morales M. 2019. Dorsal raphe dual Serotonin-Glutamate neurons drive reward by establishing excitatory synapses on VTA mesoaccumbens dopamine neurons. *Cell Reports* **26**:1128–1142. DOI: https://doi.org/10.1016/j.celrep.2019.01.014

Watanabe M, Serizawa M, Sawada T, Takeda K, Takahashi T, Yamamoto N, Koizumi F, Koh Y. 2014. A novel flow cytometry-based cell capture platform for the detection, capture and molecular characterization of rare tumor cells in blood. *Journal of Translational Medicine* **12**:143. DOI: https://doi.org/10.1186/1479-5876-12-143, PMID: 24886394

Weissbourd B, Ren J, DeLoach KE, Guenthner CJ, Miyamichi K, Luo L. 2014. Presynaptic partners of dorsal raphe serotonergic and GABAergic neurons. *Neuron* **83**:645–662. DOI: https://doi.org/10.1016/j.neuron.2014.06.024, PMID: 25102560

Wu HH, Levitt P. 2013. Prenatal expression of MET receptor tyrosine kinase in the fetal mouse dorsal raphe nuclei and the visceral motor/Sensory brainstem. *Developmental Neuroscience* **35**:1–16. DOI: https://doi.org/10.1159/000346367, PMID: 23548689

Wyler SC, Donovan LJ, Yeager M, Deneris E. 2015. Pet-1 controls tetrahydrobiopterin pathway and *Slc22a3* Transporter Genes in Serotonin Neurons. *ACS Chemical Neuroscience* **6**:1198–1205. DOI: https://doi.org/10.1021/cn500331z, PMID: 25642596

Wyler SC, Spencer WC, Green NH, Rood BD, Crawford L, Craige C, Gresch P, McMahon DG, Beck SG, Deneris E. 2016. Pet-1 switches transcriptional targets postnatally to regulate maturation of serotonin neuron excitability. *The Journal of Neuroscience* **36**:1758–1774. DOI: https://doi.org/10.1523/JNEUROSCI.3798-15.2016, PMID: 26843655

Ye W, Bouchard M, Stone D, Liu X, Vella F, Lee J, Nakamura H, Ang SL, Busslinger M, Rosenthal A. 2001. Distinct regulators control the expression of the mid-hindbrain organizer signal FGF8. *Nature Neuroscience* **4**:1175–1181. DOI: https://doi.org/10.1038/nn761, PMID: 11704761

Ye Y, Zhao Z, Xu H, Zhang X, Su X, Yang Y, Yu X, He X. 2016. Activation of sphingosine 1-Phosphate receptor 1 enhances Hippocampus neurogenesis in a rat model of traumatic brain injury: an involvement of MEK/Erk signaling pathway. *Neural Plasticity* **2016**::1–13. DOI: https://doi.org/10.1155/2016/8072156, PMID: 28018679

Zeisel A, Muñoz-Manchado AB, Codeluppi S, Lönnerberg P, La Manno G, Juréus A, Marques S, Munguba H, He L, Betsholtz C, Rolny C, Castelo-Branco G, Hjerling-Leffler J, Linnarsson S. 2015. Brain structure. Cell types in the mouse cortex and Hippocampus revealed by single-cell RNA-seq. *Science* **347**:1138–1142. DOI: https://doi.org/10.1126/science.aaa1934, PMID: 25700174

Zeisel A, Hochgerner H, Lönnerberg P, Johnsson A, Memic F, van der Zwan J, Häring M, Braun E, Borm LE, La Manno G, Codeluppi S, Furlan A, Lee K, Skene N, Harris KD, Hjerling-Leffler J, Arenas E, Ernfors P, Marklund U, Linnarsson S. 2018. Molecular architecture of the mouse nervous system. *Cell* **174**:999–1014. DOI: https://doi.org/10.1016/j.cell.2018.06.021

Zhang P, Lu H, Peixoto RT, Pines MK, Ge Y, Oku S, Siddiqui TJ, Xie Y, Wu W, Archer-Hartmann S, Yoshida K, Tanaka KF, Aricescu AR, Azadi P, Gordon MD, Sabatini BL, Wong ROL, Craig AM. 2018. Heparan sulfate organizes neuronal synapses through neurexin partnerships. *Cell* **174**:1450–1464. DOI: https://doi.org/10.1016/j.cell.2018.07.002

Zweig RM, Ross CA, Hedreen JC, Steele C, Cardillo JE, Whitehouse PJ, Folstein MF, Price DL. 1988. The neuropathology of aminergic nuclei in Alzheimer's disease. *Annals of Neurology* **24**:233–242. DOI: https://doi.org/10.1002/ana.410240210

Cognition and Behavior

Sex-Specific Role for Dopamine Receptor D2 in Dorsal Raphe Serotonergic Neuron Modulation of Defensive Acoustic Startle and Dominance Behavior

Krissy A. Lyon,[1] Benjamin D. Rood,[1] Lorna Wu,[2] Rebecca A. Senft,[1] Lisa V. Goodrich,[2] and Susan M. Dymecki[1]

https://doi.org/10.1523/ENEURO.0202-20.2020

[1]Department of Genetics, Harvard Medical School, Boston, MA 02115 and [2]Department of Neurobiology, Harvard Medical School, Boston, MA 02115

Visual Abstract

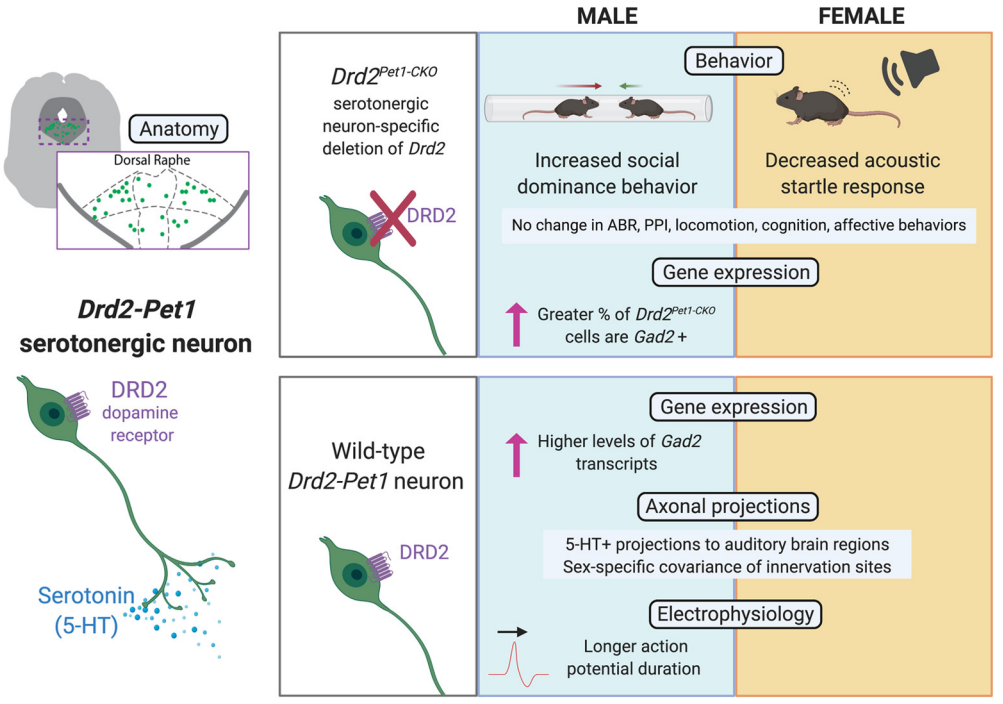

Brain networks underlying states of social and sensory alertness are normally adaptive, influenced by serotonin and dopamine (DA), and abnormal in neuropsychiatric disorders, often with sex-specific manifestations. Underlying circuits, cells, and molecules are just beginning to be delineated. Implicated is a subtype of serotonergic neuron denoted *Drd2-Pet1*, distinguished by expression of the type-2 DA receptor (*Drd2*) gene, inhibited cell-autonomously by DRD2 agonism in slice, and, when constitutively silenced in male mice, affects levels of defensive and exploratory behaviors (Niederkofler et al., 2016). Unknown has been whether DRD2 signaling in these *Pet1* neurons contributes to their capacity for shaping defensive behaviors. To address this, we generated mice in which *Drd2* gene sequences were deleted selectively in *Pet1* neurons. We found that $Drd2^{Pet1\text{-}CKO}$ males, but not females, demonstrated increased winning against sex-matched controls in a social

Significance Statement

A subtype of dorsal raphe (DR) serotonergic neuron, denoted *Drd2-Pet1*, is poised for regulation by dopamine (DA) via type-2 DA receptor (DRD2) expression. Functional removal of DRD2 in these cells through a conditional knockout (CKO) mouse strategy resulted in sex-specific behavioral abnormalities: $Drd2^{Pet1\text{-CKO}}$ females exhibited reduced acoustic startle while males showed increased social dominance. *Drd2-Pet1* neurons were similar in number and distribution in males versus females but exhibited sex-specific differences in neurotransmission-related mRNAs, action potential (AP) duration, and relative distribution of collaterals. Abnormalities in sensory processing and social behaviors akin to those reported here manifest in autism, schizophrenia, and posttraumatic stress disorder, in sex-specific ways. Our findings, thus, may point to novel circuits and modulatory pathways relevant to human neuropsychiatric conditions.

dominance assay. $Drd2^{Pet1\text{-}CKO}$ females, but not males, exhibited blunting of the acoustic startle response, a protective, defensive reflex. Indistinguishable from controls were auditory brainstem responses (ABRs), locomotion, cognition, and anxiety-like and depression-like behaviors. Analyzing wild-type *Drd2-Pet1* neurons, we found sex-specific differences in the proportional distribution of axonal collaterals, in action potential (AP) duration, and in transcript levels of *Gad2,* important for GABA synthesis. $Drd2^{Pet1\text{-}CKO}$ cells displayed sex-specific differences in the percentage of cells harboring *Gad2* transcripts. Our results suggest that DRD2 function in *Drd2-Pet1* neurons is required for normal defensive/protective behaviors in a sex-specific manner, which may be influenced by the identified sex-specific molecular and cellular features. Related behaviors in humans too show sex differences, suggesting translational relevance.

Key words: acoustic startle; dominance; dopamine receptor; raphe; serotonin; sex differences

Introduction

The serotonergic and dopaminergic neurotransmitter systems are known for their influence on and maladaptation in neuropsychiatric disorders, including posttraumatic stress disorder, autism spectrum disorder, and schizophrenia. Clinical and animal studies implicate serotonin (5-hydroxytryptamine; 5-HT) and dopamine (DA) in modulation of endophenotypes common to neuropsychiatric disorders, such as altered social interaction and sensory processing (Geyer and Braff, 1987; Meincke et al., 2004; Takahashi and Kamio, 2018). Transcriptome data coupled with structure-function maps in mice show that the serotonergic and dopaminergic neuronal systems are themselves heterogeneous, comprised of functionally specialized neuronal subtypes, manifesting distinct mRNA profiles, efferent projections, electrophysiological properties, and functions (Jensen et al., 2008; Kim et al., 2009; Crawford et al., 2013; Lammel et al., 2014; Spaethling et al., 2014; Okaty et al., 2015; Deneris and Gaspar, 2018; Poulin et al., 2018, 2020; Huang et al., 2019; Ren et al., 2019; Okaty et al., 2020). An important subtype of serotonergic neuron as relates to social and defensive behaviors is denoted *Drd2-Pet1* (Niederkofler et al., 2016), identified by expression of the type-2 DA receptor (*Drd2*) gene and the serotonergic transcription factor gene *Pet1 (*aka *Fev)*. DRD2 agonism in slice preparation drove outward (inhibitory) currents cell-autonomously in *Drd2-Pet1* neurons, suppressing their excitability; and when these cells were constitutively silenced in male mice, i.e., exocytic neurotransmitter release was cell autonomously blocked, defensive, aggressive, and exploratory behaviors increased (Niederkofler et al., 2016). Here, we query whether *Drd2* expression in *Drd2-Pet1* cells contributes to the modulation of defensive, exploratory behaviors.

While *Drd2* is expressed in many cell types throughout the midbrain and basal forebrain, expression in serotonergic neurons is restricted to a small subset of cells resident in the dorsal raphe (DR) nucleus. In these serotonergic neurons, *Drd2* expression initiates around adolescence

Received May 19, 2020; accepted November 9, 2020; First published December 19, 2020.

The authors declare no competing financial interests.

Author contributions: K.A.L. and S.M.D. designed research; K.A.L., B.D.R., and L.W. performed research; R.A.S. and L.V.G. contributed unpublished reagents/analytic tools; K.A.L., B.D.R., R.A.S., L.V.G., and S.M.D. analyzed data; K.A.L. and S.M.D. wrote the paper.

This work was supported by the National Institutes of Health National Institute on Drug Abuse Grant R01 DA034022 (to S.M.D.) and Blueprint Award NS108515 (to K.A.L.), the National Institute on Deafness and Other Communication Grant R01 DC015974 (to L.V.G.), and G.V.R. Khodadad Fund for studies of EPS (S.M.D.). K.A.L. was a Howard Hughes Medical Institute Gilliam Fellow.

B. D. Rood's present address: Department of Cell Biology and Neuroscience, Rowan University, Stratford, NJ 08084.

Acknowledgements: We thank all S.M.D. laboratory members, including G. Maddaloni, B. Okaty, R. Dosumu-Johnson, K. Lehigh, and T. Asher, for discussions; O. Alekseyenko for discussion and behavioral assay support; K. Blandino, B. Menjivar, M. Rice, and J. Mai for technical support; B. Shrestha for auditory brainstem response assistance; and the Microscopy Resources on the North Quad (MicRoN) core at Harvard Medical School for microscopy support. Graphical abstract and tube test diagram created with BioRender.com. Most behavioral work was carried out in the NeuroBehavior Laboratory Core at Harvard Medical School, we thank the support of Director Dr. Barbara Caldarone.

Correspondence should be addressed to Susan M. Dymecki at dymecki@genetics.med.harvard.edu.

https://doi.org/10.1523/ENEURO.0202-20.2020

and continues through adulthood, at which point, *Drd2* transcripts are the major DA receptor mRNA detected (Niederkofler et al., 2016). Thus, *Drd2-Pet1* neurons come under DRD2 and presumably DA regulation during the developmental transition to sexual maturity. *Drd2-Pet1* neurons project to brain regions involved in sensory processing, defensive, and mating behaviors including auditory brainstem regions and the sexually dimorphic medial preoptic area (mPOA; Niederkofler et al., 2016). These findings led us to hypothesize that DRD2 signaling in *Drd2-Pet1* neurons contributes to social and sensory alertness and defensive behavior in a sex-specific manner.

Indeed, serotonergic and dopaminergic perturbations affect social and defensive behaviors differently in male versus female rodents. Decreases in serotonergic tone associate with increased levels of aggression in males (Brown et al., 1982; Hendricks et al., 2003; Yu et al., 2014; Niederkofler et al., 2016). By contrast, lesions of the serotonergic DR in female rats decreased maternal aggression (Holschbach et al., 2018), while DR serotonergic neuron activity in female, but not male, hamsters associates with social dominance (Terranova et al., 2016). The acoustic startle reflex (ASR), an evolutionarily-conserved, defensive reflex to loud, potentially threatening stimuli (Davis et al., 1982), also shows sex-specific differences within the context of altered 5-HT levels. Reduction in 5-HT levels enhanced ASR in female but not male rats (Pettersson et al., 2016). With respect to DA, deletion of the DA re-uptake transporter gene (*Dat*) altered ASR only in male mice (Ralph et al., 2001). Genetic removal of the soluble form of catechol-O-methyltransferase (COMT), important for degradation of DA, enhanced the ASR and dominance behaviors in both sexes, but ASR especially in males (Tammimäki et al., 2010). Thus, serotonergic and dopaminergic neuronal systems influence social behaviors and sensory processing in sex-specific ways.

Here, we queried whether *Drd2* conditional deletion in serotonergic neurons would alter aggression and social dominance behavior in males. Further, we sought to examine the role of *Drd2* expression in serotonergic neurons in females with the hypothesis that other sensory or defensive behaviors would be affected, given typical lack of aggression in female mice (Lonstein and Gammie, 2002). We undertook a phenotypic analysis of mice in which we engineered *Drd2* gene deletion selectively in *ePet1-cre*-expressing serotonergic neurons ($Drd2^{Pet1\text{-}CKO}$ mice). Here, we report that $Drd2^{Pet1\text{-}CKO}$ males exhibited increased social dominance whereas females displayed a robust decrease in ASR. We also investigated sex differences in *Drd2-Pet1* neurons at the molecular, cellular, and circuit levels, identifying differences in candidate mRNA levels, electrophysiological properties, and relative distribution densities of axonal collaterals.

Materials and Methods

Ethical approval

All experimental protocols were approved by Harvard University Institutional Animal Care and Use Committees (IACUC) and were in accordance with the animal care guidelines of the National Institutes of Health.

Experimental animals

Mice were housed in a temperature-controlled environment on a 12/12 h light/dark cycle with *ad libitum* access to standard mouse chow and water. All experimental animals were virgins. For conditional knockout of *Drd2,* double transgenic mice of the genotype *ePet-Cre;* $Drd2^{loxP/loxP}$ (referred to as $Drd2^{Pet1\text{-}CKO}$) were generated by crossing BAC transgenic *ePet-Cre* (Scott et al., 2005; Jax #012712) males to homozygous $Drd2^{loxP/loxP}$ (Bello et al., 2011; Jax #020631) females. From these crosses, *ePet-Cre;*$Drd2^{loxP/wild\text{-}type}$ males were then bred to homozygous $Drd2^{loxP/loxP}$ females for *ePet-Cre;*$Drd2^{loxP/loxP}$ male and female offspring used for experiments. Experimental controls were littermates with the $Drd2^{loxP/loxP}$ genotype thus negative for Cre but of comparable genetic background (C57BL/6J, Jax #000664). For *Drd2-Pet1* neuron cell counts, triple transgenic *Drd2-Cre;Pet1-Flpe;RC-FrePe* (Gong et al., 2007; Jensen et al., 2008; Brust et al., 2014; *RC-FrePe* Jax #029486) were generated by crossing *Drd2-Cre* females to *Pet1-Flpe;RC-FrePe* double transgenic males. Likewise for axonal projection mapping, *Drd2-Cre; Pet1-Flpe; RC-FPSit* (*RC-FPSit* Jax #030206) triple transgenic mice were generated by crossing *Drd2-Cre* females to *Pet1-Flpe;RC-FPSit* double transgenic males. For both *RC-FrePe* and *RC-FPSit* crosses, all animals of each sex were from separate litters, though males and females from the same litter were used when possible. Genotypes were determined as previously described (Brust et al., 2014). Number of animals used for each assay is listed under the description for each assay.

Immunohistochemistry

Mice were briefly anesthetized with isoflurane and immediately perfused intracardially with PBS followed by 4% paraformaldehyde (PFA) in PBS. Brains were extracted, postfixed in 4% PFA overnight at 4°C, cryoprotected in 30% sucrose/PBS for 48 h, and embedded in OCT compound (Tissue-Tek). Coronal sections were cryosectioned as 30-μm free-floating sections then rinsed three times with PBS for 10 min, blocked in 5% normal donkey serum (NDS; Jackson ImmunoResearch) and permeabilized with 0.1% Triton X-100 in PBS for 1 h at room temperature. Sections were incubated for 24–48 h in primary antibodies in the same blocking buffer at 4°C. Primary antibodies used were goat polyclonal anti-5-HT (1:1000, catalog #ab66047; Abcam), chicken polyclonal anti-GFP (1:2000, RRID: AB_2307313; AVES), rabbit polyclonal anti-DsRed (1:1000; catalog #632496; Clontech), and rabbit anti-GABA (1:500, catalog #A2052; Sigma). Following primary antibody incubation, sections were rinsed three times with PBS for 10 min and incubated in secondary antibody (Alexa Fluor 488 donkey anti-chicken IgY, 703-545-155, Jackson ImmunoResearch; Alexa Fluor 546 donkey anti-rabbit IgG, A10040, Invitrogen; Alexa Fluor 647 donkey anti-goat IgG, A-21447, Invitrogen) for 1 h at room temperature, rinsed three times with PBS for 10 min, then mounted using ProLong Gold Antifade Mountant (P36930, LifeTechnologies). For *Drd2-Pet1* neuron cell counts, GFP+ cells were counted in every sixth section. The

resulting number was multiplied by 6 to obtain the number of *Drd2-Pet1* cells per animal.

Dual immunohistochemistry and fluorescent *in situ* hybridization (FISH)

For dual *in situ* hybridization with immunostaining for GFP+ *Drd2-Pet1* neuron cell bodies, PFA-perfused brain tissue from adult *Drd2-Cre;Pet1-Flpe;RC-FrePe* mice was collected as described above but cryosectioned at 20 μm onto slides (Superfrost Plus, catalog #48311-703, VWR), slides were warmed on a slide warmer set to 45°C for 30 min, and processed with RNAscope Multiplex Fluorescent Assay kit (Advanced Cell Diagnostics) following manufacturer's protocol with the exception that at the end of the protocol, tissue was stained for anti-GFP, as described above, similar to Shrestha et al. (2018). The following probes were used for the dual protocol: *Dmd* (catalog #561551-C3), *Drd2-E2* (catalog #486571-C2), *Gad2* (catalog #439371-C2), and *Serpini1* (catalog #501441). Cell nuclei were visualized with 4',6-diamidino-2-phenylindole (DAPI).

FISH

For FISH validation of *Drd2* conditional knockout and *Gad2* expression analysis, adult $Drd2^{Pet1\text{-}CKO}$ or control brain tissue was fresh frozen in OCT (TissueTek) and cryosectioned at 16 μm onto slides (Superfrost Plus, catalog #48311-703, VWR) and then processed with RNAscope Multiplex Fluorescent Assay kit (Advanced Cell Diagonstics) following manufacturer's protocol for fresh frozen tissue. The following probes were used: *Drd2-E2* (catalog #486571-C2), *Drd2*-O4 (Exon7/8; catalog #534241), *Fev (Pet1)* (catalog #413241-C3), *Gad2* (catalog #439371-C2), *Tph2* (catalog #318691), and *cre* (catalog #312281). Cell nuclei were visualized with DAPI.

Image collection

All images were acquired on a Nikon Ti inverted spinning disk confocal microscope with 488-, 561-, 647-nm laser lines and Andor Zyla 4.2 Plus sCMOS monochrome camera. Images were acquired with Nikon Elements Acquisition software AR 5.02. For RNA quantification and $Drd2^{Pet1\text{-}CKO}$ validation experiments, four images were taken of brain slices containing the DR: the first directly ventral to the aqueduct then one field of view below and to the left and right to capture each lateral wing.

FISH quantification

Quantification was conducted blind to sex and genotype. For $Drd2^{Pet1\text{-}CKO}$ validation, all *Pet1*+ (serotonergic) neurons within each image were identified, then the viewer outlined the DAPI-stained nuclei of each *Pet1*+ neuron and scored the presence of *Drd2* puncta as "positive" (having puncta) or "negative" (no puncta).The total number of *Drd2*+ *Pet1*+ neurons was then divided by the total number of *Pet1*+ neurons to yield the "% *Drd2*+*Pet1*+ neurons."

For quantification of *Dmd*, *Drd2*, *Gad2*, and *Serpini1* manual counting of each mRNA punctum per cell was conducted by a trained viewer. All cells counted fit the criteria of GFP+ with a DAPI+ nucleus. The viewer outlined the GFP+ cell body in FIJI (https://Fiji.sc/; Schindelin et al., 2012) while only viewing that channel and then counted the number of distinct RNA puncta within that cell outline. Brain sections sampled were from five males and five female animals.

For quantification of *Drd2*-Exon7/8 and *Gad2* puncta in $Drd2^{Pet1\text{-}CKO}$ tissue, DR sections corresponded to interaural −0.80 to 1.04 mm and bregma −4.60 to – 4.84 mm based on DAPI staining and anatomic landmarks (Franklin and Paxinos, 2008), where *Drd2-Pet1* neurons are most enriched. A series of custom FIJI scripts and a CellProfiler (McQuin et al., 2018) pipeline were used to process and analyze confocal images of RNAscope FISH signal in a semi-automatic manner. Analysis was performed in 2D on maximum intensity projections of 6-μm-thick *z*-stacks. First, a (step 1) preprocessing FIJI script separated channels and preprocessed them for (step 2) CellProfiler to use as input to segment nuclei. The DAPI-stained channel was preprocessed by a Gaussian blur with a diameter of 18 before segmenting with the IdentifyPrimaryObjects module with a diameter range 30–100 pixels using a minimum cross entropy global thresholding strategy. Objects outside of the diameter range or those on the edges were excluded. A threshold smoothing scale of 1.3488 was used and the image was automatically declumped based on intensity values. Finally, holes were filled in the resulting label map image, which was exported for use in FIJI (step 3). In FIJI, the user manually excluded misidentified objects or added additional nuclei that were missed by the automatic detection pipeline. A highly similar script was recently published (Okaty et al., 2020), though this current script performs additional difference of Gaussian (Marr and Hildreth, 1980) based filtering for each FISH channel. For each FISH probe, after background subtraction with a rolling ball radius of 50 pixels, the image was duplicated and a Gaussian blur was performed at two different σ levels, one which obscured small background pixels but preserved mRNA puncta, and a more extreme blur that only retained larger diffuse background puncta. The difference of these two images was then calculated and puncta localized using the Find Maxima function. To find appropriate settings for each FISH channel, we compared the performance of several sets of parameters to automatically detect puncta versus a hand count of puncta. We were able to achieve excellent concordance between the hand count and automatic puncta detection. Table 1 summarizes our settings and performance in a linear regression against the hand count for each FISH probe (statistics calculated in GraphPad Prism v8.4.3 and Microsoft Excel v2002).

Behavioral assays

All assays, except the resident-intruder assay, were conducted in an initial cohort of 15 control (eight males, seven females) and 11 $Drd2^{Pet1\text{-}CKO}$ (six males, five females) mice. All behavioral assays were conducted at postnatal day (P)90 or later. The run order for the initial cohort was open field, elevated plus maze, tail suspension test, forced swim test, social interaction, acoustic startle response, prepulse inhibition of acoustic startle, water T-

Table 1: Settings for *Gad2* quantification in *Drd2*$^{Pet1\text{-}CKO}$ tissue

Probe	S1	S2	Prominence	R^2	RMSE	MAE
E2	0.25	1	175	0.8696	0.5957	0.2458
E7/8	0.5	1	100	0.9421	0.8054	0.35
Cre	0.5	1	100	0.9679	3.829	2.2244
Fev	0.25	2	75	0.9555	4.414	3.7047
Gad2	0.25	16	150	0.8568	2.804	1.7973

Summary of settings and performance in a linear regression for semi-automated protocol versus hand counts for each FISH probe.

maze, contextual fear conditioning, tube test of social dominance and rotarod. An additional cohort of 16 controls (seven males, nine females) *Drd2*$^{Pet1\text{-}CKO}$ (six males, 10 females) was run for acoustic startle response. Resident-intruder assay of aggression was conducted in three separate cohorts of mice totaling 24 control and 26 *Drd2*$^{Pet1\text{-}CKO}$ males. The tube test of social dominance was run in the initial cohort and in the second (eight control and *Drd2*$^{Pet1\text{-}CKO}$ males) and third (11 control and *Drd2*$^{Pet1\text{-}CKO}$ males) aggression cohorts for a total of 24 control and *Drd2*$^{Pet1\text{-}CKO}$ males and a separate cohort of 16 control and 18 *Drd2*$^{Pet1\text{-}CKO}$ females. The rotarod assay was also repeated in a separate cohort of males (seven controls, six *Drd2*$^{Pet1\text{-}CKO}$). Experiments were conducted between zeitgeber time (ZT)6 and ZT10, with interspersion of control and experimental animals, and assays were run and analyzed by a trained experimenter blinded to genotype. The open field test, elevated plus maze, tail suspension test, forced swim test, social interaction, prepulse inhibition of acoustic startle, water T-maze, and contextual fear conditioning were performed as previously described (Niederkofler et al., 2016). All other behavioral assays are described in detail below.

Rotarod

The rotarod apparatus (Stoelting; Ugo Basile Apparatus) contains a rotating rod set to an accelerating speed. Mice are placed onto the rod and rotation of the rod begins. When a mouse loses its balance and falls, the apparatus automatically stops and measures the latency and rotating speed at which the mouse fell. Training consisted of exposing the mice to the apparatus for 5 min at a constant speed of 4 rpm. Mice that fall during the training session are placed back on the apparatus until the training session time has elapsed. An hour following the training session, mice are placed back on the rod for a 2-min session in which speed increases steadily over 2 min from 5 to 40 rpm. If a mouse does not fall during the 2 min, the trial ends at 2 min. Each animal was tested over 3 d and the latency to fall was averaged for each mouse. This assay was conducted in 21 control mice (14 males, seven females) and 18 *Drd2*$^{Pet1\text{-}CKO}$ (13 males, five females).

Acoustic startle response

Mice were placed in a perforated holder (acrylic cylinder with 3.2-cm internal diameter) that allowed movement to be monitored. Animal holders were placed on top of a transducer platform, measuring the active response to both weak and startle stimuli, adjacent to a speaker, within an individual acoustic chamber (Med Associates). Each session consisted of a 5 min acclimation period followed by 10 blocks of 11 trials each with white noise acoustic stimuli (20–120 dB). Each startle stimulus (20–120 dB, in 10-dB increments) was played once per block, in a quasi-random order with a variable intertrial interval of 10–20 s (average of 15 s). The duration of the stimulus was 40 ms. Responses were recorded for 150 ms from startle onset and are sampled every ms. Mice were placed back into the home cage immediately after testing. Males and female were run on different days. This assay was conducted in 30 control mice (14 males, 16 females) and 28 *Drd2*$^{Pet1\text{-}CKO}$ (13 males, 15 females), as two separate cohorts per sex.

Tube test of social dominance

Two age-matched (~P90), weight-matched mice of the same sex are introduced into opposite ends of a clear PVC tube (30.5 cm in length with an internal diameter of 2.5 cm) allowing them to interact in the middle but not pass each other within the tube. The subordinate mouse will back out allowing the dominant mouse to pass through (Lindzey et al., 1961). For each pair, five consecutive trials were run with a maximum time of 2 min per trial. Trials ended when one mouse backed out of the tube such that all four limbs are outside of the tube which was then recorded as a "backout" for that mouse. Matches lasting >2 min were excluded from analysis and scored as a draw. Side of introduction to the tube were alternated between trials and the tube was cleaned with ethanol between each trial. Opponents were from different litters and had never been housed together. This assay was conducted in 24 *Drd2*$^{Pet1\text{-}CKO}$ males versus 24 control males and 23 *Drd2*$^{Pet1\text{-}CKO}$ females versus 23 control females, conducted across three cohorts of animals.

Resident-intruder assay

Drd2$^{Pet1\text{-}CKO}$ or control mice were group-housed with male siblings until adulthood (P90) when they were single-housed for one night in the test cage to establish territorial residency. On day 1, a five-week-old Swiss Webster (Charles River) male, the "intruder," was introduced to the cage divided with a clear perforated divider for 5 min. After 5 min, the perforated divider was removed, and the mice could interact for 5 min, in which the encounter was video recorded. Number of attack bites were counted by a trained, blinded viewer. The intruder mouse was introduced for 3 d to obtain an average number of attack bites per day. The intruder mouse had a lower body weight than the resident male. This assay was conducted only in males, as female laboratory-reared mice do not display territorial aggression (Palanza, 2001; Lonstein and Gammie, 2002) This assay was conducted in 26 *Drd2*$^{Pet1\text{-}CKO}$ and 24 controls.

Auditory brainstem response (ABR)

ABRs were recorded in a separate cohort of adult mice (males: 10 control and seven *Drd2*$^{Pet1\text{-}CKO}$; females: eight control and seven *Drd2*$^{Pet1\text{-}CKO}$) aged P71–P102 to correspond to the age of animals in other assays. ABRs were conducted similar to (Maison et al., 2013). Mice were

anesthetized by intraperitoneal injection of ketamine (100 mg/kg) and xylazine (7.5 mg/kg) and placed in a soundproof chamber on a heating pad. Acoustic stimuli were delivered using EPL Cochlear Function Test Suite (CFTS) software and analyzed using ABR peak analysis software [1.1.1.9, Massachusetts Eye and Ear (MEE)]. All ABR thresholds, amplitudes, and latencies were read by an investigator blind to mouse genotype.

Electrophysiology

Slice preparation and whole-cell patch-clamp recordings were conducted as previously described (Rood et al., 2014; Niederkofler et al., 2016). Briefly, to assess membrane and action potential (AP) characteristics a protocol of repeated sweeps of 500-ms current injections stepping in 20-pA steps from −80 to 180 pA was administered to cells in current clamp. Data were analyzed using Clampfit (Molecular Devices). Some cells included in cell property analyses were also used to generate data on the function of DRD2 receptors in the DR (Niederkofler et al., 2016). However, the intrinsic cell properties data we present in this article have not been previously published and include cells not part of the Niederkofler et al. (2016) dataset.

Projection mapping

Brain tissue from six females and five males from different litters, but with a female and male from the same litter where possible, were collected at P90 and processed as previously described (Niederkofler et al., 2016). Target region identification was based on anatomic landmarks identified by DAPI staining, anti-choline acetyltransferase (goat polyclonal anti-ChAT,1:500, AB144P; EMD234 Millipore) staining, and/or anti-tyrosine hydroxylase (rabbit anti-TH, 1:1000, AB152, Millipore) staining. Staining and imaging protocols were identical among the eleven samples analyzed.

Quantification of target innervation

Target innervation was quantified in a similar manner to (Niederkofler et al., 2016). Briefly, image stacks were acquired bilaterally per brain region analyzed for each animal using a Nikon Ti inverted spinning disk microscope with a Plan Fluor 40×/1.3 Oil DIC H/N2 objective, 488-, 561-, and 647-nm laser lines, and Andor Zyla 4.2 Plus sCMOS monochrome camera. Images were acquired with Nikon Elements Acquisition software AR 5.02. Image stacks (.nd2 files) were imported to FIJI for analysis of axon projection area. Each stack contained 21 optical slices of 0.3 μm. Innervation density was quantified by a FIJI macro, such that all images, were treated identically, including background subtraction, thresholding and particle counting as described in (Niederkofler et al., 2016). We then divided the total area occupied by the projection signal by the total area of the 21 optical slices to obtain the percent area occupied by projection signal. This was then averaged within images of the same brain region across male or female samples. Brain regions analyzed were either those previously described to be innervated by *Drd2-Pet1* neurons in males only (Niederkofler et al., 2016) or those involved in auditory processing and ASR.

Statistical analyses

Data are presented as mean ± SEM. Statistical analyses were conducted in GraphPad Prism version 8.1. Statistical significance was determined by unpaired *t* test between control versus $Drd2^{Pet1\text{-}CKO}$ groups or male versus female groups except where noted: open field, forced swim test, acoustic startle response, and ABR statistical significance was determined using two-way ANOVA. For the resident-intruder assay, the tube test of social dominance, and rotarod, statistical significance was determined using the non-parametric Mann–Whitney *U* test. A result was considered significant if $p < 0.05$. Detailed statistical results are reported in Table 2.

Results

Visualization of *Drd2-Pet1* serotonergic neurons and the loss of *Drd2* gene expression in $Drd2^{Pet1\text{-}CKO}$ mice

As our first step, we confirmed the anatomic distribution of *Drd2-Pet1* neurons in the mouse brainstem, observing cell soma distributed across the rostral and lateral regions of the DR nucleus (Fig. 1*A*) as previously reported (Niederkofler et al., 2016). *Drd2-Pet1* cells were marked by GFP expression in triple transgenic *Drd2-Cre;Pet1-Flpe;RC-Frepe* (Gong et al., 2007; Jensen et al., 2008; Brust et al., 2014) mice in which cells positive for both Cre and Flpe activity – here those cells having expressed *Drd2* and *Pet1* – have recombined the *RC-FrePe* intersectional reporter allowing GFP expression; Flpe recombination alone configured *RC-FrePe* to drive mCherry expression, thus marking the remaining *Pet1*+ (*Drd2*-negative) serotonergic neurons (Fig. 1*A*,*B*). As expected (Niederkofler et al., 2016), GFP+ *Drd2-Pet1* neurons showed detectable 5-HT by immunostaining and *Drd2* mRNA by fluorescent *in situ* hybridization (FISH) (Fig. 1*C*).

To query the behavioral requirement for *Drd2* gene expression in *Drd2-Pet1* neurons, we deployed the e*Pet-cre* driver (Scott et al., 2005) to delete floxed *Drd2* gene sequences (Bello et al., 2011), creating a functional null *Drd2* allele selectively in *Pet1* neurons (Fig. 1*D*), and then subjected these $Drd2^{Pet1\text{-}CKO}$ mice to behavioral phenotyping. Cre-negative, $Drd2^{flox/flox}$ littermates served as controls. To confirm loss of *Drd2* gene expression in *Pet1* neurons, we analyzed $Drd2^{Pet1\text{-}CKO}$ and control $Drd2^{flox/flox}$ brain tissue sections by mRNA *in situ* hybridization using a probe designed to detect exon 2-containing *Drd2* mRNA, as exon 2 was the floxed gene portion to be excised by Cre recombination; concomitant identification of serotonergic neurons was by detection of *Pet1* transcripts (Fig. 1*F*,*G*). Robust loss of *Drd2* expression was observed in serotonergic neurons in both male and female mice [15.23 ± 2.41% of *Pet1*+ neurons in the DR express *Drd2* transcripts in controls ($n = 6$), consistent with prior findings, compared with 3.87 ± 0.73% in $Drd2^{Pet1\text{-}CKO}$s ($n = 6$), $p = 0.0011$, unpaired *t* test; Fig. 1*E*]. The few residual *Pet1*+ cells harboring *Drd2* transcripts likely reflects a limitation in cell capture by the

Table 2: Statistical analysis

Behavior/experiment	Line	Data structure (normality)	Type of test	Comparison	Power F/df	p
Validation of *Drd2* CKO	1E	Yes	Unpaired *t* test	Control vs $Drd2^{Pet1\text{-}CKO}$	$t = 4.514$, df = 10	$p = 0.0011$
Open field distance	2A	Yes	Repeated-measures ANOVA	F1, genotype	$F_{(1,24)} = 0.6405$	$p = 0.4314$
				F2, time	$F_{(11,264)} = 47.99$	$p < 0.0001$
				(F1 × F2)	$F_{(11,264)} = 0.8441$	$p = 0.5960$
Open field % distance traveled	2B	Yes	Unpaired *t* test	Control vs $Drd2^{Pet1\text{-}CKO}$	$t = 1.781$, df = 24	$p = 0.0876$
Rotarod	2C	No	Mann–Whitney, two-tailed	Control vs $Drd2^{Pet1\text{-}CKO}$	M–W $U = 142$	$p = 0.1899$
Elevated plus maze (% time in open arm)	2D	Yes	Unpaired *t* test	Control vs $Drd2^{Pet1\text{-}CKO}$	$t = 1.250$, df = 24	$p = 0.2234$
Tail suspension test	2E	Yes	Unpaired *t* test	Control vs $Drd2^{Pet1\text{-}CKO}$	$t = 0.3485$, df = 24	$p = 0.7305$
Forced swim test	2F	Yes	Repeated-measures ANOVA	F1, genotype	$F_{(1,24)} = 0.2678$	$p = 0.6095$
				F2, time	$F_{(5,120)} = 8.916$	$p < 0.0001$
				(F1 × F2)	$F_{(5,120)} = 0.3090$	$p = 0.9067$
Contextual fear conditioning (baseline freezing)	2G	Yes	Unpaired *t* test	Control vs $Drd2^{Pet1\text{-}CKO}$	$t = 0.6682$, df = 24	$p = 0.5104$
Contextual fear conditioning (test freezing)			Unpaired *t* test	Control vs $Drd2^{Pet1\text{-}CKO}$	$t = 0.0127$, df = 24	$p = 0.9900$
Water T maze (%correct during acquisition)	2H	Yes	Repeated-measures ANOVA	F1, genotype	$F_{(1,24)} = 0.08249$	$p = 0.7764$
				F2, time	$F_{(4,89)} = 50.12$	$p < 0.0001$
				(F1 × F2)	$F_{(4,89)} = 0.6698$	$p = 0.6147$
Water T maze (%correct during reversal)		Yes	Repeated-measures ANOVA	F1, genotype	$F_{(1,24)} = 0.1631$	$p = 0.6899$
				F2, time	$F_{(4,96)} = 172.4$	$p < 0.0001$
				(F1 × F2)	$F_{(4,96)} = 1.477$	$p = 0.2153$
ASR (M)	3C	Yes	Repeated-measures ANOVA	F1, genotype	$F_{(1,25)} = 0.0840$	$p = 0.7745$
				F2, dB	$F_{(10,250)} = 28.99$	$p < 0.0001$
				(F1 × F2)	$F_{(10,250)} = 0.3037$	$p = 0.9798$
ASR habituation (M)	3D	Yes	Pearson *r* correlation	Control trial number × startle response	$r = -0.195$	$p = 0.5893$
				$Drd2^{Pet1\text{-}CKO}$ trial number × startle response	$r = 0.136$	$p = 0.7079$
ASR latency (M)	3E	Yes	Repeated-measures ANOVA	F1, genotype	$F_{(1,25)} = 2.425$	$p = 0.1319$
				F2, dB	$F_{(10,250)} = 21.67$	$p < 0.0001$
				(F1 × F2)	$F_{(10,250)} = 0.4722$	$p = 0.9071$
ASR (F)	3F	Yes	Repeated-measures ANOVA	F1, genotype	$F_{(1,29)} = 13.26$	$p = 0.0011$
				F2, dB	$F_{(10,29)} = 35.29$	$p < 0.0001$
				(F1 × F2)	$F_{(10,290)} = 7.475$	$p < 0.0001$
ASR habituation (F)	3G	Yes	Pearson *r* correlation	Control trial number × startle response	$r = 0.1171$	$p = 0.7473$
				$Drd2^{Pet1\text{-}CKO}$ trial number × startle response	$r = 0.05165$	$p = 0.8873$
ASR latency (F)	3H	Yes	Repeated-measures ANOVA	F1, genotype	$F_{(1,29)} = 0.3748$	$p = 0.5452$
				F2, dB	$F_{(10,290)} = 20.59$	$p < 0.0001$
				(F1 × F2)	$F_{(10,290)} = 1.058$	$p = 0.3953$
PPI (M)	3I	Yes	Repeated-measures ANOVA	F1, genotype	$F_{(1,12)} = 0.6625$	$p = 0.4315$
				F2, prepulse dB	$F_{(2,24)} = 42.86$	$p < 0.0001$
				(F1 × F2)	$F_{(2,24)} = 4.104$	$p = 0.0293$
PPI (F)	3J	Yes	Repeated-measures ANOVA	F1, genotype	$F_{(1,10)} = 0.6526$	$p = 0.4380$
				F2, prepulse dB	$F_{(2,20)} = 31.34$	$p < 0.0001$
				(F1 × F2)	$F_{(2,20)} = 1.609$	$p = 0.2249$
ABR amplitude (M)	4C	Yes	Repeated-measures ANOVA	F1, genotype	$F_{(1,15)} = 1.770$	$p = 0.2032$
				F2, peak	$F_{(2,30)} = 59.09$	$p < 0.0001$
				(F1 × F2)	$F_{(2,30)} = 1.059$	$p = 0.3595$
ABR latency (M)	4D	Yes	Repeated-measures ANOVA	F1, genotype	$F_{(1,15)} = 3.515$	$p = 0.0804$
				F2, peak	$F_{(2,30)} = 1171$	$p < 0.0001$
				(F1 × F2)	$F_{(2,30)} = 3.121$	$p = 0.0587$
ABR threshold (M)	4E					
5.6		Yes	Unpaired *t* test	Control vs $Drd2^{Pet1\text{-}CKO}$	$t = 0.9535$, df = 14	$p = 0.3565$
8		Yes	Unpaired *t* test	Control vs $Drd2^{Pet1\text{-}CKO}$	$t = 1.894$, df = 14	$p = 0.0791$
16		Yes	Unpaired *t* test	Control vs $Drd2^{Pet1\text{-}CKO}$	$t = 1.103$, df = 14	$p = 0.2887$
32		Yes	Unpaired *t* test	Control vs $Drd2^{Pet1\text{-}CKO}$	$t = 2.129$, df = 7	$p = 0.0708$
ABR amplitude (F)	4F	Yes	Repeated-measures ANOVA	F1, genotype	$F_{(1,13)} = 2.489$	$p = 0.1387$
				F2, peak	$F_{(2,26)} = 72.52$	$p < 0.0001$
				(F1 × F2)	$F_{(2,26)} = 0.0487$	$p = 0.9525$
ABR latency (F)	4G	Yes	Repeated-measures ANOVA	F1, genotype	$F_{(1,13)} = 0.0053$	$p = 0.9430$
				F2, peak	$F_{(2,26)} = 4360$	$p < 0.0001$
				(F1 × F2)	$F_{(2,26)} = 0.0822$	$p = 0.9213$

(Continued)

Table 2: Continued

Behavior/experiment	Line	Data structure (normality)	Type of test	Comparison	Power *F*/df	*p*
ABR threshold (F)	4H					
5.6		Yes	Unpaired *t* test	Control vs *Drd2*$^{Pet1\text{-}CKO}$	$t = 0.1566$, df = 13	$p = 0.8770$
8		Yes	Unpaired *t* test	Control vs *Drd2*$^{Pet1\text{-}CKO}$	$t = 0.1592$, df = 14	$p = 0.8757$
16		Yes	Unpaired *t* test	Control vs *Drd2*$^{Pet1\text{-}CKO}$	$t = 0.9600$, df = 14	$p = 0.3533$
32		Yes	Unpaired *t* test	Control vs *Drd2*$^{Pet1\text{-}CKO}$	$t = 1.644$, df = 9	$p = 0.1346$
Social interaction (M, %time with stranger)	5A	Yes	Unpaired *t* test	Control vs *Drd2*$^{Pet1\text{-}CKO}$	$t = 0.6283$, df = 12	$p = 0.5415$
Social interaction (F, %time with stranger)	5B	Yes	Unpaired *t* test	Control vs *Drd2*$^{Pet1\text{-}CKO}$	$t = 0.9598$, df = 10	$p = 0.3598$
Resident-intruder assay	5C	No	Mann–Whitney, two-tailed	Control vs *Drd2*$^{Pet1\text{-}CKO}$	M–W $U = 289.5$	$p = 0.6649$
Tube test of social dominance	5E					
Male		No	Mann–Whitney, two-tailed	Control vs *Drd2*$^{Pet1\text{-}CKO}$	M–W $U = 166$	$p = 0.0065$
Female		No	Mann–Whitney, two-tailed	Control vs *Drd2*$^{Pet1\text{-}CKO}$	M–W $U = 253$	$p = 0.8123$
Drd2-Pet1 neuron count	6A	Yes	Unpaired *t* test	Male vs female	$t = 0.8160$, df = 12	$p = 0.4304$
Soma size	6C	Yes	Unpaired *t* test	Male vs female	$t = 1.021$, df = 8	$p = 0.3372$
Gene expression	6D					
Dmd		Yes	Unpaired *t* test	Male vs female	$t = 0.9581$, df = 7	$p = 0.3699$
Drd2		Yes	Unpaired *t* test	Male vs female	$t = 1.514$, df = 8	$p = 0.1686$
Gad2		Yes	Unpaired *t* test	Male vs female	$t = 2.498$, df = 8	$p = 0.0370$
Serpini1		Yes	Unpaired *t* test	Male vs female	$t = 1.459$, df = 7	$p = 0.1879$
%*Gad2*+ *Drd2-Pet1* neurons	6E	Yes	Unpaired *t* test	Male vs female	$t = 1.876$, df = 8	$p = 0.0975$
% *Drd2*-Exon7/8+	7B	Yes	Unpaired *t* test	Control vs *Drd2*$^{Pet1\text{-}CKO}$ with *Pet1* probe	$t = 0.1291$, df = 10	$p = 0.8998$
		Yes	One-way ANOVA	Control/*Pet1* probe vs *Drd2*$^{Pet1\text{-}CKO}$/*Pet1* probe vs *Drd2*$^{Pet1\text{-}CKO}$ /Cre probe	$F_{(2,19)} = 0.1003$	$p = 0.9051$
% *Gad2* in Cre+ neurons	7D	Yes	Unpaired *t* test	Male vs female	$t = 3.057$, df = 8	$p = 0.0157$
Gad2 punctae per cell	7E	Yes	Unpaired *t* test	Male vs female	$t = 1.768$, df = 8	$p = 0.1151$
Nucleus area	7F	Yes	Unpaired *t* test	Male vs female	$t = 0.9931$, df = 8	$p = 0.3497$
Resting membrane potential	8A	Yes	Unpaired *t* test	Male vs female	$t = 0.2113$, df = 61	$p = 0.8334$
Membrane resistance	8B	Yes	Unpaired *t* test	Male vs female	$t = -0.4084$, df = 61	$p = 0.6844$
AP threshold	8B	Yes	Unpaired *t* test	Male vs female	$t = 1.8197$, df = 61	$p = 0.0737$
AP amplitude	8D	Yes	Unpaired *t* test	Male vs female	$t = -1.0474$, df = 61	$p = 0.2990$
AP duration	8E	Yes	Unpaired *t* test	Male vs female	$t = -2.2583$, df = 61	$p = 0.0275$
AHP amplitude	8F	Yes	Unpaired *t* test	Male vs female	$t = 1.350$, df = 61	$p = 0.1821$
Innervation densities	9C					
DPGi		Yes	Unpaired *t* test	Male vs female	$t = 1.285$, df = 9	$p = 0.2308$
PAG		Yes	Unpaired *t* test	Male vs female	$t = 0.2398$, df = 9	$p = 0.8158$
mPOA		Yes	Unpaired *t* test	Male vs female	$t = 0.1978$, df = 9	$p = 0.8476$
DLG		Yes	Unpaired *t* test	Male vs female	$t = 0.07798$, df = 9	$p = 0.9395$
mHb		Yes	Unpaired *t* test	Male vs female	$t = 0.6732$, df = 9	$p = 0.5178$
PnC		Yes	Unpaired *t* test	Male vs female	$t = 0.7901$, df = 9	$p = 0.4498$
IC		Yes	Unpaired *t* test	Male vs female	$t = 0.5350$, df = 9	$p = 0.6056$
LL		Yes	Unpaired *t* test	Male vs female	$t = 0.9100$, df = 9	$p = 0.3865$
SOC		Yes	Unpaired *t* test	Male vs female	$t = 0.9282$, df = 9	$p = 0.3775$
CNC		Yes	Unpaired *t* test	Male vs female	$t = 0.2997$, df = 9	$p = 0.7712$

Statistical values are provided for behavioral analyses of *Drd2*$^{Pet1\text{-}CKO}$ mice and comparison of *Drd2-Pet1* neuron properties in male versus female mice. Figure numbers are included to reference corresponding graphs. Statistical analyses were conducted in GraphPad Prism version 8.1.

ePet-cre driver. Reliable immunodetection to confirm the expected parallel loss of DRD2 protein in PET1 cells remains unavailable.

Behavioral assessments in *Drd2*$^{Pet1\text{-}CKO}$ mice and the detection of sex-specific sensory, defensive, and social behaviors

Having validated effective loss of *Drd2* expression specific to *Pet1* neurons in *Drd2*$^{Pet1\text{-}CKO}$ mice, next, we screened these mice for behavioral alterations in comparison to sibling control *Drd2*$^{flox/flox}$ (Cre-negative) mice. Locomotor behaviors were explored first because they are known to be influenced by serotonergic and dopaminergic manipulations (Baik et al., 1995; Gainetdinov et al., 1999; Holmes et al., 2003; Seo et al., 2019), and because motor alterations can affect performance in and interpretation of subsequent behavioral assays. Notably, we found no differences between *Drd2*$^{Pet1\text{-}CKO}$ versus control mice (males or females) in the locomotor behaviors reflected in the open field and rotarod tests, such as distance traversed (Fig. 2*A*) and location within the field (Fig. 2*B*), vertical rearing, length of time on the rotating rod (Fig. 2*C*), which reflects balance, coordination, physical conditioning, and motor-planning. Next, we explored measures of depression-like and anxiety-like behaviors, as they are altered in various 5-HT-pathway or DA-pathway mouse models and pharmacological manipulation of these neurotransmitter systems show positive clinical effect. (Lucki, 1998; Hendricks et al., 2003; Holmes et al.,

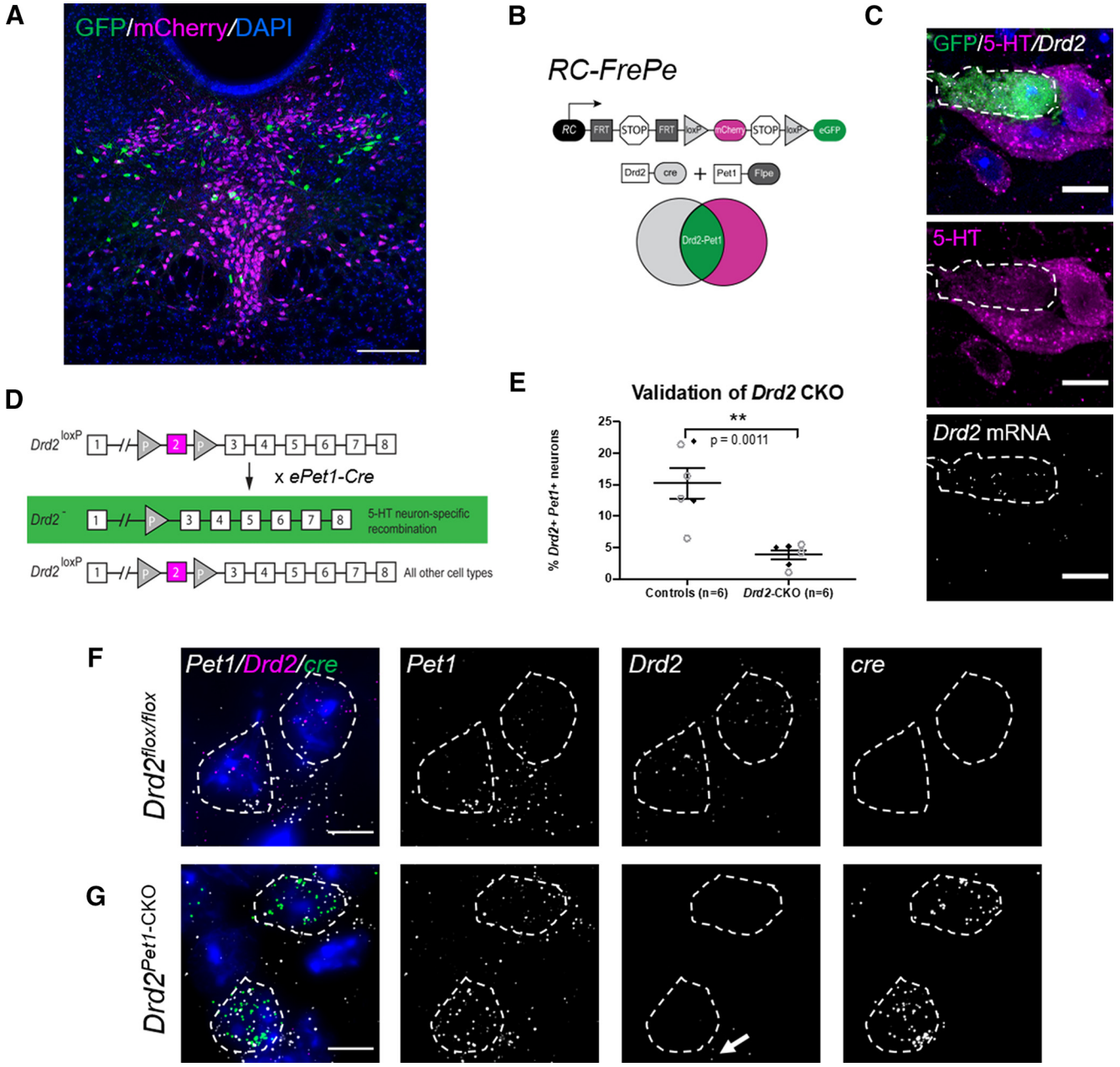

Figure 1. Visualization of *Drd2-Pet1* serotonergic neurons and the loss of *Drd2* gene expression in $Drd2^{Pet1\text{-}CKO}$ mice. ***A***, *Drd2-Pet1* neurons are intersectionally labeled with GFP (green) and *Pet1*-only positive cell bodies labeled with mCherry (magenta) in a coronal brain section of the DR from a P90 triple transgenic *Drd2-Cre;Pet1-Flpe;RC:FrePe* mouse. Scale bars: 200 μm. ***B***, Intersectional genetic strategy: expression of *Drd2-Cre* and *Pet1-Flpe* transgenes results in dual recombination of intersectional allele, *RC:FrePe*, labeling cells expressing *Drd2* and *Pet1* with GFP. ***C***, Dual immunohistochemistry for GFP (green) and 5-HT (serotonin, magenta) coupled with FISH detection of *Drd2* mRNA, which shows co-localization of intersectionally labeled *Drd2-Pet1* neuron cell bodies with 5-HT and *Drd2* mRNA. Scale bars: 10 μm. ***D***, Strategy for conditional deletion of *Drd2* in serotonergic neurons (referred to throughout as $Drd2^{Pet1\text{-}CKO}$). Cre recombination excises *Drd2* exon 2 (magenta) producing serotonergic-specific (boxed in green) deletion of *Drd2* gene sequences. ***E***, Percentage (mean ± SEM) of *Pet1*+ serotonergic neurons that express *Drd2* in control ($n = 6$) versus $Drd2^{Pet1\text{-}CKO}$ ($n = 6$) shows reduction of *Drd2* expression in *Pet1*+ neurons (controls: 15.23 ± 2.41 *Drd2-Pet1* dual positive neurons per brain, $Drd2^{Pet1\text{-}CKO}$: 3.87 ± 0.73 *Drd2-Pet1* dual positive neurons per brain, $p = 0.0011$, unpaired *t* test). Filled black diamonds represent male mice, open gray circles represent female mice. ***F***, ***G***, FISH on (***F***) control and (***G***) $Drd2^{Pet1\text{-}CKO}$ tissue. *Drd2* transcripts detected in *Pet1*+ cells in control sections, but not in $Drd2^{Pet1\text{-}CKO}$ mice, indicative of loss of *Drd2*. *cre* transcript is not present in control (***F***, far right) but is present in $Drd2^{Pet1\text{-}CKO}$ *Pet1* cells, as expected (***G,*** far right). *Pet1*, *Drd2*, and *cre* transcript are shown separately in grayscale. Note *Drd2* expression remains in non-*Pet1* cells (arrow). Dotted lines drawn to encircle DAPI nuclei. Scale bars: 25 μm.

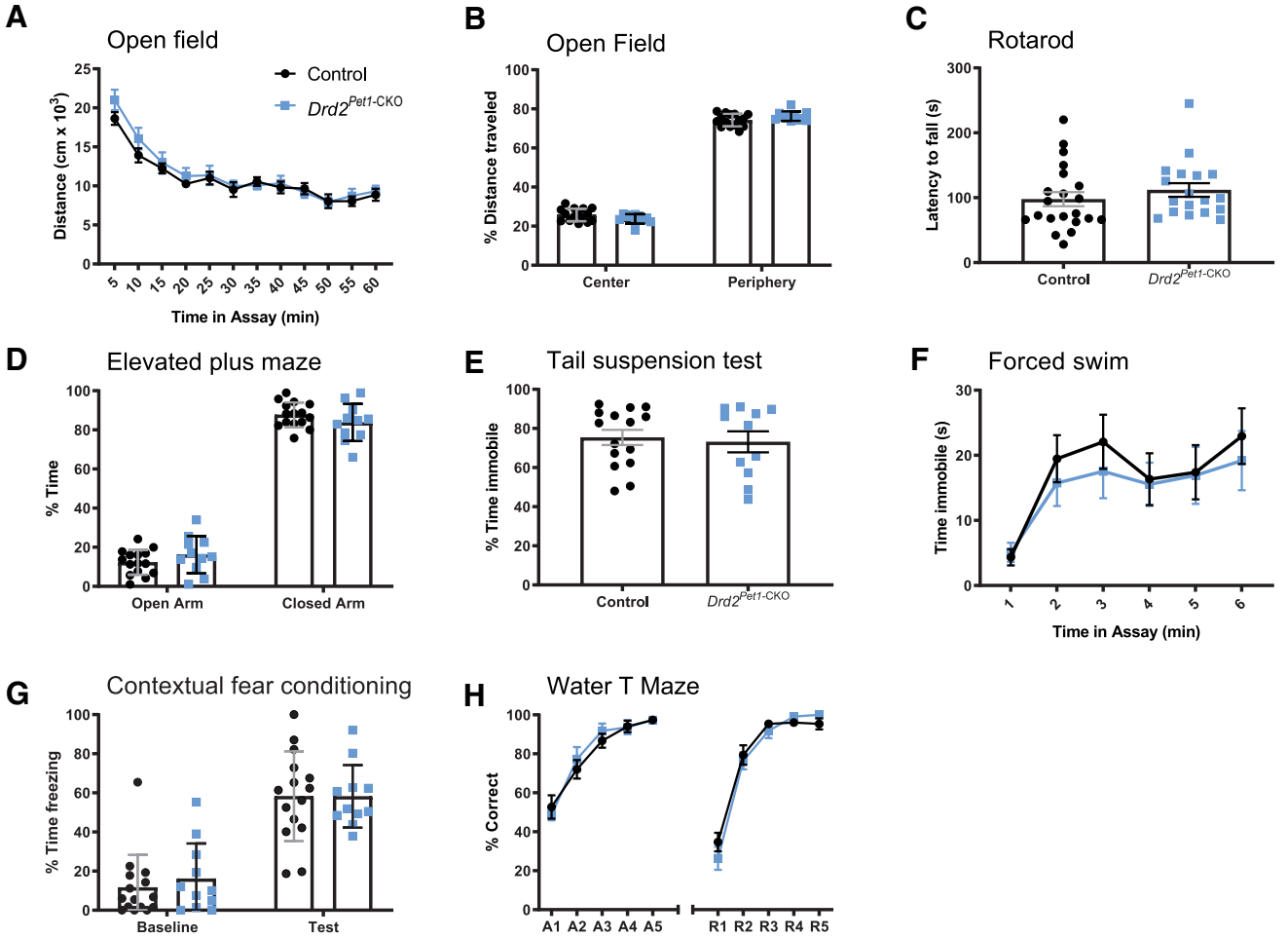

Figure 2. *Drd2*$^{Pet1\text{-}CKO}$ mice are largely behaviorally normal. *Drd2*$^{Pet1\text{-}CKO}$ (blue symbols) mice show behaviors indistinguishable from controls (black symbols) in measures of locomotion: (***A***, ***B***) open field test and (***C***) rotarod; measures of anxiety-like and depression-like behavior: (***D***) elevated plus maze, (***E***) tail suspension test, and (***F***) forced swim test; or learning and memory: (***G***) contextual fear conditioning and (***H***) water T maze; $n = 15$ control mice (8 males, 7 females) and 11 *Drd2*$^{Pet1\text{-}CKO}$ (6 males, 5 females), except for ***C*** where, $n = 21$ control mice (14 males, 7 females) and 18 *Drd2*$^{Pet1\text{-}CKO}$ (13 males, 5 females). Each symbol represents one animal, error bars represent SEM. No significant differences ($p > 0.05$) between *Drd2*$^{Pet1\text{-}CKO}$ and controls were observed. No sex-specific (male vs female) phenotypes observed. For assay details, see Materials and Methods; for statistical details, see Table 2.

2003; Grace, 2016). We observed no differences in performance in the elevated plus maze (Fig. 2*D*), tail suspension test (Fig. 2*E*), or forced swim test (Fig. 2*F*) in *Drd2*$^{Pet1\text{-}CKO}$ males and females compared with littermate controls. Additionally, contextual fear conditioning (Fig. 2*G*) and water T-maze acquisition and reversal (Fig. 2*H*) were not affected, suggesting no impairment of memory and learning in *Drd2*$^{Pet1\text{-}CKO}$ mice.

Because the serotonergic and dopaminergic systems are implicated in modulating the ASR (Davis and Aghajanian, 1976; Davis et al., 1980; Meloni and Davis, 1999, 2000a,b), we explored that next. The ASR is an evolutionarily conserved reflex involving rapid contraction of facial and skeletal muscles into a protective posture in response to a loud, threatening stimulus. We hypothesized that *Drd2-Pet1* neurons modulate this response, given their dense projections to auditory brain regions (Niederkofler et al., 2016) and the observation that following acoustic startle, the activity of certain serotonergic neurons increases in the lateral wings of the DR (Spannuth et al., 2011), a location in which we find *Drd2-Pet1* neurons. We measured startle responses to weak and startling stimuli ranging from 20 to 120 dB presented in a randomized order (Fig. 3*A*,*B*). Female *Drd2*$^{Pet1\text{-}CKO}$ mice showed a significant decrease in ASR magnitude in response to startle stimuli ($n = 15$ *Drd2*$^{Pet1\text{-}CKO}$, $n = 16$ control littermates, $p = 0.0011$, two-way ANOVA; Fig. 3*F*). By contrast, the male *Drd2*$^{Pet1\text{-}CKO}$ cohort was indistinguishable from their male littermate controls ($n = 13$ *Drd2*$^{Pet1\text{-}CKO}$, $n = 14$ control littermates, $p = 0.7745$, two-way ANOVA; Fig. 3*C*). To prevent habituation to the startle stimuli, the different stimulus intensities were presented in a quasi-random order with varied intertrial intervals (see Materials and Methods), and indeed, startle responses in late as compared with early trials were indistinguishable (shown at 110 dB, trial number is not significantly correlated with startle magnitude, males: controls, $r = -0.1950$ and *Drd2*$^{Pet1\text{-}CKO}$, $r = 0.1360$; females: controls, $r = 0.1171$

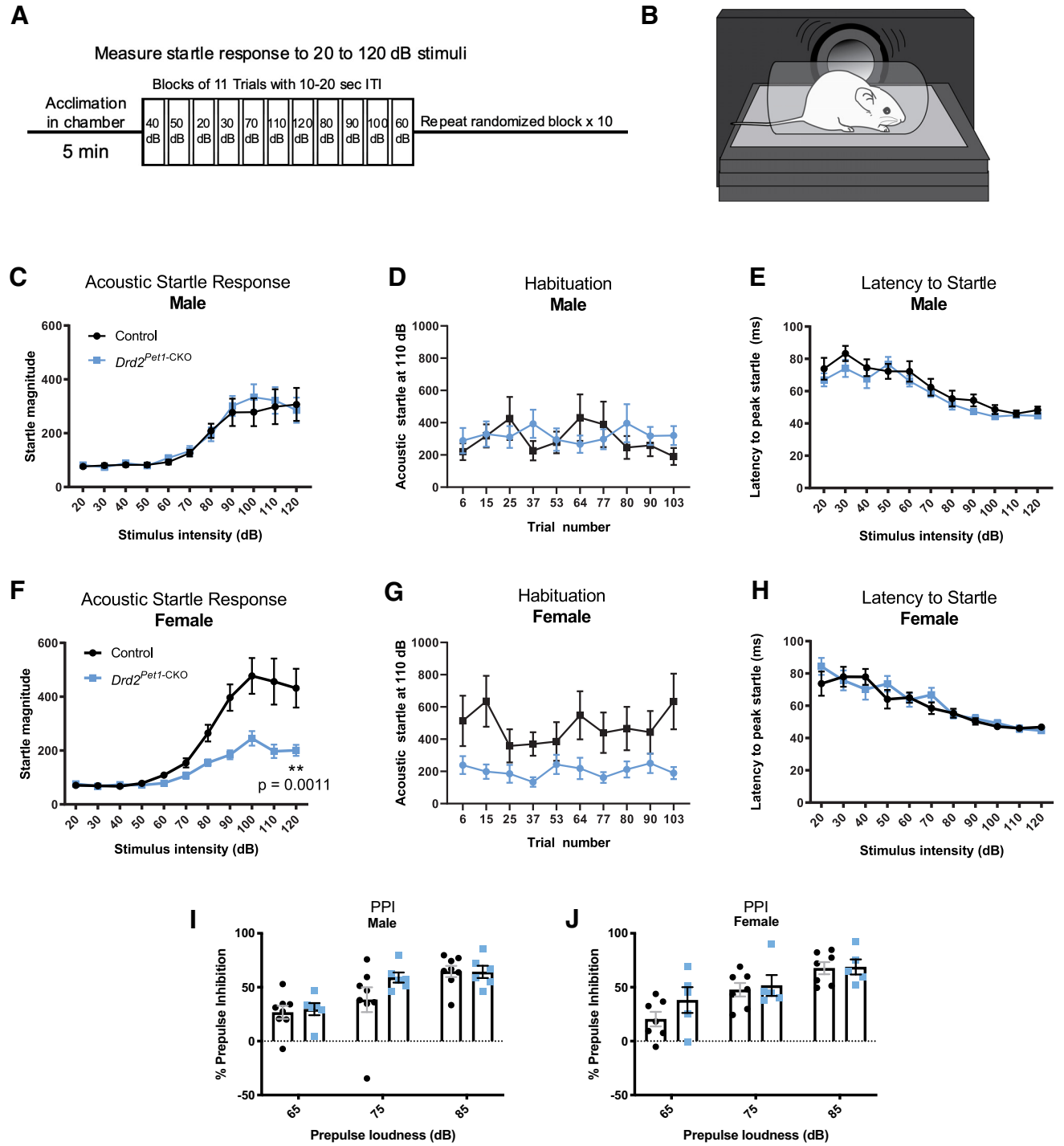

Figure 3. *Drd2*$^{Pet1\text{-CKO}}$ females, but not males, display attenuated acoustic startle responses (ASR). ***A***, Schematic of ASR experimental design. After an initial 5-min acclimation, mice are exposed to 10 blocks of 11 trials of auditory stimuli ranging from 20 to 120 dB in quasi-randomized order with a 10- to 20-s intertrial interval (ITI). ***B***, Schematic of ASR measurement apparatus, mouse is placed in a perforated holding chamber atop transducer platform adjacent to speaker (for detailed description, see Materials and Methods). ***C***, ***F***, Averaged ASR magnitudes (mean ± SEM) across increasing stimulus intensities in (***C***) male *Drd2*$^{Pet1\text{-CKO}}$ (blue, $n = 13$) and controls (black, $n = 14$), no significant difference, $p = 0.7745$, two-way ANOVA and (***F***) female *Drd2*$^{Pet1\text{-CKO}}$ (blue, $n = 15$) and controls (black, $n = 16$), *Drd2*$^{Pet1\text{-CKO}}$ females display significantly attenuated ASR, $p = 0.0011$, two-way ANOVA. ***D***, ***G***, Group averaged ASR for 10 trials at 110-dB stimulus in (***D***) males and (***G***) females, demonstrates no habituation to the startle stimulus; *x*-axis numbers refers to trial number out of 110 total trials. ***E***, ***H***, No significant differences in latency to startle are observed in (***E***) males, $p = 0.1319$, two-way ANOVA and (***H***) females, $p = 0.5452$, two-way ANOVA. ***I***, ***J***, No significant differences in prepulse inhibition of acoustic startle are observed in (***I***) males ($n = 8$ control, 6 *Drd2*$^{Pet1\text{-CKO}}$), $p = 0.4325$, two-way ANOVA or (***J***) females ($n = 7$ control, 5 *Drd2*$^{Pet1\text{-CKO}}$, $p = 0.4380$, two-way ANOVA).

and *Drd2*$^{Pet1\text{-}CKO}$, $r = 0.0517$, Pearson correlation; Fig. 3*D*,*G*). Further, we observed no differences in latency to startle in either females or males (Fig. 3*E*,*H*). Females were of similar mass (controls: 32.117 ± 3.15 g vs *Drd2*$^{Pet1\text{-}CKO}$: 37.2 ± 2.427 g, unpaired *t* test, $p = 0.2031$) regardless of genotype, thus differences in weight and its relative impact on transduction of the startle response via the piezoelectric platform were not a confound.

While *Drd2*$^{Pet1\text{-}CKO}$ females showed diminished response magnitudes to startling acoustic stimuli, they nevertheless expressed normal acoustic prepulse inhibition (PPI) whereby even the diminished response to startling acoustic stimuli (e.g., 120-dB stimuli) was further blunted proportionately when immediately preceded by a weak, non-startling stimulus (e.g., 65-, 75-, or 85-dB stimuli; Fig. 3*I*,*J*). Thus, sensorimotor gating, as measured by acoustic PPI, appeared relatively intact; the acoustic dysfunction instead centered on the ASR itself.

Having observed attenuation of the ASR in female *Drd2*$^{Pet1\text{-}CKO}$ mice, we assessed whether hearing was broadly disrupted as revealed by ABRs evoked by sound stimuli (Zhou et al., 2006). ABRs were recorded in response to pure tone stimuli at 5.6, 8, 16, and 32 kHz ($n = 8$ control females, 7 *Drd2*$^{Pet1\text{-}CKO}$ females, and 10 control males, 7 *Drd2*$^{Pet1\text{-}CKO}$ males). Across all these frequencies, the measured ABR waveforms (averaged ABR waveforms shown at 16 kHz at 80-dB SPL; Fig. 4*A*,*B*), peak amplitudes [shown for peaks 1–3 at 16 kHz at 80-dB SPL for males ($p = 0.2032$, two-way ANOVA) and females ($p = 0.1387$, two-way ANOVA); Fig. 4*C*,*F*], and latencies to peaks [shown for peaks 1–3 at 16 kHz at 80-dB SPL for males ($p = 0.0804$, two-way ANOVA) and females ($p = 0.9430$, two-way ANOVA); Fig. 4*D*,*G*] were indistinguishable between *Drd2*$^{Pet1\text{-}CKO}$ mice and littermate controls. As well, the ABR threshold to elicit a waveform was not significantly different between *Drd2*$^{Pet1\text{-}CKO}$ and control mice at 5.6, 8, 16, or 32 kHz ($p > 0.05$ at all frequencies, unpaired *t* test) in males (Fig. 4*E*) or females (Fig. 4*H*). Thus, hearing overall, as measured by ABR, appeared largely unaffected in *Drd2*$^{Pet1\text{-}CKO}$ mice.

ABRs were conducted in adult mice (ages P71–P102) to align with the age at which the other behavioral assays were performed. However at such ages, C57BL/6 mice, the strain background here, exhibit some age-related hearing loss at higher frequencies (Kane et al., 2012), which we saw here at 32 kHz with two control and three *Drd2*$^{Pet1\text{-}CKO}$ females and five control and three *Drd2*$^{Pet1\text{-}CKO}$ males. At all other tested frequencies, the ABRs were effectively normal for both genotypes, with one exception being a *Drd2*$^{Pet1\text{-}CKO}$ female that exhibited undetectable ABRs at 5.6 kHz, but otherwise normal responses at all other frequencies tested including 32 kHz. These findings at 32 and 5.6 kHz are likely independent of the ASR phenotype observed in females because all animals had normal hearing at 8 and 16 kHz, frequencies included in the white noise startle stimulus of the ASR test.

Next, we examined social behavior in *Drd2*$^{Pet1\text{-}CKO}$ mice using the three-chambered test of sociability (Moy et al., 2004) that measures preference to investigate a social stimulus (a novel "stranger" mouse inside a holder) as compared with an object (an empty holder). *Drd2*$^{Pet1\text{-}CKO}$ mice showed no alterations in sociability compared with controls and both control and *Drd2*$^{Pet1\text{-}CKO}$ spent significantly more time investigating the stranger than the object (Fig. 5*A*,*B*). Females of both genotypes displayed preference toward the social stimuli only for the first 5 min of the assay (Fig. 5*B*, white bars), while males displayed this preference throughout the 10-min assay. Similar sex differences in sustained preference for the social stimulus have been described in C57BL/6J mice (Netser et al., 2017).

We assayed intermale, territorial aggression in a separate cohort of mice using a resident-intruder assay. Females were not tested, as they have been shown to display low or no aggression in most forms of this assay (Palanza, 2001; Lonstein and Gammie, 2002). We observed no statistically significant difference in number of attack bites delivered to the intruder mouse by *Drd2*$^{Pet1\text{-}CKO}$ males ($n = 26$) compared with number of attack bites delivered to the intruder by controls ($n = 24$; *Drd2*$^{Pet1\text{-}CKO}$: 4.07 ± 1.50 bites, controls: 1.77 ± 0.39 bites, $p = 0.6649$, Mann–Whitney test; Fig. 5*C*) noting, however, that four *Drd2*$^{Pet1\text{-}CKO}$ males displayed high levels of aggression.

To assay social dominance, we performed the tube test, which has relevance in females as well as males (Lindzey et al., 1961; van den Berg et al., 2015; Zhou et al., 2017). Two mice are simultaneously released into opposite ends of a clear tube of sufficiently narrow diameter that prevents mice from passing by each other and instead requires that one back out for the other, more dominant "winning" mouse, to move forward (Fig. 5*D*). *Drd2*$^{Pet1\text{-}CKO}$ males won a higher percentage of trials against non-sibling, weight-matched, and genetic background-matched opponent males (shown as percent of trials won, *Drd2*$^{Pet1\text{-}CKO}$: $65.83 \pm 9\%$, $n = 24$; controls: $34.17 \pm 9\%$, $n = 24$; $p = 0.0065$, Mann–Whitney test; Fig. 5*E*). By contrast, we observed no difference in percent of trials won by female *Drd2*$^{Pet1\text{-}CKO}$ mice as compared with female sibling controls (*Drd2*$^{Pet1\text{-}CKO}$: $48.7 \pm 8\%$, $n = 23$; controls $51.3 \pm 8\%$, $n = 23$; $p = 0.8123$, Mann–Whitney test; Fig. 5*E*).

Drd2-Pet1 neurons in males versus females exhibit differences in candidate molecular and biophysical properties but not in cell number

Given these sex-specific differences in behaviors observed in *Drd2*$^{Pet1\text{-}CKO}$ mice, next we looked for sex-specific differences in *Drd2-Pet1* cellular properties, beginning with cell number. Analyzing triple transgenic *Drd2-Cre; Pet1-Flpe; RC-FrePe* males versus females, we found no difference in number of GFP$^+$ *Drd2-Pet1* neurons per brain (males: 410.40 ± 55.30 cells/brain, females: 313 ± 87.52 cells/brain, $p = 0.4304$, unpaired *t* test; Fig. 6*A*). Further, in both males and females, *Drd2-Pet1* neurons distributed as expected across the rostral-caudal and medial-lateral axis of the DR.

To understand whether gene expression might differ between male and female *Drd2-Pet1* neurons, we examined single-cell RNA sequencing data previously analyzed for expression of serotonergic pathway genes as validation that *Drd2-Pet1* cells were indeed serotonergic (Niederkofler et al., 2016). Comparison across sex, albeit

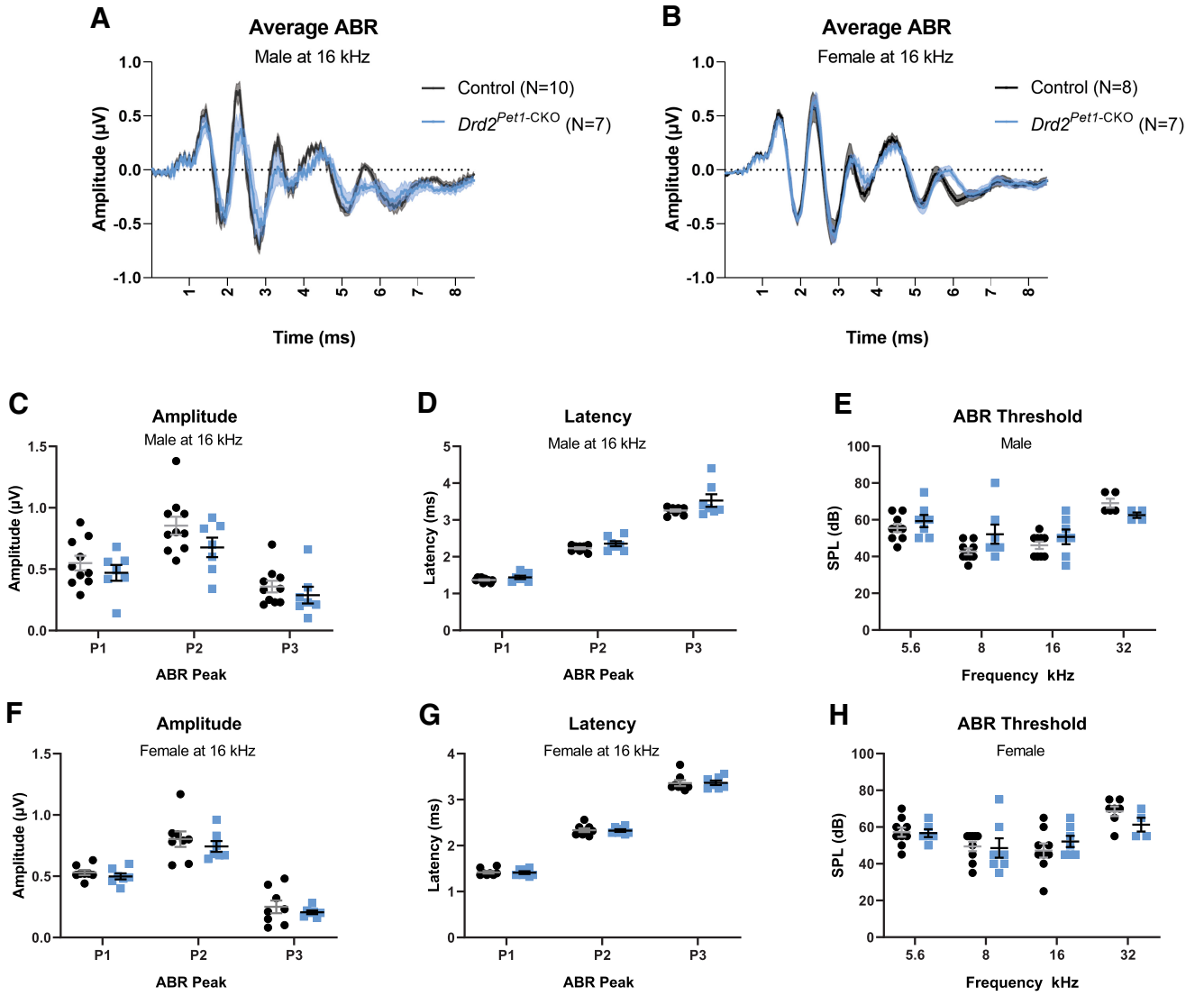

Figure 4. *Drd2*$^{Pet1\text{-CKO}}$ mice show normal auditory responses. ***A***, ***B***, Average ABR waveforms at 16 kHz for (***A***) control (black, $n = 10$) and *Drd2*$^{Pet1\text{-CKO}}$ (blue, $n = 7$) males and (***B***) for control (black, $n = 8$) and *Drd2*$^{Pet1\text{-CKO}}$ (blue, $n = 7$) females. Average is shown by darker lines and shaded area shows SEM. ***C***, ***F***, ABR amplitudes for control (black) and *Drd2*$^{Pet1\text{-CKO}}$ (blue; ***C***) male and (***F***) female mice for ABR peaks 1 through 3. No significant difference was observed between control and *Drd2*$^{Pet1\text{-CKO}}$: males, $p = 0.2032$; females, $p = 0.1387$, two-way ANOVA. ***D***, ***F***, Latencies for control (black) and *Drd2*$^{Pet1\text{-CKO}}$ (blue; ***D***) male and (***G***) female mice for ABR peaks 1 through 3. No significant difference was observed between control and *Drd2*$^{Pet1\text{-CKO}}$: males, $p = 0.0804$; females, $p = 0.9430$, two-way ANOVA. Amplitudes and latencies shown at 80-dB SPL. ***E***, ***H***, ABR thresholds for control (black) and *Drd2*$^{Pet1\text{-CKO}}$ (blue; ***E***) male and (***H***) female mice across frequencies tested (5.6, 8, 16, and 32 kHz). No significant difference was observed between control and *Drd2*$^{Pet1\text{-CKO}}$ mice, $p > 0.05$ at all frequencies, unpaired *t* test.

lacking statistical significance given the small sample size, highlighted four genes for further evaluation, *Drd2*, *Dmd* (encoding Dystrophin, a component of protein scaffolds in the CNS; Perronnet and Vaillend, 2010), *Gad2* (encoding glutamate decarboxylase 2 involved in catalyzing the production of the neurotransmitter GABA), and *Serpini1* (encoding the serine protease Neuroserpin, important for synapse formation and plasticity; Galliciotti and Sonderegger, 2006). Quantitative *in situ* mRNA detection using dual FISH with immunodetection on tissue sections from *Drd2-Cre;Pet1-Flpe;RC-FrePe* mice revealed greater abundance of average *Gad2* transcripts (puncta) per cell in males versus females [*Gad2*: 20.46 ± 2.243 in males ($n = 5$) vs 12.20 ± 2.427 in females ($n = 5$), $p = 0.0370$, unpaired *t* test; Fig. 6*D*]. There was no difference in the percentage of *Drd2-Pet1* neurons expressing *Gad2* in male versus female mice (Fig. 6*E*). No difference in soma size (GFP-stained cell body) was observed between males and females suggesting that transcript differences were not because of larger soma volume measured (Fig. 6*C*). No significant differences in mRNA abundance were observed between males and females for *Dmd*, *Drd2*, or *Serpini1* (see Table 2).

As a first step toward understanding whether sex-specific gene expression differences observed in wild-type

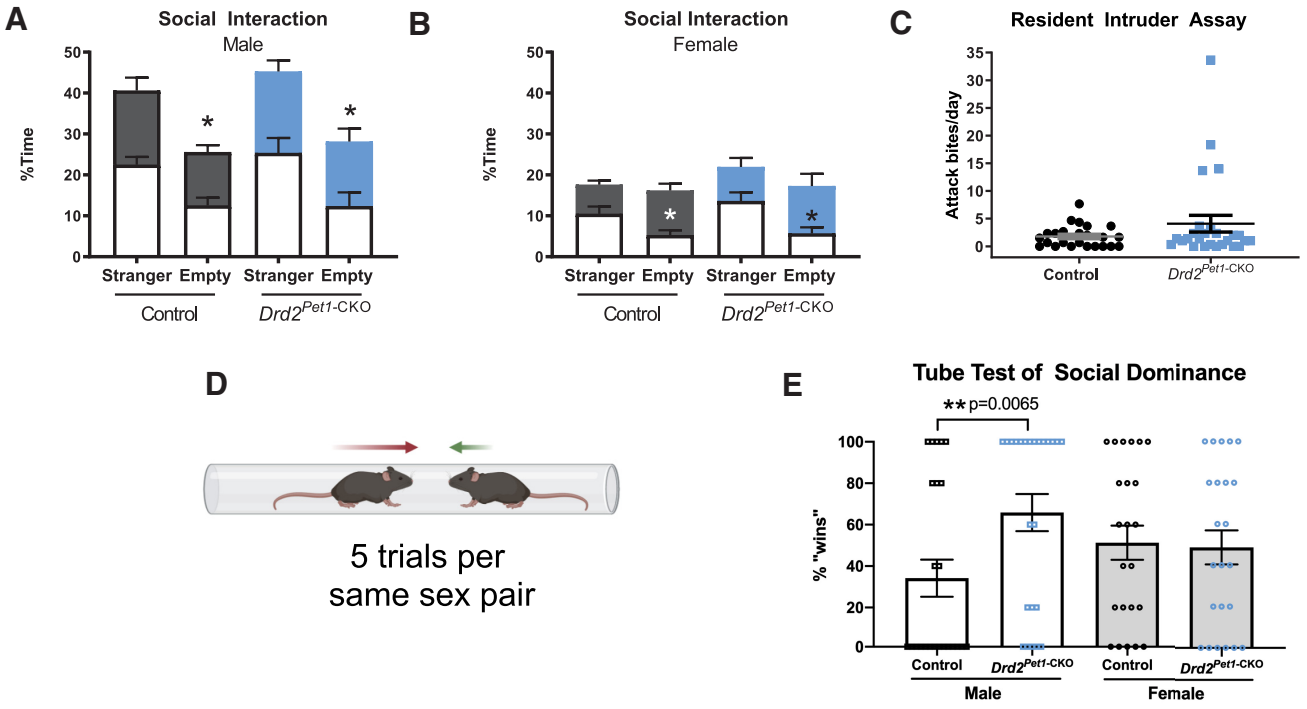

Figure 5. *Drd2*$^{Pet1\text{-}CKO}$ males, but not females, display increased social dominance. ***A***, ***B***, Three chambered social interaction assay. No significant difference in time spent investigating a stranger mouse or an empty holder for (***A***) males ($n = 8$ controls compared with 6 *Drd2*$^{Pet1\text{-}CKO}$, $p = 0.541$, unpaired *t* test) and (***B***) females ($n = 7$ controls compared with $n = 5$ *Drd2*$^{Pet1\text{-}CKO}$, $p = 0.358$, unpaired *t* test). Investigation time is binned into 5-min intervals where white bars indicate first 5 min of assay and colored bars indicate last 5 min of assay. As expected, mice of both genotypes spent significantly less time investigating the empty holder than the stranger mouse noting that females of both genotypes only did so during the first 5 min of the assay. ***C***, Resident intruder assay of aggression. No significant difference in the average attack bites per day delivered to a Swiss Webster intruder mouse was observed between *Drd2*$^{Pet1\text{-}CKO}$ males ($n = 26$, 4.07 ± 1.50 bites) aggression levels were not significantly different from controls ($n = 24$, 1.77 ± 0.39 bites; Mann–Whitney, two-tailed, $U = 289.5$, $p = 0.6649$). ***D***, Schematic of tube test (for details of assay, see Materials and Methods). Schematic created with BioRender. ***E***, *Drd2*$^{Pet1\text{-}CKO}$ males ($n = 24$) demonstrate more dominance behavior than controls ($n = 24$) as they displayed increased winning in the tube test (controls: 34.17 ± 9% wins, *Drd2*$^{Pet1\text{-}CKO}$: 65.83 ± 9% wins, $p = 0.0065$, Mann–Whitney, two-tailed, $U = 166$). Female *Drd2*$^{Pet1\text{-}CKO}$ ($n = 23$) showed no difference in social dominance compared with controls ($n = 23$; controls: 51.3 ± 8%, *Drd2*$^{Pet1\text{-}CKO}$: 48.7 ± 8% wins, $p = 0.8123$ Mann–Whitney, two-tailed, $U = 253$).

mice persist or are altered in *Drd2*$^{Pet1\text{-}CKO}$ mice, we assessed *Gad2* transcript levels in *Drd2*$^{Pet1\text{-}CKO}$ cells. In these cells, the floxed exon 2 of *Drd2* is excised by Cre recombination. Therefore, to identify mutant *Drd2* mRNA and thus the mutant *Drd2*$^{Pet1\text{-}CKO}$ cells, we used a multiprobe strategy involving one probe to intact downstream exons 7 and 8 (referred to here as *Drd2*-E7/8), another to exon 2 (referred to as *Drd2*-E2), and another to either *cre* or *Pet1*. We examined expression in the DR region most enriched with *Drd2-Pet1* neurons. We found *Drd2*-E7/8+ puncta in *Pet1*+ cells in both controls and *Drd2*$^{Pet1\text{-}CKO}$ mice, whereas *Drd2*-E2+ puncta were detectable in control tissue but greatly reduced in *Drd2*$^{Pet1\text{-}CKO}$ as expected given the efficiency of Cre-mediated gene deletion (Fig. 7*A*; see *Drd2*-E2 quantification in Fig. 1*E*). *Drd2*-E7/8 puncta were detected in 35.97 ± 2.403% of *Pet1*+ cells in control mice ($n = 6$) compared with 36.53 ± 3.621% of *Pet1*+ cells in *Drd2*$^{Pet1\text{-}CKO}$ mice ($n = 6$; $p = 0.8998$, unpaired *t* test; Fig. 7*B*). Similarly, in a separate experiment using an *in situ* probe to *cre* mRNA, 34.91 ± 2.238% of *cre*+ cells expressed *Drd2*-E7/8 ($n = 10$ mice, one-way ANOVA compared with *Pet1* control and *Drd2*$^{Pet1\text{-}CKO}$ cell expression, $p = 0.9051$; Fig. 7*B*). Next, we analyzed *Gad2* mRNA transcript levels in *Drd2*$^{Pet1\text{-}CKO}$ cells (dual *Drd2*-E7/8+ and *cre*+ cells) in the DR (Fig. 7*C*). In males, we observed 87.44 ± 3.034% of *Drd2*$^{Pet1\text{-}CKO}$ cells were *Gad2*+, while this percentage was 75.76 ± 0.5862% in females ($p = 0.0157$, unpaired *t* test; Fig. 7*D*). In these *Drd2*$^{Pet1\text{-}CKO}$ cells, there were 14.25 ± 1.325 transcripts per cell in males and 10.13 ± 2.074 transcripts per cell in females ($p = 0.1151$, unpaired *t* test; Fig. 7*E*). Because of the tightly packed distribution of cells in the DR, puncta were measured only within *cre*+ DAPI-stained nuclei to ensure puncta were not assigned to more than one cell. The area of nuclei did not differ between males (114.9 ± 3.030 μm^2) and females (110.9 ± 1.768 μm^2, $p = 0.3497$, unpaired *t* test; Fig. 7*F*). Thus, in *Drd2*$^{Pet1\text{-}CKO}$ males as compared with *Drd2*$^{Pet1\text{-}CKO}$ females, a greater percentage of the *Drd2-Pet1* cells harbored *Gad2* transcripts; of these *Gad2*-expressing cells, however, transcript levels were not significantly different between males versus female *Drd2*$^{Pet1\text{-}CKO}$ mice.

To explore potential sex differences in electrophysiological properties characterizing *Drd2-Pet1* neurons, we

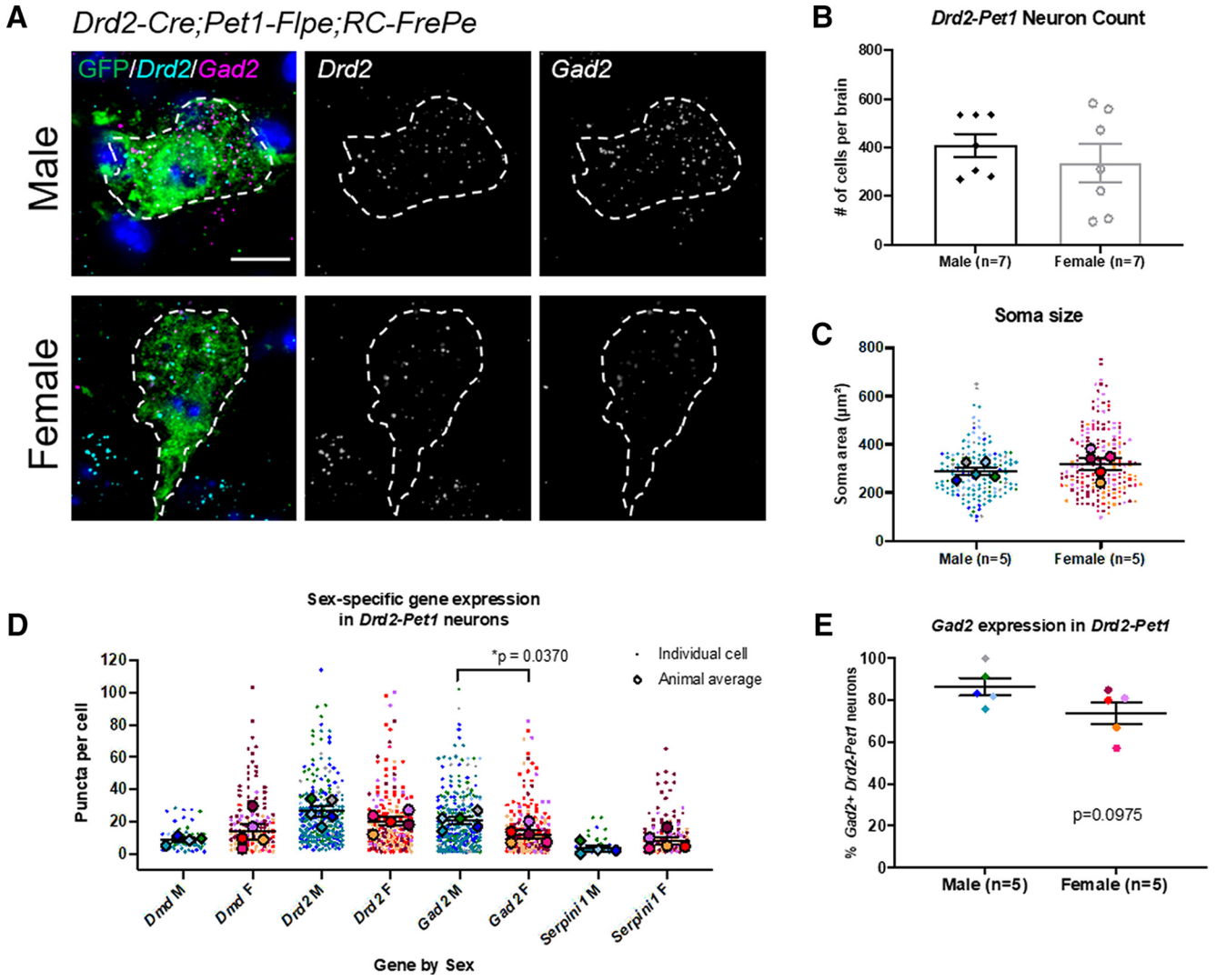

Figure 6. Sex-specific transcript level differences in *Drd2-Pet1* neurons. ***A***, Dual immunohistochemistry and FISH depicting green GFP+ *Drd2-Pet1* neurons along with transcript puncta in male (top) and female (bottom) brain sections from *Drd2-Cre;Pet1-Flpe; RC-FrePe* mice. *Drd2* (cyan) and *Gad2* (magenta) expression shown together and separately in gray scale. Scale bar: 10 μm. ***B***, Number of *Drd2-Pet1* neurons (GFP-positive cells in *Drd2-Cre;Pet1-Flpe;RC-FrePE* mice) per animal in males (black diamonds, $n = 7$) and females (open gray circles, $n = 7$) is not significantly different. Males: 410.40 $\pm$ 55.30 cells/brain, females: 313 $\pm$ 87.52 cells/brain, $p = 0.4336$, unpaired *t* test. ***C***, *Drd2-Pet1* neuron soma size (GFP+ cell body) does not differ in males ($n = 5$ males) versus females ($n = 5$ females), $p = 0.3372$, unpaired *t* test. ***D***, Number of FISH mRNA puncta per cell in males versus females. Male cells have significantly more *Gad2* puncta than female cells [20.46 $\pm$ 2.243 in males ($n = 5$) vs 12.20 $\pm$ 2.427 in females ($n = 5$), $p = 0.0370$, unpaired *t* test]. ***E***, 86.47 $\pm$ 4.181% of male *Drd2-Pet1* cells express *Gad2* versus female 74.00 $\pm$ 5.168% in female cells, $p = 0.0975$, unpaired *t* test. Error bars indicate SEM throughout. For ***C***, ***D***, larger symbols outlined in black represent animal averages used for statistical analysis, smaller symbols represent individual cells, matched in color to the average.

conducted whole-cell recordings from GFP-labeled *Drd2-Pet1* neurons in brain slices from triple transgenic *Drd2-Cre;Pet1-Flpe;RC-FrePe* males and females. Examination of cell membrane characteristics revealed no sex differences in resting membrane potential (AP; Fig. 8*A*) or resistance (Fig. 8*B*). Analyses of AP characteristics revealed an increase in AP duration (Fig. 8*E*) in male *Drd2-Pet1* cells as compared with female (2.847 $\pm$ 0.155 ms, $n = 19$ cells vs 2.54 $\pm$ 0.094 ms, $n = 44$ cells, respectively, $p = 0.0275$, unpaired *t* test], but no differences in AP threshold (Fig. 8*C*), amplitude (Fig. 8*D*), or afterhyperpolarization (AHP) amplitude (Fig. 8*F*).

Differing covariance in axonal collateral densities from *Drd2-Pet1* neurons directed to auditory targets in males versus females

As a first step in exploring sex differences in *Drd2-Pet1* neuron circuitry that may underlie the sex-specific behavioral phenotypes in *Drd2*$^{Pet1\text{-}CKO}$ mice, we compared relative innervation density to brain regions involved in sensory processing and social behavior in male and female mice. Boutons from *Drd2-Pet1* neurons were selectively marked with a Synaptophysin-GFP fusion protein using triple transgenic *Drd2-Cre;Pet1-Flpe;RC-FPsit* mice (Fig. 9*A*,*B*; Niederkofler et al., 2016). At P90, the same age

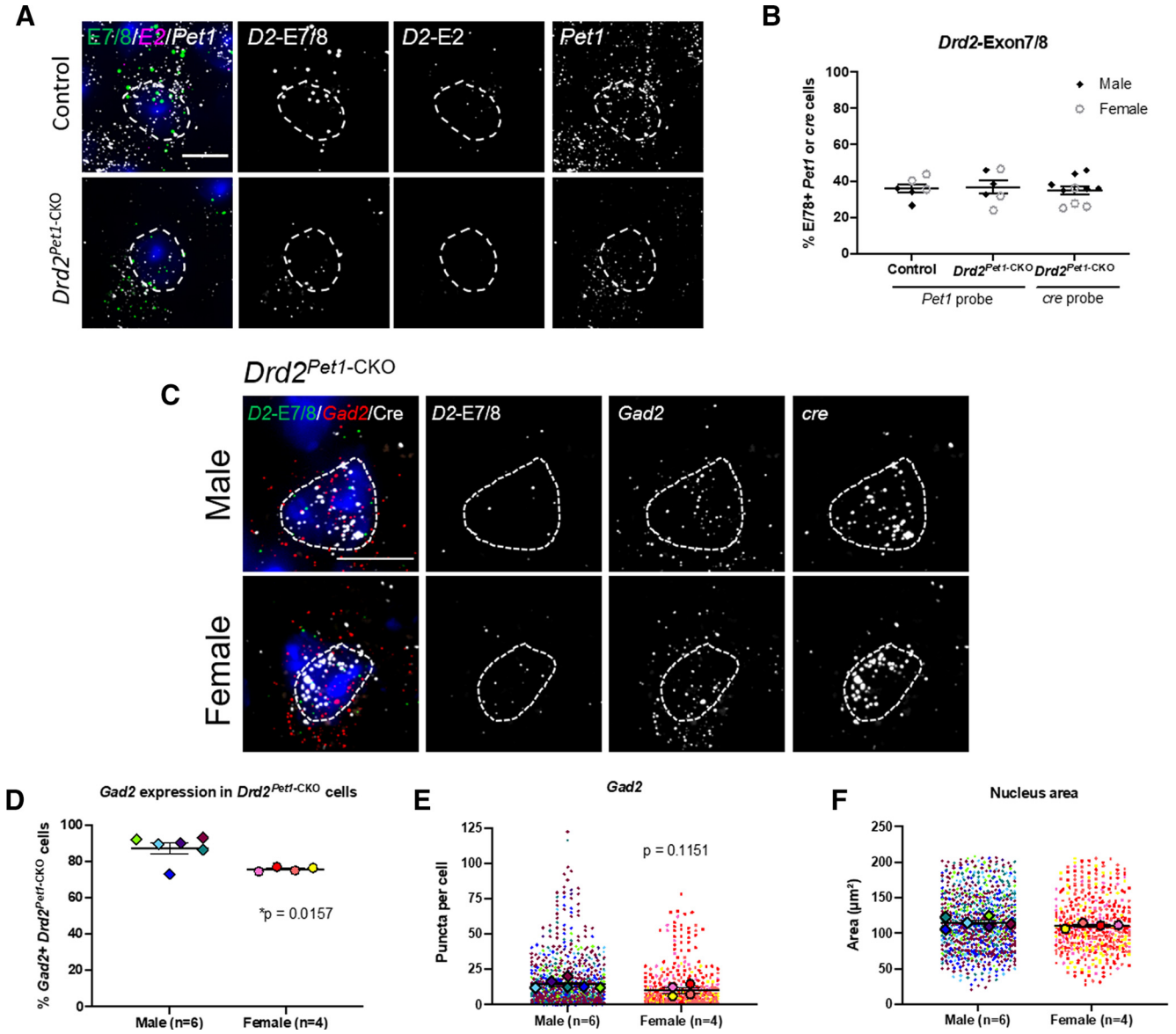

Figure 7. *Gad2* expression in *Drd2*$^{Pet1\text{-CKO}}$ cells. ***A***, FISH with probes to *Drd2* exon 7/8 (*D2*-E7/8, green) and *Drd2* exon 2 (*D2*-E2, magenta) in *Pet1* (white) cells in control (top) and *Drd2*$^{Pet1\text{-CKO}}$ (bottom) DR tissue. *D2*-E7/8, *D2*-E2, and *Pet1* expression shown together and separately in gray scale. ***B***, Percent of *Pet1*+ cells (left and middle) with *Drd2*-Exon7/8 expression in control (35.97 ± 2.403%, $n = 6$) and *Drd2*$^{Pet1\text{-CKO}}$ (36.53 ± 3.621%, $n = 6$), $p = 0.8998$, unpaired *t* test. Data also shown for percent of *cre* cells (right) with *Drd2*-Exon7/8, 34.91 ± 2.238%, compared with *Pet1* probe control and *Drd2*$^{Pet1\text{-CKO}}$ $p = 0.9051$, one-way ANOVA. Males, black diamonds, females, open gray circles. ***C***, FISH showing *cre*+ *Drd2*$^{Pet1\text{-CKO}}$ cells (white) with *Drd2-Exon7/8* (green) *and Gad2* (red) in male (top) and female (bottom) in the DR nucleus. *Drd2-Exon7/8*, *Gad2*, and *cre* are shown together and separately in gray scale. Scale bar: 10 µm. ***D***, A larger percentage of male *Drd2*$^{Pet1\text{-CKO}}$ cells (87.44 ± 3.034%) express *Gad2* versus female *Drd2*$^{Pet1\text{-CKO}}$ cells (75.76 ± 0.5862%), $^{*}p = 0.0157$, unpaired *t* test. ***E***, Number of *Gad2* mRNA puncta per cell in *Drd2*$^{Pet1\text{-CKO}}$ cells in males ($n = 6$) versus females ($n = 4$). Male cells have 14.25 ± 1.325 *Gad2* puncta per cell compared with 10.13 ± 2.074 in female cells, $p = 0.1151$, unpaired *t* test. ***F***, *Drd2*$^{Pet1\text{-CKO}}$ nucleus size (area used to quantify puncta levels) does not differ in males (n = 6 males) versus females (n = 4 females), $p = 0.3497$, unpaired *t* test. Error bars indicate SEM throughout. For ***E***, ***F***, larger symbols outlined in black represent animal averages used for statistical analysis, smaller symbols represent individual cells, matched in color to the average.

at which the behavioral assays were conducted, we collected brain tissue and quantified projections to the cochlear nucleus complex (CNC), superior olivary complex (SOC), lateral lemniscus (LL), inferior colliculus (IC), caudal pontine reticular nucleus (PNC; critical for ASR; Davis et al., 1982), dorsal lateral geniculate nucleus (dLGN), mPOA, medial habenula (mHb), periaqueductal gray (PAG), and dorsal paragigantocellular nucleus (DPGi; shown as percentage of target area occupied by projections; Fig. 9C). We observed no significant sex differences in the cohort average for absolute innervation density to each of these 10 brain regions. However, because we observed considerable interanimal variability in bouton densities at targets, we next explored correlation of innervation density across brain regions

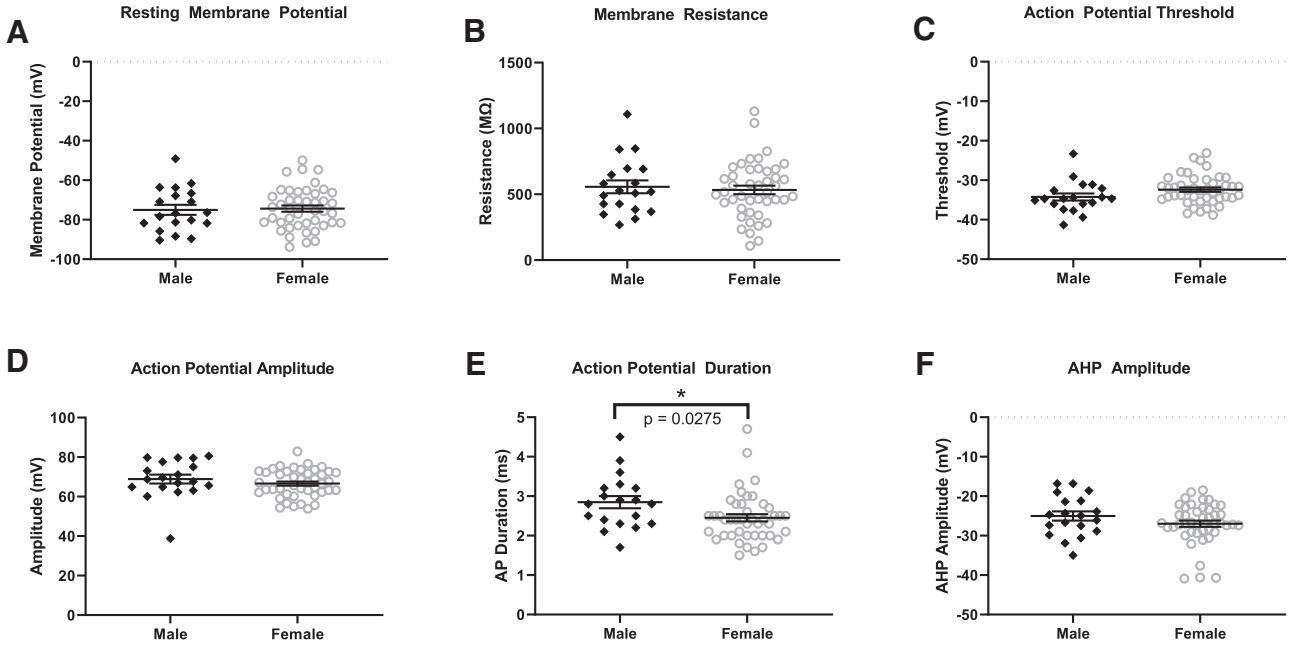

Figure 8. *Drd2-Pet1* neuron electrophysiological properties in male versus female mice. Membrane and AP characteristics were analyzed in GFP-marked *Drd2-Pet1* male and female neurons using whole-cell patch-clamp electrophysiology in acute brain slices from triple transgenic *Drd2-Cre;Pet1-Flpe;RC-FrePe* mice. Membrane potential (***A***), membrane resistance (***B***), AP threshold (***C***), AP amplitude (***D***), and AHP amplitude (***F***) do not differ in male ($n = 19$) or female ($n = 44$) *Drd2-Pet1* neurons while (***E***) male *Drd2-Pet1* neurons had a significantly longer (2.847 ± 0.155 ms, $n = 19$ cells) AP duration than in females (2.54 ± 0.094 ms, $n = 44$ cells, $p = 0.0275$, unpaired *t* test).

(Weissbourd et al., 2014). Using pairwise correlations between auditory brain regions (Fig. 9*D*), we constructed a correlation matrix that shows positively correlated regions in green and negatively correlated regions in black (Fig. 9*E*). This visualization reveals that most auditory brain regions are positively correlated in males (SOC and LL, Pearson's $r = 0.89$) with only the LL and cochlear nucleus being slightly negatively correlated (Pearson's $r = -0.28$). Interestingly, a greater number of innervated regions were negatively correlated in females, including the CNC with both the SOC and the IC ($r = -0.68$ and $r = -0.75$, respectively), as well as PNC and IC ($r = -0.67$). The innervation of the PNC and SOC was significantly negatively correlated ($r = -0.85$, $p = 0.033$, two-tailed test). Further, we expanded analyses to include the dLGN, a region critical for visually-cued potentiation of the acoustic startle (Tischler and Davis, 1983), and found that in females innervation of the dLGN was not strongly correlated with innervation of auditory brain regions, while in males this dLGN innervation was highly negatively correlated with both the SOC ($r = -0.91$, $p = 0.033$, two-tailed test) and the IC ($r = -0.91$, $p = 0.034$, two-tailed test), indicating that *Drd2-Pet1* neuron circuitry may be set up to modulate multisensory information differently in males compared with females.

GABA and 5-HT in *Drd2-Pet1* neurons

Given detection of *Gad2* mRNA in *Drd2-Pet1* neurons, we probed for GABA versus 5-HT immunopositivity in cell soma versus axonal boutons in males versus females. Punctate GABA immunostaining was indeed detectable in some *Drd2-Pet1* neuron soma (Fig. 10*A*) in both males and females. Yet, in all target brain regions examined, GABA was undetectable in the GFP-marked *Drd2-Pet1* boutons. Shown are representative images from the SOC (Fig. 10*B*) and IC (Fig. 10*C*), noting a GABA-positive cell body in the IC (boxed) and GABA-positive staining in the corpus callosum serving as a positive control for GABA immunodetection (Fig. 10*D*). By contrast, 5-HT immunostaining in *Drd2-Pet1* boutons was readily detectable (representative images from the SOC and IC; Fig. 9*B*).

Discussion

Strategy

We hypothesized that loss of *Drd2* gene expression and associated DRD2 signaling normally observed in certain DR *Pet1*$^+$ serotonergic neurons (*Drd2-Pet1* neurons) could impair sensory, social, and/or defensive behaviors. We used the transgenic driver e*Pet-cre* to delete functionally critical *Drd2* gene sequences selectively in serotonergic neurons, thereby abolishing transcript and DRD2 protein function, which would normally initiate in *Pet1* cells during adolescence. We validated these $Drd2^{Pet1\text{-}CKO}$ mice and examined behavioral responses. Further, we explored *Drd2-Pet1* neurons themselves.

Main findings

Key findings include the following. (1) Sex-specific behavioral alterations were observed in $Drd2^{Pet1\text{-}CKO}$ mice. Females showed a dramatic diminution in the protective, defensive ASR as compared with $Drd2^{flox/flox}$ controls, while no differences were observed in males. (2) $Drd2^{Pet1\text{-}CKO}$ males, but not females, showed increased winning in the

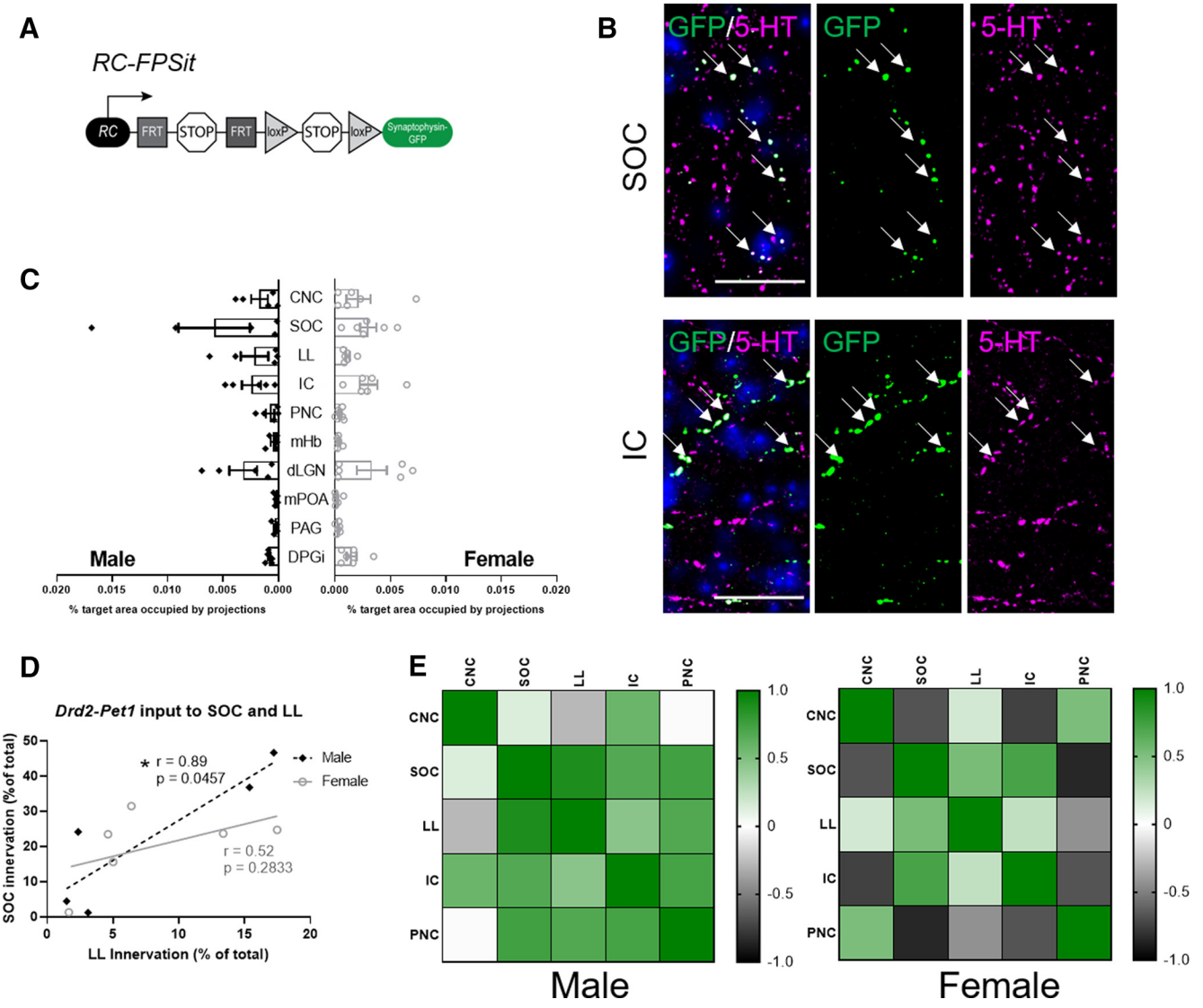

Figure 9. *Drd2-Pet1* neuron axon terminals target brain regions involved in sensory processing and defensive behavior in both male and female mice. ***A***, Intersectional genetic strategy: expression of *Drd2-Cre* and *Pet1-Flpe* transgenes results in dual recombination of intersectional allele, *RC-FPSit,* to label boutons of *Drd2-Pet1* neurons with Synaptophysin-GFP. ***B***, Representative images of *Drd2-Pet1* boutons in the SOC and IC. GFP+ (green, marked with arrows) boutons co-localize with 5-HT (magenta) staining. DAPI-stained nuclei shown in blue. Scale bar: 25 μm. ***C***, Quantification of the percent target area occupied by projections for all ten brain regions examined (for quantification protocol, see Materials and Methods). Target areas analyzed include brain regions involved in auditory processing and social behavior including the CNC, SOC, LL, IC, PNC, mHb, dLGN, mPOA, and PAG. The DPGi was also examined. No significant differences in projection area innervation were observed between males ($n = 5$) and females ($n = 6$). ***D***, Example graph showing correlation between innervation density of auditory brain regions differs in males compared with females. Each dot represents one animal. Values are shown as Pearson's correlation coefficient (r), and * indicates $p < 0.5$ in a two-tailed test. ***E***, Pairwise correlations shown for male and female innervation density in auditory brain regions. Heatmaps represent high correlation (green) and low correlation (black) between CNC, SOC, LL, IC, and PNC.

tube test of social dominance against sex-matched and age-matched controls. (3) No differences were observed in ABRs, in PPI of acoustic startle, locomotion, cognition, nor various affective behaviors. (4) No sex-specific differences were found in *Drd2-Pet1* neuron number, soma distribution, nor in the set of efferent targets; however, within-animal correlations between efferent densities across target brain regions suggest differences by sex, thus hinting at sex-specific structural differences in *Drd2-Pet1* neuronal circuitry. (5) *Drd2-Pet1* cells in males as compared with females showed longer AP durations and higher levels of *Gad2* transcripts (important for GABA synthesis); $Drd2^{Pet1\text{-}CKO}$ cells did not show a sex specific difference in *Gad2* transcript levels, but the percentage of *Drd2-Pet1* cells that were $Gad2^{+}$ in $Drd2^{Pet1\text{-}CKO}$ males was slightly higher than in $Drd2^{Pet1\text{-}CKO}$ females. These findings, coupled with our prior work (Niederkofler et al., 2016) implicating *Drd2-Pet1* neurons in setting levels of defensive aggressive and exploratory behaviors in male mice, suggest that *Drd2-Pet1* neurons may serve as a specialized neuromodulatory interface whereby DRD2

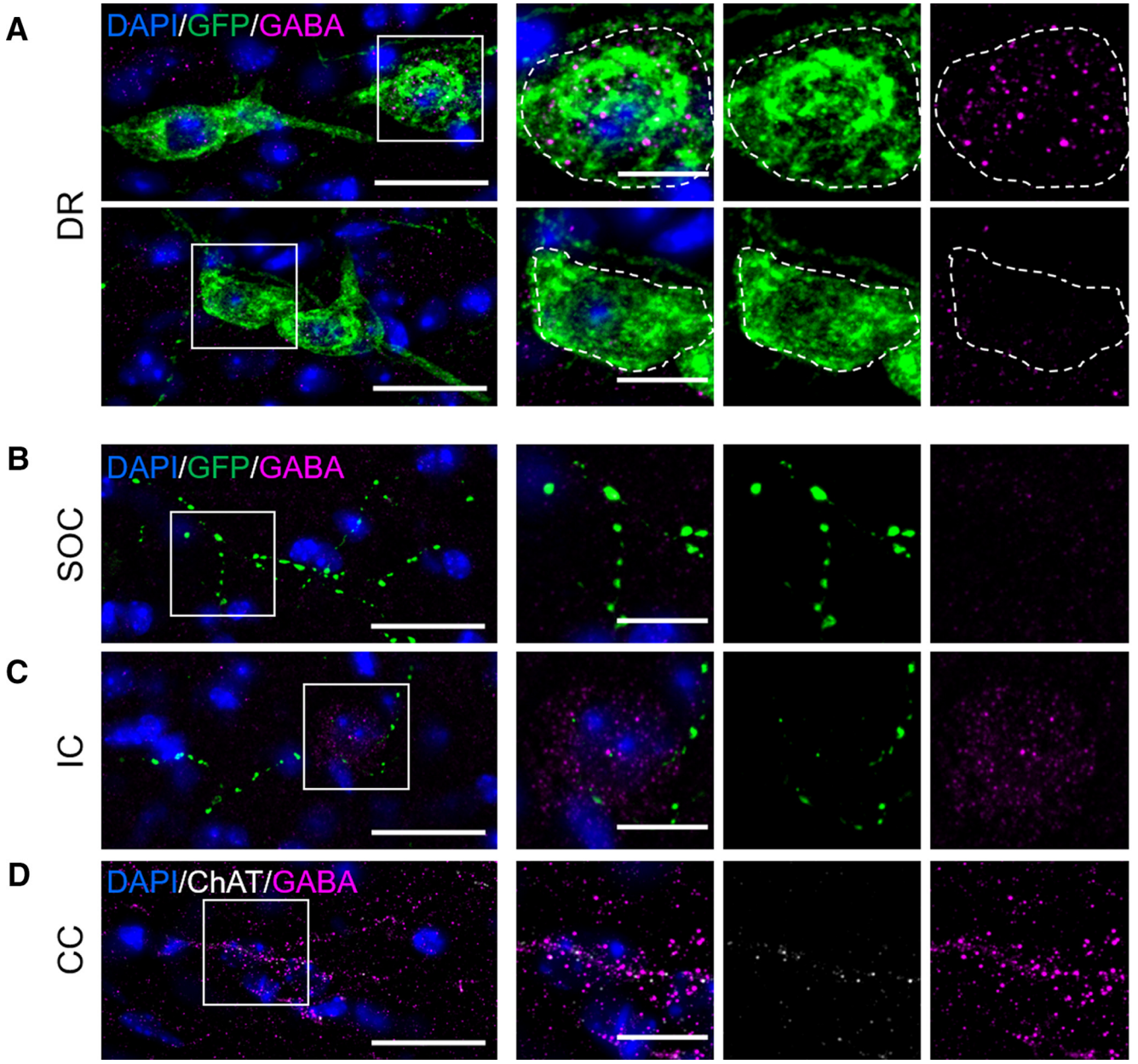

Figure 10. GABA immunoreactivity localizes to soma, but not axonal projections, of *Drd2-Pet1* neurons. ***A***, GABA staining (magenta) co-localizes with many *Drd2-Pet1* neuron soma (green GFP-positive cell bodies in *Drd2-Cre;Pet1-Flpe;RC-FPSit* mice) in the DR in a punctate manner (top), inset of boxed region showing neuron soma positive for GFP and GABA. Some *Drd2-Pet1* neuron soma are immuno-negative for GABA (bottom). Dotted lines encircle GFP-positive cell body. ***B***, ***C***, No GFP-positive *Drd2-Pet1* boutons (green) co-localize with GABA staining (magenta) in brain regions examined, shown here, representative images from SOC (***B***) and IC (***C***), noting a GABA-positive soma is visible in the image of the IC. ***D*,** GABA-positive immunoreactivity in the corpus callosum demonstrating detection of GABA boutons. ChAT (white) staining was used throughout for anatomic localization. Scale bars: 25 μm (left panel) and 10 μm (inset). DAPI-stained nuclei shown in blue.

signaling alters serotonergic neuronal activity to shape defensive, protective, and dominance behaviors in a sex-specific manner.

Protective ASR diminished in *Drd2*$^{Pet1\text{-}CKO}$ females

Defensive posturing in millisecond response to abrupt noise, be it a predator or other potential hazard, is a crucial evolutionarily conserved protective mechanism. Loss or blunting of this reflex can result in life-threatening exposure, while excessive enhancement can drive unnecessary, debilitating responses that preclude normal functioning. Thus, "tuning" of the ASR setpoint to social and environmental circumstances is likely critical for species survival and well-being. The observed ASR attenuation in female *Drd2*$^{Pet1\text{-}CKO}$ mice suggests that *Drd2-Pet1* neurons and the regulation of their activity cell autonomously by DRD2 comprises a critical

modulatory node for ASR in females. Further, this node appears separate functionally from that involved in acoustic sensorimotor gating, given that acoustic PPI appeared intact in *Drd2*$^{Pet1\text{-}CKO}$ females, and from hearing, given that ABRs were indistinguishable from controls. Thus, DRD2 signaling in *Drd2-Pet1* neurons forms a functional circuit node specialized in female mice to influence startle to acoustic stimuli.

In rats, reduction of 5-HT through synthesis inhibition increases ASR in females, but not males (Pettersson et al., 2016). Predicted reciprocally is that elevated 5-HT levels might blunt ASR in females. Relating this to our findings, it is possible that *Drd2-Pet1* neurons are more excitable in the absence of DRD2-mediated inhibition, resulting in increased 5-HT release, perhaps explaining the observed ASR blunting. In wild-type mice, this would predict that under conditions of DA elevation, for example through local DR DA neuron activity associated with arousal and vigilance (Cho et al., 2017), *Drd2-Pet1* neuron activity would be inhibited, reducing 5-HT release and thereby tuning a more sensitive ASR, conferring a protective advantage.

The ASR circuit follows from cochlea to CNC to PNC to spinal motoneurons (Davis et al., 1982; Koch et al., 1992), and receives inputs from auditory centers such as the SOC, IC, and SC (Lauer et al., 2017). *Drd2-Pet1* neurons innervate each of these areas and the PNC, and thus may impart modulation at multiple levels.

Tube test wins increased in *Drd2*$^{Pet1\text{-}CKO}$ males

The increased winning by *Drd2*$^{Pet1\text{-}CKO}$ males in the tube test suggests that loss of DRD2 results in an increase in or favoring of dominance behaviors, at least under these forced, one-on-one interaction conditions. We did not observe significant differences in levels of aggressive attack behaviors by *Drd2*$^{Pet1\text{-}CKO}$ males in a resident-intruder assay. Together, these findings suggest that in wild-type mice, DRD2 signaling in *Drd2-Pet1* neurons contributes to tempering certain dominance behaviors under particular conditions.

Understanding how the present results align with our prior work remains a pursuit. In earlier studies using a resident-intruder assay, we observed an increase in various aggressive behaviors in mice in which *Drd2-Pet1* neurons were constitutively silenced, which suggested to us that *Drd2-Pet1* neuron excitation and neurotransmitter release would normally temper such behaviors (i.e., favor nonconfrontational, even submissive behaviors). Because canonical DRD2 signaling is inhibitory and, as well, appears largely inhibitory in *Drd2-Pet1* neurons in slice, we predicted that loss of DRD2 signaling would enhance *Drd2-Pet1* cell excitability and neurotransmitter release probability, and thus would suppress or at least not enhance dominance behaviors. Yet *Drd2*$^{Pet1\text{-}CKO}$ males exhibited enhanced winning in the tube test. Perhaps DRD2 signaling in *Drd2-Pet1* neurons results in cellular activity changes that ultimately lead to a tempering of one-on-one social dominance under some conditions, while extreme, constitutive *Drd2-Pet1* neuron silencing is required to prompt the opposite, in the form of aggression escalation to an intruder. Indeed, other findings also support this notion that dominance by tube test does not necessarily correlate with aggression in a resident-intruder assay (Tammimäki et al., 2010). Differences might also be explained by whether the input conditions trigger *Drd2-Pet1* neurons to release 5-HT versus GABA, should the latter prove a capability, noting that *Drd2-Pet1* cells express *Gad2*, albeit we were unable to show GABA in *Drd2-Pet1* boutons, only their soma.

Interestingly, a subset of *Drd2*$^{Pet1\text{-}CKO}$ males (four out of 26) did display increased levels of aggressive behaviors as compared with other *Drd2*$^{Pet1\text{-}CKO}$ mice and controls, suggesting there may be other influencing variables, yet unknown. This is plausible given that mice deficient for the long isoform of DRD2 ($D_{2L}R$) are reported to show anxiety-like and depressive-like behaviors only following a stress-exposure paradigm (Shioda et al., 2019). Moreover, these stress-induced affective phenotypes in $D_{2L}R$ knock-out mice were abrogated by driving $D_{2L}R$ expression in DR *Pet1*+ serotonergic neurons (Shioda et al., 2019). Together these findings suggest that the behavioral role of *Drd2* expression in *Drd2-Pet1* neurons may be influenced by environmental factors.

Sex-specific differences in *Drd2-Pet1* neuron properties

The observed sex-specific differences in *Gad2* transcript levels in *Drd2-Pet1* neurons may contribute to the sex-specific behavioral alterations exhibited by *Drd2*$^{Pet1\text{-}CKO}$ mice. *Gad2* expression in *Drd2-Pet1* neurons is in line with prior reports showing *Gad2* expression more generally in the serotonergic DR (Nanopoulos et al., 1982; Calizo et al., 2011; Shikanai et al., 2012). It may be that *Drd2-Pet1* neurons can release GABA as well as or instead of 5-HT under certain conditions or at particular targets. This capacity may differ in males versus females, given our observation that in males, *Drd2-Pet1* neurons harbor higher levels of *Gad2* mRNA. Interestingly, *Drd2*$^{Pet1\text{-}CKO}$ cells did not display this sex specific difference in *Gad2* transcript, suggesting that *Drd2* expression, or more broadly dopaminergic signaling in *Drd2-Pet1* neurons, may affect *Gad2* transcript levels. One potential model to be tested is if DRD2 signaling, in turn, alters levels of *Gad2* expression to allow for neuronal release of GABA in addition to or instead of serotonin when behavioral or environmental conditions necessitate. Indeed, there is precedent for the differential usage of serotonin and glutamate by raphe serotonergic neurons (Liu et al., 2014; Kapoor et al., 2016; Sengupta et al., 2017; Wang et al., 2019), although GABAergic and serotonergic co-release has not been reported.

AP duration measured *ex vivo* was longer in male versus female *Drd2-Pet1* cells; this may also confer neurotransmitter release properties that could contribute to behavioral differences. Additional studies are needed to determine how *Drd2*$^{Pet1\text{-}CKO}$ affects *Drd2-Pet1* neuron electrophysiology, gene expression, or efferent targets. Such experiments may be achieved through crossing *Drd2*$^{Pet1\text{-}CKO}$ *(ePet1-Cre;Drd2*$^{f/f}$*)* mice to *Drd2-Flpo* mice (The Jackson Laboratory strain #034419 provided by Bernardo Sabatini) along with an intersectional reporter transgene which would

allow for dual Cre-mediated and Flp-mediated fluorescent labeling of mutant *Drd2*$^{Pet1\text{-}CKO}$ cells. While complex genetics, this strategy would enable mutant cell visualization for electrophysiology, single-cell RNA sequencing, and analysis of axonal projections.

In both males and females, *Drd2-Pet1* neurons densely innervate auditory brainstem regions, likely modulating auditory-related processes at one or multiple of these sites. In examining *Drd2-Pet1* efferents, we observed interanimal variability in regional innervation density. We speculate this may arise from subgroups within the *Drd2-Pet1* neuron population that target different downstream structures. For example, some *Drd2-Pet1* neurons may project specifically to the SOC while others might project specifically to the LL. If some animals have more of one subgroup than the other, averaging absolute innervation densities for each target region across all males and females may hide meaningful circuit structure. Covariance analysis of projection targets in each animal thus might hint at which brain regions come under shared regulation by *Drd2-Pet1* neurons. In males, the high correlation between auditory region efferent densities suggests shared input from the same *Drd2-Pet1* neurons. In females, the CNC/SOC, CNC/IC, SOC/PNC, LL/PNC, and IC/PNC combinations were more negatively correlated, suggesting there might exist a subgroup of *Drd2-Pet1* neurons that targets the PNC and a different subgroup, the SOC. We speculate that in males, *Drd2-Pet1* neurons contribute to a general level of serotonergic tone across the auditory brainstem, while in females, certain *Drd2-Pet1* neurons selectively target and modulate specific nuclei.

In conclusion, we found that *Drd2* gene expression in a specialized subset of *Pet1* serotonergic neurons is required for certain defensive, dominance, and protective behaviors, involving auditory processing in a sex-specific manner. Deficits in sensory processing such as altered acoustic startle and impaired social communication and dominance behaviors manifest in human disorders including autism spectrum disorder, schizophrenia, and posttraumatic stress disorder, often in sex-specific ways (King et al., 2013; Steel et al., 2014; Matsuo et al., 2016; Thye et al., 2018) and with sex-specific differences in therapeutic outcomes (Franconi et al., 2007). The presented findings, thus, may point to novel circuit nodes of relevance to human neuropsychiatric disease.

References

Baik JH, Picetti R, Saiardi A, Thiriet G, Dierich A, Depaulis A, Le Meur M, Borrelli E (1995) Parkinsonian-like locomotor impairment in mice lacking dopamine D2 receptors. Nature 377:424–428.

Bello EP, Mateo Y, Gelman DM, Noaín D, Shin JH, Low MJ, Alvarez VA, Lovinger DM, Rubinstein M (2011) Cocaine supersensitivity and enhanced motivation for reward in mice lacking dopamine D2 autoreceptors. Nat Neurosci 14:1033–1038.

Brown GL, Ebert MH, Goyer PF, Jimerson DC, Klein WJ, Bunney WE, Goodwin FK (1982) Aggression, suicide, and serotonin: relationships to CSF amine metabolites. Am J Psychiatry 139:741–746.

Brust RD, Corcoran AE, Richerson GB, Nattie E, Dymecki SM (2014) Functional and developmental identification of a molecular subtype of brain serotonergic neuron specialized to regulate breathing dynamics. Cell Rep 9:2152–2165.

Calizo LH, Akanwa A, Ma X, Pan YZ, Lemos JC, Craige C, Heemstra LA, Beck SG (2011) Raphe serotonin neurons are not homogenous: electrophysiological, morphological and neurochemical evidence. Neuropharmacology 61:524–543.

Cho JR, Treweek JB, Robinson JE, Xiao C, Bremner LR, Greenbaum A, Gradinaru V (2017) Dorsal raphe dopamine neurons modulate arousal and promote wakefulness by salient stimuli. Neuron 94:1205–1219.e8.

Crawford LK, Rahman SF, Beck SG (2013) Social stress alters inhibitory synaptic input to distinct subpopulations of raphe serotonin neurons. ACS Chem Neurosci 4:200–209.

Davis M, Aghajanian GK (1976) Effects of apomorphine and haloperidol on the acoustic startle response in rats. Psychopharmacology (Berl) 47:217–223.

Davis M, Strachan DI, Kass E (1980) Excitatory and inhibitory effects of serotonin on sensorimotor reactivity measured with acoustic startle. Science 209:521–523.

Davis M, Gendelman DS, Tischler MD, Gendelman PM (1982) A primary acoustic startle circuit: lesion and stimulation studies. J Neurosci 2:791–805.

Deneris E, Gaspar P (2018) Serotonin neuron development: shaping molecular and structural identities. Wiley Interdiscip Rev Dev Biol 7:10.1002.

Franconi F, Brunelleschi S, Steardo L, Cuomo V (2007) Gender differences in drug responses. Pharmacol Res 55:81–95.

Franklin KBJ, Paxinos G (2008) The mouse brain in stereotaxic coordinates, Vol 3. New York: Elsevier.

Gainetdinov RR, Wetsel WC, Jones SR, Levin ED, Jaber M, Caron MG (1999) Role of serotonin in the paradoxical calming effect of psychostimulants on hyperactivity. Science 283:397–401.

Galliciotti G, Sonderegger P (2006) Neuroserpin. Front Biosci 11:33–45.

Geyer MA, Braff DL (1987) Startle habituation and sensorimotor gating in schizophrenia and related animal models. Schizophr Bull 13:643–668.

Gong S, Doughty M, Harbaugh CR, Cummins A, Hatten ME, Heintz N, Gerfen CR (2007) Targeting Cre recombinase to specific neuron populations with bacterial artificial chromosome constructs. J Neurosci 27:9817–9823.

Grace AA (2016) Dysregulation of the dopamine system in the pathophysiology of schizophrenia and depression. Nat Rev Neurosci 17:524–532.

Hendricks TJ, Fyodorov DV, Wegman LJ, Lelutiu NB, Pehek EA, Yamamoto B, Silver J, Weeber EJ, Sweatt JD, Deneris ES (2003) Pet-1 ETS gene plays a critical role in 5-HT neuron development and is required for normal anxiety-like and aggressive behavior. Neuron 37:233–247.

Holmes A, Yang RJ, Lesch KP, Crawley JN, Murphy DL (2003) Mice lacking the serotonin transporter exhibit 5-HT(1A) receptor-mediated abnormalities in tests for anxiety-like behavior. Neuropsychopharmacol 28:2077–2088.

Holschbach MA, Vitale EM, Lonstein JS (2018) Serotonin-specific lesions of the dorsal raphe disrupt maternal aggression and caregiving in postpartum rats. Behav Brain Res 348:53–64.

Huang KW, Ochandarena NE, Philson AC, Hyun M, Birnbaum JE, Cicconet M, Sabatini BL (2019) Molecular and anatomical organization of the dorsal raphe nucleus. Elife 8:e46464.

Jensen P, Farago AF, Awatramani RB, Scott MM, Deneris ES, Dymecki SM (2008) Redefining the serotonergic system by genetic lineage. Nat Neurosci 11:417–419.

Kane KL, Longo-Guess CM, Gagnon LH, Ding D, Salvi RJ, Johnson KR (2012) Genetic background effects on age-related hearing loss associated with Cdh23 variants in mice. Hear Res 283:80–88.

Kapoor V, Provost AC, Agarwal P, Murthy VN (2016) Activation of raphe nuclei triggers rapid and distinct effects on parallel olfactory bulb output channels. Nat Neurosci 19:271–282.

Kim JC, Cook MN, Carey MR, Shen C, Regehr WG, Dymecki SM (2009) Linking genetically defined neurons to behavior through a broadly applicable silencing allele. Neuron 63:305–315.
King MW, Street AE, Gradus JL, Vogt DS, Resick PA (2013) Gender differences in posttraumatic stress symptoms among OEF/OIF veterans: an item response theory analysis. J Trauma Stress 26:175–183.
Koch M, Lingenhöhl K, Pilz PK (1992) Loss of the acoustic startle response following neurotoxic lesions of the caudal pontine reticular formation: possible role of giant neurons. Neuroscience 49:617–625.
Lammel S, Lim BK, Malenka RC (2014) Reward and aversion in a heterogeneous midbrain dopamine system. Neuropharmacology 76 [Pt B]:351–359.
Lauer AM, Behrens D, Klump G (2017) Acoustic startle modification as a tool for evaluating auditory function of the mouse: progress, pitfalls, and potential. Neurosci Biobehav Rev 77:194–208.
Lindzey G, Winston H, Manosevitz M (1961) Social dominance in inbred mouse strains. Nature 191:474–476.
Liu Z, Zhou J, Li Y, Hu F, Lu Y, Ma M, Feng Q, Zhang JE, Wang D, Zeng J, Bao J, Kim JY, Chen ZF, El Mestikawy S, Luo M (2014) Dorsal raphe neurons signal reward through 5-HT and glutamate. Neuron 81:1360–1374.
Lonstein JS, Gammie SC (2002) Sensory, hormonal, and neural control of maternal aggression in laboratory rodents. Neurosci Biobehav Rev 26:869–888.
Lucki I (1998) The spectrum of behaviors influenced by serotonin. Biol Psychiatry 44:151–162.
Maison SF, Usubuchi H, Liberman MC (2013) Efferent feedback minimizes cochlear neuropathy from moderate noise exposure. J Neurosci 33:5542–5552.
Marr D, Hildreth E (1980) Theory of edge detection. Proc R Soc Lond B Biol Sci 207:187–217.
Matsuo J, Ota M, Hori H, Hidese S, Teraishi T, Ishida I, Hiraishi M, Kunugi H (2016) A large single ethnicity study of prepulse inhibition in schizophrenia: separate analysis by sex focusing on effect of symptoms. J Psychiatr Res 82:155–162.
McQuin C, Goodman A, Chernyshev V, Kamentsky L, Cimini BA, Karhohs KW, Doan M, Ding L, Rafelski SM, Thirstrup D, Wiegraebe W, Singh S, Becker T, Caicedo JC, Carpenter AE (2018) CellProfiler 3.0: next-generation image processing for biology. PLoS Biol 16:e2005970.
Meincke U, Light GA, Geyer MA, Braff DL, Gouzoulis-Mayfrank E (2004) Sensitization and habituation of the acoustic startle reflex in patients with schizophrenia. Psychiatry Res 126:51–61.
Meloni EG, Davis M (1999) Enhancement of the acoustic startle response in rats by the dopamine D1 receptor agonist SKF 82958. Psychopharmacology (Berl) 144:373–380.
Meloni EG, Davis M (2000a) Enhancement of the acoustic startle response by dopamine agonists after 6-hydroxydopamine lesions of the substantia nigra pars compacta: corresponding changes in c-Fos expression in the caudate-putamen. Brain Res 879:93–104.
Meloni EG, Davis M (2000b) Synergistic enhancement of the acoustic startle reflex by dopamine D1 and 5-HT1A agonists and corresponding changes in c-Fos expression in the dorsal raphe of rats. Psychopharmacology (Berl) 151:359–367.
Moy SS, Nadler JJ, Perez A, Barbaro RP, Johns JM, Magnuson TR, Piven J, Crawley JN (2004) Sociability and preference for social novelty in five inbred strains: an approach to assess autistic-like behavior in mice. Genes Brain Behav 3:287–302.
Nanopoulos D, Belin MF, Maitre M, Vincendon G, Pujol JF (1982) Immunocytochemical evidence for the existence of GABAergic neurons in the nucleus raphe dorsalis. Possible existence of neurons containing serotonin and GABA. Brain Res 232:375–389.
Netser S, Haskal S, Magalnik H, Wagner S (2017) A novel system for tracking social preference dynamics in mice reveals sex- and strain-specific characteristics. Mol Autism 8:53.
Niederkofler V, Asher TE, Okaty BW, Rood BD, Narayan A, Hwa LS, Beck SG, Miczek KA, Dymecki SM (2016) Identification of serotonergic neuronal modules that affect aggressive behavior. Cell Rep 17:1934–1949.
Okaty BW, Freret ME, Rood BD, Brust RD, Hennessy ML, deBairos D, Kim JC, Cook MN, Dymecki SM (2015) Multi-scale molecular deconstruction of the serotonin. Neuron 88:774–791.
Okaty BW, Sturrock N, Escobedo Lozoya Y, Chang Y, Senft RA, Lyon KA, Alekseyenko OV, Dymecki SM (2020) A single-cell transcriptomic and anatomic atlas of mouse dorsal raphe Pet1 neurons. Elife 9:e55523.
Palanza P (2001) Animal models of anxiety and depression: how are females different? Neurosci Biobehav Rev 25:219–233.
Perronnet C, Vaillend C (2010) Dystrophins, utrophins, and associated scaffolding complexes: role in mammalian brain and implications for therapeutic strategies. J Biomed Biotechnol 2010:849426.
Pettersson R, Hagsäter SM, Eriksson E (2016) Serotonin depletion eliminates sex differences with respect to context-conditioned immobility in rat. Psychopharmacology (Berl) 233:1513–1521.
Poulin JF, Caronia G, Hofer C, Cui Q, Helm B, Ramakrishnan C, Chan CS, Dombeck DA, Deisseroth K, Awatramani R (2018) Mapping projections of molecularly defined dopamine neuron subtypes using intersectional genetic approaches. Nat Neurosci 21:1260–1271.
Poulin JF, Gaertner Z, Moreno-Ramos OA, Awatramani R (2020) Classification of midbrain dopamine neurons using single-cell gene expression profiling approaches. Trends Neurosci 43:155–169.
Ralph RJ, Paulus MP, Fumagalli F, Caron MG, Geyer MA (2001) Prepulse inhibition deficits and perseverative motor patterns in dopamine transporter knock-out mice: differential effects of D1 and D2 receptor antagonists. J Neurosci 21:305–313.
Ren J, Isakova A, Friedmann D, Zeng J, Grutzner SM, Pun A, Zhao GQ, Kolluru SS, Wang R, Lin R, Li P, Li A, Raymond JL, Luo Q, Luo M, Quake SR, Luo L (2019) Single-cell transcriptomes and whole-brain projections of serotonin neurons in the mouse dorsal and median raphe nuclei. Elife 8:e49424.
Rood BD, Calizo LH, Piel D, Spangler ZP, Campbell K, Beck SG (2014) Dorsal raphe serotonin neurons in mice: immature hyperexcitability transitions to adult state during first three postnatal weeks suggesting sensitive period for environmental perturbation. J Neurosci 34:4809–4821.
Schindelin J, Arganda-Carreras I, Frise E, Kaynig V, Longair M, Pietzsch T, Preibisch S, Rueden C, Saalfeld S, Schmid B, Tinevez JY, White DJ, Hartenstein V, Eliceiri K, Tomancak P, Cardona A (2012) Fiji: an open-source platform for biological-image analysis. Nat Methods 9:676–682.
Scott MM, Wylie CJ, Lerch JK, Murphy R, Lobur K, Herlitze S, Jiang W, Conlon RA, Strowbridge BW, Deneris ES (2005) A genetic approach to access serotonin neurons for in vivo and in vitro studies. Proc Natl Acad Sci USA 102:16472–16477.
Sengupta A, Bocchio M, Bannerman DM, Sharp T, Capogna M (2017) Control of amygdala circuits by 5-HT neurons via 5-HT and glutamate cotransmission. J Neurosci 37:1785–1796.
Seo C, Guru A, Jin M, Ito B, Sleezer BJ, Ho YY, Wang E, Boada C, Krupa NA, Kullakanda DS, Shen CX, Warden MR (2019) Intense threat switches dorsal raphe serotonin neurons to a paradoxical operational mode. Science 363:538–542.
Shikanai H, Yoshida T, Konno K, Yamasaki M, Izumi T, Ohmura Y, Watanabe M, Yoshioka M (2012) Distinct neurochemical and functional properties of GAD67-containing 5-HT neurons in the rat dorsal raphe nucleus. J Neurosci 32:14415–14426.
Shioda N, Imai Y, Yabuki Y, Sugimoto W, Yamaguchi K, Wang Y, Hikida T, Sasaoka T, Mieda M, Fukunaga K (2019) Dopamine D_{2L} receptor deficiency causes stress vulnerability through 5-HT_{1A} receptor dysfunction in serotonergic neurons. J Neurosci 39:7551–7563.
Shrestha BR, Chia C, Wu L, Kujawa SG, Liberman MC, Goodrich LV (2018) Sensory neuron diversity in the inner ear is shaped by activity. Cell 174:1229–1246.e17.

Spaethling JM, Piel D, Dueck H, Buckley PT, Morris JF, Fisher SA, Lee J, Sul JY, Kim J, Bartfai T, Beck SG, Eberwine JH (2014) Serotonergic neuron regulation informed by in vivo single-cell transcriptomics. FASEB J 28:771–780.

Spannuth BM, Hale MW, Evans AK, Lukkes JL, Campeau S, Lowry CA (2011) Investigation of a central nucleus of the amygdala/dorsal raphe nucleus serotonergic circuit implicated in fear-potentiated startle. Neuroscience 179:104–119.

Steel Z, Marnane C, Iranpour C, Chey T, Jackson JW, Patel V, Silove D (2014) The global prevalence of common mental disorders: a systematic review and meta-analysis 1980-2013. Int J Epidemiol 43:476–493.

Takahashi H, Kamio Y (2018) Acoustic startle response and its modulation in schizophrenia and autism spectrum disorder in Asian subjects. Schizophr Res 198:16–20.

Tammimäki A, Käenmäki M, Kambur O, Kulesskaya N, Keisala T, Karvonen E, García-Horsman JA, Rauvala H, Männistö PT (2010) Effect of S-COMT deficiency on behavior and extracellular brain dopamine concentrations in mice. Psychopharmacology (Berl) 211:389–401.

Terranova JI, Song Z, Larkin TE 2nd, Hardcastle N, Norvelle A, Riaz A, Albers HE (2016) Serotonin and arginine-vasopressin mediate sex differences in the regulation of dominance and aggression by the social brain. Proc Natl Acad Sci USA 113:13233–13238.

Thye MD, Bednarz HM, Herringshaw AJ, Sartin EB, Kana RK (2018) The impact of atypical sensory processing on social impairments in autism spectrum disorder. Dev Cogn Neurosci 29:151–167.

Tischler MD, Davis M (1983) A visual pathway that mediates fear-conditioned enhancement of acoustic startle. Brain Res 276:55–71.

van den Berg WE, Lamballais S, Kushner SA (2015) Sex-specific mechanism of social hierarchy in mice. Neuropsychopharmacology 40:1364–1372.

Wang HL, Zhang S, Qi J, Wang H, Cachope R, Mejias-Aponte CA, Gomez JA, Mateo-Semidey GE, Beaudoin GMJ, Paladini CA, Cheer JF, Morales M (2019) Dorsal raphe dual serotonin-glutamate neurons drive reward by establishing excitatory synapses on VTA mesoaccumbens dopamine neurons. Cell Rep 26:1128–1142.e7.

Weissbourd B, Ren J, DeLoach KE, Guenthner CJ, Miyamichi K, Luo L (2014) Presynaptic partners of dorsal raphe serotonergic and GABAergic neurons. Neuron 83:645–662.

Yu Q, Teixeira CM, Mahadevia D, Huang Y, Balsam D, Mann JJ, Gingrich JA, Ansorge MS (2014) Dopamine and serotonin signaling during two sensitive developmental periods differentially impact adult aggressive and affective behaviors in mice. Mol Psychiatry 19:688–698.

Zhou T, Zhu H, Fan Z, Wang F, Chen Y, Liang H, Yang Z, Zhang L, Lin L, Zhan Y, Wang Z, Hu H (2017) History of winning remodels thalamo-PFC circuit to reinforce social dominance. Science 357:162–168.

Zhou X, Jen PH, Seburn KL, Frankel WN, Zheng QY (2006) Auditory brainstem responses in 10 inbred strains of mice. Brain Res 1091:16–26.

REFERENCES

Aaron J, Chew T-L. 2021. A guide to accurate reporting in digital image processing – can anyone reproduce your quantitative analysis? J Cell Sci. 134.

Abela AR, Browne CJ, Sargin D, Prevot TD, Ji XD, Li Z, Lambe EK, Fletcher PJ. 2020. Median raphe serotonin neurons promote anxiety-like behavior via inputs to the dorsal hippocampus. Neuropharmacology. 107985.

Acsády L, Katona I, Martínez-Guijarro FJ, Buzsáki G, Freund TF. 2000. Unusual Target Selectivity of Perisomatic Inhibitory Cells in the Hilar Region of the Rat Hippocampus. J Neurosci. 20:6907–6919.

Adams RA, Bush D, Zheng F, Meyer SS, Kaplan R, Orfanos S, Marques TR, Howes OD, Burgess N. 2020. Impaired theta phase coupling underlies frontotemporal dysconnectivity in schizophrenia. Brain. 143:1261–1277.

Agnati LF, Zoli M, Strömberg I, Fuxe K. 1995. Intercellular communication in the brain: Wiring versus volume transmission. Neuroscience. 69:711–726.

Alford R, Simpson HM, Duberman J, Hill GC, Ogawa M, Regino C, Kobayashi H, Choyke PL. 2009. Toxicity of Organic Fluorophores Used in Molecular Imaging: Literature Review. Mol Imaging. 8:7290.2009.00031.

Allen JR, Ross ST, Davidson MW. 2013. Sample preparation for single molecule localization microscopy. Phys Chem Chem Phys PCCP. 15:18771–18783.

Alonso A, Merchán P, Sandoval JE, Sánchez-Arrones L, Garcia-Cazorla A, Artuch R, Ferrán JL, Martínez-de-la-Torre M, Puelles L. 2013. Development of the serotonergic cells in murine raphe nuclei and their relations with rhombomeric domains. Brain Struct Funct. 218:1229–1277.

Alonso JR, Frotscher M. 1989. Organization of the septal region in the rat brain: A Golgi/EM study of lateral septal neurons. J Comp Neurol. 286:472–487.

Amilhon B, Huh CYL, Manseau F, Ducharme G, Nichol H, Adamantidis A, Williams S. 2015. Parvalbumin Interneurons of Hippocampus Tune Population Activity at Theta Frequency. Neuron. 86:1277–1289.

Amilhon B, Lepicard È, Renoir T, Mongeau R, Popa D, Poirel O, Miot S, Gras C, Gardier AM, Gallego J, Hamon M, Lanfumey L, Gasnier B, Giros B, Mestikawy SE. 2010. VGLUT3 (Vesicular Glutamate Transporter Type 3) Contribution to the Regulation of Serotonergic Transmission and Anxiety. J Neurosci. 30:2198–2210.

Armbruster BN, Li X, Pausch MH, Herlitze S, Roth BL. 2007. Evolving the lock to fit the key to create a family of G protein-coupled receptors potently activated by an inert ligand. Proc Natl Acad Sci U S A. 104:5163–5168.

Armstrong C, Soltesz I. 2012. Basket cell dichotomy in microcircuit function. J Physiol. 590:683–694.

Art J. 2006. Photon Detectors for Confocal Microscopy. In: Pawley JB, editor. Handbook Of Biological Confocal Microscopy. Boston, MA: Springer US. p. 251–264.
Assaf SY, Miller JJ. 1978. The role of a raphe serotonin system in the control of septal unit activity and hippocampal desynchronization. Neuroscience. 3:539–550.
Awatramani R, Soriano P, Rodriguez C, Mai JJ, Dymecki SM. 2003. Cryptic boundaries in roof plate and choroid plexus identified by intersectional gene activation. Nat Genet. 35:70–75.
Azmitia EC. 1999. Serotonin Neurons, Neuroplasticity, and Homeostasis of Neural Tissue. Neuropsychopharmacology. 21:33–45.
Azmitia EC, Segal M. 1978. An autoradiographic analysis of the differential ascending projections of the dorsal and median raphe nuclei in the rat. J Comp Neurol. 179:641–667.
Aznar S, Qian Z-X, Knudsen GM. 2004. Non-serotonergic dorsal and median raphe projection onto parvalbumin- and calbindin-containing neurons in hippocampus and septum. Neuroscience. 124:573–581.
Bacallao R, Sohrab S, Phillips C. 2006. Guiding Principles of Specimen Preservation for Confocal Fluorescence Microscopy. In: Pawley JB, editor. Handbook Of Biological Confocal Microscopy. Boston, MA: Springer US. p. 368–380.
Baker KG, Halliday GM, Halasz P, Hornung JP, Geffen LB, Cotton RG, Törk I. 1991. Cytoarchitecture of serotonin-synthesizing neurons in the pontine tegmentum of the human brain. Synap N Y N. 7:301–320.
Baker KG, Halliday GM, Törk I. 1990. Cytoarchitecture of the human dorsal raphe nucleus. J Comp Neurol. 301:147–161.
Bakshi VP, Geyer MA. 1998. Multiple limbic regions mediate the disruption of prepulse inhibition produced in rats by the noncompetitive NMDA antagonist dizocilpine. J Neurosci Off J Soc Neurosci. 18:8394–8401.
Balázsfi D, Zelena D, Demeter K, Miskolczi C, Varga ZK, Nagyváradi Á, Nyíri G, Cserép C, Baranyi M, Sperlágh B, Haller J. 2018. Differential Roles of the Two Raphe Nuclei in Amiable Social Behavior and Aggression – An Optogenetic Study. Front Behav Neurosci. 12.
Bang SJ, Jensen P, Dymecki SM, Commons KG. 2012. Projections and interconnections of genetically defined serotonin neurons in mice. Eur J Neurosci. 35:85–96.
Bartos M, Elgueta C. 2012. Functional characteristics of parvalbumin- and cholecystokinin-expressing basket cells. J Physiol. 590:669–681.
Baskin BM, Mai JJ, Dymecki SM, Kantak KM. 2020. Cocaine reward and memory after chemogenetic inhibition of distinct serotonin neuron subtypes in mice. Psychopharmacology (Berl).
Baudry A, Pietri M, Launay J-M, Kellermann O, Schneider B. 2019. Multifaceted Regulations of the Serotonin Transporter: Impact on Antidepressant Response. Front Neurosci. 13:91.
Beaudet A, Descarries L. 1981. The fine structure of central serotonin neurons. J Physiol (Paris). 77:193–203.
Beauvillain JC, Mitchell V, Tramu G, Mazzuca M. 1991. GABA and enkephalin in the lateral septum of the guinea pig: Light and electron microscopic evidence for interrelations. J Comp Neurol. 308:103–114.

Belmer A, Beecher K, Jacques A, Patkar OL, Sicherre F, Bartlett SE. 2019. Axonal Non-segregation of the Vesicular Glutamate Transporter VGLUT3 Within Serotonergic Projections in the Mouse Forebrain. Front Cell Neurosci. 13.
Belousov AB, Fontes JD. 2013. Neuronal gap junctions: making and breaking connections during development and injury. Trends Neurosci. 36:227–236.
Bennett MVL, Zukin RS. 2004. Electrical Coupling and Neuronal Synchronization in the Mammalian Brain. Neuron. 41:495–511.
Benninger RKP, Piston DW. 2013. Two-Photon Excitation Microscopy for the Study of Living Cells and Tissues. Curr Protoc Cell Biol. 59:4.11.1-4.11.24.
Bergen DC. 2006. Do Seizures Harm the Brain? Epilepsy Curr. 6:117–118.
Besnard A, Miller SM, Sahay A. 2020. Distinct Dorsal and Ventral Hippocampal CA3 Outputs Govern Contextual Fear Discrimination. Cell Rep. 30:2360-2373.e5.
Bland BH, Bland CE, MacIver MB. 2016. Median raphe stimulation-induced motor inhibition concurrent with suppression of type 1 and type 2 hippocampal theta. Hippocampus. 26:289–300.
Bocian R, Posluszny A, Kowalczyk T, Kazmierska P, Konopacki J. 2011. Gap junction modulation of hippocampal formation theta and local cell discharges in anesthetized rats. Eur J Neurosci. 33:471–481.
Booker SA, Vida I. 2018. Morphological diversity and connectivity of hippocampal interneurons. Cell Tissue Res. 373:619–641.
Bradbury MJ, Dement WC, Edgar DM. 1997. Serotonin-containing fibers in the suprachiasmatic hypothalamus attenuate light-induced phase delays in mice. Brain Res. 768:125–134.
Brown CM. 2007. Fluorescence microscopy--avoiding the pitfalls. J Cell Sci. 120:1703–1705.
Brown RM, Short JL, Lawrence AJ. 2010. Identification of Brain Nuclei Implicated in Cocaine-Primed Reinstatement of Conditioned Place Preference: A Behaviour Dissociable from Sensitization. PLOS ONE. 5:e15889.
Brust RD, Corcoran AE, Richerson GB, Nattie E, Dymecki SM. 2014. Functional and Developmental Identification of a Molecular Subtype of Brain Serotonergic Neuron Specialized to Regulate Breathing Dynamics. Cell Rep. 9:2152–2165.
Brzosko Z, Mierau SB, Paulsen O. 2019. Neuromodulation of Spike-Timing-Dependent Plasticity: Past, Present, and Future. Neuron. 103:563–581.
Buchanan GF, Murray NM, Hajek MA, Richerson GB. 2014. Serotonin neurones have anti-convulsant effects and reduce seizure-induced mortality. J Physiol. 592:4395–4410.
Buhot M-C, Martin S, Segu L. 2000. Role of serotonin in memory impairment. Ann Med. 32:210–221.
Burry RW. 2010. Immunocytochemistry: A Practical Guide for Biomedical Research. New York: Springer-Verlag.
Buzsáki G. 2002. Theta oscillations in the hippocampus. Neuron. 33:325–340.
Buzsáki G, Moser EI. 2013. Memory, navigation and theta rhythm in the hippocampal-entorhinal system. Nat Neurosci. 16:130–138.
Calandreau L, Jaffard R, Desmedt A. 2007. Dissociated roles for the lateral and medial septum in elemental and contextual fear conditioning. Learn Mem. 14:422–429.

Carceller H, Guirado R, Ripolles-Campos E, Teruel-Marti V, Nacher J. 2020. Perineuronal Nets Regulate the Inhibitory Perisomatic Input onto Parvalbumin Interneurons and γ Activity in the Prefrontal Cortex. J Neurosci. 40:5008–5018.
Chambers D, Wilson LJ, Alfonsi F, Hunter E, Saxena U, Blanc E, Lumsden A. 2009. Rhombomere-specific analysis reveals the repertoire of genetic cues expressed across the developing hindbrain. Neural Develop. 4:6.
Chang W, Kanda H, Ikeda R, Ling J, DeBerry JJ, Gu JG. 2016. Merkel disc is a serotonergic synapse in the epidermis for transmitting tactile signals in mammals. Proc Natl Acad Sci. 113:E5491–E5500.
Chattopadhyaya B, Cristo GD, Higashiyama H, Knott GW, Kuhlman SJ, Welker E, Huang ZJ. 2004. Experience and Activity-Dependent Maturation of Perisomatic GABAergic Innervation in Primary Visual Cortex during a Postnatal Critical Period. J Neurosci. 24:9598–9611.
Cho K-O, Lybrand ZR, Ito N, Brulet R, Tafacory F, Zhang L, Good L, Ure K, Kernie SG, Birnbaum SG, Scharfman HE, Eisch AJ, Hsieh J. 2015. Aberrant hippocampal neurogenesis contributes to epilepsy and associated cognitive decline. Nat Commun. 6:ncomms7606.
Choi H-S, Park JH, Ahn JH, Hong S, Cho JH, Won M-H, Lee C-H. 2015. The anti-inflammatory activity of duloxetine, a serotonin/norepinephrine reuptake inhibitor, prevents kainic acid-induced hippocampal neuronal death in mice. J Neurol Sci. 358:390–397.
Clemens AM, Wang H, Brecht M. 2020. The lateral septum mediates kinship behavior in the rat. Nat Commun. 11:3161.
Clinckers R, Smolders I, Meurs A, Ebinger G, Michotte Y. 2004. Anticonvulsant action of hippocampal dopamine and serotonin is independently mediated by D2 and 5-HT1A receptors. J Neurochem. 89:834–843.
Cole RW, Jinadasa T, Brown CM. 2011. Measuring and interpreting point spread functions to determine confocal microscope resolution and ensure quality control. Nat Protoc. 6:1929–1941.
Cole RW, Thibault M, Bayles CJ, Eason B, Girard A-M, Jinadasa T, Opansky C, Schulz K, Brown CM. 2013. International test results for objective lens quality, resolution, spectral accuracy and spectral separation for confocal laser scanning microscopes. Microsc Microanal Off J Microsc Soc Am Microbeam Anal Soc Microsc Soc Can. 19:1653–1668.
Cover KK, Mathur BN. 2021. Axo-axonic synapses: Diversity in neural circuit function. J Comp Neurol. 529:2391–2401.
Cranfill PJ, Sell BR, Baird MA, Allen JR, Lavagnino Z, de Gruiter HM, Kremers G-J, Davidson MW, Ustione A, Piston DW. 2016. Quantitative assessment of fluorescent proteins. Nat Methods. 13:557–562.
Crupi R, Impellizzeri D, Cuzzocrea S. 2019. Role of Metabotropic Glutamate Receptors in Neurological Disorders. Front Mol Neurosci. 12.
Curley JP, Jensen CL, Franks B, Champagne FA. 2012. Variation in maternal and anxiety-like behavior associated with discrete patterns of oxytocin and vasopressin 1a receptor density in the lateral septum. Horm Behav. 61:454–461.
Curtis DR, Felix D, McLellan H. 1970. GABA and hippocampal inhibition. Br J Pharmacol. 40:881–883.

Dahlstroem A, Fuxe K. 1964. Evidence for the existence of monoamine-containing neurons in the central nervous system. I. Demonstration of monoamines in the cell bodies of brain stem neurons. Acta Physiol Scand Suppl. SUPPL 232:1-55.
De Paola V, Arber S, Caroni P. 2003. AMPA receptors regulate dynamic equilibrium of presynaptic terminals in mature hippocampal networks. Nat Neurosci. 6:491–500.
DeFelipe J, Hendry SH, Hashikawa T, Jones EG. 1991. Synaptic relationships of serotonin-immunoreactive terminal baskets on GABA neurons in the cat auditory cortex. Cereb Cortex N Y N 1991. 1:117–133.
De-Miguel FF, Trueta C. 2005. Synaptic and extrasynaptic secretion of serotonin. Cell Mol Neurobiol. 25:297–312.
Deneris E, Gaspar P. 2018. Serotonin neuron development: shaping molecular and structural identities. Wiley Interdiscip Rev Dev Biol. 7:e301.
Deneris ES, Wyler SC. 2012. Serotonergic transcriptional networks and potential importance to mental health. Nat Neurosci. 15:519–527.
Deng K, Yang L, Xie J, Tang H, Wu G-S, Luo H-R. 2019. Whole-brain mapping of projection from mouse lateral septal nucleus. Biol Open. 8.
Denk W, Piston DW, Webb WW. 2006. Multi-Photon Molecular Excitation in Laser-Scanning Microscopy. In: Pawley JB, editor. Handbook Of Biological Confocal Microscopy. Boston, MA: Springer US. p. 535–549.
Deschamps J, van den Akker E, Forlani S, De Graaff W, Oosterveen T, Roelen B, Roelfsema J. 1999. Initiation, establishment and maintenance of Hox gene expression patterns in the mouse. Int J Dev Biol. 43:635–650.
Diaspro A, Chirico G, Usai C, Ramoino P, Dobrucki J. 2006. Photobleaching. In: Pawley JB, editor. Handbook Of Biological Confocal Microscopy. Boston, MA: Springer US. p. 690–702.
Diel EE, Lichtman JW, Richardson DS. 2020. Tutorial: avoiding and correcting sample-induced spherical aberration artifacts in 3D fluorescence microscopy. Nat Protoc. 15:2773–2784.
Dingledine R, Varvel NH, Dudek FE. 2014. When and How Do Seizures Kill Neurons, and Is Cell Death Relevant to Epileptogenesis? Adv Exp Med Biol. 813:109–122.
Dinopoulos A, Dori I, Parnavelas JG. 1993. Serotonergic innervation of the mature and developing lateral septum of the rat: A light and electron microscopic immunocytochemical analysis. Neuroscience. 55:209–222.
Dixit R, Cyr R. 2003. Cell damage and reactive oxygen species production induced by fluorescence microscopy: effect on mitosis and guidelines for non-invasive fluorescence microscopy. Plant J Cell Mol Biol. 36:280–290.
Doischer D, Aurel Hosp J, Yanagawa Y, Obata K, Jonas P, Vida I, Bartos M. 2008. Postnatal Differentiation of Basket Cells from Slow to Fast Signaling Devices. J Neurosci. 28:12956–12968.
Domonkos A, Nikitidou Ledri L, Laszlovszky T, Cserép C, Borhegyi Z, Papp E, Nyiri G, Freund TF, Varga V. 2016. Divergent in vivo activity of non-serotonergic and serotonergic VGluT3-neurones in the median raphe region. J Physiol. 594:3775–3790.
Duguid IC, Smart TG. 2009. Presynaptic NMDA Receptors. In: Van Dongen AM, editor. Biology of the NMDA Receptor. Frontiers in Neuroscience. Boca Raton (FL): CRC Press/Taylor & Francis.

Dulac C, O'Connell LA, Wu Z. 2014. Neural control of maternal and paternal behaviors. Science. 345:765–770.
Dulawa SC, Gross C, Stark KL, Hen R, Geyer MA. 2000. Knockout Mice Reveal Opposite Roles for Serotonin 1A and 1B Receptors in Prepulse Inhibition. Neuropsychopharmacology. 22:650–659.
Dymecki SM, Ray RS, Kim JC. 2010. Mapping cell fate and function using recombinase-based intersectional strategies. Methods Enzymol. 477:183–213.
Eiden LE, Weihe E. 2011. VMAT2: a dynamic regulator of brain monoaminergic neuronal function interacting with drugs of abuse. Ann N Y Acad Sci. 1216:86–98.
El Mestikawy S, Wallén-Mackenzie Å, Fortin GM, Descarries L, Trudeau L-E. 2011. From glutamate co-release to vesicular synergy: vesicular glutamate transporters. Nat Rev Neurosci. 12:204–216.
Ellenberg J, Swedlow JR, Barlow M, Cook CE, Sarkans U, Patwardhan A, Brazma A, Birney E. 2018. A call for public archives for biological image data. Nat Methods. 15:849–854.
Ettinger A, Wittmann T. 2014. Fluorescence live cell imaging. Methods Cell Biol. 123:77–94.
Fasano C, Rocchetti J, Pietrajtis K, Zander J-F, Manseau F, Sakae DY, Marcus-Sells M, Ramet L, Morel LJ, Carrel D, Dumas S, Bolte S, Bernard V, Vigneault E, Goutagny R, Ahnert-Hilger G, Giros B, Daumas S, Williams S, El Mestikawy S. 2017. Regulation of the Hippocampal Network by VGLUT3-Positive CCK- GABAergic Basket Cells. Front Cell Neurosci. 11.
Favale E, Audenino D, Cocito L, Albano C. 2003. The anticonvulsant effect of citalopram as an indirect evidence of serotonergic impairment in human epileptogenesis. Seizure. 12:316–318.
Fawcett JW, Oohashi T, Pizzorusso T. 2019. The roles of perineuronal nets and the perinodal extracellular matrix in neuronal function. Nat Rev Neurosci. 20:451–465.
Feng D, Lau C, Ng L, Li Y, Kuan L, Sunkin SM, Dang C, Hawrylycz M. 2015. Exploration and visualization of connectivity in the adult mouse brain. Methods, Spatial mapping of multi-modal data in neuroscience. 73:90–97.
Fenno LE, Mattis J, Ramakrishnan C, Hyun M, Lee SY, He M, Tucciarone J, Selimbeyoglu A, Berndt A, Grosenick L, Zalocusky KA, Bernstein H, Swanson H, Perry C, Diester I, Boyce FM, Bass CE, Neve R, Huang ZJ, Deisseroth K. 2014. INTRSECT: single-component targeting of cells using multiple-feature Boolean logic. Nat Methods. 11:763–772.
Férézou I, Cauli B, Hill EL, Rossier J, Hamel E, Lambolez B. 2002. 5-HT3 Receptors Mediate Serotonergic Fast Synaptic Excitation of Neocortical Vasoactive Intestinal Peptide/Cholecystokinin Interneurons. J Neurosci. 22:7389–7397.
Finnegan KT, DeLanney LE, Irwin I, Ricaurte GA, Langston JW. 1989. The amine-depleting effects of 5,7-dihydroxytryptamine (5,7-DHT) in C57BL/6 mice do not increase with age. Brain Res. 496:251–256.
Fletcher PJ, Selhi ZF, Azampanah A, Sills TL. 2001. Reduced Brain Serotonin Activity Disrupts Prepulse Inhibition of the Acoustic Startle Reflex: Effects of 5,7-dihydroxytryptamine and p -chlorophenylalanine. Neuropsychopharmacology. 24:399–409.
Font C, Martínez-Marcos A, Lanuza E, Hoogland PV, Martínez-García F. 1997. Septal complex of the telencephalon of the lizard Podarcis hispanica. II. Afferent connections. J Comp Neurol. 383:489–511.

Franklin K, Paxinos G. 2008. The Mouse Brain in Stereotaxic Coordinates, Compact. 3rd ed. Academic Press-Elsevier.
Fremeau RT, Voglmaier S, Seal RP, Edwards RH. 2004. VGLUTs define subsets of excitatory neurons and suggest novel roles for glutamate. Trends Neurosci. 27:98–103.
Freund TF, Gulyás AI, Acsády L, Görcs T, Tóth K. 1990. Serotonergic control of the hippocampus via local inhibitory interneurons. Proc Natl Acad Sci U S A. 87:8501–8505.
Frigault MM, Lacoste J, Swift JL, Brown CM. 2009. Live-cell microscopy - tips and tools. J Cell Sci. 122:753–767.
Fyodorov D, Nelson T, Deneris E. 1998. Pet-1, a novel ETS domain factor that can activate neuronal nAchR gene transcription. J Neurobiol. 34:151–163.
Gall C, Moore RY. 1984. Distribution of enkephalin, substance P, tyrosine hydroxylase, and 5-hydroxytryptamine immunoreactivity in the septal region of the rat. J Comp Neurol. 225:212–227.
Gaspar P, Lillesaar C. 2012. Probing the diversity of serotonin neurons. Philos Trans R Soc Lond B Biol Sci. 367:2382–2394.
Geyer MA, McIlwain KL, Paylor R. 2002. Mouse genetic models for prepulse inhibition: an early review. Mol Psychiatry. 7:1039–1053.
Glass JD, Grossman GH, Farnbauch L, DiNardo L. 2003. Midbrain Raphe Modulation of Nonphotic Circadian Clock Resetting and 5-HT Release in the Mammalian Suprachiasmatic Nucleus. J Neurosci. 23:7451–7460.
Goodson JL, Evans AK, Lindberg L. 2004. Chemoarchitectonic subdivisions of the songbird septum and a comparative overview of septum chemical anatomy in jawed vertebrates. J Comp Neurol. 473:293–314.
Goodwin PC. 2013. Chapter 15 - Evaluating Optical Aberrations Using Fluorescent Microspheres: Methods, Analysis, and Corrective Actions. In: Sluder G,, Wolf DE, editors. Methods in Cell Biology. Digital Microscopy. Academic Press. p. 369–385.
Gras C, Amilhon B, Lepicard ÈM, Poirel O, Vinatier J, Herbin M, Dumas S, Tzavara ET, Wade MR, Nomikos GG, Hanoun N, Saurini F, Kemel M-L, Gasnier B, Giros B, Mestikawy SE. 2008. The vesicular glutamate transporter VGLUT3 synergizes striatal acetylcholine tone. Nat Neurosci. 11:292–300.
Grillon C, Morgan CA, Southwick SM, Davis M, Charney DS. 1996. Baseline startle amplitude and prepulse inhibition in Vietnam veterans with posttraumatic stress disorder. Psychiatry Res. 64:169–178.
Guo J, Luo X, Li B, Chang Q, Sun L, Song Y. 2020. Abnormal modulation of theta oscillations in children with attention-deficit/hyperactivity disorder. NeuroImage Clin. 27.
Gutiérrez-Guzmán BE, Hernández-Pérez JJ, Olvera-Cortés ME. 2017. Serotonergic modulation of septo-hippocampal and septo-mammillary theta activity during spatial learning, in the rat. Behav Brain Res. 319:73–86.
Hagan CE, McDevitt RA, Liu Y, Furay AR, Neumaier JF. 2012. 5-HT1B autoreceptor regulation of serotonin transporter activity in synaptosomes. Synap N Y N. 66:1024–1034.
Hakvoort Schwerdtfeger RM, Menard JL. 2008. The lateral hypothalamus and anterior hypothalamic nucleus differentially contribute to rats' defensive responses in the elevated plus-maze and shock-probe burying tests. Physiol Behav. 93:697–705.

Halasy K, Miettinen R, Szabat E, Freund TF. 1992. GABAergic Interneurons are the Major Postsynaptic Targets of Median Raphe Afferents in the Rat Dentate Gyrus. Eur J Neurosci. 4:144–153.
Hale MW, Shekhar A, Lowry CA. 2011. Development by environment interactions controlling tryptophan hydroxylase expression. J Chem Neuroanat. 41:219–226.
Halliday GM, Li YW, Joh TH, Cotton RG, Howe PR, Geffen LB, Blessing WW. 1988. Distribution of monoamine-synthesizing neurons in the human medulla oblongata. J Comp Neurol. 273:301–317.
Hammer M, Huisman M, Rigano A, Boehm U, Chambers JJ, Gaudreault N, North AJ, Pimentel JA, Sudar D, Bajcsy P, Brown CM, Corbett AD, Faklaris O, Lacoste J, Laude A, Nelson G, Nitschke R, Farzam F, Smith CS, Grunwald D, Strambio-De-Castillia C. 2021. Towards community-driven metadata standards for light microscopy: tiered specifications extending the OME model. bioRxiv. 2021.04.25.441198.
Hannon J, Hoyer D. 2008. Molecular biology of 5-HT receptors. Behav Brain Res, Serotonin and cognition: mechanisms and applications. 195:198–213.
Harris KD, Hochgerner H, Skene NG, Magno L, Katona L, Gonzales CB, Somogyi P, Kessaris N, Linnarsson S, Hjerling-Leffler J. 2018. Classes and continua of hippocampal CA1 inhibitory neurons revealed by single-cell transcriptomics. PLOS Biol. 16:e2006387.
Hasen NS, Gammie SC. 2005. Differential fos activation in virgin and lactating mice in response to an intruder. Physiol Behav. 84:681–695.
Hasselmo ME. 2005. What is the function of hippocampal theta rhythm?--Linking behavioral data to phasic properties of field potential and unit recording data. Hippocampus. 15:936–949.
Heddleston JM, Aaron JS, Khuon S, Chew T-L. 2021. A guide to accurate reporting in digital image acquisition – can anyone replicate your microscopy data? J Cell Sci. 134.
Hendricks TJ, Fyodorov DV, Wegman LJ, Lelutiu NB, Pehek EA, Yamamoto B, Silver J, Weeber EJ, Sweatt JD, Deneris ES. 2003. Pet-1 ETS Gene Plays a Critical Role in 5-HT Neuron Development and Is Required for Normal Anxiety-like and Aggressive Behavior. Neuron. 37:233–247.
Heppert JK, Dickinson DJ, Pani AM, Higgins CD, Steward A, Ahringer J, Kuhn JR, Goldstein B. 2016. Comparative assessment of fluorescent proteins for in vivo imaging in an animal model system. Mol Biol Cell. 27:3385–3394.
Herman MA, Trimbuch T, Rosenmund C. 2018. Differential pH Dynamics in Synaptic Vesicles From Intact Glutamatergic and GABAergic Synapses. Front Synaptic Neurosci. 10.
Herzog E, Gilchrist J, Gras C, Muzerelle A, Ravassard P, Giros B, Gaspar P, El Mestikawy S. 2004. Localization of VGLUT3, the vesicular glutamate transporter type 3, in the rat brain. Neuroscience. 123:983–1002.
Hioki H, Fujiyama F, Nakamura K, Wu S-X, Matsuda W, Kaneko T. 2004. Chemically Specific Circuit Composed of Vesicular Glutamate Transporter 3- and Preprotachykinin B-producing Interneurons in the Rat Neocortex. Cereb Cortex. 14:1266–1275.
Hioki H, Nakamura H, Ma Y-F, Konno M, Hayakawa T, Nakamura KC, Fujiyama F, Kaneko T. 2010. Vesicular glutamate transporter 3-expressing nonserotonergic projection neurons constitute a subregion in the rat midbrain raphe nuclei. J Comp Neurol. 518:668–686.

Hitchcock LN, Lattal KM. 2018. Involvement of the dorsal hippocampus in expression and extinction of cocaine-induced conditioned place preference. Hippocampus. 28:226–238.
Hodgson L, Shen F, Hahn K. 2010. Biosensors for Characterizing the Dynamics of Rho Family GTPases in Living Cells. Curr Protoc Cell Biol. 46:14.11.1-14.11.26.
Hoebe RA, Van der Voort HTM, Stap J, Van Noorden CJF, Manders EMM. 2008. Quantitative determination of the reduction of phototoxicity and photobleaching by controlled light exposure microscopy. J Microsc. 231:9–20.
Holschbach MA, Vitale EV, Lonstein JS. 2018. Serotonin-specific lesions of the dorsal raphe disrupt maternal aggression and caregiving in postpartum rats. Behav Brain Res. 348:53–64.
Hornung J-P. 2003. The human raphe nuclei and the serotonergic system. J Chem Neuroanat. 26:331–343.
Hornung JP, Celio MR. 1992. The selective innervation by serotoninergic axons of calbindin-containing interneurons in the neocortex and hippocampus of the marmoset. J Comp Neurol. 320:457–467.
Hornung JP, Fritschy JM, Törk I. 1990. Distribution of two morphologically distinct subsets of serotoninergic axons in the cerebral cortex of the marmoset. J Comp Neurol. 297:165–181.
Hsiao Y-T, Yi P-L, Cheng C-H, Chang F-C. 2013. Disruption of footshock-induced theta rhythms by stimulating median raphe nucleus reduces anxiety in rats. Behav Brain Res. 247:193–200.
Huh CYL, Goutagny R, Williams S. 2010. Glutamatergic Neurons of the Mouse Medial Septum and Diagonal Band of Broca Synaptically Drive Hippocampal Pyramidal Cells: Relevance for Hippocampal Theta Rhythm. J Neurosci. 30:15951–15961.
Hutchison IC, Rathore S. 2015. The role of REM sleep theta activity in emotional memory. Front Psychol. 6:1439.
Icha J, Weber M, Waters JC, Norden C. 2017. Phototoxicity in live fluorescence microscopy, and how to avoid it. BioEssays. 39:1700003.
Ichikawa R, Yamasaki M, Miyazaki T, Konno K, Hashimoto K, Tatsumi H, Inoue Y, Kano M, Watanabe M. 2011. Developmental Switching of Perisomatic Innervation from Climbing Fibers to Basket Cell Fibers in Cerebellar Purkinje Cells. J Neurosci. 31:16916–16927.
Iwasaki K, Komiya H, Kakizaki M, Miyoshi C, Abe M, Sakimura K, Funato H, Yanagisawa M. 2018. Ablation of Central Serotonergic Neurons Decreased REM Sleep and Attenuated Arousal Response. Front Neurosci. 12.
Iyer A, Tole S. 2020. Neuronal diversity and reciprocal connectivity between the vertebrate hippocampus and septum. WIREs Dev Biol. 9:e370.
Jaako K, Aonurm-Helm A, Kalda A, Anier K, Zharkovsky T, Shastin D, Zharkovsky A. 2011. Repeated citalopram administration counteracts kainic acid-induced spreading of PSA-NCAM-immunoreactive cells and loss of reelin in the adult mouse hippocampus. Eur J Pharmacol. 666:61–71.
Jaako K, Zharkovsky T, Zharkovsky A. 2009. Effects of repeated citalopram treatment on kainic acid-induced neurogenesis in adult mouse hippocampus. Brain Res. 1288:18–28.
Jackson J, Bland BH, Antle MC. 2009. Nonserotonergic projection neurons in the midbrain raphe nuclei contain the vesicular glutamate transporter VGLUT3. Synapse. 63:31–41.

Jackson J, Dickson CT, Bland BH. 2008. Median Raphe Stimulation Disrupts Hippocampal Theta Via Rapid Inhibition and State-Dependent Phase Reset of Theta-Related Neural Circuitry. J Neurophysiol. 99:3009–3026.
Jacobs BL, Azmitia EC. 1992. Structure and function of the brain serotonin system. Physiol Rev. 72:165–229.
Jacobsen KX, Czesak M, Deria M, Le François B, Albert PR. 2011. Region-specific regulation of 5-HT1A receptor expression by Pet-1-dependent mechanisms in vivo. J Neurochem. 116:1066–1076.
Jakab RL, Leranth C. 1995. Septum. In: The Rat Nervous System. 2nd ed.
Janzsó G, Valcz G, Thuma Á, Szőke B, Lendvai Z, Ábrahám H, Kozicz T, Halasy K. 2010. Cocaine- and amphetamine-regulated transcript (CART) peptide- immunopositive neuronal elements in the lateral septum: Rostrocaudal distribution in the male rat. Brain Res. 1362:40–47.
Jensen P, Farago AF, Awatramani RB, Scott MM, Deneris ES, Dymecki SM. 2008. Redefining the serotonergic system by genetic lineage. Nat Neurosci. 11:417–419.
Jerome J. 2001. Protein Localization by Fluorescence Microscopy: A Practical Approach Edited by Victoria J. Allan. 2000. Oxford University Press, New York, NY. 256 pages. (paperback $55). Microsc Microanal. 7:370–371.
Jin Y, Lim C-M, Kim S-W, Park J-Y, Seo J-S, Han P-L, Yoon SH, Lee J-K. 2009. Fluoxetine attenuates kainic acid-induced neuronal cell death in the mouse hippocampus. Brain Res. 1281:108–116.
Johnson MD. 1994. Synaptic glutamate release by postnatal rat serotonergic neurons in microculture. Neuron. 12:433–442.
Jonkman J, Brown CM, Wright GD, Anderson KI, North AJ. 2020. Guidance for quantitative confocal microscopy. Nat Protoc. 1–1.
Jost AP-T, Waters JC. 2019. Designing a rigorous microscopy experiment: Validating methods and avoiding bias. J Cell Biol. 218:1452–1466.
Keller HE. 2006. Objective Lenses for Confocal Microscopy. In: Pawley JB, editor. Handbook Of Biological Confocal Microscopy. Boston, MA: Springer US. p. 145–161.
Kelley SP, Bratt AM, Hodge CW. 2003. Targeted gene deletion of the 5-HT3A receptor subunit produces an anxiolytic phenotype in mice. Eur J Pharmacol. 461:19–25.
Kelsch W, Lin C-W, Lois C. 2008. Sequential development of synapses in dendritic domains during adult neurogenesis. Proc Natl Acad Sci U S A. 105:16803–16808.
Keynes R, Lumsden A. 1990. Segmentation and the origin of regional diversity in the vertebrate central nervous system. Neuron. 4:1–9.
Khakpai F, Nasehi M, Haeri-Rohani A, Eidi A, Zarrindast MR. 2013. Septo-Hippocampo-Septal Loop and Memory Formation. Basic Clin Neurosci. 4:5–23.
Kiepas A, Voorand E, Mubaid F, Siegel PM, Brown CM. 2020. Optimizing live-cell fluorescence imaging conditions to minimize phototoxicity. J Cell Sci. 133.
Kim JC, Cook MN, Carey MR, Shen C, Regehr WG, Dymecki SM. 2009. Linking Genetically Defined Neurons to Behavior through a Broadly Applicable Silencing Allele. Neuron. 63:305–315.

Kimmel RA, Turnbull DH, Blanquet V, Wurst W, Loomis CA, Joyner AL. 2000. Two lineage boundaries coordinate vertebrate apical ectodermal ridge formation. Genes Dev. 14:1377–1389.
Kind PC, Sengpiel F, Beaver CJ, Crocker-Buque A, Kelly GM, Matthews RT, Mitchell DE. 2013. The development and activity-dependent expression of aggrecan in the cat visual cortex. Cereb Cortex N Y N 1991. 23:349–360.
Kinney GG, Kocsis B, Vertes RP. 1996. Medial septal unit firing characteristics following injections of 8-OH-DPAT into the median raphe nucleus. Brain Res. 708:116–122.
Kiyasova V, Gaspar P. 2011. Development of raphe serotonin neurons from specification to guidance. Eur J Neurosci. 34:1553–1562.
Klausberger T, Marton LF, O'Neill J, Huck JHJ, Dalezios Y, Fuentealba P, Suen WY, Papp E, Kaneko T, Watanabe M, Csicsvari J, Somogyi P. 2005. Complementary Roles of Cholecystokinin- and Parvalbumin-Expressing GABAergic Neurons in Hippocampal Network Oscillations. J Neurosci. 25:9782–9793.
Klausberger T, Somogyi P. 2008. Neuronal Diversity and Temporal Dynamics: The Unity of Hippocampal Circuit Operations. Science. 321:53–57.
Kocsis B, Varga V, Dahan L, Sik A. 2006. Serotonergic neuron diversity: Identification of raphe neurons with discharges time-locked to the hippocampal theta rhythm. Proc Natl Acad Sci. 103:1059–1064.
Köhler C, Chan-Palay V, Steinbusch H. 1982. The distribution and origin of serotonin-containing fibers in the septal area: a combined immunohistochemical and fluorescent retrograde tracing study in the rat. J Comp Neurol. 209:91–111.
Kondo M, Nakamura Y, Ishida Y, Yamada T, Shimada S. 2013. The 5-HT3A receptor is essential for fear extinction. Learn Mem. 21:740–743.
Kosofsky BE, Molliver ME. 1987. The serotoninergic innervation of cerebral cortex: Different classes of axon terminals arise from dorsal and median raphe nuclei. Synapse. 1:153–168.
Koyama Y, Kondo M, Shimada S. 2017. Building a 5-HT3A Receptor Expression Map in the Mouse Brain. Sci Rep. 7:42884.
Kraus B, Ziegler M, Wolff H. 2007. Modern research and educational topics in microscopy, Formatex microscopy series. Badajoz, Spain: Formatex.
Kunis S, Hänsch S, Schmidt C, Wong F, Weidtkamp-Peters S. 2021. OMERO.mde in a use case for microscopy metadata harmonization: Facilitating FAIR principles in practical application with metadata annotation tools. ArXiv210302942 Cs Q-Bio.
Lambert TJ. 2019. FPbase: a community-editable fluorescent protein database. Nat Methods. 16:277–278.
Lambert TJ, Waters JC. 2014. Assessing camera performance for quantitative microscopy. Methods Cell Biol. 123:35–53.
Landgraf D, Okumus B, Chien P, Baker TA, Paulsson J. 2012. Segregation of molecules at cell division reveals native protein localization. Nat Methods. 9:480–482.
Lee J-Y, Kitaoka M. 2018. A beginner's guide to rigor and reproducibility in fluorescence imaging experiments. Mol Biol Cell. 29:1519–1525.

Lee S, Hjerling-Leffler J, Zagha E, Fishell G, Rudy B. 2010. The largest group of superficial neocortical GABAergic interneurons expresses ionotropic serotonin receptors. J Neurosci Off J Soc Neurosci. 30:16796–16808.
Lee SY, Soltesz I. 2011. Cholecystokinin: A multi-functional molecular switch of neuronal circuits. Dev Neurobiol. 71:83–91.
Leger L, Charnay Y, Hof PR, Bouras C, Cespuglio R. 2001. Anatomical distribution of serotonin-containing neurons and axons in the central nervous system of the cat. J Comp Neurol. 433:157–182.
Lewandoski M, Meyers EN, Martin GR. 1997. Analysis of Fgf8 gene function in vertebrate development. Cold Spring Harb Symp Quant Biol. 62:159–168.
Li L, Tasic B, Micheva KD, Ivanov VM, Spletter ML, Smith SJ, Luo L. 2010. Visualizing the Distribution of Synapses from Individual Neurons in the Mouse Brain. PLOS ONE. 5:e11503.
Li L-B, Zhang L, Sun Y-N, Han L-N, Wu Z-H, Zhang Q-J, Liu J. 2015. Activation of serotonin2A receptors in the medial septum-diagonal band of Broca complex enhanced working memory in the hemiparkinsonian rats. Neuropharmacology. 91:23–33.
Lidov HG, Molliver ME. 1982. Immunohistochemical study of the development of serotonergic neurons in the rat CNS. Brain Res Bull. 9:559–604.
Liu C, Maejima T, Wyler SC, Casadesus G, Herlitze S, Deneris ES. 2010. Pet-1 is required across different stages of life to regulate serotonergic function. Nat Neurosci. 13:1190–1198.
Liu L, Wang L, Cao C, Cao X, Zhu Y, Liu P, Luo S, Zhang J. 2018. Serotonin transporter 5-HTTLPR genotype is associated with intrusion and avoidance symptoms of DSM-5 posttraumatic stress disorder (PTSD) in Chinese earthquake survivors. Anxiety Stress Coping. 31:318–327.
Liu Z, Zhou J, Li Y, Hu F, Lu Y, Ma M, Feng Q, Zhang J, Wang D, Zeng J, Bao J, Kim J-Y, Chen Z-F, El Mestikawy S, Luo M. 2014. Dorsal Raphe Neurons Signal Reward through 5-HT and Glutamate. Neuron. 81:1360–1374.
Ljungdahl Å, Hökfelt T, Nilsson G, Goldstein M. 1978. Distribution of substance P-like immunoreactivity in the central nervous system of the rat—II. Light microscopic localization in relation to catecholamine-containing neurons. Neuroscience. 3:945–976.
Lonstein JS, Gréco B, Vries GJD, Stern JM, Blaustein JD. 2000. Maternal Behavior Stimulates c-fos Activity within Estrogen Receptor Alpha-Containing Neurons in Lactating Rats. Neuroendocrinology. 72:91–101.
Luiten PG, Kuipers F, Schuitmaker H. 1982. Organization of diencephalic and brainstem afferent projections to the lateral septum in the rat. Neurosci Lett. 30:211–216.
Lumsden A. 1990. The cellular basis of segmentation in the developing hindbrain. Trends Neurosci. 13:329–335.
Lumsden A, Krumlauf R. 1996. Patterning the Vertebrate Neuraxis. Science. 274:1109–1115.
Lyon KA, Rood BD, Wu L, Senft RA, Goodrich LV, Dymecki SM. 2020. Sex-specific role for dopamine receptor D2 in dorsal raphe serotonergic neuron modulation of defensive acoustic startle and dominance behavior. eNeuro.
Maddaloni G, Bertero A, Pratelli M, Barsotti N, Boonstra A, Giorgi A, Migliarini S, Pasqualetti M. 2017. Development of Serotonergic Fibers in the Post-Natal Mouse Brain. Front Cell Neurosci. 11.

Madisen L, Garner AR, Shimaoka D, Chuong AS, Klapoetke NC, Li L, van der Bourg A, Niino Y, Egolf L, Monetti C, Gu H, Mills M, Cheng A, Tasic B, Nguyen TN, Sunkin SM, Benucci A, Nagy A, Miyawaki A, Helmchen F, Empson RM, Knöpfel T, Boyden ES, Reid RC, Carandini M, Zeng H. 2015. Transgenic mice for intersectional targeting of neural sensors and effectors with high specificity and performance. Neuron. 85:942–958.

Madisen L, Mao T, Koch H, Zhuo J, Berenyi A, Fujisawa S, Hsu Y-WA, Iii AJG, Gu X, Zanella S, Kidney J, Gu H, Mao Y, Hooks BM, Boyden ES, Buzsáki G, Ramirez JM, Jones AR, Svoboda K, Han X, Turner EE, Zeng H. 2012. A toolbox of Cre-dependent optogenetic transgenic mice for light-induced activation and silencing. Nat Neurosci. 15:793–802.

Magidson V, Khodjakov A. 2013. Circumventing photodamage in live-cell microscopy. Methods Cell Biol. 114:545–560.

Maia GH, Brazete CS, Soares JI, Luz LL, Lukoyanov NV. 2017. Serotonin depletion increases seizure susceptibility and worsens neuropathological outcomes in kainate model of epilepsy. Brain Res Bull. 134:109–120.

Mann C, Croft RJ, Scholes KE, Dunne A, O'Neill BV, Leung S, Copolov D, Phan KL, Nathan PJ. 2008. Differential Effects of Acute Serotonin and Dopamine Depletion on Prepulse Inhibition and P50 Suppression Measures of Sensorimotor and Sensory Gating in Humans. Neuropsychopharmacology. 33:1653–1666.

Manseau F, Goutagny R, Danik M, Williams S. 2008. The Hippocamposeptal Pathway Generates Rhythmic Firing of GABAergic Neurons in the Medial Septum and Diagonal Bands: An Investigation Using a Complete Septohippocampal Preparation In Vitro. J Neurosci. 28:4096–4107.

Marin-Padilla M. 1969. Origin of the pericellular baskets of the pyramidal cells of the human motor cortex: A golgi study. Brain Res. 14:633–646.

Marin-Padilla M. 1974. Three-dimensional reconstruction of the pericellular nests (baskets) of the motor (area 4) and visual (area 17) areas of the human cerebral cortex: A Golgi study. Z Für Anat Entwicklungsgeschichte. 144:123–135.

Marques CM, Caboclo LOSF, da Silva TI, Noffs MH da S, Carrete H, Lin K, Lin J, Sakamoto AC, Yacubian EMT. 2007. Cognitive decline in temporal lobe epilepsy due to unilateral hippocampal sclerosis. Epilepsy Behav EB. 10:477–485.

Marqués G, Pengo T, Sanders MA. 2020. Imaging methods are vastly underreported in biomedical research. eLife. 9:e55133.

Marvin JS, Borghuis BG, Tian L, Cichon J, Harnett MT, Akerboom J, Gordus A, Renninger SL, Chen T-W, Bargmann CI, Orger MB, Schreiter ER, Demb JB, Gan W-B, Hires SA, Looger LL. 2013. An optimized fluorescent probe for visualizing glutamate neurotransmission. Nat Methods. 10:162.

Matthews RT, Kelly GM, Zerillo CA, Gray G, Tiemeyer M, Hockfield S. 2002. Aggrecan glycoforms contribute to the molecular heterogeneity of perineuronal nets. J Neurosci Off J Soc Neurosci. 22:7536–7547.

McKay IJ, Muchamore I, Krumlauf R, Maden M, Lumsden A, Lewis J. 1994. The kreisler mouse: a hindbrain segmentation mutant that lacks two rhombomeres. Development. 120:2199–2211.

McKendrick G, Graziane NM. 2020. Drug-Induced Conditioned Place Preference and Its Practical Use in Substance Use Disorder Research. Front Behav Neurosci. 14.

McKenna JT, Vertes RP. 2001. Collateral projections from the median raphe nucleus to the medial septum and hippocampus. Brain Res Bull. 54:619–630.
Mena A, Ruiz-Salas JC, Puentes A, Dorado I, Ruiz-Veguilla M, De la Casa LG. 2016. Reduced Prepulse Inhibition as a Biomarker of Schizophrenia. Front Behav Neurosci. 10.
Meneses A. 2015. Serotonin, neural markers, and memory. Front Pharmacol. 6.
Meyer-Bernstein L, Morin P. 1996. Differential Serotonergic Innervation of the Suprachiasmatic Nucleus and the lntergeniculate Leaflet and its Role in Circadian Rhythm Modulation. J Neurosci. 15.
Miles R, Tóth K, Gulyás AI, Hájos N, Freund TF. 1996. Differences between somatic and dendritic inhibition in the hippocampus. Neuron. 16:815–823.
Mische SM, Fisher NC, Meyn SM, Sol-Church K, Hegstad-Davies RL, Weis-Garcia F, Adams M, Ashton JM, Delventhal KM, Dragon JA, Holmes L, Jagtap P, Kubow KE, Mason CE, Palmblad M, Searle BC, Turck CW, Knudtson KL. 2020. A Review of the Scientific Rigor, Reproducibility, and Transparency Studies Conducted by the ABRF Research Groups. J Biomol Tech JBT. 31:11–26.
Mitra SW, Hoskin E, Yudkovitz J, Pear L, Wilkinson HA, Hayashi S, Pfaff DW, Ogawa S, Rohrer SP, Schaeffer JM, McEwen BS, Alves SE. 2003. Immunolocalization of Estrogen Receptor β in the Mouse Brain: Comparison with Estrogen Receptor α. Endocrinology. 144:2055–2067.
Miura K, Nørrelykke SF. 2021. Reproducible image handling and analysis. EMBO J. 40:e105889.
Model MA. 2006. Intensity calibration and shading correction for fluorescence microscopes. Curr Protoc Cytom. Chapter 10:Unit10.14.
Model MA, Blank JL. 2008. Concentrated dyes as a source of two-dimensional fluorescent field for characterization of a confocal microscope. J Microsc. 229:12–16.
Montecinos-Franjola F, Bauer BL, Mears JA, Ramachandran R. 2020. GFP fluorescence tagging alters dynamin-related protein 1 oligomerization dynamics and creates disassembly-refractory puncta to mediate mitochondrial fission. Sci Rep. 10:14777.
Morecraft RJ, Ugolini G, Lanciego JL, Wouterlood FG, Pandya DN. 2014. Chapter 17 - Classic and Contemporary Neural Tract-Tracing Techniques. In: Johansen-Berg H,, Behrens TEJ, editors. Diffusion MRI (Second Edition). San Diego: Academic Press. p. 359–399.
Morikawa S, Ikegaya Y, Narita M, Tamura H. 2017. Activation of perineuronal net-expressing excitatory neurons during associative memory encoding and retrieval. Sci Rep. 7:46024.
Morin LP, Meyer-Bernstein EL. 1999. The ascending serotonergic system in the hamster: comparison with projections of the dorsal and median raphe nuclei. Neuroscience. 91:81–105.
Mubaid F, Kaufman D, Wee T-L, Nguyen-Huu D-S, Young D, Anghelopoulou M, Brown CM. 2019. Fluorescence microscope light source stability. Histochem Cell Biol. 151:357–366.
Mukhopadhyay S, Chatterjee A, Tiwari P, Ghai U, Vaidya VA. 2021. Postnatal Fluoxetine Treatment Alters Perineuronal Net Formation and Maintenance in the Hippocampus. eNeuro. 8.
Munn RGK, Tyree SM, McNaughton N, Bilkey DK. 2015. The frequency of hippocampal theta rhythm is modulated on a circadian period and is entrained by food availability. Front Behav Neurosci. 9:61.

Murphy DB, Davidson MW. 2012. Fundamentals of Light Microscopy and Electronic Imaging. Second. ed. John Wiley & Sons, Ltd.

Muzerelle A, Soiza-Reilly M, Hainer C, Ruet P-L, Lesch K-P, Bader M, Alenina N, Scotto-Lomassese S, Gaspar P. 2021. Dorsal raphe serotonin neurotransmission is required for the expression of nursing behavior and for pup survival. Sci Rep. 11:6004.

Nelson G, Boehm U, Bagley S, Bajcsy P, Bischof J, Brown CM, Dauphin A, Dobbie IM, Eriksson JE, Faklaris O, Fernandez-Rodriguez J, Ferrand A, Gelman L, Gheisari A, Hartmann H, Kukat C, Laude A, Mitkovski M, Munck S, North AJ, Rasse TM, Resch-Genger U, Schuetz LC, Seitz A, Strambio-De-Castillia C, Swedlow JR, Alexopoulos I, Aumayr K, Avilov S, Bakker G-J, Bammann RR, Bassi A, Beckert H, Beer S, Belyaev Y, Bierwagen J, Birngruber KA, Bosch M, Breitlow J, Cameron LA, Chalfoun J, Chambers JJ, Chen C-L, Conde-Sousa E, Corbett AD, Cordelieres FP, Del Nery E, Dietzel R, Eismann F, Fazeli E, Felscher A, Fried H, Gaudreault N, Goh WI, Guilbert T, Hadleigh R, Hemmerich P, Holst GA, Itano MS, Jaffe CB, Jambor HK, Jarvis SC, Keppler A, Kirchenbuechler D, Kirchner M, Kobayashi N, Krens G, Kunis S, Lacoste J, Marcello M, Martins GG, Metcalf DJ, Mitchell CA, Moore J, Mueller T, Nelson MS, Ogg S, Onami S, Palmer AL, Paul-Gilloteaux P, Pimentel JA, Plantard L, Podder S, Rexhepaj E, Royon A, Saari MA, Schapman D, Schoonderwoert V, Schroth-Diez B, Schwartz S, Shaw M, Spitaler M, Stoeckl MT, Sudar D, Teillon J, Terjung S, Thuenauer R, Wilms CD, Wright GD, Nitschke R. 2021. QUAREP-LiMi: A community-driven initiative to establish guidelines for quality assessment and reproducibility for instruments and images in light microscopy. ArXiv210109153 Phys Q-Bio.

Nelson RJ, Trainor BC. 2007. Neural mechanisms of aggression. Nat Rev Neurosci. 8:536–546.

Niederkofler V, Asher TE, Dymecki SM. 2015. Functional Interplay between Dopaminergic and Serotonergic Neuronal Systems during Development and Adulthood. ACS Chem Neurosci. 6:1055–1070.

Niederkofler V, Asher TE, Okaty BW, Rood BD, Narayan A, Hwa LS, Beck SG, Miczek KA, Dymecki SM. 2016. Identification of Serotonergic Neuronal Modules that Affect Aggressive Behavior. Cell Rep. 17:1934–1949.

Nishigaki T, Wood CD, Shiba K, Baba SA, Darszon A. 2006. Stroboscopic illumination using light-emitting diodes reduces phototoxicity in fluorescence cell imaging. BioTechniques. 41:191–197.

Nishimaru H, Restrepo CE, Ryge J, Yanagawa Y, Kiehn O. 2005. Mammalian motor neurons corelease glutamate and acetylcholine at central synapses. Proc Natl Acad Sci. 102:5245–5249.

North AJ. 2006. Seeing is believing? A beginners' guide to practical pitfalls in image acquisition. J Cell Biol. 172:9–18.

Oh SW, Harris JA, Ng L, Winslow B, Cain N, Mihalas S, Wang Q, Lau C, Kuan L, Henry AM, Mortrud MT, Ouellette B, Nguyen TN, Sorensen SA, Slaughterbeck CR, Wakeman W, Li Y, Feng D, Ho A, Nicholas E, Hirokawa KE, Bohn P, Joines KM, Peng H, Hawrylycz MJ, Phillips JW, Hohmann JG, Wohnoutka P, Gerfen CR, Koch C, Bernard A, Dang C, Jones AR, Zeng H. 2014. A mesoscale connectome of the mouse brain. Nature. 508:207–214.

Ohmura Y, Izumi T, Yamaguchi T, Tsutsui-Kimura I, Yoshida T, Yoshioka M. 2010. The Serotonergic Projection from the Median Raphe Nucleus to the Ventral Hippocampus is

Involved in the Retrieval of Fear Memory Through the Corticotropin-Releasing Factor Type 2 Receptor. Neuropsychopharmacology. 35:1271–1278.
Okaty BW, Commons KG, Dymecki SM. 2019. Embracing diversity in the 5-HT neuronal system. Nat Rev Neurosci. 20:397–424.
Okaty BW, Freret ME, Rood BD, Brust RD, Hennessy ML, deBairos D, Kim JC, Cook MN, Dymecki SM. 2015. Multi-Scale Molecular Deconstruction of the Serotonin Neuron System. Neuron. 88:774–791.
Okaty BW, Sturrock N, Escobedo Lozoya Y, Chang Y, Senft RA, Lyon KA, Alekseyenko OV, Dymecki SM. 2020. A single-cell transcriptomic and anatomic atlas of mouse dorsal raphe Pet1 neurons. eLife. 9.
Olson L, Seiger A. 1972. Early prenatal ontogeny of central monoamine neurons in the rat: fluorescence histochemical observations. Z Anat Entwicklungsgesch. 137:301–316.
Olucha-Bordonau FE, Otero-García M, Sánchez-Pérez AM, Núñez A, Ma S, Gundlach AL. 2012. Distribution and targets of the relaxin-3 innervation of the septal area in the rat. J Comp Neurol. 520:1903–1939.
Olvera-Cortés ME, Gutiérrez-Guzmán BE, López-Loeza E, Hernández-Pérez JJ, López-Vázquez MÁ. 2013. Serotonergic modulation of hippocampal theta activity in relation to hippocampal information processing. Exp Brain Res. 230:407–426.
Onukwufor JO, Trewin AJ, Baran TM, Almast A, Foster TH, Wojtovich AP. 2020. Quantification of reactive oxygen species production by the red fluorescent proteins KillerRed, SuperNova and mCherry. Free Radic Biol Med. 147:1–7.
Palacios JM, Pazos A, Hoyer D. 2017. A short history of the 5-HT2C receptor: from the choroid plexus to depression, obesity and addiction treatment. Psychopharmacology (Berl). 234:1395–1418.
Papp EC, Hájos N, Acsády L, Freund TF. 1999. Medial septal and median raphe innervation of vasoactive intestinal polypeptide-containing interneurons in the hippocampus. Neuroscience. 90:369–382.
Parsons SM. 2000. Transport mechanisms in acetylcholine and monoamine storage. FASEB J Off Publ Fed Am Soc Exp Biol. 14:2423–2434.
Paspalas CD, Papadopoulos GC. 1999. Noradrenergic Innervation of Peptidergic Interneurons in the Rat Visual Cortex. Cereb Cortex. 9:844–853.
Pasqualetti M, Díaz C, Renaud J-S, Rijli FM, Glover JC. 2007. Fate-Mapping the Mammalian Hindbrain: Segmental Origins of Vestibular Projection Neurons Assessed Using Rhombomere-Specific Hoxa2 Enhancer Elements in the Mouse Embryo. J Neurosci. 27:9670–9681.
Paterak J, Stefański R. 2014. 5,6- and 5,7-Dihydroxytryptamines as Serotoninergic Neurotoxins. In: Kostrzewa RM, editor. Handbook of Neurotoxicity. New York, NY: Springer. p. 299–325.
Patterson GH, Piston DW. 2000. Photobleaching in two-photon excitation microscopy. Biophys J. 78:2159–2162.
Pattyn A, Vallstedt A, Dias JM, Samad OA, Krumlauf R, Rijli FM, Brunet J-F, Ericson J. 2003. Coordinated temporal and spatial control of motor neuron and serotonergic neuron generation from a common pool of CNS progenitors. Genes Dev. 17:729–737.

Pelkey KA, Calvigioni D, Fang C, Vargish G, Ekins T, Auville K, Wester JC, Lai M, Scott CM-G, Yuan X, Hunt S, Abebe D, Xu Q, Dimidschstein J, Fishell G, Chittajallu R, McBain CJ. 2020. Paradoxical network excitation by glutamate release from VGluT3+ GABAergic interneurons [WWW Document]. eLife. URL https://elifesciences.org/articles/51996/figures

Pelkey KA, Chittajallu R, Craig MT, Tricoire L, Wester JC, McBain CJ. 2017. Hippocampal GABAergic Inhibitory Interneurons. Physiol Rev. 97:1619–1747.

Pelosi B, Migliarini S, Pacini G, Pratelli M, Pasqualetti M. 2014. Generation of Pet1210-Cre Transgenic Mouse Line Reveals Non-Serotonergic Expression Domains of Pet1 Both in CNS and Periphery. PLOS ONE. 9:e104318.

Pfaar H, von Holst A, Vogt Weisenhorn DM, Brodski C, Guimera J, Wurst W. 2002. mPet-1, a mouse ETS-domain transcription factor, is expressed in central serotonergic neurons. Dev Genes Evol. 212:43–46.

Phelan KD, Twery MJ, Gallagher JP. 1993. Morphological and electrophysiological evidence for electrotonic coupling of rat dorsolateral septal nucleus neurons in vitro. Synap N Y N. 13:39–49.

Pickavance LC, Staines WA, Fryer JN. 1992. Distributions and colocalization of neuropeptide Y and somatostatin in the goldfish brain. J Chem Neuroanat. 5:221–233.

Pineles SL, Blumenthal TD, Curreri AJ, Nillni YI, Putnam KM, Resick PA, Rasmusson AM, Orr SP. 2016. Prepulse inhibition deficits in women with PTSD. Psychophysiology. 53:1377–1385.

Plummer NW, Evsyukova IY, Robertson SD, de Marchena J, Tucker CJ, Jensen P. 2015. Expanding the power of recombinase-based labeling to uncover cellular diversity. Dev Camb Engl. 142:4385–4393.

Quentin E, Belmer A, Maroteaux L. 2018. Somato-Dendritic Regulation of Raphe Serotonin Neurons; A Key to Antidepressant Action. Front Neurosci. 12:982.

Raghanti MA, Stimpson CD, Marcinkiewicz JL, Erwin JM, Hof PR, Sherwood CC. 2008. Differences in Cortical Serotonergic Innervation among Humans, Chimpanzees, and Macaque Monkeys: A Comparative Study. Cereb Cortex. 18:584–597.

Ray R, Corcoran A, Brust R, Kim JC, Richerson GB, Nattie E, Dymecki SM. 2011. Impaired Respiratory and Body Temperature Control Upon Acute Serotonergic Neuron Inhibition. Science. 333:637–642.

Reigoto AM, Andrade SA, Seixas MCRR, Costa ML, Mermelstein C. 2021. A comparative study on the use of microscopy in pharmacology and cell biology research. PloS One. 16:e0245795.

Ren J, Friedmann D, Xiong J, Liu CD, Ferguson BR, Weerakkody T, DeLoach KE, Ran C, Pun A, Sun Y, Weissbourd B, Neve RL, Huguenard J, Horowitz MA, Luo L. 2018. Anatomically Defined and Functionally Distinct Dorsal Raphe Serotonin Sub-systems. Cell. 175:472-487.e20.

Ren J, Isakova A, Friedmann D, Zeng J, Grutzner SM, Pun A, Zhao GQ, Kolluru SS, Wang R, Lin R, Li P, Li A, Raymond JL, Luo Q, Luo M, Quake SR, Luo L. 2019. Single-cell transcriptomes and whole-brain projections of serotonin neurons in the mouse dorsal and median raphe nuclei. eLife. 8:e49424.

Richerson GB, Buchanan GF. 2011. The serotonin axis: Shared mechanisms in seizures, depression and SUDEP. Epilepsia. 52:28–38.
Riedel A, Westerholz S, Braun K, Edwards RH, Arendt T, Härtig W. 2008. Vesicular glutamate transporter 3-immunoreactive pericellular baskets ensheath a distinct population of neurons in the lateral septum. J Chem Neuroanat. 36:177–190.
Risold PY, Swanson LW. 1997. Connections of the rat lateral septal complex1Published on the World Wide Web on 2 June 1997.1. Brain Res Rev. 24:115–195.
Rohleder C, Wiedermann D, Neumaier B, Drzezga A, Timmermann L, Graf R, Leweke FM, Endepols H. 2016. The Functional Networks of Prepulse Inhibition: Neuronal Connectivity Analysis Based on FDG-PET in Awake and Unrestrained Rats. Front Behav Neurosci. 10:148.
Ross ST, Allen JR, Davidson MW. 2014. Practical considerations of objective lenses for application in cell biology. Methods Cell Biol. 123:19–34.
Ruan H, Saur T, Yao W-D. 2014. Dopamine-enabled anti-Hebbian timing-dependent plasticity in prefrontal circuitry. Front Neural Circuits. 8.
Salazar-Juárez A, Escobar C, Aguilar-Roblero R. 2002. Anterior paraventricular thalamus modulates light-induced phase shifts in circadian rhythmicity in rats. Am J Physiol Regul Integr Comp Physiol. 283:R897-904.
Schäfer MK-H, Varoqui H, Defamie N, Weihe E, Erickson JD. 2002. Molecular cloning and functional identification of mouse vesicular glutamate transporter 3 and its expression in subsets of novel excitatory neurons. J Biol Chem. 277:50734–50748.
Schallier A, Smolders I, Van Dam D, Loyens E, De Deyn PP, Michotte A, Michotte Y, Massie A. 2011. Region- and age-specific changes in glutamate transport in the AβPP23 mouse model for Alzheimer's disease. J Alzheimers Dis JAD. 24:287–300.
Schindelin J, Arganda-Carreras I, Frise E, Kaynig V, Longair M, Pietzsch T, Preibisch S, Rueden C, Saalfeld S, Schmid B, Tinevez J-Y, White DJ, Hartenstein V, Eliceiri K, Tomancak P, Cardona A. 2012. Fiji: an open-source platform for biological-image analysis. Nat Methods. 9:676–682.
Schmidt GW, Cuny AP, Rudolf F. 2020. Preventing Photomorbidity in Long-Term Multi-color Fluorescence Imaging of Saccharomyces cerevisiae and S. pombe. G3 Bethesda Md. 10:4373–4385.
Schneider CA, Rasband WS, Eliceiri KW. 2012. NIH Image to ImageJ: 25 years of image analysis. Nat Methods. 9:671–675.
Schneider-Maunoury S, Topilko P, Seitanidou T, Levi G, Cohen-Tannoudji M, Pournin S, Babinet C, Charnay P. 1993. Disruption of Krox-20 results in alteration of rhombomeres 3 and 5 in the developing hindbrain. Cell. 75:1199–1214.
Sciolino NR, Plummer NW, Chen Y-W, Alexander GM, Robertson SD, Dudek SM, McElligott ZA, Jensen P. 2016. Recombinase-Dependent Mouse Lines for Chemogenetic Activation of Genetically Defined Cell Types. Cell Rep. 15:2563–2573.
Scott MM, Wylie CJ, Lerch JK, Murphy R, Lobur K, Herlitze S, Jiang W, Conlon RA, Strowbridge BW, Deneris ES. 2005. A genetic approach to access serotonin neurons for in vivo and in vitro studies. Proc Natl Acad Sci. 102:16472–16477.

Senft RA, Freret ME, Sturrock N, Dymecki SM. 2021. Neurochemically and hodologically distinct ascending VGLUT3 versus serotonin subsystems comprise the r2-Pet1 median raphe. J Neurosci.

Sengupta A, Bocchio M, Bannerman DM, Sharp T, Capogna M. 2017. Control of Amygdala Circuits by 5-HT Neurons via 5-HT and Glutamate Cotransmission. J Neurosci. 37:1785–1796.

Shaner NC. 2014. Fluorescent proteins for quantitative microscopy: important properties and practical evaluation. Methods Cell Biol. 123:95–111.

Shoji H, Miyakawa T. 2018. Relationships between the acoustic startle response and prepulse inhibition in C57BL/6J mice: a large-scale meta-analytic study. Mol Brain. 11:42.

Shutoh F, Ina A, Yoshida S, Konno J, Hisano S. 2008. Two distinct subtypes of serotonergic fibers classified by co-expression with vesicular glutamate transporter 3 in rat forebrain. Neurosci Lett. 432:132–136.

Sipes TA, Geyer MA. 1994. Multiple serotonin receptor subtypes modulate prepulse inhibition of the startle response in rats. Neuropharmacology. 33:441–448.

Somogyi J, Baude A, Omori Y, Shimizu H, Mestikawy SE, Fukaya M, Shigemoto R, Watanabe M, Somogyi P. 2004. GABAergic basket cells expressing cholecystokinin contain vesicular glutamate transporter type 3 (VGLUT3) in their synaptic terminals in hippocampus and isocortex of the rat. Eur J Neurosci. 19:552–569.

Sorg BA, Berretta S, Blacktop JM, Fawcett JW, Kitagawa H, Kwok JCF, Miquel M. 2016. Casting a Wide Net: Role of Perineuronal Nets in Neural Plasticity. J Neurosci. 36:11459–11468.

Sörman E, Wang D, Hajos M, Kocsis B. 2011. Control of hippocampal theta rhythm by serotonin: Role of 5-HT2c receptors. Neuropharmacology. 61:489–494.

Sos KE, Mayer MI, Cserép C, Takács FS, Szőnyi A, Freund TF, Nyiri G. 2017. Cellular architecture and transmitter phenotypes of neurons of the mouse median raphe region. Brain Struct Funct. 222:287–299.

Specht EA, Braselmann E, Palmer AE. 2017. A Critical and Comparative Review of Fluorescent Tools for Live-Cell Imaging. Annu Rev Physiol. 79:93–117.

Spracklen AJ, Fagan TN, Lovander KE, Tootle TL. 2014. The pros and cons of common actin labeling tools for visualizing actin dynamics during Drosophila oogenesis. Dev Biol. 393:209–226.

Stack RF, Bayles CJ, Girard A-M, Martin K, Opansky C, Schulz K, Cole RW. 2011. Quality assurance testing for modern optical imaging systems. Microsc Microanal Off J Microsc Soc Am Microbeam Anal Soc Microsc Soc Can. 17:598–606.

Staubli U, Xu FB. 1995. Effects of 5-HT3 receptor antagonism on hippocampal theta rhythm, memory, and LTP induction in the freely moving rat. J Neurosci. 15:2445–2452.

Strüber M, Jonas P, Bartos M. 2015. Strength and duration of perisomatic GABAergic inhibition depend on distance between synaptically connected cells. Proc Natl Acad Sci. 112:1220–1225.

Swerdlow N, Geyer M, Braff D. 2001. Neural circuit regulation of prepulse inhibition of startle in the rat: current knowledge and future challenges. Psychopharmacology (Berl). 156:194–215.

Szeidemann Z, Shanabrough M, Leranth C. 1995. Hypothalamic Leu-enkephalin-immunoreactive fibers terminate on calbindin-containing somatospiny cells in the lateral septal area of the rat. J Comp Neurol. 358:573–583.
Szőnyi A, Mayer MI, Cserép C, Takács VT, Watanabe M, Freund TF, Nyiri G. 2016. The ascending median raphe projections are mainly glutamatergic in the mouse forebrain. Brain Struct Funct. 221:735–751.
Szőnyi A, Zichó K, Barth AM, Gönczi RT, Schlingloff D, Török B, Sipos E, Major A, Bardóczi Z, Sos KE, Gulyás AI, Varga V, Zelena D, Freund TF, Nyiri G. 2019a. Median raphe controls acquisition of negative experience in the mouse. Science. 366.
Szőnyi A, Zichó K, Barth AM, Gönczi RT, Schlingloff D, Török B, Sipos E, Major A, Bardóczi Z, Sos KE, Gulyás AI, Varga V, Zelena D, Freund TF, Nyiri G. 2019b. Median raphe controls acquisition of negative experience in the mouse. Science. 366.
Teissier A, Chemiakine A, Inbar B, Bagchi S, Ray RS, Palmiter RD, Dymecki SM, Moore H, Ansorge MS. 2015. Activity of Raphé Serotonergic Neurons Controls Emotional Behaviors. Cell Rep. 13:1965–1976.
Theer P, Mongis C, Knop M. 2014. PSFj: know your fluorescence microscope. Nat Methods. 11:981–982.
Tiger M, Varnäs K, Okubo Y, Lundberg J. 2018. The 5-HT1B receptor - a potential target for antidepressant treatment. Psychopharmacology (Berl). 235:1317–1334.
Tóth K, Freund TF. 1992. Calbindin D28k-containing nonpyramidal cells in the rat hippocampus: Their immunoreactivity for GABA and projection to the medial septum. Neuroscience. 49:793–805.
Tripathi PP, Giovannantonio LGD, Viegi A, Wurst W, Simeone A, Bozzi Y. 2008. Serotonin Hyperinnervation Abolishes Seizure Susceptibility in Otx2 Conditional Mutant Mice. J Neurosci. 28:9271–9276.
Tripodi M, Stepien AE, Arber S. 2011. Motor antagonism exposed by spatial segregation and timing of neurogenesis. Nature. 479:61–66.
Trudeau L-É. 2004. Glutamate co-transmission as an emerging concept in monoamine neuron function. J Psychiatry Neurosci. 29:296–310.
Trudeau L-E, El Mestikawy S. 2018. Glutamate Cotransmission in Cholinergic, GABAergic and Monoamine Systems: Contrasts and Commonalities. Front Neural Circuits. 12:113.
Trueta C, De-Miguel FF. 2012. Extrasynaptic exocytosis and its mechanisms: a source of molecules mediating volume transmission in the nervous system. Front Physiol. 3:319.
Tsanov M. 2018. Differential and complementary roles of medial and lateral septum in the orchestration of limbic oscillations and signal integration. Eur J Neurosci. 48:2783–2794.
Tse K, Puttachary S, Beamer E, Sills GJ, Thippeswamy T. 2014. Advantages of Repeated Low Dose against Single High Dose of Kainate in C57BL/6J Mouse Model of Status Epilepticus: Behavioral and Electroencephalographic Studies. PLoS ONE. 9.
Umpierre AD, Bennett IV, Nebeker LD, Newell TG, Tian BB, Thomson KE, White HS, White JA, Wilcox KS. 2016. Repeated low-dose kainate administration in C57BL/6J mice produces temporal lobe epilepsy pathology but infrequent spontaneous seizures. Exp Neurol. 279:116–126.
Vaaga CE, Borisovska M, Westbrook GL. 2014. Dual-transmitter neurons: Functional implications of co-release and co-transmission. Curr Opin Neurobiol. 0:25–32.

Varga V, Losonczy A, Zemelman BV, Borhegyi Z, Nyiri G, Domonkos A, Hangya B, Holderith N, Magee JC, Freund TF. 2009. Fast Synaptic Subcortical Control of Hippocampal Circuits. Science. 326:449–453.
Veres JM, Nagy GA, Hájos N. 2017. Perisomatic GABAergic synapses of basket cells effectively control principal neuron activity in amygdala networks. eLife. 6:e20721.
Verney C, Gaspar P, Alvarez C, Berger B. 1987. Postnatal sequential development of dopaminergic and enkephalinergic perineuronal formations in the lateral septal nucleus of the rat correlated with local neuronal maturation. Anat Embryol (Berl). 176:463–475.
Vertes RP. 1981. An analysis of ascending brain stem systems involved in hippocampal synchronization and desynchronization. J Neurophysiol. 46:1140–1159.
Vertes RP. 2005. Hippocampal theta rhythm: a tag for short-term memory. Hippocampus. 15:923–935.
Vicente NB, Zamboni JED, Adur JF, Paravani EV, Casco VH. 2007. Photobleaching correction in fluorescence microscopy images. J Phys Conf Ser. 90:012068.
Vigli D, Rusconi L, Valenti D, La Montanara P, Cosentino L, Lacivita E, Leopoldo M, Amendola E, Gross C, Landsberger N, Laviola G, Kilstrup-Nielsen C, Vacca RA, De Filippis B. 2019. Rescue of prepulse inhibition deficit and brain mitochondrial dysfunction by pharmacological stimulation of the central serotonin receptor 7 in a mouse model of CDKL5 Deficiency Disorder. Neuropharmacology. 144:104–114.
Vinogradova OS, Kitchigina VF, Kudina TA, Zenchenko KI. 1999. Spontaneous activity and sensory responses of hippocampal neurons during persistent theta-rhythm evoked by median raphe nucleus blockade in rabbit. Neuroscience. 94:745–753.
Vu DH, Törk I. 1992. Differential development of the dual serotoninergic fiber system in the cerebral cortex of the cat. J Comp Neurol. 317:156–174.
Wähle P, Meyer G, Albus K. 1986. Localization of NPY-immunoreactivity in the cat's visual cortex. Exp Brain Res. 61:364–374.
Wait EC, Reiche MA, Chew T-L. 2020. Hypothesis-driven quantitative fluorescence microscopy – the importance of reverse-thinking in experimental design. J Cell Sci. 133.
Wallace JA, Lauder JM. 1983. Development of the serotonergic system in the rat embryo: an immunocytochemical study. Brain Res Bull. 10:459–479.
Wan J, Peng W, Li X, Qian T, Song K, Zeng J, Deng F, Hao S, Feng J, Zhang P, Zhang Y, Zou J, Pan S, Shin M, Venton BJ, Zhu JJ, Jing M, Xu M, Li Y. 2021. A genetically encoded sensor for measuring serotonin dynamics. Nat Neurosci. 24:746–752.
Wang DV, Yau H-J, Broker CJ, Tsou J-H, Bonci A, Ikemoto S. 2015. Mesopontine median raphe regulates hippocampal ripple oscillation and memory consolidation. Nat Neurosci. 18:728–735.
Wang E, Babbey CM, Dunn KW. 2005. Performance comparison between the high-speed Yokogawa spinning disc confocal system and single-point scanning confocal systems. J Microsc. 218:148–159.
Wang F, Flanagan J, Su N, Wang L-C, Bui S, Nielson A, Wu X, Vo H-T, Ma X-J, Luo Y. 2012. RNAscope. J Mol Diagn JMD. 14:22–29.
Wang H-L, Zhang S, Qi J, Wang H, Cachope R, Mejias-Aponte CA, Gomez JA, Mateo-Semidey GE, Beaudoin GMJ, Paladini CA, Cheer JF, Morales M. 2019. Dorsal Raphe Dual Serotonin-

Glutamate Neurons Drive Reward by Establishing Excitatory Synapses on VTA Mesoaccumbens Dopamine Neurons. Cell Rep. 26:1128-1142.e7.
Wang L, Simms J, Peters CJ, Tynan-La Fontaine M, Li K, Gill TM, Jan YN, Jan LY. 2019. TMEM16B Calcium-Activated Chloride Channels Regulate Action Potential Firing in Lateral Septum and Aggression in Male Mice. J Neurosci. 39:7102–7117.
Waters JC. 2007. Live-cell fluorescence imaging. Methods Cell Biol. 81:115–140.
Waters JC. 2009. Accuracy and precision in quantitative fluorescence microscopy. J Cell Biol. 185:1135–1148.
Waters JC. 2020. A Novel Paradigm for Expert Core Facility Staff Training. Trends Cell Biol. 30:669–672.
Weber ET, Gannon RL, Rea MA. 1998. Local administration of serotonin agonists blocks light-induced phase advances of the circadian activity rhythm in the hamster. J Biol Rhythms. 13:209–218.
Whissell PD, Bang JY, Khan I, Xie Y-F, Parfitt GM, Grenon M, Plummer NW, Jensen P, Bonin RP, Kim JC. 2019. Selective Activation of Cholecystokinin-Expressing GABA (CCK-GABA) Neurons Enhances Memory and Cognition. eNeuro. 6.
Wolf DE, Samarasekera C, Swedlow JR. 2013. Quantitative analysis of digital microscope images. Methods Cell Biol. 114:337–367.
Woo S-H, Ranade S, Weyer AD, Dubin AE, Baba Y, Qiu Z, Petrus M, Miyamoto T, Reddy K, Lumpkin EA, Stucky CL, Patapoutian A. 2014. Piezo2 is required for Merkel-cell mechanotransduction. Nature. 509:622–626.
Wyler SC, Spencer WC, Green NH, Rood BD, Crawford L, Craige C, Gresch P, McMahon DG, Beck SG, Deneris E. 2016. Pet-1 Switches Transcriptional Targets Postnatally to Regulate Maturation of Serotonin Neuron Excitability. J Neurosci. 36:1758–1774.
Yan Q-S, Jobe PC, Cheong JH, Ko KH, Dailey JW. 1994. Role of serotonin in the anticonvulsant effect of fluoxetine in genetically epilepsy-prone rats. Naunyn Schmiedebergs Arch Pharmacol. 350:149–152.
Yang Z, Li L, Ling J, Liu T, Huang X, Ying Y, Zhao Y, Zhao Y, Lei K, Chen L, Chen Z. 2020. Cyclooctatetraene-conjugated cyanine mitochondrial probes minimize phototoxicity in fluorescence and nanoscopic imaging. Chem Sci. 11:8506–8516.
Yurino H, Tsukahara S, Korányi L, Yamanouchi K. 2001. Inhibitory Effect of Postpartum Lesions or Cuts in Median Raphe Nucleus on Maternal Behavior in Female Rats. Zoolog Sci. 18:1225–1230.
Zhang G, Stackman RW. 2015. The role of serotonin 5-HT2A receptors in memory and cognition. Front Pharmacol. 6.
Zhao M, Yang J, Wang W, Ma J, Zhang J, Zhao X, Qiu X, Yang X, Qiao Z, Song X, Wang L, Jiang S, Zhao E, Yang Y. 2017. Meta-analysis of the interaction between serotonin transporter promoter variant, stress, and posttraumatic stress disorder. Sci Rep. 7:16532.
Zhou J, Brown AM, Lackey EP, Arancillo M, Lin T, Sillitoe RV. 2020. Purkinje cell neurotransmission patterns cerebellar basket cells into zonal modules defined by distinct pinceau sizes. eLife. 9:e55569.